

Institut National de la Recherche Scientifique (INRS)
Centre Énergie, Matériaux et Télécommunications (EMT)

TERAHERTZ RADIATION FOR THE CHARACTERIZATION OF PLASMONIC NANOPARTICLES AND ITS BIOMEDICAL APPLICATIONS

by

Holger Breitenborn

A thesis submitted to obtain the degree of
Philosophy Doctor (Ph.D.)
in Energy and Materials Science

Jury Members

President of the Jury and Internal Reviewer	Prof. Annie Castonguay Armand-Frappier Santé Biotechnologie (AFSB) Institut National de la Recherche Scientifique, Laval, Canada
External Reviewer	Prof. Anie Philip Department of Surgery, Faculty of Medicine McGill University, Montreal, Canada
External Reviewer	Prof. Alina Karabchevsky Department of Electrooptics and Photonics Ben-Gurion University of the Negev, Beersheba, Israel
Research Director	Prof. Roberto Morandotti Énergie, Matériaux et Télécommunications (EMT) Institut National de la Recherche Scientifique, Montreal, Canada
Research Co-Director	Prof. Rafik Naccache Department of Chemistry and Biochemistry and Centre for NanoScience Research Concordia University, Montreal, Canada

ACKNOWLEDGMENTS

I am fortunate and grateful for having had the chance to pursue my Ph.D. in the group of my supervisor Prof. Roberto Morandotti. I benefitted from a wealth of opportunities and experiences, which helped me to develop various laboratory skills and diverse knowledge in optics and photonics, especially in ultrafast lasers and terahertz technology.

Additionally, I want to thank my co-supervisor, Prof. Rafik Naccache, for his guidance, suggestions, and the opportunity to use his characterization equipment often on short notice. Moreover, I also would like to acknowledge the generous support and insightful discussions with Prof. Luca Razzari and Prof. Fiorenzo Vetrone, who allowed me to use their laboratory and equipment as well.

My deepest gratitude goes to Dr. Junliang Dong and Dr. Riccardo Piccoli for their invaluable theoretical and practical support, companionship, and tremendous patience and effort in guiding me throughout my doctoral studies. Their contributions to conceptual and experimental activities were crucial for the success of my Ph.D. work. Many pleasurable and thought-provoking discussions with them have led to new ideas and personal growth.

I am indebted to Dr. Andrew Bruhacs and Dr. Lucas Vazquez Besteiro for their priceless contributions to the success of my thesis. It would have been impossible to get the study done without their assistance and expertise. A special acknowledgment goes to Dr. Alessandro Tomasino, with whom I spent numerous nights in the laboratory. He taught me many useful and practical skills while I was taking my first steps within the field of experimental optics at the beginning of my Ph.D. I also want to thank him for his friendship, invaluable support, and precious help in many other academic concerns.

Moreover, I want to acknowledge Artiom Skripka and Dr. Riccardo Marin for the supply of nanoparticles, characterization work, as well as for sharing their knowledge about a scientific field that had been new to me. Additionally, I want to thank Dr. Diego Caraffini for his programming efforts and resilience to help me make our THz-TDS system operating.

My special thanks go to Robin Helsten for the unconventional technical support, to Dr. Anna Mazhorova for her guidance at the beginning of my Ph.D. project, and Giacomo Balistreri for limitless coffee preparation.

I also would like to thank Dr. Yoann Jestin, Dr. Christian Reimer, and Piotr Roztocki, with whom I co-founded the university-spin off company Ki3 Photonics Technologies Inc.

I wish to thank my colleagues at Friedrich Schiller University and Fraunhofer Institute for Applied Optics and Precision Engineering IOF for a great time that we spent together during numerous activities in the framework of the international research training group of the DFG and the NSERC CREATE program in collaboration with INRS-EMT, University of Toronto and Laval University. In particular, I want to mention and acknowledge the support and friendship of Prof. Andreas Tünnermann and Prof. Stefan Nolte, who initiated my fruitful collaboration with Prof. Roberto Morandotti in 2013 and have generously supported my work and studies since then.

Finally, I wish to thank my parents, Adelheid and Jürgen Breitenborn, without whom my whole path would have been impossible. I am also deeply thankful to my wife, Maria Jose Lopez Perez, for her tremendous emotional and practical support, especially in difficult times during my Ph.D.

ABSTRACT

The precise evaluation of the photothermal effect of nanomaterials is an essential prerequisite for a variety of fields, such as biology, chemistry, and nanomedicine. In particular, photothermal therapies to destroy cancer cells require an accurate determination of the light conversion capabilities of plasmonic nanoparticles to attain the necessary temperature-induced effects in biological tissue. In this Ph.D. work, a new method has been developed for the quantification of the photothermal effect of nanoparticles in aqueous solutions. The photothermal conversion efficiency linked to the morphology of plasmonic nanoparticles was evaluated in a non-contact and non-invasive manner by combining spatial and temporal thermal dynamics derived at terahertz frequencies. The method is extendable to the characterization of all nanomaterials that experience a temperature-dependent variation of their refractive index in the terahertz frequency regime.

Moreover, the capabilities of the new method were extended to the biomedical realm to observe and evaluate nanoparticle-assisted laser tissue interaction. For example, laser tissue soldering assisted by plasmonic nanoparticles is a minimally invasive wound closure procedure that could replace commonly used, highly invasive sutures. The tissue fusing process is assisted by a nanoparticle-containing solder gel, which facilitates the absorption and transformation of laser energy into heat locally confined in the tissue edges. Meticulous monitoring of the photothermally heated solder and the tissue underneath is vital to minimize or even prevent photothermal damage inflicted by the intense laser radiation as well as optimize the tensile strength of the fused tissue. The new method constitutes a non-contact, non-invasive, and non-ionizing modality for evaluating photothermally induced damage enabled by the high sensitivity of terahertz radiation to the humidity content of biological tissue. Terahertz radiation was utilized to trace the evolution of the photothermal damage during the soldering procedure and to create a tomographic image allowing a quantitative evaluation of the incurred damage as a function of depth. In the future, this method could be implemented in a variety of medical applications that involve laser tissue interaction, including laser ablation and photothermal therapies.

Keywords: Terahertz Radiation, Terahertz Time-Domain Spectroscopy, Nanoparticles, Plasmonic Heating, Photothermal Heating, Photothermal Therapy, Photothermal Conversion Efficiency, Laser Tissue Interaction, Terahertz Biomedical Imaging, Terahertz Tomography

RÉSUMÉ

L'évaluation précise de l'effet photo-thermique des nanomatériaux est une condition fondamentale pour diverses applications, telles que la biologie, la chimie et la nano-médecine. En particulier, les thérapies photo-thermiques visant à détruire les cellules cancéreuses nécessitent une détermination précise des capacités de conversion lumineuse des nanoparticules plasmoniques utilisées, afin d'obtenir les effets nécessaires induits par la température dans les tissus biologiques considérés. Dans cette étude de doctorat, une nouvelle méthode a été développée pour la quantification de l'effet photo-thermique de nanoparticules dans des solutions aqueuses. L'efficacité de la conversion photo-thermique liée à la morphologie des nanoparticules plasmoniques a été évaluée de manière non-invasive et sans contact en combinant des dynamiques thermiques spatiales et temporelles dérivées à des fréquences térahertz. La méthode peut être étendue à la caractérisation de tous les nanomatériaux qui subissent une variation de leur indice de réfraction en fonction de la température dans le régime de fréquence térahertz. De plus, les capacités de la nouvelle méthode ont été étendues au domaine biomédical pour observer et évaluer les interactions laser-tissu assistées par nanoparticules. Par exemple, le soudage laser des tissus assisté par des nanoparticules plasmoniques est une procédure de fermeture de plaie peu invasive capable de remplacer les sutures très invasives couramment utilisées. Le processus de fusion tissulaire est assisté par un gel d'assemblage contenant des nanoparticules, ce qui facilite l'absorption et la transformation de l'énergie laser en chaleur localement confinée dans les bords du tissu. Un contrôle méticuleux de la soudure chauffée par photo-thermie et du tissu sous-jacent est essentiel pour minimiser ou même empêcher les dommages photo-thermiques causés par le fort rayonnement laser, ainsi que pour optimiser la résistance à la traction du tissu fondu. Par conséquent, la nouvelle méthode constitue une modalité sans contact, non-invasive et non-ionisante pour évaluer les dommages induits par photo-thermie rendus possibles par la sensibilité élevée du rayonnement térahertz à la teneur en humidité du tissu biomédical. Le rayonnement térahertz a été utilisé pour suivre l'évolution des dommages photo-thermiques au cours de la procédure de soudage et pour créer une image tomographique permettant une évaluation quantitative de la profondeur des dommages. Cette méthode peut être rapidement étendue et déployée pour une variété d'applications médicales impliquant une interaction laser-tissu, par exemple l'ablation au laser et les thérapies photo-thermiques.

Mots-clés: rayonnement térahertz, spectroscopie térahertz temps-domaine, nanoparticules, chauffage plasmonique, chauffage photo-thermique, thérapie photo-thermique, efficacité de la conversion photo-thermique, interaction laser-tissu, imagerie biomédicale THz, tomographie THz

TABLE OF CONTENTS

ACKNOWLEDGMENTS	III
ABSTRACT	V
RÉSUMÉ	VII
TABLE OF CONTENTS	IX
LIST OF FIGURES	XI
LIST OF TABLES	XIX
LIST OF EQUATIONS	XXI
LIST OF ABBREVIATIONS	XXVII
1 INTRODUCTION	1
1.1 MOTIVATION AND OBJECTIVES.....	1
1.2 SCOPE OF THE THESIS.....	3
1.3 TERAHERTZ RADIATION.....	5
1.3.1 THz Generation by using Photoconductive Antennas (PCAs)	7
1.3.2 THz Time-Domain Spectroscopy (THz-TDS)	10
1.3.3 THz Imaging.....	12
1.4 NANOPARTICLES	21
1.4.1 Localized Surface Plasmon Resonance Effect (LSPR)	23
1.4.2 Quantification of the Photothermal Effect of Nanoparticles	26
1.4.3 Photothermal Conversion Based Therapy for Wound Closure Procedures	29
2 CHARACTERIZATION OF THE PHOTOTHERMAL EFFECT OF PLASMONIC NANOPARTICLES BY TERAHERTZ LIGHT	33
2.1 SETUP FOR NANOPARTICLE CHARACTERIZATION AND IMAGING	33
2.2 DECONVOLUTION ALGORITHMS AND SIGNAL SELF-REFERENCING METHOD	35
2.2.1 Sparse Deconvolution Algorithm.....	36
2.2.2 Frequency-Wavelet Domain Deconvolution (FWDD)	39
2.2.3 Signal Self-Referencing Method	41
2.3 THEORETICAL MODEL FOR THE DETERMINATION OF THE PHOTOTHERMAL CONVERSION EFFICIENCY	42
2.4 GOLD NANOROD DISPERSIONS FOR BENCHMARK TESTS	45
2.5 CALIBRATION CURVE FOR TEMPERATURE MEASUREMENTS USING THZ-TDS	47
2.6 QUANTIFICATION OF THE PHOTOTHERMAL EFFECT VIA THZ-TDS.....	51
2.7 CHARACTERIZATION OF THE PHOTOTHERMAL EFFECTS OF COPPER SULFIDE NANOPARTICLE DISPERSIONS	60
2.8 ACCESSING THE SECOND BIOLOGICAL WINDOW BY EFFICIENT BROADBAND OPTICAL PARAMETRIC AMPLIFICATION IN NON-UNIFORM BULK CRYSTALS	68

3	THREE-DIMENSIONAL MONITORING OF NANOPARTICLE-ASSISTED LASER TISSUE SOLDERING BY TERAHERTZ LIGHT	75
3.1	SPATIOTEMPORAL HEAT TRANSFER MODELLING OF NANOPARTICLE-ASSISTED LASER TISSUE INTERACTION.....	77
3.2	DYNAMIC THZ INVESTIGATION OF NANOPARTICLE-ASSISTED LASER TISSUE INTERACTION	81
3.3	THZ THREE-DIMENSIONAL CHARACTERIZATION OF NANOPARTICLE-ASSISTED LASER TISSUE SOLDERING	88
4	CONCLUSION.....	97
5	BIBLIOGRAPHY	101
6	ANNEX I	117
6.1	ARTICLES PUBLISHED IN PEER-REVIEWED SCIENTIFIC JOURNALS	117
6.2	CONFERENCE PROCEEDINGS	117
6.3	FILED PATENT	119
	SOMMAIRE RÉCAPITULATIF.....	121
1.	MOTIVATION ET OBJECTIFS.....	121
2.	RADIATION TERAHERTZ.....	123
3.	NANOPARTICLES PLASMONIQUES	125
4.	QUANTIFICATION DE L'EFFET PHOTO-THERMIQUE DES NANOPARTICULES	127
5.	THÉRAPIE À BASE DE CONVERSION PHOTO-THERMIQUE POUR LES PROCÉDURES DE FERMETURE DE PLAIE	133

LIST OF FIGURES

FIGURE 1.1: ELECTROMAGNETIC SPECTRUM HIGHLIGHTING THE THZ FREQUENCY SECTION. (ADAPTED FROM THE NATIONAL INSTITUTE OF INFORMATION AND COMMUNICATIONS TECHNOLOGY (NICT)).....	6
FIGURE 1.2: TEMPERATURE-DEPENDENT (A) REFRACTIVE INDEX AND (B) ABSORPTION COEFFICIENT OF WATER IN THE THZ FREQUENCY REGIME. (FIGURE ADAPTED FROM REFERENCES [25], [26])	7
FIGURE 1.3: SCHEMATIC REPRESENTATION OF (A) THE WORKING PRINCIPLE OF A PHOTOCONDUCTIVE SWITCH IN WHICH A PHOTOCURRENT FLOWS THROUGH THE CIRCUIT WHEN LIGHT GENERATES FREE ELECTRONS AND HOLES. (FIGURE ADAPTED FROM REFERENCE [37]). (B) A PCA BIASED WITH A DC VOLTAGE AND ILLUMINATED BY A FEMTOSECOND LASER PULSE GENERATES SUB-PICOSECOND THZ TRANSIENTS. (FIGURE ADAPTED FROM REFERENCE [38]).....	8
FIGURE 1.4: ILLUSTRATIVE EXAMPLE OF A PCA FOR BROADBAND GENERATION AND DETECTION OF THZ PULSES. (FIGURE ADAPTED FROM REFERENCE [25])	9
FIGURE 1.5: (A) SCHEMATIC DIAGRAM FOR A TIME-RESOLVED MEASUREMENT OF THZ ELECTRIC FIELDS BY USING A PCA RECEIVER. (B) THE SIDE VIEW OF A PCA SHOWS A HIGH RESISTIVITY SILICON LENS ATTACHED IN FRONT OF THE SEMICONDUCTOR CHIP TO STRONGLY FOCUS THE INCIDENT THZ RADIATION INTO THE GAP BETWEEN THE TWO ELECTRODES. (FIGURES ADAPTED FROM REFERENCE [37]).....	10
FIGURE 1.6: THZ TIME-DOMAIN SPECTROSCOPY SETUPS BASED ON PCAs IN (A) TRANSMISSION AND (B) REFLECTION CONFIGURATION. FEMTOSECOND LONG PULSES EMANATED FROM A LASER SYSTEM ARE SPLIT AT A BEAM SPLITTER AND GUIDED TO THE THZ TRANSMITTER AND RECEIVER. THE PROBE PULSE BEAM IS OPTICALLY DELAYED BY A TRANSLATION STAGE TO ALTER ITS ARRIVAL TIME WITH RESPECT TO THE THZ PULSE BEAM AT THE THZ RECEIVER.	11
FIGURE 1.7: A) REPRESENTATIVE REFERENCE THZ TRANSIENT AND ITS B) SPECTRUM OF THE THZ TIME-DOMAIN SPECTROSCOPY SYSTEM USED TO PERFORM THE EXPERIMENTS IN CHAPTERS 2 AND 3.	12
FIGURE 1.8: (A) THZ TRANSIENT IN THE TIME-DOMAIN AND ITS FOURIER TRANSFORMATION IN THE (B) FREQUENCY DOMAIN. THE PLOTS HIGHLIGHT SPECIFIC FEATURES, WHICH CAN BE CHOSEN TO GENERATE CONTRAST IN ORDER TO CONSTRUCT A TWO-DIMENSIONAL THZ IMAGE PIXEL BY PIXEL. (FIGURES ADAPTED FROM REFERENCE [42])... ..	12
FIGURE 1.9: THZ-ToF IMAGING IN REFLECTION MODE, THE TEMPORAL POSITIONS OF THE REFLECTED THZ ECHOES CAN BE USED FOR THICKNESS CALCULATIONS AND TO INTERROGATE MATERIAL PROPERTIES IN A BI- OR MULTILAYER STRUCTURE. (A) DIGITAL IMAGE OF A THZ REFLECTION SCHEME USED IN CHAPTER 2. AN INCIDENT THZ PULSE ENCOUNTERS A CUVETTE CONTAINING A GNR DISPERSION UNDER STUDY. THE PULSES ARE BEING PARTLY TRANSMITTED AND REFLECTED FROM BOTH THE CUVETTE'S SURFACE AND THE INTERNAL INTERFACE, WHICH CREATES TWO DISTINCT THZ REFLECTION ECHOES. AN X-Y TRANSLATION STAGE IMPARTS IMAGING CAPABILITIES. (B) CROSS-SECTION OF A BILAYER STRUCTURE CONTAINING A PE CUVETTE WINDOW AND AN AQUEOUS NP	

DISPERSION. (C) TIME-DOMAIN PLOT DEPICTING A THZ TRACE WITH SEVERAL ECHOES ORIGINATING FROM THE AIR/PE SURFACE, THE PE/NP DISPERSION INTERFACE, AND ITS SECOND-ROUND REFLECTION DUE TO THE ETALON EFFECT. 14

FIGURE 1.10: (A) THZ MAP DISPLAYING THE COATING THICKNESS OF A MULTILAYER STRUCTURE OF AN M&M CHOCOLATE TABLET. (B) DIGITAL IMAGE OF THE CROSS-SECTION OF THE CHOCOLATE TABLET. (C) THZ B-SCAN OF THE TABLET REFERRING TO THE TABLET'S CROSS-SECTION. (FIGURES ADAPTED FROM REFERENCE [46]) 15

FIGURE 1.11: 0.1 THZ TRANSMISSION IMAGE OF A COMPUTER BAG CONTAINING TWO GUNS (FIGURES ADAPTED FROM REFERENCE [42]) 16

FIGURE 1.12: THZ IMAGE OF A SEMICONDUCTOR INTEGRATED CIRCUIT CHIP PACKAGED IN PLASTIC MATERIAL 16

FIGURE 1.13: (A) DIGITAL IMAGE OF THE MASTERPIECE TITLED *AFTER FISHING* BY AUSONIO TANDA. (B) THZ C-SCAN IMAGE HIGHLIGHTING DEFECT SPOTS. (C) THZ B-SCAN IMAGE OF THE CROSS-SECTION AT POSITION Y=176. THE DEFECT SPOTS ARE DISCERNIBLE AND MARKED. THEIR POSITION AND DEPTH WITHIN THE STRATIGRAPHY IS NOW UNVEILED (FIGURES ADAPTED FROM REFERENCE [48]) 17

FIGURE 1.14: THZ IMAGES OF A RAT SKIN BURN *IN VIVO*: (A) UNBURNED SKIN. (B) BURNED SKIN AFTER 10 MIN. (C) BURNED SKIN AFTER 1:16 H. (C) BURNED SKIN AFTER 7:11 H. THE LIGHTER AREAS CORRESPOND TO EDEMATOUS RESPONSE AREAS POST-BURN DUE TO THE HIGHER REFLECTED THZ SIGNAL OF LOCAL WATER. (FIGURES ADAPTED FROM REFERENCE [52]) 18

FIGURE 1.15: THE FIRST *IN VIVO* MEASUREMENTS OF A BASAL CELL CARCINOMA: (A) DIGITAL IMAGE OF THE CANCER REGION. (B) THZ IMAGE GENERATED BY PLOTTING THE THZ VALUE AT *E_{min}*, SHOWING SURFACE FEATURES. (C) NORMALIZED THZ IMAGE CREATED BY PLOTTING THE THZ PEAK AT THE OPTICAL DELAY OF 2.8 PS. HERE, THZ RADIATION PENETRATES BELOW THE SURFACE AND REVEALS SUBSURFACE FEATURES INDICATING THE EXTENT OF THE TUMOR AT DEPTH (~ 250 MM). (D) THZ TIME-DOMAIN TRACE ILLUSTRATES THE THZ CONTRAST BETWEEN HEALTHY AND DISEASED TISSUE. (FIGURES ADAPTED FROM REFERENCE [54]) 19

FIGURE 1.16: CANCER CELL IMAGES WITH AND WITHOUT GNRS: (A) DIGITAL IMAGE. (B) THZ IMAGE WITHOUT IR IRRADIATION. (C) THZ IMAGE WITH IR IRRADIATION. THE THZ AMPLITUDE IS THE HIGHEST FOR THE SAMPLE CONTAINING GNRS UNDER IR LASER IRRADIATION. (FIGURE ADAPTED FROM REFERENCE [57]) 19

FIGURE 1.17: *IN VIVO* AND *EX VIVO* THZ IMAGES OF TUMORS AFTER INJECTION OF GNRS CONJUGATED WITH A TUMOR-CELL TARGETING RECEPTOR IN THE CIRCULATORY SYSTEM OF A MOUSE: (A) AND (B) DIGITAL IMAGES OF THE MOUSE WITH A TUMOR. (C) THZ MOLECULAR IMAGE OF (B). (D) DIGITAL IMAGES OF THE TUMOR, LIVER, SPLEEN, KIDNEY, AND BRAIN. (E) THZ IMAGES OF (D), THE GNRS AGGREGATED IN THE CANCER CELLS, LIVER, AND SPLEEN. (FIGURES ADAPTED FROM REFERENCE [59]) 20

FIGURE 1.18: TERAMOMETRY (TEMPERATURE MEASUREMENTS BY USING THZ RADIATION) FOR THERMAL IMAGING OF PORCINE SKIN *IN VITRO*: (A) DIGITAL IMAGE DEPICTING THE PORCINE SKIN, INCLUDING THE GNR AND IBUPROFEN INJECTION SITES AS WELL AS THE MARKED SCANNING AREA. (B) THERMAL MAP OBTAINED UNDER PLASMONIC

HEATING BY NIR LASER ILLUMINATION, PLOTTING THE THERMAL DISTRIBUTION AROUND THE INJECTION SITE. (C) THZ IMAGE OF THE SPECTRAL DISTRIBUTION OF AN IBUPROFEN DRUG COMPOUND SUBCUTANEOUSLY INJECTED INTO THE SKIN (FIGURES ADAPTED FROM REFERENCE [60])..... 21

FIGURE 1.19: A) SCHEMATIC ILLUSTRATION OF THE LSPR ARISING FROM THE COHERENT OSCILLATION OF CONDUCTION BAND ELECTRONS IN RESONANCE WITH INCIDENT LIGHT FOR A SPHERICAL NP. B) A TYPICAL LSPR ABSORBANCE SPECTRUM OF A SPHERICAL NP. (FIGURES ADAPTED FROM REFERENCES [83], [86])..... 23

FIGURE 1.20: THE SEQUENCE OF EVENTS AND TIME SCALES FOLLOWING THE ABSORPTION OF PHOTONS BY NPs. (FIGURE ADAPTED FROM REFERENCE [87]) 24

FIGURE 1.21: PLOT OF THE WAVELENGTH-DEPENDENT EFFECTIVE ATTENUATION COEFFICIENT OF BIOLOGICAL TISSUE HIGHLIGHTING THE TWO BIOLOGICAL WINDOWS. (FIGURE ADAPTED FROM REFERENCE [90]) 25

FIGURE 1.22: SCHEMATIC ILLUSTRATION OF THE (A) LONGITUDINAL AND TRANSVERSE LSPR OF A ROD-SHAPED NP. (B) A TYPICAL LSPR ABSORBANCE SPECTRUM OF A GNR EXHIBITING THE TRANSVERSE AND LONGITUDINAL LSPR PEAKS. (FIGURES ADAPTED FROM REFERENCES [83], [86]) 25

FIGURE 1.23: (A) – (F) TEM IMAGES OF GNRs HAVING AN ASPECT RATIO OF (A) 1.2 (B) 1.7 (C) 2.4 (D) 3.3 (E) 4.2 (F) 5.3 (G) EXTINCTION SPECTRA OF THE GNRs (A) TO (F) ILLUSTRATING THE EFFECT OF THE GNR'S ASPECT RATIO CHANGE ON THE POSITION OF THE LONGITUDINAL LSPR PEAK. (FIGURES ADAPTED FROM REFERENCE [91]) 26

FIGURE 1.24: EXPERIMENTAL SETUP FOR MEASURING THE TEMPERATURE PROFILE OF GOLD NP SOLUTIONS: (A) BY USING A THERMOCOUPLE (FIGURE ADAPTED FROM REFERENCE [8]). (B) BY USING IR THERMOGRAPHY (FIGURE ADAPTED FROM REFERENCE [9])..... 27

FIGURE 1.25: WOUND CLOSING STUDY OVER 9 DAYS OF SEVERAL SKIN INCISIONS MADE IN MICE *IN VIVO*: (A) CONTROL SAMPLE (NO TREATMENT). INCISIONS WERE CLOSED BY USING: (B) LASER-ASSISTED TISSUE SOLDERING, (C) MEDICAL SUTURING, (D) LASER-ASSISTED TISSUE SOLDERING INVOLVING A NP-PROTEIN COMPOUND. (FIGURE ADAPTED FROM REFERENCE [14])..... 30

FIGURE 2.1: (A) SKETCH OF THE THZ PART IN THE THZ-TDS SETUP CONFIGURED IN REFLECTION GEOMETRY USED TO CHARACTERIZE THE PHOTOTHERMAL EFFECT OF NP DISPERSIONS. (B) GAUSSIAN BEAM INTENSITY PROFILE OF THE THZ FOCUS SPOT..... 33

FIGURE 2.2: DIGITAL IMAGE OF THE THZ PART IN THE THZ-TDS SETUP CONFIGURED IN REFLECTION GEOMETRY, SHOWN IN FIGURE 2.1(A). 34

FIGURE 2.3: THE THZ AMPLITUDES OF THE 1ST AND 2ND ECHOES BEFORE AND AFTER SIGNAL PROCESSING. (FIGURE ADAPTED FROM REFERENCE [137])..... 42

FIGURE 2.4: DIGITAL IMAGES OF THE SAMPLE CUVETTE CONTAINING THE DISPERSED GNRs WITH THE DIMENSIONS OF (A) 10 NM X 41 NM, (B) 25 NM X 90 NM, AND (C) 50 NM X 150 NM, AS WELL AS THEIR REPRESENTATIVE TEM IMAGES. (D) VIS-NIR ABSORBANCE SPECTRA OF THE THREE GNR DISPERSIONS HIGHLIGHTING THE LASER

EMISSION LINE AT 786 NM AT WHICH THE GNRs WERE PLASMONICALLY EXCITED DURING THE EXPERIMENTS. (FIGURES ADAPTED FROM REFERENCE [137]) 46

FIGURE 2.5: (A) SCHEMATIC DIAGRAM OF THz TEMPERATURE MEASUREMENTS BASED ON A THz-TDS SYSTEM IN REFLECTION GEOMETRY DEPICTING AN ULTRAFAST LASER SYSTEM EMITTING A PULSE TRAIN THAT WAS SPLIT BY A BEAM SPLITTER (BS) INTO A PUMP AND PROBE BEAM AND SUBSEQUENTLY GUIDED TO THE THz EMITTER AND DETECTOR, RESPECTIVELY. THE PROBE BEAM PASSED THROUGH A TEMPORAL DELAY IN ORDER TO PERFORM THz-TDS. A 786-NM CW NIR LASER BEAM USED TO PLASMONICALLY HEAT THE GNR DISPERSIONS WAS OVERLAPPED WITH THE THz FOCUSING SPOT. THE POWER OF THE NIR ILLUMINATION TRANSMITTED THROUGH THE CUVETTE WAS RECORDED WITH A POWER METER. (B) SCHEMATIC DIAGRAM DEPICTING THE THz RASTER-SCAN IMAGING PROCESS OF THE FRONT AND REAR WINDOW OF THE CUVETTE. DURING THE SCANNING PROCESS, THE THz BEAM WAS RIGID, AND THE CUVETTE MOVED TOGETHER WITH THE NIR LASER PIXEL-BY-PIXEL. (FIGURES ADAPTED FROM REFERENCE [137]) 48

FIGURE 2.6: REPRESENTATIVE EXAMPLE OF A RECORDED THz TRANSIENT REFLECTED OFF THE CUVETTE. THE SEPARATED 1ST AND 2ND ECHO AFTER APPLYING A SPARSE DECONVOLUTION ALGORITHM ARE ALSO DISPLAYED, IN WHICH THE INFLUENCE OF THE “RINGING” EFFECT DUE TO THE AMBIENT WATER VAPOR IN THE AIR WAS ELIMINATED. (FIGURE ADAPTED FROM REFERENCE [137]) 49

FIGURE 2.7: TEMPERATURE-DEPENDENT REFLECTIVITY OF THE 2ND THz ECHO AS A FUNCTION OF TEMPERATURE FOR GNR10. (A) TIME-DOMAIN TRACE OF THE THREE THz ECHOES HIGHLIGHTING THE MODIFICATION ON THE 2ND ECHO INTRODUCED BY THE PHOTOTHERMAL HEATING EFFECT. (B) CLOSE-UP OF THE 2ND ECHO HIGHLIGHTING ITS MODIFICATIONS AS A FUNCTION OF THE STEADY-STATE TEMPERATURE VALUE OF THE NP DISPERSION. (FIGURES ADAPTED FROM REFERENCE [137])..... 49

FIGURE 2.8: CALIBRATION CURVES FEATURING A LINEAR THERMOMETRIC RELATIONSHIP BETWEEN THz AMPLITUDE AND TEMPERATURE FOR EACH OF THE GNR DISPERSIONS. (FIGURE ADAPTED FROM REFERENCE [137]) 51

FIGURE 2.9: TYPICAL TEMPERATURE TRANSIENTS MEASURED BY THz-TDS. THE PROCEDURE AND PARAMETERS WERE THE SAME FOR EACH OF THE THREE GNR DISPERSIONS. A CONSTANT NIR LASER INTENSITY OF 31.8 W/cm² WAS EXERTED FOR 12 MINUTES TO RECORD THE HEATING CURVE. THEN, THE LASER WAS TURNED OFF TO OBTAIN THE COOLING CURVE. (FIGURE ADAPTED FROM REFERENCE [137])..... 53

FIGURE 2.10: EXTRACTION OF THE HEAT DISSIPATION RATE **B** AND THE ENERGY ABSORPTION RATE **A** BY FITTING THE EXPERIMENTAL DATA (SYMBOLS) WITH EQUATION 2.24 FOR EACH OF THE THREE GNR DISPERSIONS. THE FITTING RESULTS (SOLID LINES) FOR THE COOLING CYCLES ARE SHOWN IN (A1), (B1), AND (C1), AND THE FITTING RESULTS (SOLID LINES) FOR THE HEATING CYCLES ARE SHOWN IN (A2), (B2), AND (C2), ACCORDINGLY. (FIGURES ADAPTED FROM REFERENCE [137])..... 54

FIGURE 2.11: THz IMAGING SETUP CONFIGURATION IN REFLECTION GEOMETRY. BOTH THE CUVETTE AND THE NIR LASER ARE ATTACHED TO THE SAME CAGE STRUCTURE THAT CAN BE MOVED BY AN X-Y TRANSLATION STAGE. THIS GEOMETRY ALLOWED THEM TO TRAVERSE TOGETHER ACROSS THE THz BEAM..... 54

FIGURE 2.12: THZ THERMOGRAPHS OF THE GNR10 DISPERSION TAKEN BY USING THZ-TDS RASTER-SCANS ILLUSTRATING THE THERMAL DISTRIBUTION WHEN THE STEADY-STATE LEVEL BY PLASMONIC HEATING WAS REACHED. (A) DIGITAL IMAGE OF THE FRONT SURFACE OF THE CUVETTE WITH THE LASER SPOT MARKED IN RED. THZ THERMOGRAPHS OF THE TEMPERATURE DISTRIBUTION ΔT (RELATIVE TO THE AMBIENT VALUE) OF (B) THE FRONT AND (C) REAR WINDOW OF THE CUVETTE. (FIGURES ADAPTED FROM REFERENCE [137]) 55

FIGURE 2.13: EXPERIMENTALLY ATTAINED PCEs η (RED BARS) AND MHR (ORANGE BARS) OF THE THREE GNR DISPERSIONS WITH PARTICLE DIMENSIONS OF 10 NM X 41 NM, 25 NM X 90 NM, AND 50 NM X 150 NM. FURTHERMORE, THE PCEs APPROXIMATED BY THE THEORETICAL INTERACTION CROSS-SECTIONS ARE DISPLAYED AS WELL (PINK BARS). (FIGURE ADAPTED FROM REFERENCE [137]) 56

FIGURE 2.14: (A) SCHEMATIC ILLUSTRATION DEPICTING THE FUNDAMENTAL PROPERTIES PRESENTED IN FIGURE 2.13, ESPECIALLY THE RISE IN OVERALL EXTINCTION PER NP AND INCREASING SIGNIFICANCE OF SCATTERING AS THE NP VOLUME ENLARGES. (B) THEORETICAL EXTINCTION CROSS-SECTIONS σ_{ext} OF THE THREE GNR DIMENSIONS AND THE RATIO BETWEEN THEIR SCATTERING CROSS-SECTIONS σ_{scat} TO THE TOTAL EXTINCTION. (FIGURES ADAPTED FROM REFERENCE [137]) 57

FIGURE 2.15: THEORETICAL ASSESSMENT OF THE PCEs η , CALCULATED BY USING EQUATION 2.32, CONSIDERING THE CALCULATED CROSS-SECTIONS AND THE ABSORPTION COEFFICIENT OF WATER μ_{water} , ALSO SHOWN IN THIS PANEL. CHOOSING AN IRRADIATION WAVELENGTH OUTSIDE THE ABSORPTION LINES OF WATER IS CRUCIAL FOR EFFICIENT LOCALIZED HEAT DELIVERY. (FIGURE ADAPTED FROM REFERENCE [137]) 59

FIGURE 2.16: REPRESENTATIVE TEM IMAGES OF THE CUS NP DISPERSIONS WITH DIFFERENT CAPPING LIGANDS: (A) CUS CTAB. (B) CUS PAA. (C) CUS PEG. 61

FIGURE 2.17: VIS-IR SPECTROSCOPY ANALYSIS OF (A) THE STOCK DISPERSIONS. (B) DISPERSIONS ADJUSTED TO AN ABSORBANCE VALUE OF 0.8 AT 976 NM BY DILUTION WITH DEIONIZED WATER. 61

FIGURE 2.18: (A) THZ PROPAGATION IN REFLECTION GEOMETRY THROUGH THE INTERFACES AIR/PE AND PE/NP DISPERSION. (B) THE RESULTING TWO REFLECTED THZ PULSE ECHOES IN THE TIME-DOMAIN ARE STRONGLY OVERLAPPED. 63

FIGURE 2.19: TIME-DOMAIN PLOTS OF THE TEMPERATURE CALIBRATION MEASUREMENTS. THE DECONVOLVED 2ND THZ REFLECTION ECHO ORIGINATING FROM THE PE/NP DISPERSION INTERFACE EXHIBITS A CHANGE IN THE AMPLITUDE DEPENDING ON THE TEMPERATURE VALUE. 64

FIGURE 2.20: (A) DECONVOLVED 1ST ECHO ORIGINATING FROM THE AIR/PE INTERFACE. (B) DECONVOLVED 2ND THZ ECHO FROM THE PE/NP DISPERSION INTERFACE CLEANED FROM THE INTERFERENCE WITH THE 1ST THZ ECHO. . 64

FIGURE 2.21: CALIBRATION MEASUREMENTS: (A) DIGITAL IMAGE OF THE THERMOELECTRIC HEATING/COOLING ELEMENT ATTACHED TO THE CUSTOM-MADE CUVETTE. (B) CALIBRATION CURVES FOR THE THREE CUS NP DISPERSIONS BETWEEN 22 °C AND 40 °C ILLUSTRATING THE THERMOMETRIC RELATIONSHIP BETWEEN TEMPERATURE AND THZ AMPLITUDE. 65

FIGURE 2.22: DIGITAL IMAGE OF THE CUSTOM-MADE CUVETTE ATTACHED TO A SAMPLE HOLDER AND ILLUMINATED BY A NIR LASER BEAM OF 976 NM WAVELENGTH. 66

FIGURE 2.23: TIME-RESOLVED HEATING CURVES AT A NIR POWER INTENSITY OF 0.68 W/CM²: (A) CHANGE IN THZ REFLECTIVITY WITH TIME. (B) THZ REFLECTIVITY CORRELATION WITH TEMPERATURE USING THE CALIBRATION VALUES OF EACH CuS NP SYSTEM. (C) TEMPERATURE CHANGE NORMALIZED TO THE Cu ION CONCENTRATION OF THE THREE DISPERSIONS. 67

FIGURE 2.24: NORMALIZED PARTICLE SIZE DISTRIBUTION OF THE THREE CuS NP DISPERSIONS DERIVED FROM A DLS ANALYSIS. 67

FIGURE 2.25: (A) FLOW DIAGRAM OF THE TWM PROCESS IN A NONLINEAR MEDIUM ILLUSTRATING THE INPUT AND OUTPUT LASER BEAMS HAVING DIFFERENT FREQUENCIES. (B) ENERGY DIAGRAM OF THE TWM PROCESS, WHICH CAN BE PERCEIVED AS STIMULATED EMISSION OF SIGNAL PHOTONS FROM A VIRTUAL ENERGY LEVEL EXCITED BY THE PUMP. (FIGURE ADAPTED FROM REFERENCE [158]) 69

FIGURE 2.26: A) SIMULATED CONVERSION EFFICIENCIES AS A FUNCTION OF WAVELENGTH FOR THREE TEMPERATURE DISTRIBUTIONS INSIDE AN LBO CRYSTAL. EXPONENTIAL (RED LINE) AND LINEAR (GREEN LINE) TEMPERATURE GRADIENTS HAVING A TEMPERATURE CONTRAST OF 60 °C (100 °C – 160 °C) ARE COMPARED TO THE CONSTANT TEMPERATURE PROFILE OF 130 °C (BLACK LINE). B) MODELED CONVERSION EFFICIENCIES AS A FUNCTION OF WAVELENGTH FOR DIFFERENT LINEAR TEMPERATURE DISTRIBUTIONS INSIDE AN LBO CRYSTAL. TEMPERATURE CONTRASTS OF 40 °C (110 °C – 150 °C) AND 60 °C (100 °C – 160 °C) POSSESS THE HIGHEST CONVERSION EFFICIENCY AND BANDWIDTH. (FIGURES ADAPTED FROM REFERENCE [157])..... 71

FIGURE 2.27: SCHEMATIC REPRESENTATION OF THE EXPERIMENTAL SETUP. A PUMP AND A SEED BEAM WERE GUIDED THROUGH THE LEFT FACET OF AN LBO CRYSTAL WITH AN APPLIED TEMPERATURE GRADIENT ALONG ITS LENGTH. AFTER EXITING THE CRYSTAL, THE RESIDUAL DEPLETED PUMP BEAM WAS BLOCKED BY A LONG-PASS FILTER, WHEREAS A PHOTODIODE MEASURED THE AMPLIFIED SIGNAL WAVE. (FIGURE ADAPTED FROM REFERENCE [157]) 72

FIGURE 2.28: A CUSTOMIZED CRYSTAL HOLDER FEATURING FOUR EQUIDISTANTLY SPACED THERMOELECTRIC HEATERS AND THEIR RESPECTIVE THERMISTORS FOR TEMPERATURE CONTROL DIRECTLY CONNECTED TO THE CRYSTAL SURFACE. (FIGURE ADAPTED FROM REFERENCE [157]) 73

FIGURE 2.29: MEASURED CONVERSION EFFICIENCIES AS A FUNCTION OF THE SEED BEAM WAVELENGTH: A) EXPONENTIAL AND LINEAR TEMPERATURE GRADIENTS (100 °C TO 160 °C). B) LINEAR TEMPERATURE GRADIENTS (EACH CENTERED AROUND 130 °C HAVING A DIFFERENT TOTAL TEMPERATURE CONTRAST) AND A CONSTANT TEMPERATURE OF 130 °C. (FIGURES ADAPTED FROM REFERENCE [157]) 74

FIGURE 3.1: SCHEMATIC DEPICTION OF TISSUE EXCISED FROM PORCINE EAR SKIN PLOTTING DIFFERENT STAGES OF PHOTOTHERMAL REACTIONS DURING A NP-ASSISTED LASER TISSUE SOLDERING PROCESS. ADDITIONALLY, A THZ MULTIDIMENSIONAL IMAGING MODALITY IS DISPLAYED REPRESENTED BY AN INCOMING THZ REFERENCE PULSE BEING REFLECTED MULTIPLE TIMES OFF VARIOUS INTERFACES. THIS PRODUCES A TRAIN OF CONVOLVED THZ

ECHOES CONTAINING MULTIDIMENSIONAL INFORMATION THAT IS REQUIRED TO ASSESS THE DEPTH AND SEVERITY OF THE PHOTOTHERMAL DAMAGE, WHICH WAS INFLICTED ON THE SKIN INCISION AREA BY NIR LASER IRRADIATION. (FIGURE ADAPTED FROM REFERENCE [166]) 75

FIGURE 3.2: (A) SCHEMATIC DIAGRAM OF THE NP-ASSISTED LASER TISSUE INTERACTION PROCESS CREATED BY A FINITE ELEMENT MODEL ENCOMPASSING A TWO-LAYER STRUCTURE MADE OF SOLDER GEL AND SKIN TISSUE SURROUNDED BY AIR. (B) SIMULATED TEMPERATURE TRANSIENTS ON THE SURFACE OF THE SKIN, WITH AND WITHOUT MODELING THE RESULTING TISSUE DAMAGE. THE INSET SHOWS A ZOOM IN ON THE TEMPERATURE TRANSIENT OF THE BARE SKIN WITHOUT THE APPLICATION OF A SOLDER GEL. (C) SIMULATED THREE-DIMENSIONAL THERMAL DISTRIBUTION IN SKIN TISSUE COATED WITH SOLDER GEL AFTER A LASER EXPOSURE TIME OF 250 S. TEMPERATURE CONTOURS OF 60 °C AND 100 °C ARE HIGHLIGHTED IN WHITE AND BLACK, RESPECTIVELY. (D) THE THERMAL DISTRIBUTION AS A FUNCTION OF DISTANCE BELOW AND ABOVE THE SKIN TISSUE SURFACE. THE SURFACE WAS COATED WITH A NP CONTAINING SOLDER GEL. (E) ESTIMATED DAMAGE DISTRIBUTION IN THE SKIN WITH THE APPLICATION OF THE SOLDER GEL AFTER 250 S OF LASER EXPOSURE. (FIGURES ADAPTED FROM REFERENCE [166]) 77

FIGURE 3.3: EXPERIMENTAL THz-TDS SETUP CONFIGURED TO REFLECTION GEOMETRY DEPICTING AN ULTRAFAST LASER EMITTING PULSES THAT ARE SPLIT BY A BEAM SPLITTER (BS) INTO A PUMP AND PROBE BEAM. BOTH BEAMS ARE GUIDED TO THE THz EMITTER AND DETECTOR, RESPECTIVELY. THE PROBE BEAM PASSES THROUGH A DELAY LINE TO INTRODUCE A TEMPORAL DELAY TO PERFORM THz-TDS. A 786-NM NIR CW LASER BEAM PLASMONICALLY HEATED A GNR BLENDED SOLDER GEL, WHICH COVERED THE PORCINE EAR SKIN SAMPLE. (FIGURE ADAPTED FROM REFERENCE [166]) 81

FIGURE 3.4: (A) REPRESENTATIVE TEM IMAGE OF GNRs FEATURING A DIMENSION OF 10 NM X 41 NM. (B) VIS-NIR ABSORBANCE SPECTRUM OF THE GNR DISPERSION HIGHLIGHTING THE EXCITATION WAVELENGTH AT 786 NM, WHICH WAS USED TO EXCITE PLASMONICALLY THE GNRs DURING THE EXPERIMENT. 82

FIGURE 3.5 DIGITAL IMAGES OF A PORCINE EAR SKIN SAMPLE COATED WITH A GNR BLENDED SOLDER GEL. (A) THINLY APPLIED ON THE SURFACE BEFORE NIR CW LASER ILLUMINATION. (B) AFTER PLASMONIC LASER HEATING FOR 250 S FEATURING A SKIN SURFACE DAMAGE IN THE FORM OF CARBONIZED SKIN AND SOLDER GEL. (FIGURES ADAPTED FROM REFERENCE [166])..... 83

FIGURE 3.6: (A) DYNAMIC THz SINGLE-POINT MEASUREMENT DEPICTING 250 REFLECTED THz TRACES SUCCESSIVELY RECORDED AT A SAMPLING RATE OF ONE THz TRACE PER SECOND DURING NIR LASER ILLUMINATION WITH AN INTENSITY OF 4.2 W/cm². (B) DYNAMIC THz SINGLE-POINT MEASUREMENT PRESENTING 250 DECONVOLVED THz TIME-DOMAIN TRACES ATTAINED AFTER THE APPLICATION OF AN FWDD ALGORITHM. (FIGURES ADAPTED FROM REFERENCE [166])..... 84

FIGURE 3.7: TYPICAL THz RAW AND DECONVOLVED SIGNALS AT SPECIFIC TIME STEPS *t* DERIVED FROM THE DYNAMIC THz SINGLE-POINT MEASUREMENT. (A1-A8) CORRESPOND TO THE RAW THz SIGNALS RECORDED AT *t* = 1 s, 20 s, 40 s, 50 s, 70 s, 160 s, 200 s, AND 250 s, RESPECTIVELY. (B1-B8) CORRESPOND TO THE DECONVOLVED

SIGNALS AFTER APPLYING AN FWDD ALGORITHM TO THE RAW THZ SIGNALS. THE DECONVOLVED SIGNAL IS NORMALIZED TO ITS MAXIMUM PEAK LEVEL. (FIGURES ADAPTED FROM REFERENCE [166]) 85

FIGURE 3.8: DIGITAL CROSS-SECTIONAL IMAGE OF THE PORCINE EAR SKIN SAMPLE COATED WITH SOLDER GEL AFTER 250 S OF NIR LASER EXPOSURE. THE THERMAL DAMAGE SUBDIVIDED INTO DIFFERENT ZONES IS VISIBLE. THE SUPERFICIAL LAYER BULGED, CAUSING A BUMP ON THE SKIN. 87

FIGURE 3.9: (A) PORCINE EAR SKIN SAMPLE WITH A LINE-SHAPED INCISION OF 10-MM LENGTH WAS EVENLY COATED WITH A GNR BLENDED PROTEIN SOLDER GEL. (B) SOLDERED SKIN INCISION AFTER 250 S OF PLASMONIC NIR CW LASER HEATING ACHIEVED BY EXERTING A LASER INTENSITY OF 40 W/CM². (C) NIR LASER TISSUE SOLDERING PROCEDURE. THE SOLDER GEL COVERING THE SKIN INCISION WAS PLASMONICALLY HEATED BY NIR LASER RADIATION TO FUSE THE INCISION EDGES. A TWO-DIMENSIONAL TRANSLATION STAGE MOVED THE SKIN TO PERFORM THREE CONSECUTIVE LINE SCANS. 88

FIGURE 3.10: THZ REFLECTIVE IMAGING CONFIGURATION COMPOSED OF A THZ EMITTER, DETECTOR, 2D TRANSLATION STAGE, AND TPX LENSES TO GUIDE THE THZ RADIATION TO THE SAMPLE STAGE AND THE THZ DETECTOR. THE SAMPLE HOLDER COULD BE MOVED IN THE X-Y DIRECTION TO PERFORM THZ RASTER-SCANS... 89

FIGURE 3.11: (A1-A3) DIGITAL IMAGES OF THE PORCINE EAR SKIN SAMPLES AFTER NP-ASSISTED LASER SOLDERING WITH A 20 W/CM², 30 W/CM², AND 40 W/CM² LASER INTENSITY. (B1-B3) THZ C-SCAN IMAGES, (C1-C3) THZ CROSS-SECTIONAL IMAGES, AND (D) BINARY THZ CROSS-SECTIONAL IMAGES. THE CROSS-SECTIONAL IMAGES (C1-C3) AND (D1-D3) ARE TAKEN ALONG THE DASHED LINE MARKED IN (B1-B3). (FIGURES ADAPTED FROM REFERENCE [166]) 91

FIGURE 3.12: THZ THREE-DIMENSIONAL IMAGES OF THE PORCINE EAR SKIN SAMPLES AFTER NP-ASSISTED LASER TISSUE SOLDERING WITH AN INTENSITY OF (A) 20 W/CM², (B) 30 W/CM², AND (C) 40 W/CM² DEPICTING THE DEPTH OF THE PHOTOTHERMAL DAMAGE INFLICTED BY PLASMONIC HEATING EFFECT AFTER 250 S OF NIR CW LASER EXPOSURE. (FIGURES ADAPTED FROM REFERENCE [166]) 92

LIST OF TABLES

TABLE 2.1: PHYSICAL AND CHEMICAL PARAMETERS OF THE INVESTIGATED GNR DISPERSIONS.	47
TABLE 2.2: SPECIFICS OF THE STUDIED CuS NP DISPERSIONS.	62
TABLE 3.1: PHYSICAL AND CHEMICAL PARAMETERS OF THE GNR DISPERSION BLENDED WITH A BSA POWDER TO FORM A SOLDER GEL.	83
TABLE 3.2: DESCRIPTION OF THE PHOTOTHERMAL EFFECTS IN THE PORCINE EAR SKIN SAMPLE DURING THE SINGLE-POINT MEASUREMENT.	86

LIST OF EQUATIONS

$$J(t) = N(t)e\mu E_b \quad 1.1$$

$$E_{\text{THz}} = \frac{1}{4\pi\epsilon_0} \frac{A}{c^2 z} \frac{\partial J(t)}{\partial t} \quad 1.2$$

$$E_{\text{THz}} = \frac{Ae}{4\pi\epsilon_0 c^2 z} \frac{\partial N(t)}{\partial t} \mu E_b \quad 1.3$$

$$\bar{J}(\tau) = \bar{N}e\mu E(\tau) \quad 1.4$$

$$\Delta t = \frac{2nd}{c \cos\varphi} \quad 1.5$$

$$E_{\text{diff}} = \frac{\text{Max}(E_{\text{ref}}(t)) - \text{Max}(E_{\text{pixel}}(t))}{\text{Max}(E_{\text{ref}}(t))} \quad 1.6$$

$$AV = \log_{10} \left(\frac{P_{\text{incident}}}{P_{\text{transmitted}}} \right) \quad 1.7$$

$$DR(t) = \frac{\text{maximum value of temporal amplitude}}{\text{RMS of noise floor}} \quad 2.1$$

$$SNR(t) = \frac{\text{mean value of temporal amplitude}}{\text{STD of temporal amplitude}} \quad 2.2$$

$$r(t) = i(t) \otimes f(t) = \int_{-\infty}^{+\infty} i(\tau) f(t - \tau) d\tau \quad 2.3$$

$$r_n = \sum_{m=0}^{M-1} i_m f_{n-m} + e_n \quad 2.4$$

$$r = Af + e \quad 2.5$$

$$\min_f \frac{1}{2} \|Af - r\|_2^2 + \lambda \|f\|_0 \quad 2.6$$

$$\min_f \frac{1}{2} \|Af - r\|_2^2 + \lambda \|f\|_1 \quad 2.7$$

$$\min_f \|f\|_1 = \sum_{n=0}^{N-1} |f_n| \quad 2.8$$

$$f_{i+1} = S_{\lambda\tau}(f_i - \tau A^T(Af_i - r)) \quad 2.9$$

$$\tau < \frac{2}{\|A^T A\|_2} \quad 2.10$$

$$S_{\lambda\tau}(f[n]) = \begin{cases} f[n] + \lambda\tau & f[n] \leq -\lambda\tau \\ 0 & f[n] < \lambda\tau \\ f[n] - \lambda\tau & f[n] \geq \lambda\tau \end{cases} \quad 2.11$$

$$f(t) = \text{FFT}^{-1} \left[\frac{\text{FFT}(r(t))}{\text{FFT}(i(t))} \right] \quad 2.12$$

$$f(t) = \text{FFT}^{-1} \left[\text{FFT}(g(t)) \times \frac{\text{FFT}(r(t))}{\text{FFT}(i(t))} \right] \quad 2.13$$

$$f'(t) = g(t) \otimes f(t) \quad 2.14$$

$$G(\omega) = \begin{cases} e^{i\omega t_0} \cos^2\left(\frac{\omega}{4g_c}\right) & |\omega| \leq 2\pi g_c \\ 0 & |\omega| > 2\pi g_c \end{cases} \quad 2.15$$

$$E_{x^{\text{th}}}^{\text{corr}} = \frac{E_{1^{\text{st}}}^{\text{const}}}{E_{1^{\text{st}}}} E_{x^{\text{th}}} \quad 2.16$$

$$Q_{\text{abs}} - Q_{\text{diss}} = \sum_i m_i C_i \frac{dT}{dt} \quad 2.17$$

$$Q_{\text{abs}} = P(1 - 10^{-AV\lambda})\eta \quad 2.18$$

$$Q_{\text{diss}} = hS[T(t) - T_0] \quad 2.19$$

$$\frac{dT}{dt} = \frac{P(1 - 10^{-AV\lambda})\eta}{\sum_i m_i C_i} - \frac{hS}{\sum_i m_i C_i} [T(t) - T_0] \quad 2.20$$

$$A = \frac{P(1 - 10^{-AV\lambda})\eta}{\sum_i m_i C_i} \quad 2.21$$

$$B = \frac{hS}{\sum_i m_i C_i} \quad 2.22$$

$$\frac{dT}{dt} = A - B[T(t) - T_0] \quad 2.23$$

$$T(t) = T_0 + \frac{A}{B}(1 - e^{-Bt}) + (T_{\text{initial}} - T_0)e^{-Bt} \quad 2.24$$

$$\eta = \frac{A \sum_i m_i C_i}{P(1 - 10^{-AV\lambda})} \quad 2.25$$

$$MHR = \frac{A}{c} \quad 2.26$$

$$I = \frac{2P}{\pi \left(\frac{d}{2}\right)^2} \quad 2.27$$

$$T(t) = T_0 + (T_{\max} - T_0)e^{-Bt} \quad 2.28$$

$$Bt = -\ln[(T(t) - T_0)/(T_{\max} - T_0)] \quad 2.29$$

$$m_{\text{eff}}^{\text{dis}} = \frac{\iint T(x, y) dx dy}{S_A} m_{\text{dis}} \quad 2.30$$

$$m_{\text{eff}}^{\text{cuv}} = \frac{m_{\text{eff}}^{\text{dis}}}{m_{\text{dis}}} m_{\text{cuv}} \quad 2.31$$

$$\eta = \frac{Q_{\text{dispersion}} - Q_{\text{solvent}}}{Q_{\text{extinction}}} = \frac{e^{-\mu_{\text{water}}L} - e^{-(\sigma_{\text{abs}}n_{\text{GNR}} + \mu_{\text{water}})L}}{(1 - e^{-\sigma_{\text{ext}}n_{\text{GNR}}L})} \quad 2.32$$

$$\varepsilon_{\text{broad}} = \varepsilon_{\text{gold,experimental}} + \frac{\omega_{\text{p}}^2}{\omega(\omega + i\Gamma)} - \frac{\omega_{\text{p}}^2}{\omega(\omega + i2\Gamma)} \quad 2.33$$

$$j \frac{\partial A_{1,2}}{\partial z} + \frac{\omega_{1,2}}{n_{1,2}c} \chi_{\text{eff}} A_{2,1} A_3 \exp \left[+j \int_0^z \Delta k(\zeta) d\zeta \right] = 0 \quad 2.34$$

$$j \frac{\partial A_3}{\partial z} + \frac{\omega_3}{n_3c} \chi_{\text{eff}} A_1 A_2 \exp \left[-j \int_0^z \Delta k(\zeta) d\zeta \right] = 0 \quad 2.35$$

$$\Delta k(z) = k_3(z) - k_1(z) - k_2(z), \quad k_{1,2,3}(z) = \frac{2\pi}{\lambda_{1,2,3}} n_{1,2,3}(z) \quad 2.36$$

$$Q_{\text{ext}} = \rho C_p \frac{\partial T}{\partial t} + \nabla(-k\nabla T) \quad 3.1$$

$$Q_{\text{laser}} = -\left. \frac{\partial I(r, z)}{\partial z} \right|_{\text{abs}} = \mu_{\text{abs}} I(r, z) \quad 3.2$$

$$I(r, z) = I_0(r) e^{-(\mu_{\text{abs}} + \mu_{\text{scat}})z} \quad 3.3$$

$$Q_{\text{conv}} = -h(T - T_0) \quad 3.4$$

$$Q_{\text{rad}} = -\varepsilon\sigma(T^4 - T_0^4) \quad 3.5$$

LIST OF ABBREVIATIONS

2D	two-dimensional
3D	three-dimensional
BSA	bovine serum albumin
CTAB	hexadecyltrimethylammonium bromide
Cu	copper
CuS	copper sulfide
CV	coefficient of variation
CW	continuous wave
DC	direct current
DLS	dynamic light scattering
DR	dynamic range
FWDD	frequency-wavelet domain deconvolution
GNR	gold nanorod
ICP-MS	inductively coupled plasma mass spectrometry
IR	infrared
LBO	lithium triborate
LSPR	localized surface plasmon resonance
LT-GaAs	low-temperature grown gallium arsenide
MHR	molar heating rate
NETS	nanoantenna enhanced terahertz spectroscopy
NIR	near-infrared
NP	nanoparticle
NPs	nanoparticles
OPA	optical parametric amplifier

PAA	polyacrylic acid
PCA	photoconductive antenna
PCE	photothermal conversion efficiency
PE	polyethylene
PEG	polyethylene glycol
PMMA	poly(methylmethacrylate)
PTT	photothermal therapy
RMS	root-mean-square
SEIRAS	surface-enhanced infrared absorption spectroscopy
SERS	surface-enhanced Raman scattering
SNR	signal-to-noise ratio
STD	standard deviation
TEM	transmission electron microscopy
THz	terahertz
THz-TDS	terahertz time-domain-spectroscopy
THz-ToF	terahertz time-of-flight
TWM	three-wave mixing

1 Introduction

1.1 Motivation and Objectives

Heat describes the energy that a system exchanges with the environment. Exchanged heat, in turn, changes the average kinetic energy of the particles in a system, which is measured by means of temperature. Comprehensively understanding the properties of heat diffusion according to the properties of nanostructures, not just on a macroscale but also on a micro- and nanoscale, will augment the capability of new modern-day heating applications in which optical-to-thermal energy conversion in aqueous systems is required, such as photothermal therapy, nano-chemistry, nanosurgery, photoacoustic imaging, optofluidics, and photothermal imaging [1], [2]. Plasmonic systems open the route to nano-photonics due to their unique ability to confine electromagnetic energy down to ultra-small volumes that enable nanometer-scale light manipulation. Localized heating through the irradiation of metal nanostructures, so-called thermo-plasmonics, has thrived in recent years because it uniquely provides remotely controllable nanometer-scale heat sources to control temperature on the nanoscale. Under illumination with intense electromagnetic fields at its plasmonic resonance, such as those originating from light-emitting laser sources, a metal nanoparticle (NP) possesses enhanced light absorption properties, turning it into an ideal remotely controllable nano-source of heat in aqueous systems [3], [4]. These properties allow to significantly increase the temperature in and around NPs by using low-intensity irradiation, which will not heat the overall system, thus conferring spatial control over the energy deposition. Recent research efforts have been directed towards optimizing the NP's photothermal conversion efficiency (PCE) [5]–[8], meaning its capacity to convert light into heat. The higher the PCE, the lower is the necessary laser power and the dose of NPs that are required to induce the desired heating effects, which is especially relevant for biomedical applications within tissue. However, even nowadays, it is still difficult to accurately measure the temperature of NP dispersions under obstructed conditions. The measurement of the precise temperature and thermal distribution during heating and cooling procedures of NP dispersions is crucial for the determination of the PCE to be able to benchmark NPs differing, for instance, in material properties, composition, size, and morphology. Conventional contact and non-contact methods to quantify the PCE of NP dispersions are inconvenient and inaccurate. Contact methods, for instance, thermocouples [8], are invasive, influence the measurement, and do not work when the aqueous system is closed or otherwise inaccessible. Non-contact measurement methods like infrared (IR) thermometers [9] determine only the surface temperature of a vessel, which houses the aqueous system in a direct

line of sight. The measured result does not necessarily represent the temperature value of a liquid inside this vessel. Moreover, the NP dispersion must be consistently homogenized by a magnetic stir bar to achieve an equal temperature distribution within the vessel, a process that is both invasive and can lead to contamination.

The work in this thesis utilizes recently developed pulsed radiation sources at terahertz (THz) frequencies (30 μm to 3 mm wavelength range) [10], [11] to measure the temperature inside vessels housing aqueous systems in a time- and spatially- resolved manner. THz radiation has low photon energy and therefore is non-ionizing. Additionally, it is highly sensitive to the refractive index changes of water-based systems as a function of temperature. Moreover, pulsed THz radiation can be coherently detected, which means time-resolved amplitude and phase information are accessible for spectroscopy and THz time-of-flight (THz-ToF) evaluations [12]. The ToF analysis allows determining the temperature directly at the interface between an aqueous system and its vessel if the vessel is made of a non-metallic low THz absorbing material such as plastic. THz radiation can penetrate, for example, polymers, as they consist of non-polar molecules that do not feature a permanent dipole moment to which THz radiation could couple to.

In this thesis, a novel method has been devised (chapter 2), which combines spatial and time-resolved information of pulses at THz frequencies to quantify the PCE of NP dispersions in vessels without the need for stirring. The technique harnesses various intrinsic physical parameters of pulsed THz radiation, such as amplitude, frequency, ToF, as well as spatial information for the accurate determination of the PCE of NPs in aqueous dispersions. As a well-studied reference to corroborate the novel method, rod-shaped gold NPs, so-called gold nanorods (GNRs), were used as a benchmark test. Among many applications, GNRs have been used for photothermal conversion-based biomedical therapies [13], due to their chemical inertness and well-known synthesis recipe. This recipe enables the GNRs to be produced reliably in size- and morphological uniformity, with high extinction cross-section, and tunable longitudinal localized surface plasmon resonance (LSPR) in the near-infrared (NIR). In this wavelength range, light can penetrate deeply in biological tissue.

Three different GNR volumes were investigated, having the same longitudinal LSPR peak and approximately the same aspect ratio, but different dimensions. Both experimental measurements and theoretical simulations were used to elucidate the effect of the GNR volume on the PCE. The novel method devised in this thesis and its capabilities can be extended to other situations in which temperature modifies the refractive index of aqueous systems, including tissue water in the

skin. As a proof of concept, the temperature-induced changes in a multilayer biological model system containing a high water content were studied by using THz light (chapter 3). Specifically, a new and promising medical procedure named “laser-assisted tissue soldering” [14] was used, wherein contrast to conventional sutures, a NP containing solder gel aids the approximation of incision edges. Because this laser tissue bonding method is a non-contact and non-mechanical technique, it is ideally suited for surgeries where suturing and stapling is hard or even impossible to apply, for example, in endoscopic and laparoscopic procedures. This procedure’s side effect is localized thermal damage that is inflicted on the tissue surrounding the incision due to the intense laser radiation. This thermal damage forms a multilayer structure inside the tissue with different refractive indices. The evolution of the thermal damage during the soldering procedure was monitored employing a THz radiation source, while its spatial distribution was mapped to unveil the extent of the surface and subsurface structural changes within the tissue. The experimental results were complemented by theoretical simulations of the temperature dynamics inside the tissue showing the extent of the photothermal damage incurred by the laser heating procedure. The new method has the potential to be employed in medical procedures like photothermal therapy (PTT) to monitor the treated tissue in order to minimize or even prevent further thermal damage. Therefore, the new method could be an essential factor in making these promising medical treatments more relevant in clinical applications.

1.2 Scope of the Thesis

This thesis covers several disciplines and comprises investigations combining multiple fields of ongoing research. The goal herein is to exploit recently developed pulsed laser sources operating at THz frequencies in conjunction with nanoscale materials to both alter, as well as accurately map, the temperature within the framework of a wide range of water-based systems. The results can be used to glean more information about the properties of nanoscale materials under laser illumination, as well as to quantify heat dissipation, even in biological contexts where the temperature changes in water and tissue play a key role.

The introductory chapter gives a theoretical background and the state-of-the-art of all relevant topics within this thesis. The THz related subjects are described in subchapter 1.3, including the characteristics of THz radiation, its generation and detection via photoconductive antennas (PCAs), as well as terahertz time-domain-spectroscopy (THz-TDS) as a coherent detection technique, which can retrieve the amplitude and phase information of THz radiation resolved in time. Additionally, the concept of THz-ToF and its application for THz tomography is presented,

concentrating on state-of-the-art THz biomedical imaging. Within this context, plasmonic gold NPs will be discussed in subchapter 1.4, with a focus on GNRs. The phenomenon of LSPR is described, and the concept of PCE, as well as existing methods for its quantification, will be introduced. Moreover, a new medical treatment procedure for wound closure is presented, which is based on NP-assisted laser tissue soldering.

Thus far, it is still challenging to precisely determine the PCE of plasmonic NPs in a convenient, and reliable way, in order to identify the most efficient NP composition and morphology for laser-based localized heating applications, such as PTT. Therefore, a new method for the non-invasive, non-contact, and non-destructive characterization of the photothermal effect of plasmonic NPs within aqueous dispersions utilizing pulsed THz radiation is introduced in Chapter 2.

First, subchapter 2.1 describes the THz setup that I built and deployed to perform all experiments in this thesis. Then, subchapter 2.2 explains the algorithms that I applied to post-process the experimental data. These algorithms, namely sparse and THz frequency-wavelet domain deconvolution (FWDD), as well as self-referencing, were recently developed and optimized to post-process THz signals. Moreover, subchapter 2.3 introduces a theoretical model that I applied to calculate the PCE and molar heating rate (MHR) based on the recordings of the heating and cooling cycles. Then, I fully characterized and experimentally determined the PCE and MHR of three standard gold nanorod (GNR) dispersions as a benchmark test for the new method (subchapters 2.4-2.6). Moreover, the fidelity of the achieved results was corroborated by carrying out numerical simulations that were performed in collaboration with Prof. Alexander O. Govorov (Ohio University). Notably, the proposed technique can be extended to the characterization of any nanomaterial that features a temperature-dependent change of its refractive index in the THz regime.

Additionally, I studied three differently capped but equally sized copper sulfide (CuS) NPs, dispersed in aqueous solutions by using THz-TDS (subchapter 2.7). The time-resolved thermal measurements compared their photothermal heating performance. The CuS NPs were synthesized by the group of Prof. Fiorenzo Vetrone (INRS-EMT). In this study, I characterized the NPs, designed, and built the THz setup and sample vessels, performed the experiment, as well as analyzed the experimental data.

Due to an increased demand for tunable lasers to excite NPs in the second biological window (1000 nm to 1350 nm), this thesis presents in subchapter 2.8 a method to optimize the parametric gain of optical parametric amplifiers (OPA) by performing a quasi-phase-matched wavelength conversion based on a three-wave mixing (TWM) process in a lithium triborate (LBO) nonlinear

crystal. The presented method optimizes the conversion efficiency and bandwidth of standard OPA systems and could be used, for example, for time-resolved pump-probe experiments involving THz sources based on organic crystals as well as the photoexcitation of NP samples in the second biological window. My contribution to this study lies in its experimental realization by building the setup, aligning, and operating it.

In chapter 3, I applied the THz-TDS method to a multilayer biological model system to investigate a NP-assisted laser tissue interaction process in real-time and in depth. A theoretical simulation was performed in collaboration with the group of Prof. Alexander O. Govorov (Ohio University), predicting the temperature increase in the laser illumination area and estimating the photothermal damage incurred to the skin tissue (subchapter 3.1). I experimentally showed that THz-TDS is a versatile tool to reveal the photothermal damage during the process of NP-assisted laser tissue soldering for wound closures (subchapter 3.2). Specifically, I designed and built the THz-TDS setup, prepared the skin samples and solder gel, and performed the soldering as well as experimental measurements. Besides, I traced the photothermal damage evolution by THz-TDS and subsequently evaluated the experimental data by using a deconvolution algorithm that was also recently adapted for THz signal post-processing. Moreover, I performed the experimental work to image the extent of the photothermal damage in three dimensions (subchapter 3.3) within the skin tissue by using a raster-scan imaging modality that I designed and constructed.

The non-ionizing photon energy level renders THz radiation a suitable diagnostic tool for *in vivo* imaging of laser-assisted incision soldering. The new method can enable clinicians to receive instant feedback regarding the photothermal damage inside the tissue while performing the medical procedures. The approach can be easily extended and applied across a broad range of clinical applications involving laser tissue interaction, like laser ablation and photothermal therapies. Consequently, the presented method can complement and even extend conventional skin imaging methods, which currently lack imaging contrast and resolution in depth.

In all experiments, I designed, built, aligned, and operated the THz setups as well as prepared the samples, vessels, and holders. The research directions and outcomes were discussed with my supervisors and the co-authors of the respective publications.

1.3 Terahertz Radiation

THz radiation covers the electromagnetic spectrum from 0.1×10^{12} to 10×10^{12} Hz, corresponding to a wavelength range of 3 mm to 30 μm , which positions it between the IR and microwave frequency regimes (Figure 1.1).

Dielectric non-polar materials, such as fabric, paper, and plastic, which are opaque to visible and NIR waves, are transparent in the THz frequency range. This property enables non-contact and non-invasive sensing under obstructed conditions, including measurements inside of enclosures and vessels made of these materials. Due to this property, THz radiation can have a high-impact in applications ranging from biomedicine to sensing, for example, under medical gauzes, inside of cuvettes or capillaries, as well as microfluidic lab-on-chip devices [15].

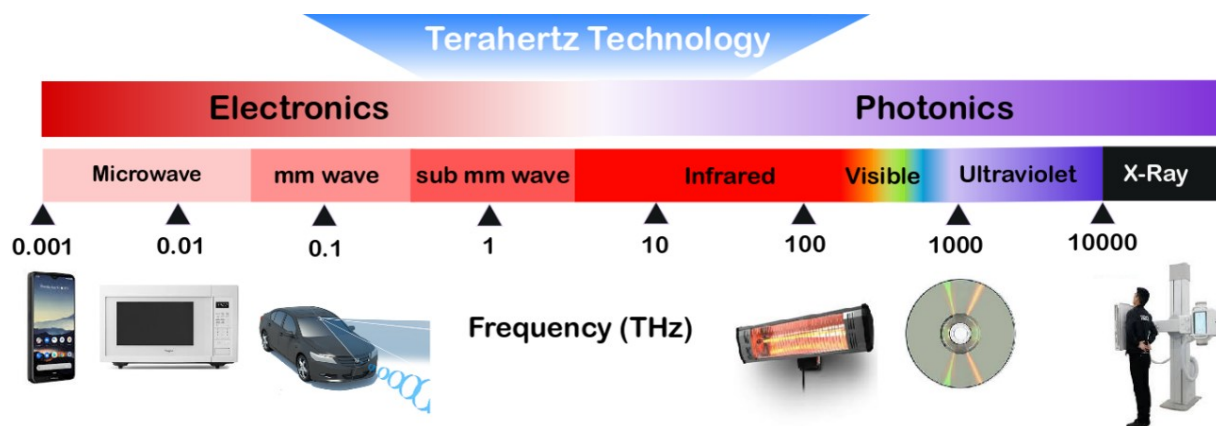


Figure 1.1: Electromagnetic spectrum highlighting the THz frequency section. (adapted from the National Institute of Information and Communications Technology (NICT))

THz radiation exhibits strong absorption by polar molecules, such as water. Therefore, it is highly sensitive to the humidity of the environment and the hydration level of samples, such as biological tissue [16]. This unique property is heavily used for biomedical applications to, for example, accurately discriminate between healthy and cancerous tissue as well as for burn wound evaluations [17] due to the different or changing water content [18]. Moreover, aqueous solutions experience a significant temperature-dependent refractive index and absorption coefficient change in the THz regime (Figure 1.2), which in turn enables accurate temperature determination. This fundamental principle was used to develop a new method for the photothermal characterization of NPs, as described in chapter 2.

THz radiation has non-invasive and non-ionizing properties due to its low photon energy (0.4 meV to 40 meV) that ensures the physicochemical integrity of a sample without influencing the measurement. These properties make THz waves suitable for medical imaging since its non-invasive nature can be utilized for *in vivo* real-time diagnosis without causing ionization damage, unlike X-rays, for example. Moreover, scattering losses of THz radiation in biological tissue are negligible due to its long wavelength, which is in contrast to visible and IR light [19].

The photon energy of THz radiation coincides with the energy levels of low-frequency motions, such as the vibration, rotation, and translation of various molecules [12]. These motions are

molecule-specific and allow to identify materials, especially biomolecules, by measuring their characteristic spectral signatures in the THz frequency range. Additionally, THz radiation can reveal time-resolved dynamics on a sub-picosecond to picosecond temporal resolution to, for example, monitor the dynamics of transient photoconductivity in semiconductors [20]. Many industries exploit the described merits of THz radiation for numerous applications, such as non-destructive quality control [21], security [11], spectroscopy, and imaging [22]. Since THz radiation is harmless to biological tissue, much research attention has been directed [23] towards high impact applications in biomedicine and biochemical sensing [19], [24].

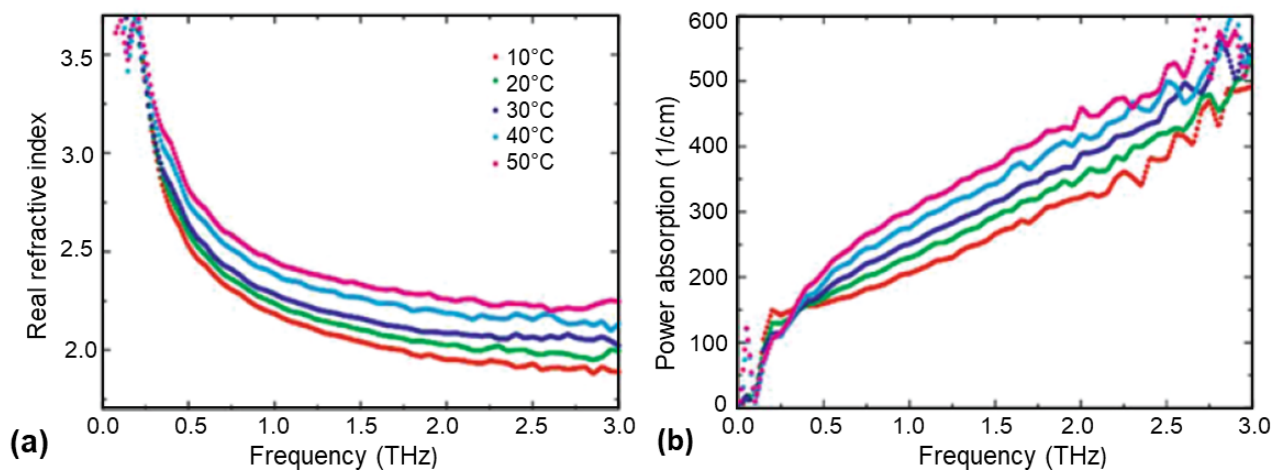


Figure 1.2: Temperature-dependent (a) refractive index and (b) absorption coefficient of water in the THz frequency regime. (Figure adapted from references [25], [26])

1.3.1 THz Generation by using Photoconductive Antennas (PCAs)

Several methods can be deployed for the generation and detection of THz pulses featuring a broad bandwidth. The most widespread generation techniques are transient photo-induced currents in PCAs and optical rectification in second-order nonlinear media [27], [28], whereas, for detection, photoconductive sampling [29]–[34] and electro-optic sampling [35], [36] are typically employed. In our case, a THz system, based on PCAs as a THz transmitter and detector, was used to perform the studies described in chapters 2 and 3 of this thesis. Therefore, the fundamental mechanism of PCAs is explained in detail hereafter.

A PCA consists of two metal electrodes that can have various geometries (e.g., a bow-tie, strip-line, or simply Hertzian dipole). The electrodes are deposited over a semiconductor substrate, which is commonly made of low-temperature grown gallium arsenide (LT-GaAs) due to its bandgap around 1.45 eV or 850 nm wavelength. This wavelength is well matched to excitation pump lasers that emit femtosecond pulses such as Ti:sapphire laser systems (radiating at a

center wavelength around 800 nm) or wavelength-duplicated (via second harmonic generation) erbium-doped fiber lasers (emitting at a center wavelength of 1550 nm). A PCA is a fast “optically-activated” switch utilizing the rise in electrical conductivity of semiconductors when they are exposed to light. This photoconductivity is caused by a surge in the number of free charge carriers (electrons and holes) created by the absorbed photons [37]. The working principle of PCAs is that first, a direct (DC) voltage is applied across the two electrodes, and since the substrate is semi-insulating, electric energy is stored in the gap area.

Femtosecond long laser pulses focused into the gap between the two electrodes act like transient switches (Figure 1.3(a)) and create electron-hole pairs in the semiconductor, which open a reservoir of electric energy (Figure 1.3(b)). The static bias field across the gap accelerates the free photo-generated charge carriers and produces a transient photocurrent, which is described as [12], [37]:

$$J(t) = N(t)e\mu E_b \quad 1.1$$

where N is the density of photocarriers, e denotes the elementary charge, μ is the mobility of the carriers, t represents the time, and E_b is the bias electric field.

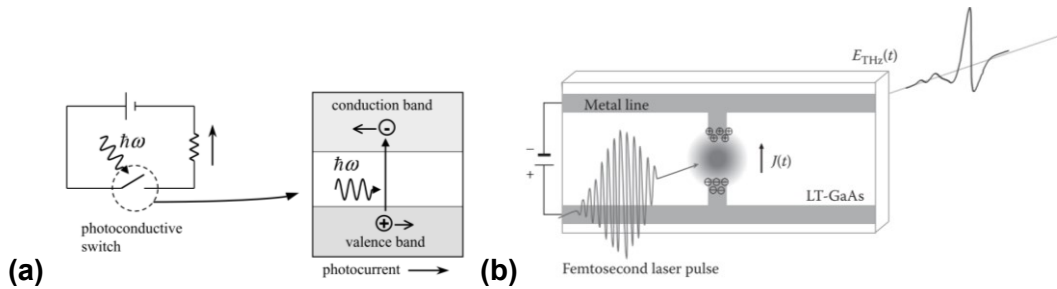


Figure 1.3: Schematic representation of (a) The working principle of a photoconductive switch in which a photocurrent flows through the circuit when light generates free electrons and holes. (Figure adapted from reference [37]). (b) A PCA biased with a DC voltage and illuminated by a femtosecond laser pulse generates sub-picosecond THz transients. (Figure adapted from reference [38])

The photocurrent, arising from the acceleration and decay of free carriers, is the source of the sub-picosecond THz pulses, whose electric field is the derivative of the time-variant photocurrent and can be described by:

$$E_{THz} = \frac{1}{4\pi\epsilon_0} \frac{A}{c^2 z} \frac{\partial J(t)}{\partial t} \quad 1.2$$

$$E_{THz} = \frac{Ae}{4\pi\epsilon_0 c^2 z} \frac{\partial N(t)}{\partial t} \mu E_b \quad 1.3$$

where A is the area in the gap between the two electrodes illuminated by the laser light, ϵ_0 is the vacuum permittivity, c is the speed of light, and z is the penetration of the laser pulse into the semiconductor.

The recombination of the electron-hole pairs causes a subsequent decrease in photocurrent on a picosecond timescale that depends on the semiconductor carrier lifetime, which is around 100 fs for LT-GaAs [39]. The photo-carrier density declines primarily due to carrier trapping in defect sites. Therefore, the first half-cycle of the THz electric field is mostly governed by the pulse duration of the optical pulse, whereas the second half-cycle is affected by the electron recombination time of the semiconductor material. Thus, to achieve broadband THz pulses, a short recombination time in the semiconductor is required together with a short femtosecond laser pulse. The polarization of the radiated THz wave is parallel to the bias field, which is perpendicular to the two electrodes. Usually, THz pulses in free space are immediately guided by a high resistivity silicon lens typically attached directly to the output of the semiconductor substrate (Figure 1.4).

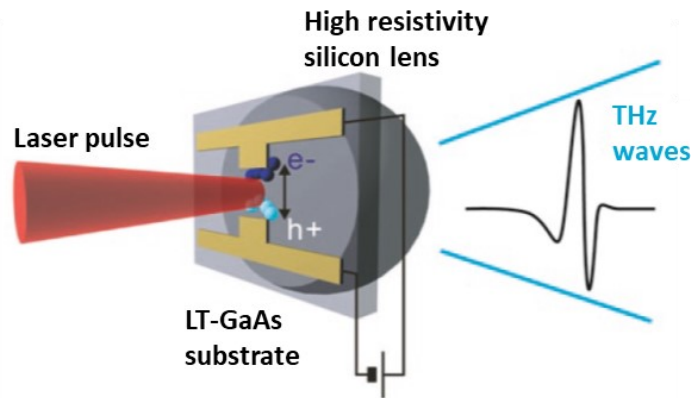


Figure 1.4: Illustrative example of a PCA for broadband generation and detection of THz pulses. (Figure adapted from reference [25])

The THz pulse variations occur on a picosecond time scale, which makes it impossible to measure them with electronic equipment like oscilloscopes. Thus, a common way to coherently detect such broadband THz pulses is by using PCAs as THz detectors. The underlying mechanism of THz field detection in PCAs is almost identical to that of the THz emission in PCA emitters.

The slowly varying THz electric field can be considered when compared to the optical pulse as constant over the time duration of an optical pulse cycle. This allows measuring the THz electric field using the ultrafast probe laser, assuming that the carrier creation and recombination are much faster than the slowly varying THz electric field. Thereby, the impinging THz electric field acts as a bias field and, thus, drives a current in the photoconductive gap between the two

electrodes when photocarriers are created by the optical probe pulse (Figure 1.5) [37]. The THz field induced current \bar{J} in a first approximation can be calculated as:

$$\bar{J}(\tau) = \bar{N}e\mu E(\tau) \quad 1.4$$

where \bar{N} represents the average electron density, $E(\tau)$ denotes the amplitude of the THz electric field at time delay τ between the probe and the THz pulse. The induced current is proportional to the THz field amplitude. The full THz transient can be reconstructed as a function of τ by varying the optical temporal delay between the THz pulse and the probe beam. The THz power typically emitted is below 1 μW ; thus, the measurement is non-invasive since there is no thermal strain on samples.

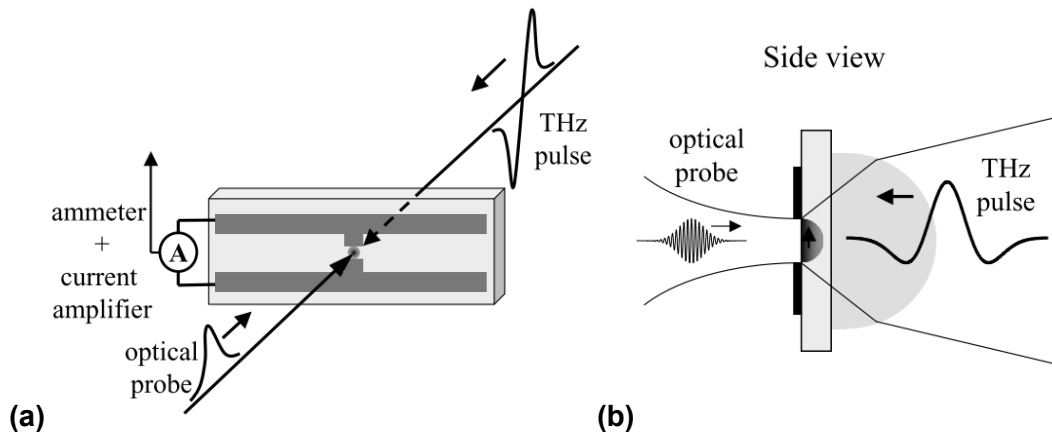


Figure 1.5: (a) Schematic diagram for a time-resolved measurement of THz electric fields by using a PCA receiver. (b) The side view of a PCA shows a high resistivity silicon lens attached in front of the semiconductor chip to strongly focus the incident THz radiation into the gap between the two electrodes. (Figures adapted from reference [37])

1.3.2 THz Time-Domain Spectroscopy (THz-TDS)

THz-TDS is based on pulsed THz radiation generated, for example, by using PCAs. It has been used for numerous applications, including THz imaging, which is described in more detail in subchapter 1.3.3. Figure 1.6(a)-(b) shows the basic experimental THz-TDS setup for THz generation and detection based on PCAs in transmission and reflection configuration.

A beam splitter splits pulses from a femtosecond laser. One portion, which is referred to as “pump beam,” is directed towards the THz emitter to generate THz pulses. The generated THz beam is collimated either by off-axis parabolic mirrors or polymer lenses and sent to the sample. Depending on the design of the setup, either in transmission (Figure 1.6(a)) or reflection (Figure

1.6(b)) configuration, the transmitted or reflected THz radiation is guided towards and focused on a THz receiver.

A beam splitter splits pulses from a femtosecond laser. One portion, which is referred to as “pump beam,” is directed towards the THz emitter to generate THz pulses. The generated THz beam is collimated either by off-axis parabolic mirrors or polymer lenses and sent to the sample. Depending on the design of the setup, either in transmission (Figure 1.6(a)) or reflection (Figure 1.6(b)) configuration, the transmitted or reflected THz radiation is guided towards and focused on a THz receiver.

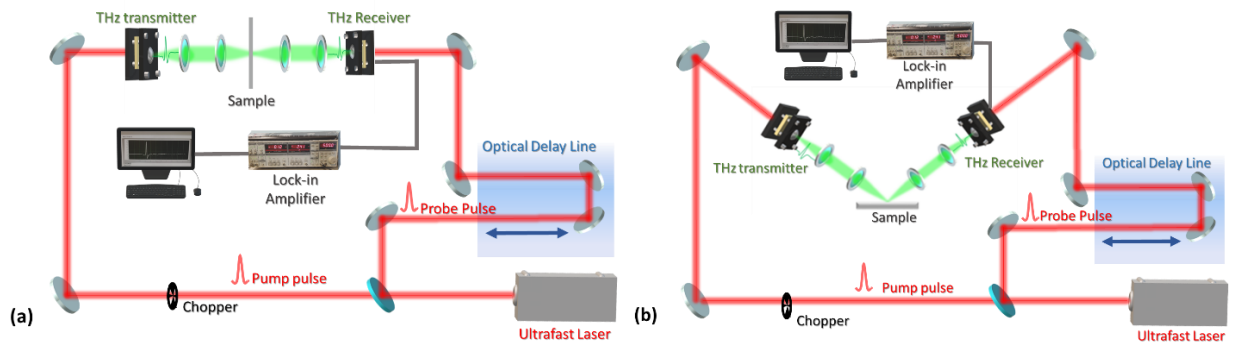


Figure 1.6: THz time-domain spectroscopy setups based on PCAs in (a) transmission and (b) reflection configuration. Femtosecond long pulses emanated from a laser system are split at a beam splitter and guided to the THz transmitter and receiver. The probe pulse beam is optically delayed by a translation stage to alter its arrival time with respect to the THz pulse beam at the THz receiver.

The other portion of the femtosecond pulse beam referred to as “probe beam” travels through a variable time delay, before being focused on the THz receiver. By varying the time delay and recording the detector value according to this delay, it is possible to trace the THz electric field coherently as a function of time. Thus, the measurement records not only amplitude but also phase information of the THz pulse that can subsequently be used to compute spectral information by using Fourier transformation. An example of a THz transient and its spectrum is shown in Figure 1.7.

In order to enhance the signal-to-noise (SNR) ratio, the signal is processed by a lock-in amplifier synchronized with an optical intensity modulator, such as an optical chopper or the bias voltage of the PCA emitter modulated by a square wave generator [12], [37].

A sample introduced into the THz beam path either in transmission or reflection geometry affects both the phase and amplitude of THz pulses. By comparing the THz pulses with and without a sample present in the setup, it is possible to characterize the sample and obtain its THz absorption spectrum and dispersion properties. Thus, coherent detection permits a complete

characterization of the optical properties of the sample, i.e., its complex dielectric function [40], [41]. This coherent detection technique of broadband THz pulses is called THz-TDS.

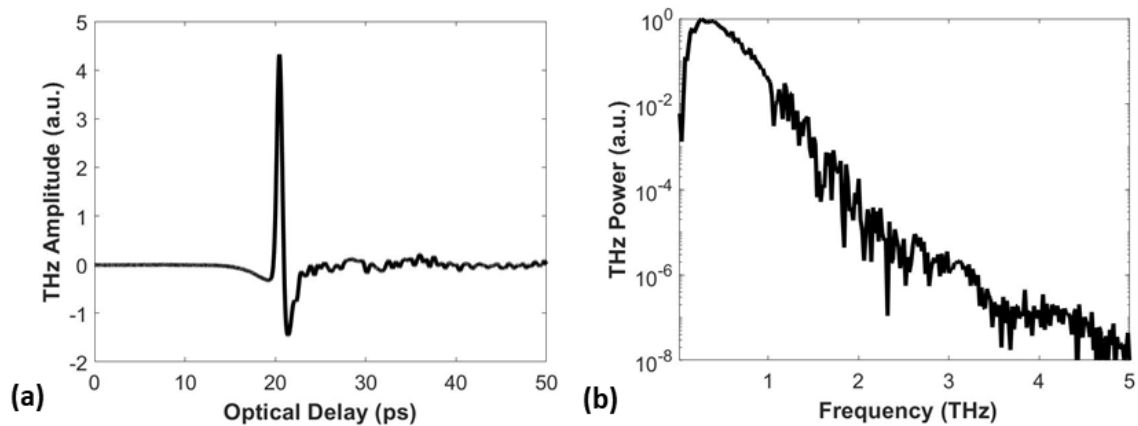


Figure 1.7: a) Representative reference THz transient and its b) spectrum of the THz time-domain spectroscopy system used to perform the experiments in chapters 2 and 3.

1.3.3 THz Imaging

THz-TDS, in combination with a raster-scan imaging technique enabled by an X-Y translation stage, can perform two- and three-dimensional THz imaging. Figure 1.8 plots a THz trace and its spectrum highlighting specific parameters, for example, amplitude, phase, or spectral features. Spatial differences in these parameters are used to confer contrast in two-dimensional THz images pixel by pixel using transmitted or reflected THz beams.

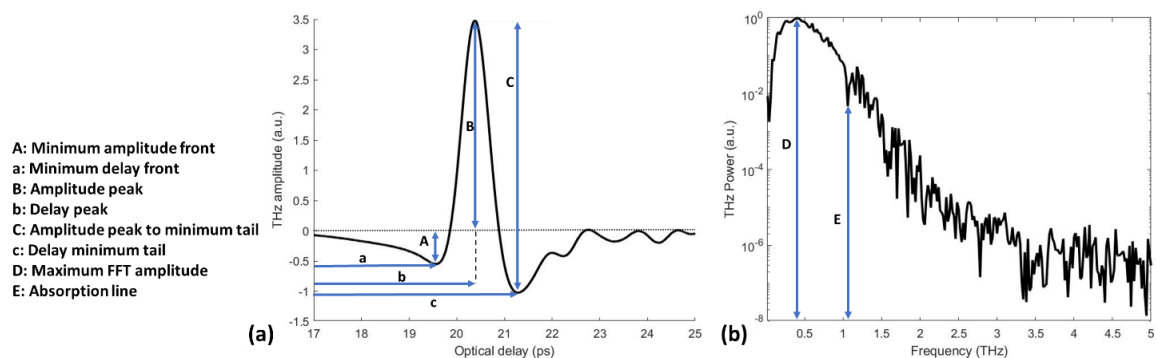


Figure 1.8: (a) THz transient in the time-domain and its Fourier transformation in the (b) frequency domain. The plots highlight specific features, which can be chosen to generate contrast in order to construct a two-dimensional THz image pixel by pixel. (Figures adapted from reference [42])

This imaging method is limited by a slow image acquisition rate, which is not suitable for many applications, such as for biomedical imaging, when the sample is deteriorating quickly. Due to the single-point raster scan technique, the image acquisition rate depends on the size of the image and its resolution.

Moreover, a sufficient frequency resolution is necessary to construct spectral fingerprint maps, also considering that the frequency resolution is linked to the inverse of the temporal window, which ultimately poses a tradeoff between scan duration and frequency resolution. In the experiments presented in chapter 3, a porcine skin sample was imaged, which deteriorated after one hour of uncooled exposure to a typical environment (e.g., room temperature (~ 21 °C), relative humidity ($\sim 50\%$)). Therefore, a fast-optical delay line was utilized to perform the experiment using a sampling rate of 1 Hz and a temporal window of 50 ps that limited the acquisition time to 30 minutes for the entire image.

1.3.3.1 THz Time-of-Flight Analysis (THz-ToF)

By using a THz-ToF analysis technique, THz-TDS systems equipped with a raster-scan X-Y translation stage can perform three-dimensional imaging pixel by pixel and, thus, construct THz tomographic profiles [43], [44]. Moreover, THz cross-sectional images of a sample can be obtained to map structural details in depth. The THz-ToF method has been used for the studies described in chapters 2 and 3, in order to monitor properties at specific internal interfaces of objects, for example, refractive index changes according to temperature or phase changes of materials.

THz-ToF measurements are enabled by the time-resolved coherent detection capability of THz-TDS [22]. Several THz echoes can be observed in a time-domain trace at different time delays when THz pulses travel through a medium that has one or more partly reflective or transmissive interfaces located at different depths. These interfaces produce multiple THz reflections that represent refractive index discontinuities as a function of depth. In this way, the internal structure of objects containing one or multiple layers can be unveiled and evaluated. The respective temporal position in the time-domain can be used to compute depth and thickness information. At an internal angle φ in a sample in a THz setup set to reflection geometry, the time delay Δt of the reflected pulse is determined by:

$$\Delta t = \frac{2nd}{c \cos\varphi} \quad 1.5$$

where n, d, c are the refractive index, the thickness of each layer, and the speed of light, respectively. The refractive index is assumed to be constant across all frequencies in the THz bandwidth and along the THz spot size.

Figure 1.9(a) depicts the THz measurement configuration zoomed in on a cuvette made of polyethylene (PE) containing a NP dispersion for studying the photothermal effect of NPs (chapter 2). An X-Y translation stage imparts THz imaging capabilities. The digital image also shows the THz pulse propagation of the incident pulse and its reflections on the cuvette interfaces. This pulse propagation and the concept of THz-ToF imaging are illustrated in more detail in a schematic representation of the cross-section of the cuvette (Figure 1.9(b)) and its time-domain trace (Figure 1.9(c)).

At first, the focused THz pulses impinge on the air/PE surface and are partly reflected and transmitted due to the property of THz radiation, which allows penetration into non-polar dielectric materials. The reflection creates a 1st echo attributed to the air/PE surface, which can be observed in the THz time-domain trace illustrated in Figure 1.9(c).

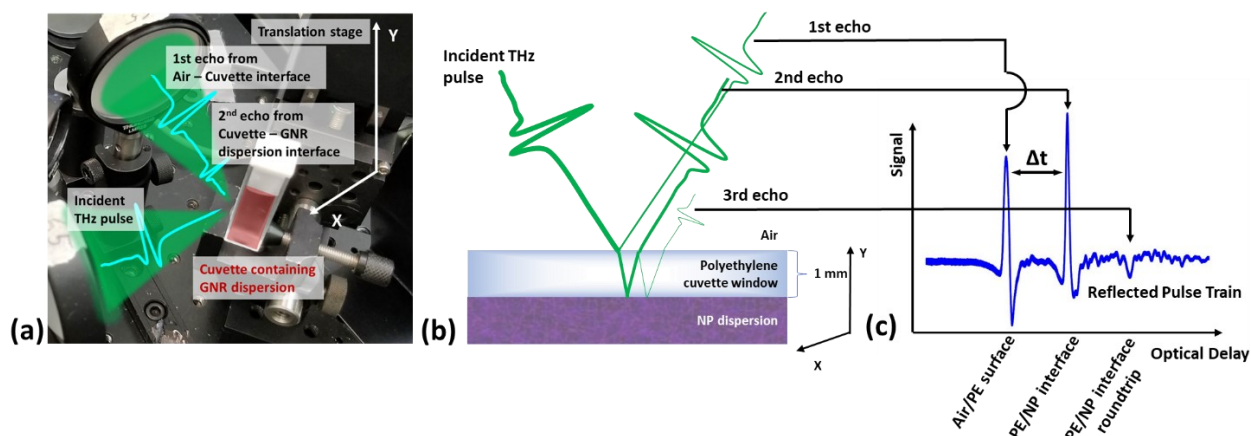


Figure 1.9: THz-ToF imaging in reflection mode, the temporal positions of the reflected THz echoes can be used for thickness calculations and to interrogate material properties in a bi- or multilayer structure. (a) Digital image of a THz reflection scheme used in chapter 2. An incident THz pulse encounters a cuvette containing a GNR dispersion under study. The pulses are being partly transmitted and reflected from both the cuvette’s surface and the internal interface, which creates two distinct THz reflection echoes. An X-Y translation stage imparts imaging capabilities. (b) Cross-section of a bilayer structure containing a PE cuvette window and an aqueous NP dispersion. (c) Time-domain plot depicting a THz trace with several echoes originating from the air/PE surface, the PE/NP dispersion interface, and its second-round reflection due to the etalon effect.

The transmitted THz radiation is then again partly reflected as well as absorbed by the aqueous dispersion at the PE/NP dispersion interface, which results in a 2nd echo observable in the THz time-domain trace. The 3rd echo is a roundtrip reflection due to the etalon effect in the PE cuvette material. It is reversed because the pulse is reflected off an interface between an optically dense (PE) to an optically less dense (air) medium, leading to a phase change of 180 deg and a flipped pulse-echo. Moreover, the 2nd echo of the THz trace is the largest of the two, given that the sample holder was mounted on a translation stage that allowed to move the sample transversely into the direction of the THz beam. In this way, the focus point of the THz signal was shifted from the surface of the cuvette to the PE/NP interface. At this position, the 2nd echo is the highest, and the

1st echo is distorted and attenuated. Consequently, the spot size of the THz pulse is the smallest and enables the most precise measurement at this specific interface.

1.3.3.2 Diverse THz Imaging Applications

Numerous proof-of-concept experiments for promising applications have been performed using THz two- and three-dimensional imaging capabilities. However, just a few applications have been implemented in industry so far. Some examples are presented in this subchapter.

For instance, THz imaging has been utilized for quality control purposes, where the non-destructive testing capabilities of THz radiation was used to analyze the thickness of paint layers of car parts [45], as well as in the food and pharmaceutical industry to analyze the internal structure of tablets [46] (Figure 1.10). In such applications, the coating thickness and interface uniformity can be determined directly from the THz time-domain waveform by using THz-ToF analysis. Even a chemical map of a sample can be obtained by using THz frequency-domain data [46] to, for instance, map the chemical composition of drug tablets.

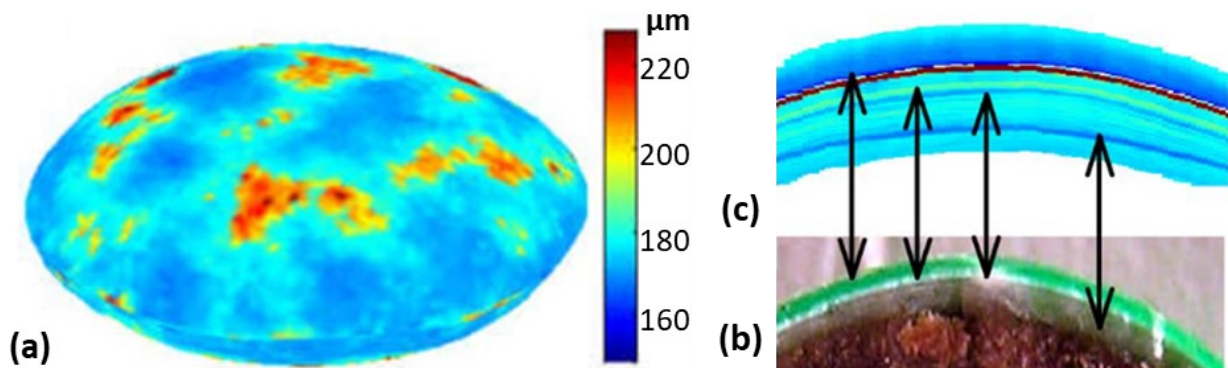


Figure 1.10: (a) THz map displaying the coating thickness of a multilayer structure of an M&M chocolate tablet. (b) Digital image of the cross-section of the chocolate tablet. (c) THz B-scan of the tablet referring to the tablet's cross-section. (Figures adapted from reference [46])

Guillet *et al.* [42] (Figure 1.11) demonstrated the usage of THz radiation for luggage inspection. Dangerous metallic items like guns become visible by their shapes and can be identified by pattern recognition algorithms. Notably, metallic packages are opaque to THz waves; therefore, THz-TDS systems will not substitute X-ray scanners. However, THz systems can provide supplementary information on samples made of low-density dielectric materials and chemicals, such as explosives and illicit drugs.

Hu *et al.* [47] showed, for the first time, a THz image of a semiconductor integrated-circuit chip packaged in plastic material (Figure 1.12). The image represents the THz power integrated over a 1 THz to 3 THz frequency range. The plastic packaging material experiences only small

absorption, whereas metals are entirely and doped semiconductors are partially absorbing in the THz spectral range. Thus, the image displays the silicon chip area as well as the metal leads connecting to the package pins.

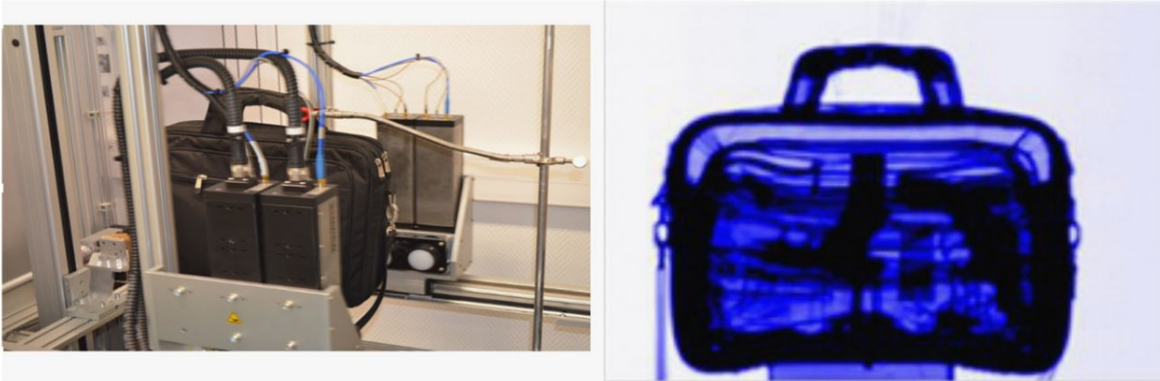


Figure 1.11: 0.1 THz transmission image of a computer bag containing two guns (Figures adapted from reference [42])

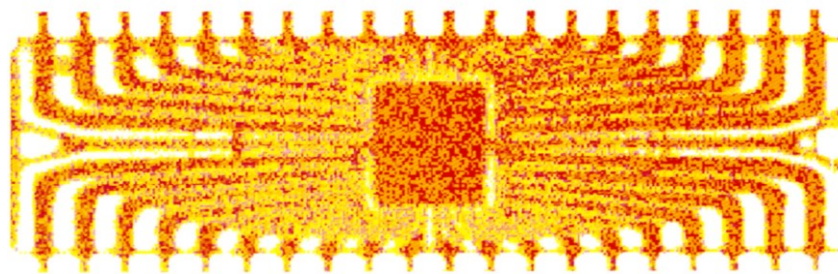


Figure 1.12: THz image of a semiconductor integrated circuit chip packaged in plastic material.

THz imaging has also been applied successfully for the preservation of cultural heritage artwork. Dong *et al.* [48] utilized the post-processing technique THz FWDD for a stratigraphic and subsurface investigation of art paintings. This technique has also been used in the experiment of chapter 3 to resolve optically thin layers by deconvolving overlapping THz echoes.

Dong *et al.* investigated a mid-20th-century Italian oil painting on paperboard titled *After Fishing* by Ausonio Tanda (Figure 1.13(a)). The stratigraphy of the painting, including the paint layers, was reconstructed using deconvolved THz echoes, and subsurface features were revealed that would be imperceptible based on the raw data alone since the separation of the paint layers above the paperboard was not resolvable [49].

Figure 1.13(c) shows a THz B-scan of the cross-section $Y = 176$ in Figure 1.13(b), illustrating four typical defects located in depth within the stratigraphy of the paperboard. These defects are organic materials exhibiting low radiological contrast; therefore, they are challenging to identify by standard computer tomography systems based on X-ray technology.

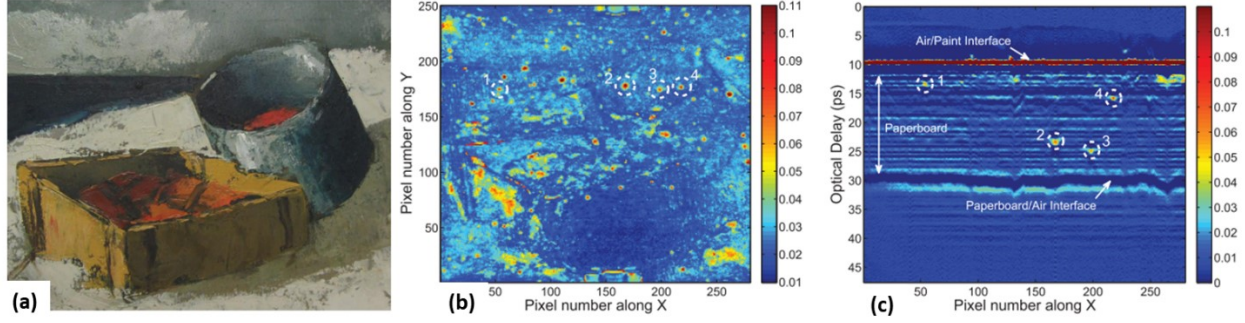


Figure 1.13: (a) Digital image of the masterpiece titled *After Fishing* by Ausonio Tanda. (b) THz C-scan image highlighting defect spots. (c) THz B-scan image of the cross-section at position Y=176. The defect spots are discernible and marked. Their position and depth within the stratigraphy is now unveiled (Figures adapted from reference [48])

1.3.3.3 THz Biomedical Imaging

THz radiation is especially suited for biomedical applications since its non-destructive, non-ionizing nature allows the tissue to be exposed to its radiation unharmed over a long time. Many proof-of-concept biomedical studies have been performed recently to explore the capabilities of THz radiation to display contrast in order to discern healthy and diseased tissue in the time (Figure 1.8(a)) and frequency (Figure 1.8(b)) domain. Notably, visualization methods rooted in the time-domain discriminate between different areas of the tissue by retrieving the differentiating THz electric field E_{diff} and calculate, for example, the relative reduction of the pulse maximum:

$$E_{\text{diff}} = \frac{\text{Max}(E_{\text{ref}}(t)) - \text{Max}(E_{\text{pixel}}(t))}{\text{Max}(E_{\text{ref}}(t))} \quad 1.6$$

where E_{ref} is the THz transient of the reference trace, and E_{pixel} is the THz trace of the individual pixel under study. The result represents the mean relative signal loss due to absorption or scattering. Another often used contrast mechanism to map subsurface features of tissue is the ratio of the maximum to the minimum amplitude of the THz pulse or the ratio of amplitudes at pre-selected delays, which correspond to certain depth positions depending on the refractive index of the tissue.

In 1995, Hu and Nuss [47] first proposed THz time-domain imaging to be utilized in the biomedical realm to relate the degree of tissue hydration with the state of a disease. Due to the limited penetration depth of THz waves into the tissue, the skin has been the preferred object for THz studies so far, due to its accessibility and low water content by volume compared to other tissue types. For example, Mittleman *et al.* [50] used a THz-TDS system to image laser-induced tissue burns in chicken breast *in vitro*. This work evaluated surface or near-surface skin burn depth and

severity induced by intense laser radiation. The resulting THz images mapped changes in THz reflectivity related to the different tissue-water concentrations. Cole *et al.* [51] were the first to present a dynamic study in which hydration level changes in the stratum corneum were measured *in vivo* and in real-time by using a THz setup. Partial-thickness skin burns inflicted by branding using a brass iron were performed by Tewari *et al.* [52]. This study recorded the first dynamic changes in rat skin burns by THz *in vivo* imaging and unveiled that regions of increased and decreased THz reflectivity correlate to the zones of coagulation and stasis of the skin. The zone of stasis containing dehydrated tissue became discernable in the THz images (Figure 1.14).

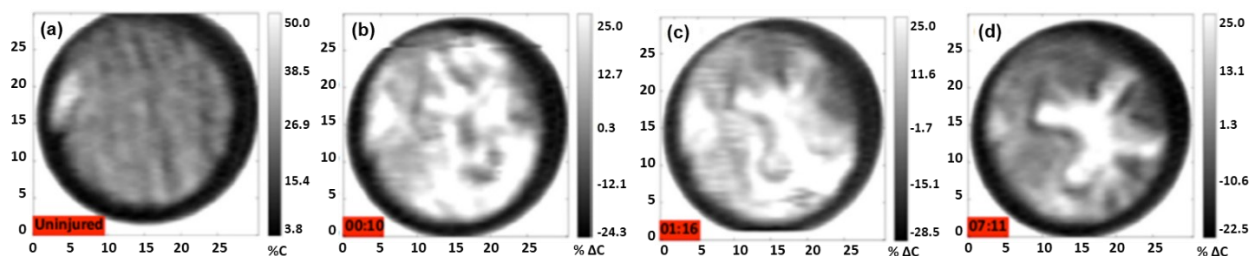


Figure 1.14: THz images of a rat skin burn *in vivo*: (a) Unburned skin. (b) Burned skin after 10 min. (c) Burned skin after 1:16 h. (d) Burned skin after 7:11 h. The lighter areas correspond to edematous response areas post-burn due to the higher reflected THz signal of local water. (Figures adapted from reference [52])

Woodward *et al.* [53] showed for the first time THz images *in vitro* of excised basal cell carcinoma, a skin cancer type with weakly defined margins. The resulting THz images displayed a sharp contrast between healthy and cancerous tissue. Wallace *et al.* [54] reported, for the first time, *in vivo* measurements of cancer on the skin surface and even in depth, which can be used to mark cancer margins in advance of resection (Figure 1.15(a)-(c)). The depth measurements were enabled by using a time post-peak evaluation technique in which the reflected peak values are normalized to the THz amplitude values (Figure 1.15(d)). The THz pulse at the time delay of 2.8 ps interacted with the tissue in depth and, therefore, maximized the contrast between the cancerous (higher THz reflectivity) and healthy tissue.

The concept of using the hydration level of tissue to generate contrast in THz images and the advantage of the non-ionizing nature of THz radiation had since been used for numerous medical imaging applications, for example, diabetes diagnostics, colon [55] and breast [56] neoplasm, as well as corneal hydration measurements in order to establish THz *in vitro* and *in vivo* imaging as a label-free method complementing conventional pathological examinations.

Water possesses a temperature-dependent refractive index in the THz frequency regime, which was used as a contrast mechanism for the first time by Oh *et al.* [57] in 2009 to perform THz biomedical imaging. The temperature change was introduced by NPs that are dispersed in

aqueous media and excited by a NIR laser. The energy absorbed by the NPs is transferred in the form of heat to the water that surrounds the NPs. This effect leads to a change in the refractive index of the aqueous dispersion in the THz frequency range. The phenomenon, linearly dependent on the incident laser fluence, can be observed as a THz amplitude modulation either of the THz reflectivity in a THz setup configured to reflection geometry or higher THz absorption in a setup configured to transmission geometry. The study uses this effect to utilize NPs as contrast agents for THz imaging of liquid samples containing cancerous cells with GNRs (Figure 1.16). The work compared the THz signal reflected from the liquid sample with and without GNRs. The experimental study observed a significant increase in THz reflectivity during IR laser irradiation with the sample containing cancer cells and GNRs.

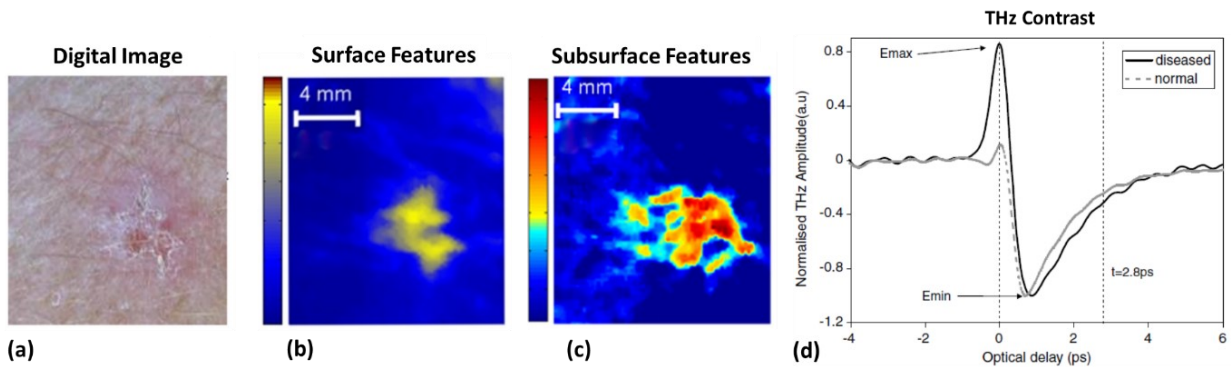


Figure 1.15: The first *in vivo* measurements of a basal cell carcinoma: (a) Digital image of the cancer region. (b) THz image generated by plotting the THz value at E_{min} , showing surface features. (c) Normalized THz image created by plotting the THz peak at the optical delay of 2.8 ps. Here, THz radiation penetrates below the surface and reveals subsurface features indicating the extent of the tumor at depth ($\sim 250 \mu\text{m}$). (d) THz time-domain trace illustrates the THz contrast between healthy and diseased tissue. (Figures adapted from reference [54])

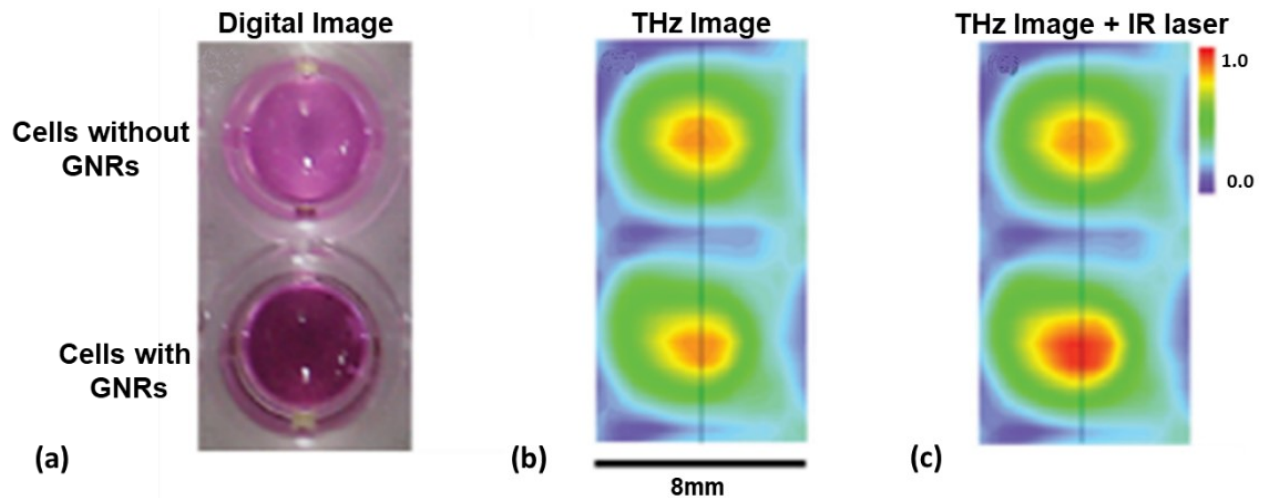


Figure 1.16: Cancer cell images with and without GNRs: (a) Digital image. (b) THz image without IR irradiation. (c) THz image with IR irradiation. The THz amplitude is the highest for the sample containing GNRs under IR laser irradiation. (Figure adapted from reference [57])

The same principle was applied *in vivo* and *ex vivo* studies of tumors by Oh *et al.* in 2011 [58] (Figure 1.17) and 2012 [59]. This so-called THz molecular imaging technique discriminates between tumor and healthy tissue by utilizing THz reflectivity modulations prompted by subcutaneously injected photoexcited NPs inside mice organs. The NP contrast agents function similarly to the nanoprobe used in magnetic resonance imaging or optical molecular imaging.

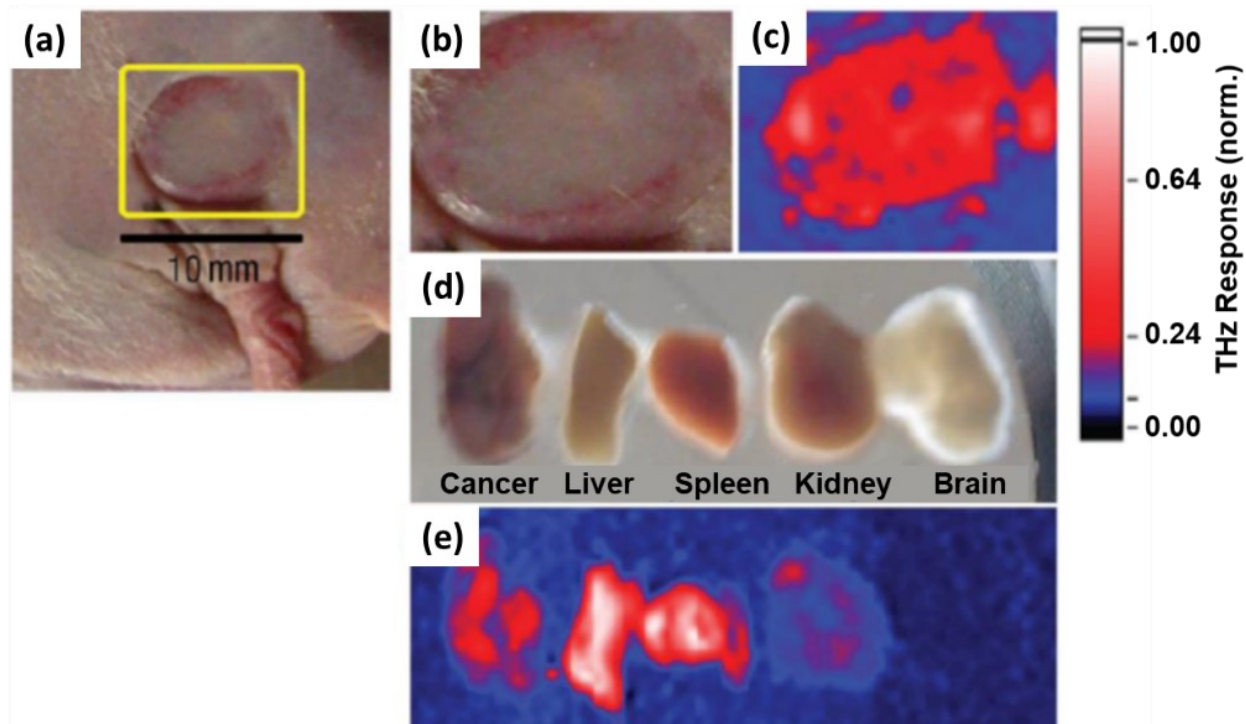


Figure 1.17: *In vivo* and *ex vivo* THz images of tumors after injection of GNRs conjugated with a tumor-cell targeting receptor in the circulatory system of a mouse: (a) and (b) Digital images of the mouse with a tumor. (c) THz molecular image of (b). (d) Digital images of the tumor, liver, spleen, kidney, and brain. (e) THz images of (d), the GNRs aggregated in the cancer cells, liver, and spleen. (Figures adapted from reference [59])

Naccache *et al.* [60] exploited the temperature-dependent refractive index change in the THz frequency regime to map the surface temperature of excised porcine skin tissue *in vitro* by employing a THz power – temperature calibration method. A GNR dispersion was subcutaneously injected into porcine skin tissue and subsequently excited by continuous wave (CW) NIR laser illumination (Figure 1.18(a)-(b)). Moreover, at the same time, a subsurface distribution of a subcutaneously injected drug compound was mapped (Figure 1.18(c)) containing ibuprofen, which exhibits a spectral fingerprint at 1.04 THz. The resulting hyperspectral image discriminated areas of different ibuprofen concentrations by evaluating the intensity of the ibuprofen spectral fingerprint in the frequency domain.

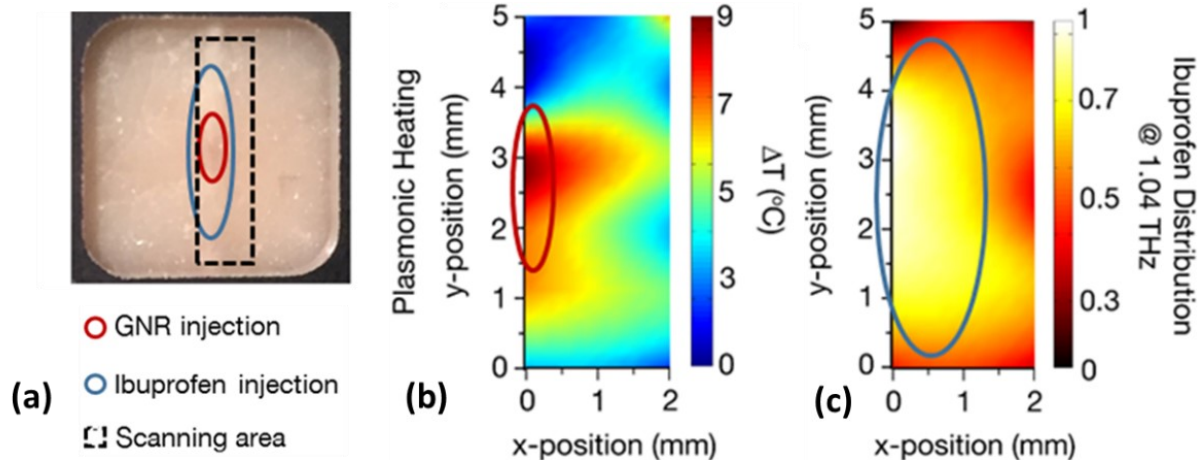


Figure 1.18: Terametry (temperature measurements by using THz radiation) for thermal imaging of porcine skin *in vitro*: (a) Digital image depicting the porcine skin, including the GNR and ibuprofen injection sites as well as the marked scanning area. (b) Thermal map obtained under plasmonic heating by NIR laser illumination, plotting the thermal distribution around the injection site. (c) THz image of the spectral distribution of an ibuprofen drug compound subcutaneously injected into the skin (Figures adapted from reference [60])

1.4 Nanoparticles

The term “nanomaterials” describes materials in which the dimensions, at least along one axis, is between 1 nm to 100 nm. NPs have several unique properties that distinguish them from their bulk version, which include high surface-to-volume ratio, high surface energy, unique optical, magnetic, electrical, thermal, and mechanical behaviors. These properties can be tailored, thus substantially extending their range of capabilities in comparison to their bulk counterparts. By using nanotechnology, materials can effectively be made stronger, lighter, more durable, more reactive, while improving, e.g., electrical conductivity. Nanotechnology can, for instance, lead to better computer processors, insulation materials, cutting tools, pollution reduction, more efficient batteries, highly improved sensors, and greener catalysis [61]. For example, the luminescence from molecules or semiconductor nanostructures can be enhanced by nearby NPs, a property that has ushered a new generation of light-emitting devices. Plasmonic NPs can reduce the footprint, and thus increase the performance of photodetectors as well as improve the efficiency of solar energy conversion [62]. The ability of nanoplasmonics to confine light down to nanoscale volumes provides unprecedented resolution for near-field optical microscopy, optical patterning, and optically assisted data storage [63].

Additionally, modern time-resolved spectroscopy allows studying the effects of “hot” electrons during laser light absorption on an ultra-short time scale [64], [65]. For example, plasmon resonances in NPs enable highly sensitive chemical sensing and identification down to the level of single molecules by using surface-enhanced Raman scattering (SERS). This surface-sensitive

technique enhances the Raman scattering of molecules when they are adsorbed on nanostructures [66]. Surface-enhanced IR absorption spectroscopy (SEIRAS) exploits the signal enhancement exerted by the plasmon resonance of nanostructured metal thin films to selectively probe biological molecules bound to the solid surface [67]. Nanoantenna enhanced terahertz spectroscopy (NETS) uses light-matter coupling phenomena to sense spectroscopic signatures of a nano-sized material or molecules at minuscule concentrations [68].

Specifically, inorganic NPs are most suitable for novel medical applications, since they are small-sized, offer adequate colloidal stability, and resistance to degradation. These properties have led to an increase in research activities in the development of nanoprobe for diagnostic medical imaging as well as heating agents for externally activated therapies. For example, inorganic NPs made of semiconductor materials, so-called “quantum dots,” can be excited by ultraviolet or visible light that induces a strong autofluorescence effect utilized for optical bioimaging. Another example is upconversion NPs based on lanthanide ions dispersed in a dielectric host lattice. These NPs display wavelength-selective upconversion capabilities in the NIR or visible wavelength regime that can be used for, e.g., high-contrast deep tissue and single-molecule imaging [69]. Notably, plasmonic NPs made of noble metals (e.g., gold, silver, platinum) have been widely used in various biomedical imaging and heating applications due to their chemical inertness (i.e., low toxicity) and well-established colloidal synthetic routes that make them physicochemically stable and confer tunability of their optical properties [70]–[74]. This customizability allows for optical imaging using elastically scattered light, spectroscopic imaging utilizing inelastically scattered light, and photoacoustic imaging deploying absorbed light. The scattering and absorption properties of NPs can be easily engineered [8], [75] by varying or modifying, for example, their morphology (e.g., spheres, rods, stars, shells, cages), their surface conditions, as well as size, i.e., larger NPs tend to scatter light more and absorb less [71]. Thus, the design of noble metal NPs can be tailored for specific biomedical applications. For absorption-based applications, such as PTT or photoacoustic imaging, smaller NPs are preferred due to their greater PCE (i.e., absorption dominates over scattering). For imaging applications, larger NPs are desirable for their increased scattering properties. Moreover, selective heating of noble metal NPs is similarly being investigated for the laser-assisted remote release of tethered medication for targeted drug delivery [76].

Of interest are gold NPs as they exhibit powerful intrinsic light absorption properties, which induce spatially confined heat that is applicable for PTT treatments. Herein, plasmonic gold NPs act as intense heating agents to damage and consequently destroy cancer cells. This new and minimally

invasive selective treatment option [77] uses the conversion of light-to-heat towards inducing hyperthermia in malignant cells. This phenomenon occurs when cells are exposed to temperatures above 42 °C for several minutes. It results in cell death from irreversible damage to protein and membrane structures.

Besides, the surface chemistry of gold NPs is adjustable to enable the NPs to selectively target cell populations without adversely affecting nearby untargeted tissue. Moreover, tuning the surface chemistry can enhance cellular uptake as well as minimize cytotoxicity for improved biocompatibility [78]–[81]. Additionally, photodynamic therapy combines PTT with a photosensitizing chemical substance used to generate molecular oxygen to elicit cancer cell death [82].

1.4.1 Localized Surface Plasmon Resonance Effect (LSPR)

The physical principle of the strong absorption properties of plasmonic gold NPs is the plasmon resonance effect [83]–[85]. Plasmons are collective oscillations of free electrons in metals at a well-defined wavelength. They can be explained as a negatively charged electron cloud coherently displaced from its equilibrium position around a lattice made of positively charged ions [85]. Specific plasmon modes can exist on the particle's surface, which is surrounded by a dielectric medium. An external electric field can excite this mode, as illustrated in Figure 1.19(a) for the spherical NP case.

Figure 1.19(b) plots a typical absorbance spectrum of a spherical NP exhibiting a peak at around 550 nm.

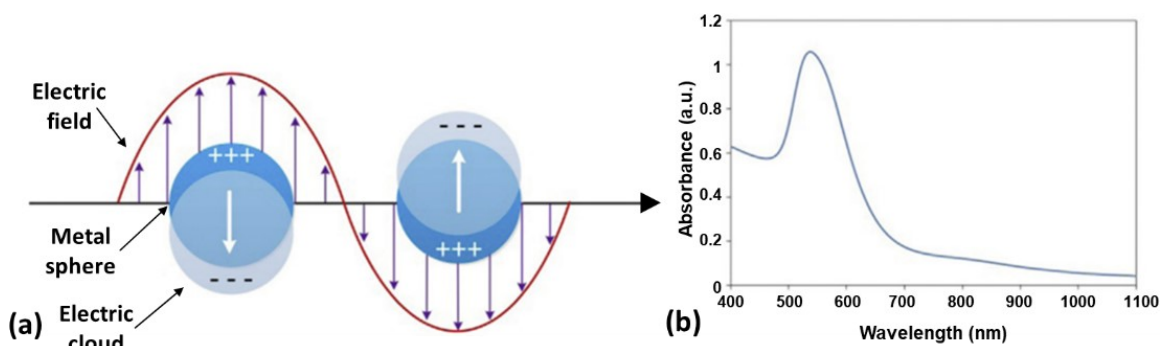


Figure 1.19: a) Schematic illustration of the LSPR arising from the coherent oscillation of conduction band electrons in resonance with incident light for a spherical NP. b) A typical LSPR absorbance spectrum of a spherical NP. (Figures adapted from references [83], [86])

Plasmons in NPs with a size much smaller than the photon wavelength are non-propagating excitations, therefore referred to as a LSPR, since the plasmon oscillation is distributed over the

entire particle volume [85]. The coherent electron displacement prompts a restoring force, which brings the polarized electrons back to the lattice. Therefore, the plasmon in a NP can be described by a mass-spring harmonic oscillator model, driven by the resonant electric field of a light wave. Only light with a wavelength in resonance with the oscillation can excite the LSPR [85]. The scattered light is a radiatively decaying LSPR that forms the basis of many optical and spectroscopic imaging applications. In contrast, photon absorption is a non-radiative decay in which a dephasing process of the LSPR begins following the optical absorption of the electromagnetic energy associated with the incident light wave.

This phenomenon leads to internal relaxation of the electrons via electron-electron scattering and electron-phonon coupling and ends with energy dissipation in the form of heat into the surrounding environment (Figure 1.20) [85], [87]. Especially in nanomedicine, this significant temperature increase of the surrounding constitutes the foundation of applications related to light-to-heat conversion [88].

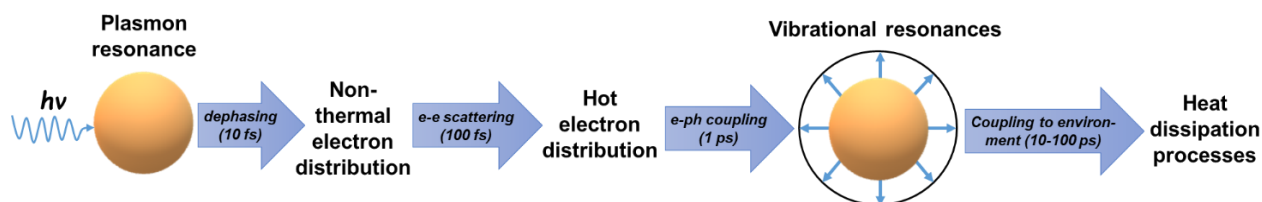


Figure 1.20: The sequence of events and time scales following the absorption of photons by NPs. (Figure adapted from reference [87])

Most notably, rod-shaped gold NPs, known as GNRs, are usually preferred for biomedical applications, since their LSPR wavelength can be easily shifted to the NIR wavelength domain, between 650 nm to 1350 nm. Light attenuation by tissue and blood is minimized in this so-called biological window (Figure 1.21). It is most suitable for deep tissue penetration of laser light during, for example, PTT treatments [89].

Therefore, GNRs were chosen in the experiments described in chapters 2 and 3; first, to evaluate their PCE and then to apply them into a photothermal conversion based biomedical context. It is important to mention that by breaking the NP symmetry of a spherical NP (elongating it into a rod-like shape), the GNR's aspect ratio (length/width ratio) is being changed.

Consequently, the conduction band electrons can oscillate in two directions, along the short axis and the long axis of the GNR, resulting in transverse and longitudinal LSPR modes (Figure 1.22(a)) that resonate in the visible as well as in the NIR wavelength range, respectively [83]. Figure 1.22(b) plots a typical absorbance spectrum of a GNR featuring the transverse and longitudinal LSPR peaks at around 530 nm and 780 nm, respectively.

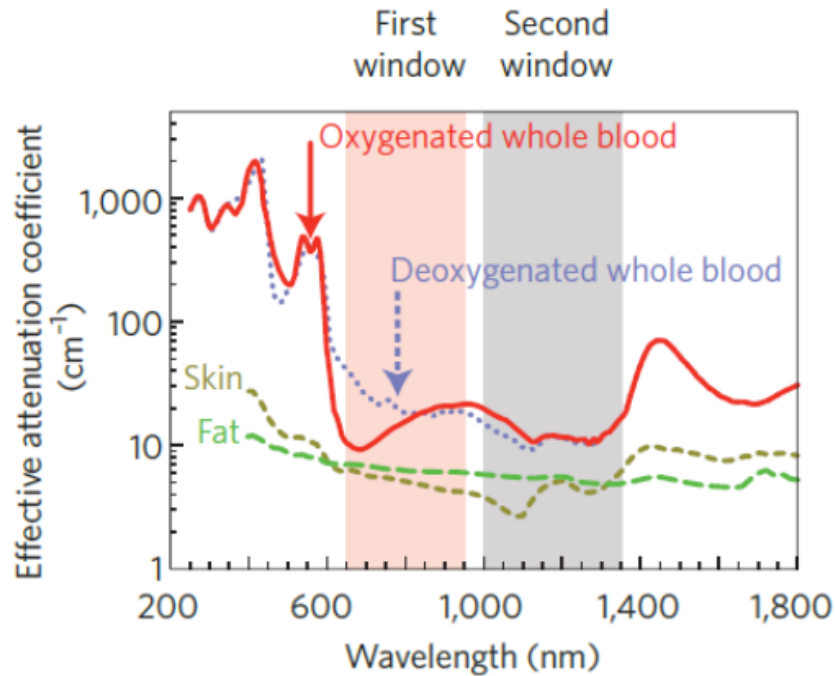


Figure 1.21: Plot of the wavelength-dependent effective attenuation coefficient of biological tissue highlighting the two biological windows. (Figure adapted from reference [90])

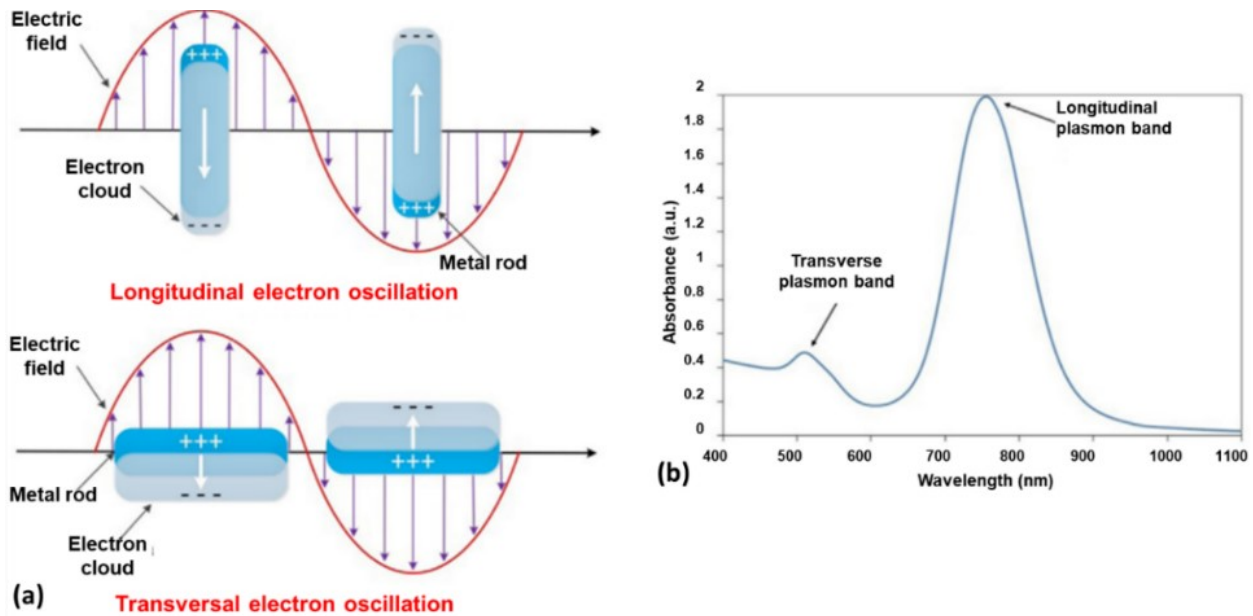


Figure 1.22: Schematic illustration of the (a) longitudinal and transverse LSPR of a rod-shaped NP. (b) A typical LSPR absorbance spectrum of a GNR exhibiting the transverse and longitudinal LSPR peaks. (Figures adapted from references [83], [86])

Figure 1.23(a)-(f) show TEM images of GNRs with lengths and diameters in the ranges of 20 nm to 65 nm and 10 nm to 20 nm, respectively. The aspect ratios accordingly range between 1.2 and 5.3. Figure 1.23(g) illustrates a shift in the longitudinal LSPR ranging from 520 nm to 960 nm as a function of an increasing aspect ratio.

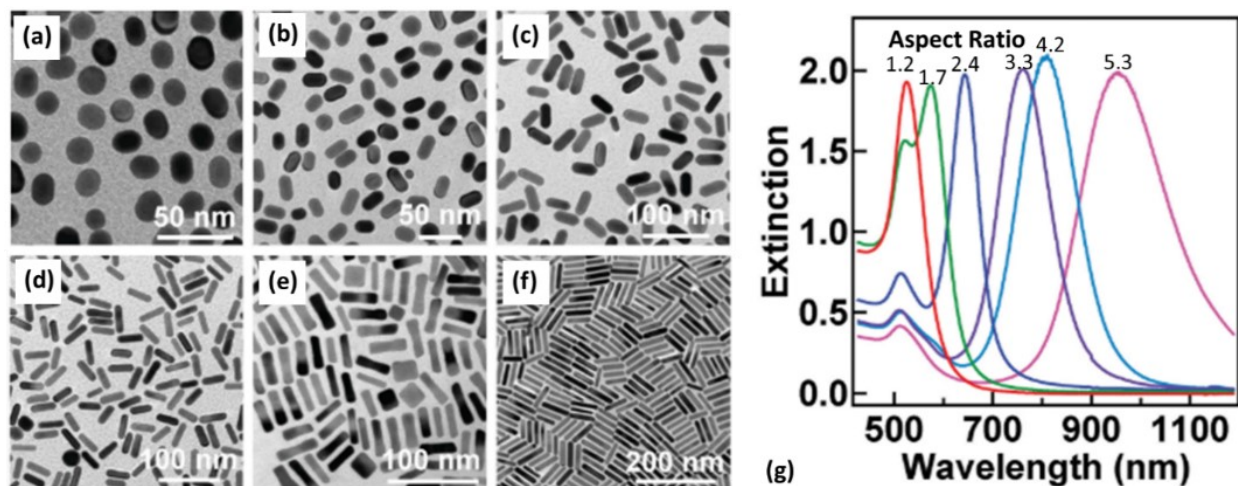


Figure 1.23: (a) – (f) TEM images of GNRs having an aspect ratio of (a) 1.2 (b) 1.7 (c) 2.4 (d) 3.3 (e) 4.2 (f) 5.3 (g) Extinction spectra of the GNRs (a) to (f) illustrating the effect of the GNR’s aspect ratio change on the position of the longitudinal LSPR peak. (Figures adapted from reference [91])

1.4.2 Quantification of the Photothermal Effect of Nanoparticles

The current high interest in plasmonic NPs is primarily due to past improvements in the ability to model, reliably synthesize, and characterize these nanostructures [85], which has led to the development of property-enhanced NPs with a significant impact on nanomedicine. Therefore, current research [5]–[7] is focused on, for example, optimizing the gold NP size and morphology to increase their tumor accumulation and PCE so that lower laser powers are required to perform PTT procedures. The PCE is a property of NPs that is used as a standard indicator to benchmark a NP’s capability to convert light into heat. It is defined as the ratio between the heat generated by a NP dispersion and the associated power loss of the excitation laser.

Unfortunately, the PCE of NPs dispersed in aqueous solutions cannot be easily quantified by just a single measurement. At first, the absorbance value AV of the NP dispersion under study must be determined, which is defined as:

$$AV = \log_{10} \left(\frac{P_{\text{incident}}}{P_{\text{transmitted}}} \right) \quad 1.7$$

where P_{incident} and $P_{\text{transmitted}}$ are the incident optical power originating from a laser source and the optical power transmitted through the sample, respectively. The absorbance can be determined by a UV-VIS-NIR spectrometer. This value depends on, e.g., the NPs’ size, concentration, morphology, and aggregation state. It contains a scattering and absorption term, where the latter relates to the heat increase of the NPs. Then, the PCE can be determined by either using an integrating sphere or an energy balance method.

The integrating sphere method has been reported recently and is a fast and straightforward method to determine the PCE of NPs based on the use of a sphere containing a laser source, the sample, and a power meter [92]. It accounts for light scattered, reflected as well as transmitted by the sample. However, this method does not reveal the local absolute temperature value and requires the sample to be placed into the integrating sphere, which in turn can hamper its broader applicability in real-world environments.

The energy balance method is the most often used standard technique relying on a numerical model reported by Roper *et al.* [93]. It allows direct heat performance studies of NPs comparing, e.g., different morphologies [6], [94], materials [95], sizes [8], and LSPR wavelengths [91]. This method encompasses the retrieval of temperature transients during photothermal heating and subsequent cooling cycles of a NP dispersion under study. Then, the PCE can be calculated by fitting the temperature transients to the numerical model and considering input parameters, including the mass and heat capacity of the constituents, incident laser power, as well as the sample's extinction value.

Thus far, the most popular method for measuring light-induced temperature changes in NP dispersions employs resistance thermometers (Figure 1.24(a)).

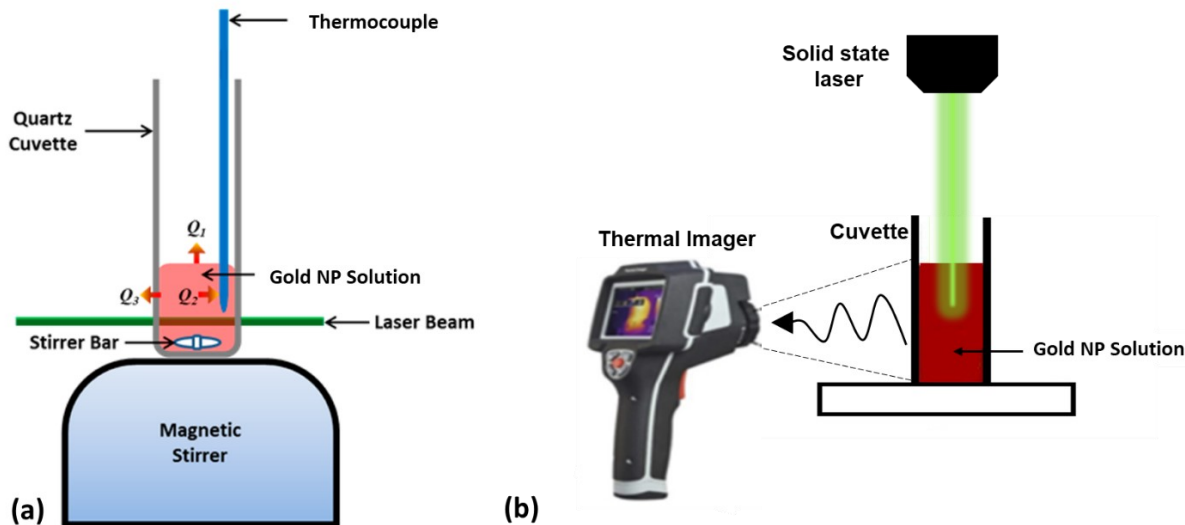


Figure 1.24: Experimental setup for measuring the temperature profile of gold NP solutions: (a) by using a thermocouple (Figure adapted from reference [8]). (b) by using IR thermography (Figure adapted from reference [9])

It measures a resistance value of a wire that depends on the temperature of its surroundings. Alternatively, thermocouples can be used that work based on the thermoelectric effect. A temperature-dependent voltage between two dissimilar electrical conductors is produced that can

be correlated to temperature [8]. Usually, either one or more resistance thermometers /thermocouples are inserted into a cuvette containing the NP dispersion to measure the temperature changes during the photothermal heating procedure. Both temperature measurement methods rely on physical contact with the NP sample, which can damage or contaminate it, as well as lead, e.g., to precipitation of the NPs. In addition, a magnetic stirrer must be used in order to guarantee a homogeneous temperature distribution as required by the numerical model that calculates the PCE. However, this method does not allow to instantaneously and reliably measure thermal dynamics within the illuminating laser spot. Moreover, it requires direct contact, thus potentially damaging or contaminating the sample, as well as altering the measurement itself.

More sophisticated methods, including IR thermometry and thermography, rely on detecting IR radiation emitted by an object to infer its temperature [9], [94] (Figure 1.24(b)). Although they offer non-contact and non-destructive detection capabilities, these methods can only measure surface temperatures within direct line-of-sight. This limits its usefulness since textiles, for example, are opaque to IR radiation.

In a pioneering work, Novelli *et al.* [96] measured the temperature of water dispersed gold nanospheres in a THz setup in transmission geometry during their photoexcitation with femtosecond laser pulses. The transmission configuration requires a high-power THz source, such as THz generation in a lithium niobite crystal, and a short sample-path length due to the high absorption property of THz radiation in water. Moreover, a THz-TDS setup in transmission geometry does not allow temperature measurements directly at the cuvette/NP dispersion interface.

A completely different approach, namely nanothermometry, relies instead on measuring changes in the luminescent properties of nano-sized probes to investigate local temperatures with sub-micrometric spatial resolution [97]. Even though this method is highly sensitive, it requires the injection of luminescent nanoprobess, which can potentially contaminate the sample and still cannot be used to measure the temperature when the sample is obstructed or beyond the line-of-sight [98].

To overcome these problems, a new method based on THz-TDS to characterize the photothermal effect of NPs in a non-contact and non-invasive manner has been developed within the work of this thesis.

1.4.3 Photothermal Conversion Based Therapy for Wound Closure Procedures

A recently developed minimally invasive medical procedure for wound closures [99] use NPs for laser-assisted tissue approximation with high potential to change future wound treatment procedures in clinical applications [100], [101]. Bonding of the edges of tissues is an essential step in every surgical procedure. The tissue borders must be joined to permit the starting of the natural healing process (Figure 1.25(a)). Today, the standard procedure for wound closure relies on surgical sutures (Figure 1.25(c)), which either involve a needle with an attached thread, or metallic or polymeric staples as well as clips. These procedures are easily adapted to most tissue types. However, they are inherently traumatic, injure the tissue and leave a foreign material inside. The wound closure is not comprehensive and watertight, and consequently, small gaps between the stitches can remain. Moreover, these bonding methods cannot be readily adjusted for endoscopic techniques, and their quality is highly dependent on the physician's skills.

In the 1970s, studies unveiled that the effect of local tissue heating speed up closure and healing of wounds, a process akin to the welding of solids. Several studies investigated laser soldering (Figure 1.25(b)) as a novel minimally invasive sutureless method for bonding of incisions in tissues [102]–[106]. Moreover, various works explored the photothermal effects of laser-assisted tissue soldering [107] to optimize the laser exposure time [108], laser intensity [109], and wound tensile strength [110], [111], as well as minimize its thermal injury potential. Recent findings suggest that a biological substance based on proteins, such as albumin, could be applied over the incision and heated together with the underlying tissue, hence functioning as a biological glue [112]. This laser soldering technique typically produces a more robust bond (Figure 1.25(d)).

The basic idea is to use laser light in combination with a solder gel to “stitch” surface wound openings together. When laser light illuminates the applied solder gel, the underlying tissue heats up and a continuous bond is created, reconnecting collagen. The soldering process can be enhanced by combining albumin with plasmonic NPs, e.g., GNRs, to form a photothermal nanocomposite that facilitates rapid wound sealing using heat-induced changes in the solder material and the tissue [99], [112]–[114]. The NPs act as localized absorbers that effectively and controllably transfer the impinging laser light into heat, spatially limited to the incision area of the tissue. In this way, less NIR laser power is needed, reducing potential detrimental thermal effects to the surrounding skin tissue, which facilitates the subsequent healing process. The result is a comprehensive watertight seal along the entire wound, blocking access to pathogens and not requiring suture removal. Advantages of laser-assisted tissue soldering over conventional sutures are a less inflammatory response of the tissue, a reduced chance of post-surgery infection, and

no allergic reactions to foreign materials being introduced by traditional stitches. Moreover, laser-assisted wound sealing is less traumatic and retains less scarred tissue, usually just a single line in contrast to crosshatch marks that are left behind by conventional stitching. It is also faster and easier to apply and much less skill dependent.



Figure 1.25: Wound closing study over 9 days of several skin incisions made in mice *in vivo*: (A) control sample (no treatment). Incisions were closed by using: (B) laser-assisted tissue soldering, (C) medical suturing, (D) laser-assisted tissue soldering involving a NP-protein compound. (Figure adapted from reference [14])

Additionally, laser-assisted tissue soldering can be used for intricate and complex tissues, such as the cornea, blood vessels, and nerves, that would otherwise be damaged by conventional suturing. Nevertheless, laser-assisted tissue soldering has not been widely used in clinical settings. The underlying reason is that elevated temperatures reached due to laser light absorption and concomitant heat generation can cause significant photothermal tissue damage, which limits the success of the laser-based tissue approximation approach. When the local temperature in tissue reaches a critical limit of around 60 °C, cells coagulate, which leads to the disruption of cell activity and possibly cell death [115]. Therefore, rigorous monitoring of the heated solder gel and underlying tissue is necessary to minimize damage and optimize the tensile strength of the bond. Current conventional non-invasive and non-contact biomedical imaging methods to measure burn depth and severity suffer from various limitations. For example, polarization-sensitive optical coherence tomography measures a change in the optical polarization of tissue resulting from thermal destruction of collagen fibers by detecting only the directly reflected photons [116]. Such a method is hampered by strong optical scattering and is unable to distinguish between different degrees of skin burns. Laser Doppler imaging has

emerged as a combination of Doppler flowmetry and laser imaging [117]. However, it is an indirect measure of burn depth and correlates the flow of blood in a burned area with the depth of the wound to assess its severity, which can eventually lead to misinterpretations. The main principle of IR thermography for assessing burn images relies on temperature differences on the surface of burned tissue, in order to distinguish between partial and full-thickness burns. The surface temperature of tissue decreases with increasing burn depth as time progresses due to a change in blood circulation. However, IR imaging suffers from scattering effects and limited contrast between tissues, which can cause misinterpretation, since it interprets natural heat loss from burned tissue as burn depth [118], [119]. Motivated by these challenges and drawbacks, a new method to perform non-invasive, non-contact, and non-ionizing THz imaging to monitor heat-related changes within skin tissue has been developed in this thesis.

2 CHARACTERIZATION OF THE PHOTOTHERMAL EFFECT OF PLASMONIC NANOPARTICLES BY TERAHERTZ LIGHT

This chapter describes a new method based on THz-TDS to characterize the photothermal effect of NPs in a non-contact and non-invasive manner. Specifically, the presented investigation shows how to determine the PCE and MHR of NPs dispersions. This approach is validated by characterizing three standard GNR dispersions. Similar measurements performed with other evaluation methods confirmed the results and numerical simulations further corroborated their reliability.

2.1 Setup for Nanoparticle Characterization and Imaging

As already mentioned in subchapter 1.3.1, a THz-TDS and imaging system based on PCAs was utilized to perform the experiments described in this thesis. The system was equipped with two PCAs (Tera8-1 from Menlo Systems) featuring a gap size of $5\ \mu\text{m}$ made of LT-GaAs as THz transmitter and detector. The emitted pulses of a wavelength duplicated Erbium-doped fiber laser source, providing a $775\ \text{nm}$, $50\ \text{mW}$, $100\ \text{fs}$, $100\ \text{MHz}$ pulse train (FemtoFiber smart from Toptica) were split into the pump and probe beams via a 50/50 beam splitter in order to generate photocarriers in the THz transmitter and detector, respectively. The transmitter antenna was biased by using a 30-Vpp square wave voltage running at $1\ \text{kHz}$. The emitted THz pulses were collimated and focused by four polymethylpentene (TPX) lenses (BATOP Optoelectronics) (Figure 2.1(a) and Figure 2.2) to realize a THz-TDS setup in reflection geometry.

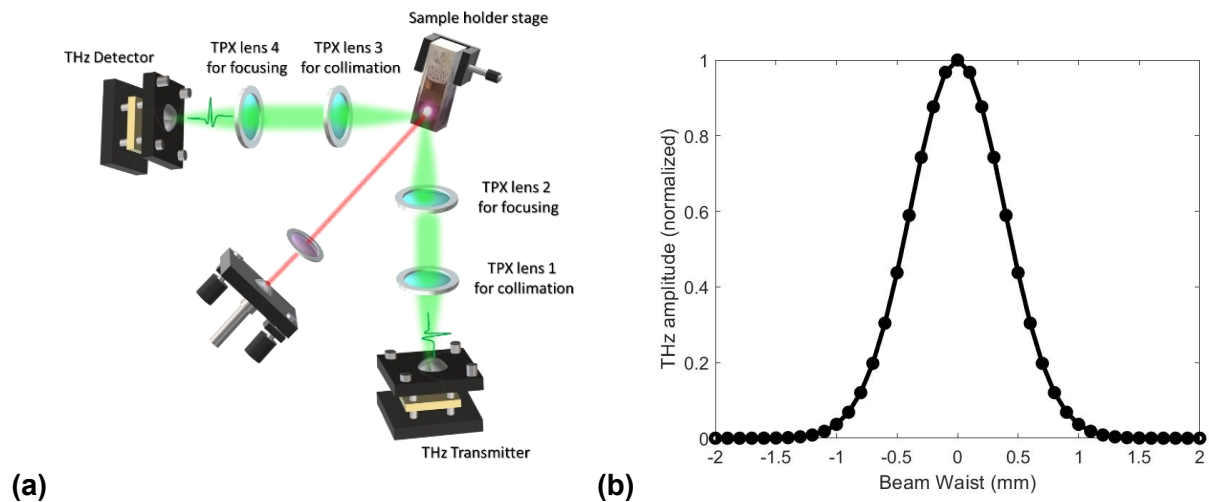


Figure 2.1: (a) Sketch of the THz part in the THz-TDS setup configured in reflection geometry used to characterize the photothermal effect of NP dispersions. (b) Gaussian beam intensity profile of the THz focus spot.

In particular, the first TPX lens with a focal length of 65 mm collimated the THz beam out of the PCA emitter, whereas a second 35-mm TPX lens focused the beam to a 1.5 mm ($1/e^2$) – diameter spot size (Figure 2.2(b)).

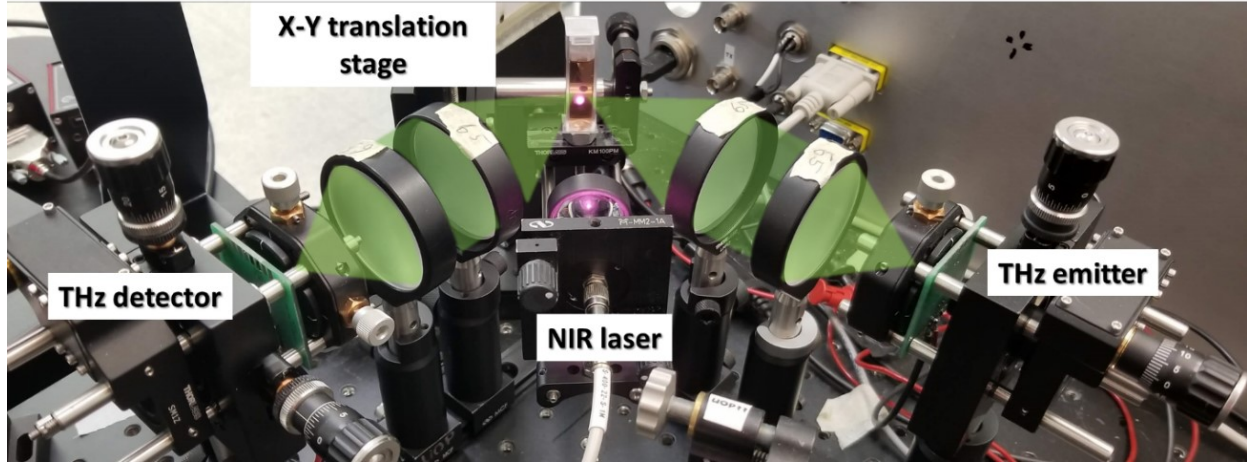


Figure 2.2: Digital image of the THz part in the THz-TDS setup configured in reflection geometry, shown in Figure 2.1(a).

A sample holder was installed in the focal plane of the second TPX lens. This holder accommodated a PE cuvette containing aqueous samples for the characterization of the photothermal effect of plasmonic NPs (subchapter 2.6). For monitoring the NP-assisted laser tissue soldering process (chapter 3), the holder was used to attach the biological tissue sample. The angle of incidence and reflection was 45 deg relative to the normal axis of the sample holder. The reflected beam was gathered and collimated via another 35-mm TPX lens. Finally, the THz beam was focused onto the detection PCA through a 65-mm TPX lens. A 50-mm long translational stage (T-LSM050A from Zaber) was used to delay the probe with respect to the pump beam in order to read out the THz transients. Moreover, a high-speed optical delay line (scanDelay 50 from APE) of 3.75 mm length (optical delay of 50 ps) was employed to retrieve each THz transient within 1 s. The THz induced photocurrent was read out by using a lock-in amplifier (SR860 from Stanford Research Systems) synchronized to the bias modulation frequency and further processed and displayed by a Labview based software suite. The averaging time constant was set to 300 μ s. The THz reference transient and its spectrum are illustrated in Figure 1.7. The power spectrum of the emitted THz transient peaked at around 0.3 THz and exceeded 3 THz. The signal-to-noise ratio (*SNR*) and dynamic range (*DR*) were evaluated as [120]:

$$DR(t) = \frac{\text{maximum value of temporal amplitude}}{\text{RMS of noise floor}} \quad 2.1$$

$$SNR(t) = \frac{\text{mean value of temporal amplitude}}{\text{STD of temporal amplitude}} \quad 2.2$$

where *RMS* stands for root-mean-square and *STD* is the standard deviation. *DR* and *SNR* are not constant over the entire THz time trace, but they maximize where the THz signal assumes its highest value. In order to achieve optimum parameters, equations 2.1 and 2.2 were evaluated at the peak of the THz transient, as suggested in [120]. This approach verifies the quality of the measurements. The *DR* and *SNR* of the THz signal in the time-domain were 60 dB and 419, respectively. They were recorded by using the high-speed optical delay line.

2.2 Deconvolution Algorithms and Signal Self-Referencing Method

Due to dielectric discontinuities as a function of depth, the reflected THz echoes associated with the Fresnel coefficients (i.e., reflections) between various interfaces, such as between a cuvette/NP dispersion, are recorded as a function of the transverse position in both amplitude and time delay. The accurate and precise determination of, for example, temperature values on multilayered structures relies on the precise extraction of THz echo parameters from the THz signal reflected off these interfaces.

Two THz pulse echoes can influence each other if they are either closely spaced or even overlapped in the time-domain, which usually happens with optically thin subwavelength structures, as shown in Figure 1.9(b). Specifically, the tail of a THz echo possesses an enduring signal, also called “ringing” [121] due to the ambient water vapor, which interferes with the subsequent echo if its temporal position is close. In this case, the two echoes cannot be distinguished and interfere with each other, which ultimately leads to phase and amplitude modulation as well as distortions. In order to well separate the echoes in the experimental data, a sparsity-based and FWDD deconvolution method were applied to extract the distinct waveforms of the THz reflections. Both numerical methods assume that the THz echoes represent time-shifted, amplitude-scaled copies of the incident THz signal. These computational approaches were used for the first time towards applications in THz signal post-processing by Parrott *et al.* [122] and recently further developed and enhanced by Dong *et al.* [48], [123].

The sparsity-based deconvolution method based on an iterative shrinkage algorithm was used to process the data acquired in the experiment described in chapter 2. The cuvette used here to hold the NP dispersion represents a distinct multilayer structure, which allows the impulse-response-function to fulfill the sparsity constraint of comprising only a few data points with non-

zero values. Moreover, the cuvette made of polyethylene is almost transparent in the THz frequency range, leading to minimal dispersion effects. Therefore, the reflected echoes can be considered as formed by time-invariant pulses without pulse spreading effects and well suited for the sparsity-based deconvolution algorithm.

Moreover, sparse deconvolution is better than FWDD in resolving small echoes due to Fabry-Perot reflections in the samples, as it is the case in the experiment reported in chapter 2. Another advantage of the sparse deconvolution method in contrast to FWDD and other conventional deconvolution techniques is that it is a pure time-domain method; thus, high- and low-frequency noise is not created.

FWDD was used for processing the experimental data described in chapter 3. The algorithm operates in the frequency-domain and is better suited to resolve THz echoes reflected off interfaces located inside biological samples. The reason is the high frequency-dependent attenuation and dispersion that THz waves experience during their propagation through biological tissue. This leads to pulse spreading and significantly lowers the performance of the sparsity-based deconvolution algorithm. FWDD, however, can process THz echoes that underwent dispersion better than the sparsity-based deconvolution method but offers a lower depth resolution.

For both, FWDD and sparse deconvolution, the minimal thickness resolution, corresponding to the depth resolution, depends on the coherence length, the sampling frequency, and the SNR.

2.2.1 Sparse Deconvolution Algorithm

In a THz-TDS system in reflection geometry, an impulse-response function [124]–[126] describes the input-output relationship between an incident THz reference signal and its reflection from a sample. First, the sparse deconvolution algorithm isolates the echoes in the impulse-response function corresponding to the interfaces of the sample from the convolved reflected THz time trace. Then, in a subsequent step, filtered THz time transients can be derived by re-convolving the deconvolved echoes with the THz reference signal. The resulting transients are associated with the respective interfaces of the sample structure.

In detail, the reflected THz signals originating from multilayer structures, such as a cuvette containing an aqueous dispersion (Figure 1.9(b)), comprise only a limited number of echoes since there are only a limited number of discrete layers. The impulse-response function can, therefore, fulfill the sparsity constraint of comprising only a few data points with non-zero values. Hence, the

temporal response of the deconvolution algorithm to the THz echoes is a sparse representation of the THz impulse-response function, which resembles a spike train sequence computed utilizing a sparse deconvolution algorithm [123].

A THz reflected signal is the convolution of the incident THz pulse $i(t)$ with the impulse-response function $f(t)$, which corresponds to the structure and properties of the sample at a specific point of depth [49]. The reflected signal $r(t)$ is described as:

$$r(t) = i(t) \otimes f(t) = \int_{-\infty}^{+\infty} i(\tau)f(t - \tau)d\tau \quad 2.3$$

For reflective THz imaging, the incident THz pulse $i(t)$ is attained by recording the THz reference signal and multiplying it by a factor of -1 for phase correction [49]. The discretized version of equation 2.3 is:

$$r_n = \sum_{m=0}^{M-1} i_m f_{n-m} + e_n \quad 2.4$$

where $r_n = r(nT_s)$, $i_m = i(mT_s)$, and e_n accounts for the noise originating from the measurement system. n and m are the indices associated with the data points ($m < n$), and M is the overall quantity of data points. The THz transients were recorded with a sampling step size T_s of 5 fs. The sample points of r_n , i_n , f_n , and e_n link to the column vectors r , i , f , and e , respectively. Therefore, equation 2.4 is a system of linear equations that must be satisfied, and the sparsest solution for f is desired. Thus, the core sparse representation problem is defined as the pursuit of the sparsest possible representation of f satisfying:

$$r = Af + e \quad 2.5$$

where A is an $m \times n$ convolution matrix, the columns of which are delayed versions of i . f is the sparse vector of the impulse-response function that has only a few non-zero components. Sparse deconvolution aims at approximating the received THz signal r with Af . The sparse vector f is computed by solving the l_0 regularized optimization problem, which is defined as

$$\min_f \frac{1}{2} \|Af - r\|_2^2 + \lambda \|f\|_0 \quad 2.6$$

where $\|f\|_0$ is a regularization term constituting the l_0 norm of f , which is, in turn, defined to be the number of nonzero entries in f . $\lambda > 0$ is the regularization parameter, which controls the

importance of the regularization term and constitutes a trade-off between the sparsity of f and the reconstruction fidelity (residue norm $\|Af - r\|_2^2$) [49]. The regularization parameter was chosen according to the level of system noise. However, solving the non-convex l_0 regularized optimization problem is difficult since it is a non-deterministic polynomial; hence, the global optimum cannot be guaranteed [127]. Therefore, a technique known as Basis Pursuit De-noising was used to relax the l_0 norm and replace it with the convex l_1 norm. This led to the convex mathematical optimization problem:

$$\min_f \frac{1}{2} \|Af - r\|_2^2 + \lambda \|f\|_1 \quad 2.7$$

where $\|f\|_1$ is the l_1 norm of f , which is a $n \times 1$ solution vector (impulse-response function), and is defined as the sum of the absolute values of its components:

$$\min_f \|f\|_1 = \sum_{n=0}^{N-1} |f_n| \quad 2.8$$

Since the l_1 norm is convex, a global optimum is guaranteed. The solution of equation 2.7 cannot be written in an explicit form and can only be found by running an iterative numerical shrinkage algorithm in a closed-form expression [49], [128]. It can solve the optimization problem with a limited number of parameters that need to be tuned. Each iteration performs matrix-vector multiplication involving A and A^T followed by a shrinkage or soft-thresholding step.

The general iterative procedure is given by:

$$f_{i+1} = S_{\lambda\tau}(f_i - \tau A^T(Af_i - r)) \quad 2.9$$

where τ is an appropriate gradient step size, which should obey the relation:

$$\tau < \frac{2}{\|A^T A\|_2} \quad 2.10$$

In order to guarantee convergence, the shrinkage or soft-thresholding operator $S_{\lambda\tau}$ [49], [128] is defined as:

$$S_{\lambda\tau}(f[n]) = \begin{cases} f[n] + \lambda\tau & f[n] \leq -\lambda\tau \\ 0 & f[n] < \lambda\tau \\ f[n] - \lambda\tau & f[n] \geq \lambda\tau \end{cases} \quad 2.11$$

This iterative shrinkage algorithm guarantees that the solution is a global minimizer for a convex norm [128]. For processing the reflected THz signals, the iteration based on equation 2.9 was performed 3000 times with a regulation parameter of $\lambda = 0.4$ and a step size of $\frac{1}{\|A^T A\|_2}$ [49].

2.2.2 Frequency-Wavelet Domain Deconvolution (FWDD)

FWDD [48], [129] was used to post-process the THz traces recorded during the study of NP-assisted laser tissue soldering by THz radiation, as shown in chapter 3. It is a deconvolution algorithm based on inverse filtering and was previously deployed for unveiling defects and probing properties of multilayered structures, for example, paintings [48], polymer layers [130], human skin tissue [129], and fiber-reinforced composites [131]. The algorithm wants to recover the impulse-response function by deploying the inverse Fourier transform of the transfer function (ratio between the THz frequency spectra of the reflected and incident THz traces). Nevertheless, by using this inverse technique, noise in the high- and low-frequency range can be created and leads to a detrimental effect in the recovered impulse-response function [132].

The fundamental principle of FWDD is to improve the deconvolution process by applying three steps: first, employing frequency-domain filtering, second, further improving the SNR by wavelet denoising, and third, cancel slow fluctuations by performing baseline subtraction. Moreover, the depth and time resolution of FWDD depends on the width of the frequency-domain filter, the SNR, and the data sampling period of the measurement.

As already mentioned in subchapter 2.2.1, the THz signal $r(t)$ reflected from an inhomogeneous sample is the convolution between the incident THz pulse $i(t)$ and the impulse-response function $f(t)$, which consists of a sequence of ideal impulses corresponding to the external and internal layer structure of the sample [133].

$$r(t) = i(t) \otimes f(t)$$

$f(t)$ can be determined by performing the inverse Fourier transform based on the convolution theorem [48].

$$f(t) = \text{FFT}^{-1} \left[\frac{\text{FFT}(r(t))}{\text{FFT}(i(t))} \right] \quad 2.12$$

where FFT and FFT^{-1} represent the standard and inverse Fourier transformation, respectively. Nevertheless, a frequency-domain filtering step must be performed to suppress noise in the high-

frequency range that arises from the division by small numbers, which results in large spikes in the high-frequency part and creates severe ringing in the time-domain. Frequency-domain filtering is performed as follows:

$$f(t) = \text{FFT}^{-1} \left[\text{FFT}(g(t)) \times \frac{\text{FFT}(r(t))}{\text{FFT}(i(t))} \right] \quad 2.13$$

where $g(t)$ is the filter function in the time-domain [48]. Equation 2.13 can be transformed using the convolution theorem:

$$f'(t) = g(t) \otimes f(t) \quad 2.14$$

where $f'(t)$ can be considered as a reconstructed signal obtained by entering a new function $g(t)$ instead of the incident THz reference signal $i(t)$.

The time duration of the new function $g(t)$ has to be short enough to resolve the time intervals between discrete THz echoes to achieve a successful reconstruction of the signal. Moreover, the new function must not contain additional signal cycles prior to or after the central THz peak. Otherwise, the echo to be resolved can be hidden in the reconstructed THz time trace. The design of the new function $g(t)$ is a trade-off between time resolution and noise filtering [134]. If the time duration of the new function $g(t)$ is too short, its frequency spectrum could include large spikes at high frequencies. This can reduce the fidelity of the reconstructed THz signal in the time domain.

A Hann window was chosen as filter function $g(t)$, and its frequency spectrum $G(\omega)$ is expressed as

$$G(\omega) = \begin{cases} e^{i\omega t_0} \cos^2\left(\frac{\omega}{4g_c}\right) & |\omega| \leq 2\pi g_c \\ 0 & |\omega| > 2\pi g_c \end{cases} \quad 2.15$$

where t_0 denotes the arrival time of the THz central peak, and g_c is the cut-off frequency. The configuration of the parameters of g_c is a trade-off between SNR and time resolution. If a precisely resolved THz echo is needed, for example, to perform spectral characterizations, a high time resolution must be ensured by choosing a high cut-off frequency (3 THz in this study), which, in turn, will lower the SNR.

If a high value of g_c is chosen, and therefore, the SNR is insufficient, a stationary wavelet shrinkage method [135], [136] should be applied to lower the remaining noise in the time-domain.

Wavelet shrinkage is a signal de-noising technique based on the principle of thresholding the wavelet coefficients given that the shape of THz pulses resembles conventional wavelet basis functions. This method decomposes a 1D signal into the approximation coefficients, specifically vector and detail coefficients, by performing convolution operations with a low-pass and high-pass filter along the temporal axis at each level [136]. Wavelet coefficients with small absolute values should be treated as noise, while wavelet coefficients with large absolute values are considered as the essential content of the THz signal [17]. Eliminating the small absolute value coefficients by applying a threshold and afterward reconstructing the THz signal should lead to a THz trace with diminished noise contribution. Specifically, *symlet* (sym4) wavelets, a modified version of Daubechies wavelets [48], were applied for wavelet decomposition up to a maximum level of 7 (higher levels did not result in a better decomposition outcome).

Occasionally, after the application of the FWDD algorithm, the THz time trace contained noise in the low-frequency range in the form of slow fluctuations. This phenomenon was generated by THz transmitter deficiencies in the low-frequency range. This noise can be reduced by subtracting the baseline of the reconstructed THz signal, which represents the impulse-response function that can uncover layers having a subwavelength thickness.

2.2.3 Signal Self-Referencing Method

A THz-TDS system shows frequent amplitude fluctuations and phase shifts during operation due to temperature variations of the surrounding environment, vibrations, and delay line drifts, which hinders a precise determination of changes in the THz reflectivity introduced by dielectric property modifications of a sample. Therefore, a self-referencing technique was deployed after the successful deconvolution of the THz echoes originating from different interfaces within a sample. The fluctuations in amplitude and phase of these reflected echoes are correlated since they arise from the same intrinsic system noise.

The fundamental concept of the utilized self-referencing technique is to relate all echoes within a THz trace to the 1st echo, which originates from the sample's surface. This 1st echo remains constant during the entire measurement even though the properties of the subsequent interfaces alter due to, for example, temperature changes. If the amplitude or phase of the 1st echo changes during the measurement, all subsequent echoes can be corrected accordingly, which eliminates the influence of system fluctuations from echo variations that are caused by changes in the dielectric properties of the sample at specific interfaces. The following equation normalizes and, therefore, corrects the subsequent echoes to the 1st echo:

$$E_{x^{th}}^{corr} = \frac{E_{1^{st}}^{const}}{E_{1^{st}}} E_{x^{th}} \quad 2.16$$

where $E_{1^{st}}^{const}$ represent the THz electric field of the 1st echo that is set to be the reference for all subsequently measured 1st echoes ($E_{1^{st}}$). $E_{x^{th}}$ stands for each subsequent echo that is changed due to either system fluctuations or modifications in the dielectric properties of an interface. $E_{x^{th}}^{corr}$ denotes the corrected THz electric field of each specific echo originating from internal interfaces.

Figure 2.3 illustrates the impact of the self-referencing technique and deconvolution method to the calibration data used during the characterization of the photothermal effects by NPs (subchapter 2.5). The dynamics of the 1st and 2nd echo amplitudes extracted from the raw THz signal data as a function of temperature changes are plotted in blue while their corrected versions after deconvolution and self-referencing are traced in red. The results in Figure 2.3 substantiates that the employed signal processing techniques successfully filter the THz trace data from system fluctuations and inherent echo interferences due to the structure of the sample. This procedure can, therefore, improve the accuracy and precision of measurements relating to the changes in the dielectric properties of different layers and interfaces inside of samples.

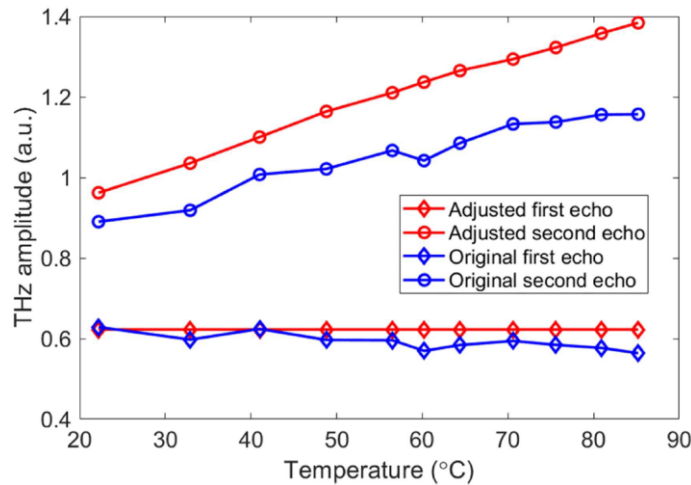


Figure 2.3: The THz amplitudes of the 1st and 2nd echoes before and after signal processing. (Figure adapted from reference [137])

2.3 Theoretical Model for the Determination of the Photothermal Conversion Efficiency

The PCE can be calculated by employing a macroscopic model [93] that describes the collective particle heating effect in an aqueous solution encompassing heat generation and dissipation inside an enclosure.

The variation in temperature induced by NIR illumination can be defined by using an energy balance equation:

$$Q_{\text{abs}} - Q_{\text{diss}} = \sum_i m_i C_i \frac{dT}{dt} \quad 2.17$$

where Q_{abs} denotes the energy introduced by the absorption of NPs, Q_{diss} is the heat dissipated into the surrounding medium, T is temperature, t represents time, m_i and C_i are the mass and the specific heat capacities of the elements i encompassing the whole physical system (i.e., GNRs, deionized water, and PE cuvette), respectively. This equation describes the temperature evolution over time given the amount of energy absorbed by the NP dispersion and dissipated out of the vessel. Heat diffusion and convection affect the calculation of the PCE. Indeed, conventional methods homogenize the thermal distribution inside the cuvette to be able to use the entire mass of the NP dispersion/cuvette system in equation 2.17. Though, the present non-contact method does not homogenize the temperature distribution inside the cuvette and, this “spatial” information is included in the effective mass of the NP dispersion/cuvette system. The effective mass is extracted experimentally from THz thermograms of the NP dispersion/cuvette interface inside the cuvette directly where the heating occurs, as detailed further in the text.

It is important to note that the mass of the actual NPs is usually insignificant in comparison to that of the solvent (3 g) and the PE cuvette (2.5 g); therefore, it can be neglected. In this case, the weight concentrations were 109 $\mu\text{g/mL}$, 165 $\mu\text{g/mL}$, and 150 $\mu\text{g/mL}$ of gold for the three standard GNR dispersions.

Furthermore, the specific heat capacity of gold (0.129 J/gK) is also much smaller than that of water (4.18 J/gK) and PE (1.33 J/gK). Hence, the mass and heat capacity of the entire NP dispersion is assumed to be that of water.

The absorption and dissipation energy in equation 2.17 can be written as follows:

$$Q_{\text{abs}} = P(1 - 10^{-AV_\lambda})\eta \quad 2.18$$

$$Q_{\text{diss}} = hS[T(t) - T_0] \quad 2.19$$

where P stands for the incident NIR laser power used to photoexcite the LSPR of the NPs, η is the PCE, S is the surface area covered by the NP dispersion in the enclosure, AV_λ is the absorbance value of the NPs at the excitation wavelength of the laser, T_0 is the ambient temperature, and h is the heat transfer coefficient.

Then, equation 2.17 can be rewritten as follows:

$$\frac{dT}{dt} = \frac{P(1 - 10^{-AV\lambda})\eta}{\sum_i m_i C_i} - \frac{hS}{\sum_i m_i C_i} [T(t) - T_0] \quad 2.20$$

The two variables A and B are defined as:

$$A = \frac{P(1 - 10^{-AV\lambda})\eta}{\sum_i m_i C_i} \quad 2.21$$

$$B = \frac{hS}{\sum_i m_i C_i} \quad 2.22$$

where A is the rate of energy absorption, and B is the rate of heat dissipation, which allows for a simplified version of equation 2.20:

$$\frac{dT}{dt} = A - B[T(t) - T_0] \quad 2.23$$

The temperature transient for an arbitrary initial temperature value T_{initial} can be calculated by integrating equation 2.23 from 0 to t :

$$T(t) = T_0 + \frac{A}{B}(1 - e^{-Bt}) + (T_{\text{initial}} - T_0)e^{-Bt} \quad 2.24$$

In order to compute the PCE, it is necessary to measure the temperature variation of the NP dispersions as a function of time during the photothermal heating (under laser excitation, $A \neq 0$ and $T_{\text{initial}} = T_0$) and the subsequent cooling cycle ($A = 0$ and $T_{\text{initial}} > T_0$). By fitting the experimental curve with equation 2.24, the values of A and B can be extracted and used to calculate the experimental PCE η :

$$\eta = \frac{A \sum_i m_i C_i}{P(1 - 10^{-AV\lambda})} \quad 2.25$$

The MHR has been recently introduced to measure the photothermal properties of NPs in the biomedical domain [6] and is defined as the initial rate of change in temperature divided by the molar concentration. The MHR is calculated as:

$$MHR = \frac{A}{c} \quad 2.26$$

where A denotes the energy absorption rate and represents the initial rate of variation in temperature (specifically, the time derivative evaluated at $t = 0$). It corresponds to the heating rate [138] of the NP dispersion, where c represents the molar concentration (molarity) of the NP dispersion. Theoretically, the energy absorption rate A can be approximated by calculating the time derivative at $t = 0$, but tracing the whole temperature transient gives a more consistent set of data for the precise extraction of the energy absorption rate A .

2.4 Gold Nanorod Dispersions for Benchmark Tests

In this study, three distinct dimensions of commercially available (Nanopartz™) GNRs were used as a benchmark to validate the proposed approach. Their performance was compared to determine which particle size produces the highest temperature increase under NIR plasmonic excitation at a wavelength of 786 nm, as well as prove the underlying physical mechanism.

Multiple techniques are often used in parallel to characterize the size, shape, surface chemistry, and aggregation state of NPs, which is required to be able to compare different types of NPs objectively. Among the essential methods are transmission electron microscopy (TEM) that allows for the direct observation of the size and shape of colloidal or substrate stabilized NPs [139]. Figure 2.4(a)-(c) shows PE cuvettes containing the GNR dispersions and their representative TEM images performed using a Phillips CM-100 100kV device. The average dimensions (diameter x length) of the three GNR types were 10 nm x 41 nm, 25 nm x 90 nm, and 50 nm x 150 nm. The three GNR dispersions will be referred to as GNR10, GNR25, and GNR50 throughout the text. Their aspect ratios (diameter to length ratio) were 3, 3.6, and 4.1, respectively. These GNRs were explicitly designed to provide the same LSPR wavelength of around 808 nm for all three dispersions. Moreover, their respective transverse LSPR was located at around 520 nm, which is far from the excitation laser emission line of 786 nm, as shown in Figure 2.4(d).

Moreover, zeta potential measurements were performed by using a Dynamic Light Scattering (DLS) technique carried out by employing a Malvern Nano ZS device. Such a piece of equipment measures fluctuations in scattered light intensity due to the Brownian motion of dispersed NPs. The DLS device determines the diffusion coefficient of NPs, which is related to their hydrodynamic size [140]. This size encompasses not only the NP core but also its surrounding capping ligand. In this way, the degree of monodispersity (i.e., the level of agglomeration in the NP dispersion), the NP's surface charge (i.e., its colloidal stability), and the surface chemistry [141] can be evaluated. All three GNR dispersions were passivated with hexadecyltrimethylammonium bromide (CTAB) ligands and dispersed in deionized water. The GNRs of each dimension possessed Zeta potentials of around 35 mV, which indicate adequate colloidal stability. The

coefficient of variation (CV) of the size monodispersity was determined to be less than 10%. The dispersions were purified of any reactive chemicals, and the CTAB concentration was maintained below 5 mM.

Additionally, gold mass measurements were performed by using inductively coupled plasma mass spectrometry (ICP-MS) using a Varian 820-MS device. ICP-MS is a method to measure the metal ion concentration within a NP dispersion to determine its particle number concentration. The GNR10, GNR25, GNR50 dispersions contained 1.9×10^{12} , 2.1×10^{11} , and 3×10^{10} GNRs per mL, respectively.

Moreover, all three GNR dispersions were further characterized via measuring absorbance spectra acquired by using a UV-VIS (Agilent 8453) and NIR (Agilent Cary 500) spectrophotometer utilizing a 10-mm optical path length quartz cuvette. Figure 2.4(d) plots the spectra over a range of 450 nm - 1100 nm. GNR25 showed the highest absorbance value of 3.31 at the LSPR wavelength of around 808 nm, followed by GNR50 with 3.21, and GNR10 with 3.05. The absorbance at the NIR laser wavelength of 786 nm (emission line of the photoexciting laser source) was 2.70, 3.15, and 3.05 for GNR10, GNR25, and GNR50, respectively. Table 2.1 lists the physico-optical properties of the three GNR dimensions.

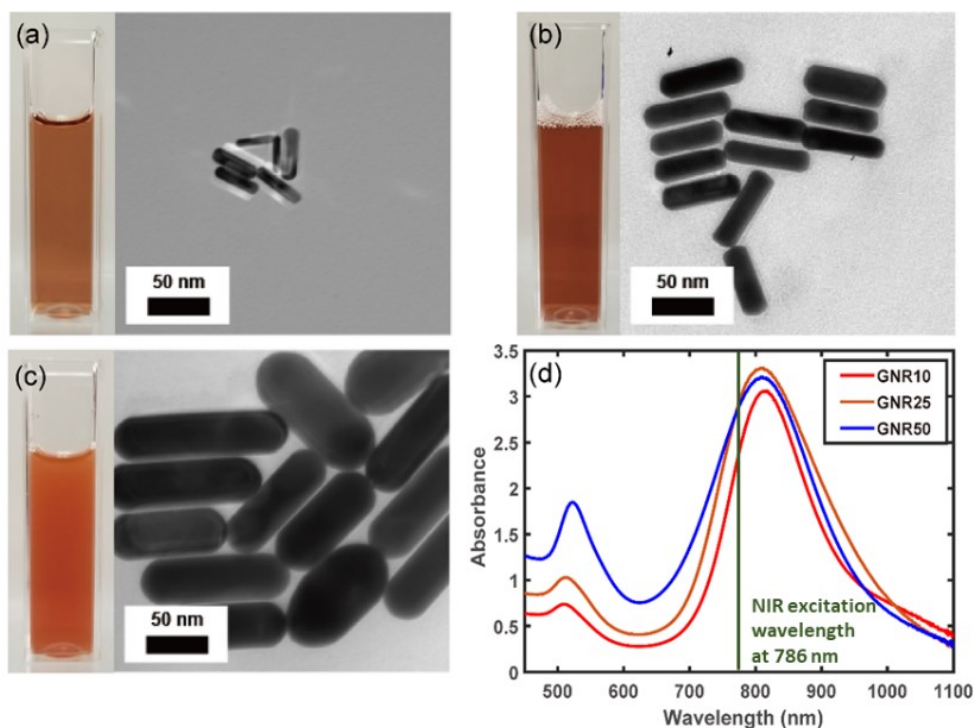


Figure 2.4: Digital images of the sample cuvette containing the dispersed GNRs with the dimensions of (a) 10 nm x 41 nm, (b) 25 nm x 90 nm, and (c) 50 nm x 150 nm, as well as their representative TEM images. (d) VIS-NIR absorbance spectra of the three GNR dispersions highlighting the laser emission line at 786 nm at which the GNRs were plasmonically excited during the experiments. (Figures adapted from reference [137])

Table 2.1: Physical and chemical parameters of the investigated GNR dispersions.

	GNR10	GNR25	GNR50
Longitudinal SPR Peak (nm)	815	810	811
Absorbance at LSPR peak	3.05	3.31	3.21
Absorbance at 786 nm [A_{λ}]	2.70	3.15	3.05
Transverse SPR Peak (nm)	510	512	523
Potential of Hydrogen pH	6	6	7
Weight Concentration ($^{mg}/_{mL}$)	0.109	0.165	0.150
Aspect Ratio	4.1	3.6	3
Length (nm) × Diameter (nm)	41 × 10	90 × 25	150 × 50
Zeta Potential (mV)	37	34	35
Concentration ($^{NPs}/_{mL}$)	1.9×10^{12}	2.1×10^{11}	3×10^{10}
Molarity (nM)	3.172	0.356	0.050
Molar Extinction ($^{1}/_{M \cdot cm}$)	9.8×10^8	9.3×10^9	6.1×10^{10}

2.5 Calibration Curve for Temperature Measurements using THz-TDS

Thermal sensing, using THz reflectivity modulations that originated from temperature-induced refractive index changes of an aqueous NP sample, requires a temperature-dependent calibration curve. This curve is a function correlating the reflected THz amplitudes to the actual temperature variations of the sample and was experimentally determined for all three GNR dispersions.

A THz-TDS system described in subchapter 1.3.2, configured to reflection geometry, was deployed for the measurements.

Figure 2.5(a) shows the central part of the THz setup containing a sealable PE cuvette with a 10-mm path length. The cuvette was placed in the THz focusing spot. The sample cuvette was a disposable Eppendorf Vis macro cuvette made of Poly(methylmethacrylate) (PMMA). The cuvette

was transparent to radiation in the spectral range between 300 nm and 900 nm. The sample light path length inside the cuvette was 10 mm, and the outer dimensions were 12.5 mm × 12.5 mm × 45 mm. The cuvette's maximum filling volume was 4.5 mL. During the measurement, the cuvette contained 3 mL of the GNR dispersion under study, leading to a volume for the aqueous dilution of 10 mm × 10 mm × 32 mm. The cuvette was tightly sealed by using a lid made of Teflon to prevent any evaporation of the dispersion inside the cuvette. A NIR laser (LSR793H-FC-3W from Lasever) emitting a CW laser beam at 786 nm wavelength was utilized to photoexcite the GNR particles inside the sealed cuvette.

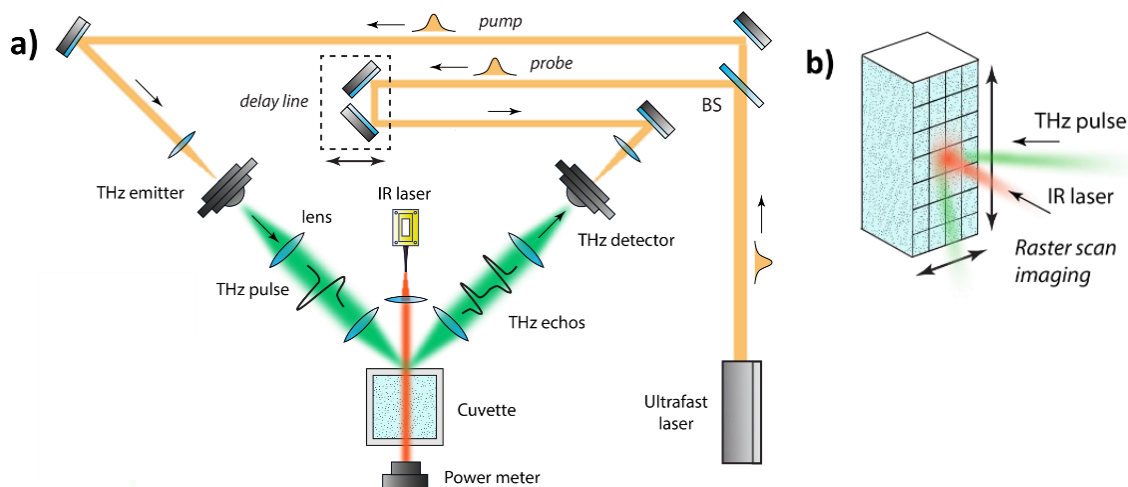


Figure 2.5: (a) Schematic diagram of THz temperature measurements based on a THz-TDS system in reflection geometry depicting an ultrafast laser system emitting a pulse train that was split by a beam splitter (BS) into a pump and probe beam and subsequently guided to the THz emitter and detector, respectively. The probe beam passed through a temporal delay in order to perform THz-TDS. A 786-nm CW NIR laser beam used to plasmonically heat the GNR dispersions was overlapped with the THz focusing spot. The power of the NIR illumination transmitted through the cuvette was recorded with a power meter. (b) Schematic diagram depicting the THz raster-scan imaging process of the front and rear window of the cuvette. During the scanning process, the THz beam was rigid, and the cuvette moved together with the NIR laser pixel-by-pixel. (Figures adapted from reference [137])

Figure 2.6 shows a representative THz transient reflected off the sample. Three THz echoes can be recognized that refer to each interface: 1st echo (air/cuvette), 2nd echo (cuvette/GNR dispersion), and 3rd echo (second-round reflection due to the etalon effect).

The THz focal spot diameter was approximately 1.5 mm ($1/e^2$) at an angle of incident on the sample of 45 deg relative to the normal axis of the cuvette. The NIR laser spot size diameter was around 2 mm ($1/e^2$) and focused onto the cuvette at the surface normal. Both beams were overlapped, which was confirmed by replacing the sample with a silicon wafer. As soon as the NIR laser and the THz beam were superimposed, the THz amplitude decreased. The underlying mechanism is that the NIR laser photoexcited carriers from the valence band to the conduction

band, where they interact with the THz radiation causing strong photoinduced absorption of the THz radiation as witnessed by an immediate sharp decline in amplitude. In this way, it was possible to trace the temperature-induced THz modulations precisely within the heating spot at the interface between the cuvette and the NP dispersion.

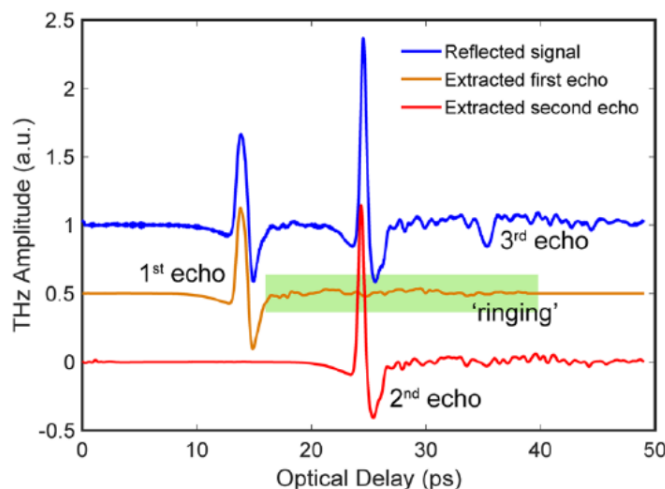


Figure 2.6: Representative example of a recorded THz transient reflected off the cuvette. The separated 1st and 2nd echo after applying a sparse deconvolution algorithm are also displayed, in which the influence of the “ringing” effect due to the ambient water vapor in the air was eliminated. (Figure adapted from reference [137])

The 2nd echo originating from the cuvette/GNR dispersion interface (Figure 2.7(a)) was used to record the temperature change during the heating and cooling cycles when the NIR laser photoexcited the GNRs within the aqueous dispersion. The 1st echo reflected off the cuvette’s surface (Figure 2.7(a)) was exploited for self-referencing, as described in subchapter 2.2.3, to eliminate the influence of intrinsic system noise and temperature fluctuations in the surrounding environment.

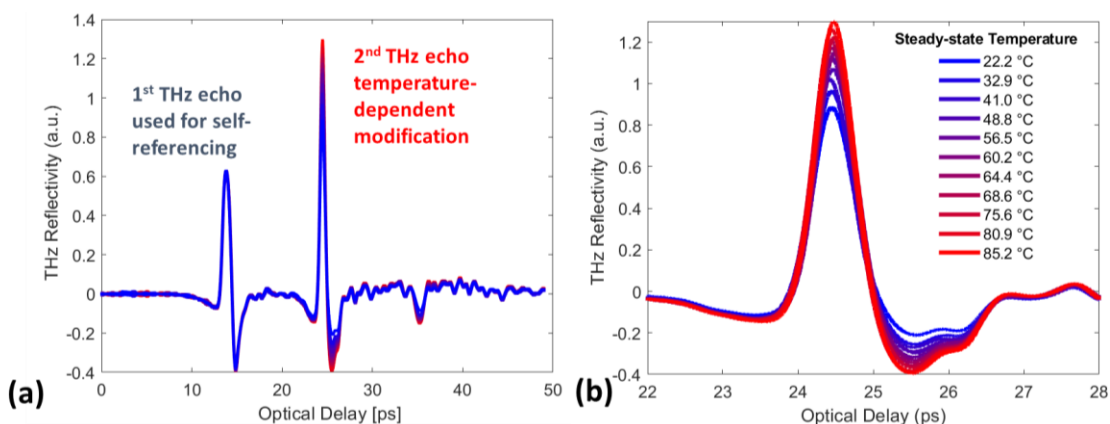


Figure 2.7: Temperature-dependent reflectivity of the 2nd THz echo as a function of temperature for GNR10. (a) Time-domain trace of the three THz echoes highlighting the modification on the 2nd echo introduced by the photothermal heating effect. (b) Close-up of the 2nd echo highlighting its modifications as a function of the steady-state temperature value of the NP dispersion. (Figures adapted from reference [137])

Reliable thermal measurements require a precise extraction of the THz amplitude of the 2nd echo (cuvette/GNR dispersion interface). The extended tail of the 1st echo experiences a modulation (Figure 2.6) known as the “ringing” effect that originates from the humidity in the surrounding air [121]. This effect interferes with the 2nd echo, which contains the temperature information of the heated GNR dispersion. Indeed, accurate thermal measurements are not possible without accounting for this interference. Thus, a sparsity-based deconvolution technique [123] was utilized to extract the authentic THz waveforms from the entire THz trace and separate these to avoid any interference, as illustrated in Figure 2.6. Commonly, THz experiments are performed under a nitrogen atmosphere to eliminate THz absorption due to the humidity of the surrounding environment, which is usually done by implementing the whole THz setup in a sealed housing. This procedure is time-consuming, expensive, and makes the THz setup bulky as well as immobile. The removal of the “ringing” effect on the THz pulse allows the use of the presented method under normal atmospheric conditions and can, therefore, be employed in an out-of-the-lab environment.

Additionally, THz-TDS systems experience inherent amplitude fluctuations and phase shifts that hinder precise and consistent measurements [142]. These intrinsic modulations originated from system noise and temperature fluctuations of the surrounding environment. They were effectively mitigated by applying a self-referencing technique [143] described in subchapter 2.2.3. Therefore, the 2nd echo was adjusted to the fluctuations of its corresponding 1st echo. Consequently, a precise measurement of the authentic 2nd echo’s peak value was achieved by employing the mentioned signal post-processing techniques, namely sparsity-based deconvolution algorithm and self-referencing.

Calibration measurements were performed to correlate the THz reflectivity value with temperature under plasmonic NIR heating of the GNR dispersions varying the laser power intensity I in the range from 0.95 to 60.4 W/cm². The laser power intensity I is defined by:

$$I = \frac{2P}{\pi \left(\frac{d}{2}\right)^2} \quad 2.27$$

for a Gaussian-shaped beam intensity profile, where d is the beam diameter of the NIR source, and P denotes the NIR laser power. The temperature was measured by inserting a digital thermometer (HH306A from OMEGA) equipped with a type-K mini-hypodermic thermocouple (HYP-0 from Omega) inside the cuvette close to the illuminating laser spot after the temperature reached a steady-state level. This level was usually reached after around 10 minutes when the

temperature had leveled off. The temperature was recorded by tracing the THz reflectivity modulations of the 2nd echo bouncing off the cuvette/GNR dispersion interface. The fundamental principle is a heat-induced change in the dielectric property of the water solution, which alters its refractive index in the THz frequency domain. The temperature value was subsequently matched to the respective THz amplitude value of the 2nd echo, unveiling a linear thermometric relationship with a coefficient of determination R^2 of approximately 0.99 (Figure 2.8).

As Figure 2.8 confirms, the slopes of all three calibration curves are almost identical since the dispersions contain mostly water. Consequently, it is not necessary to repeat the calibration curve for every new sample if the main constituents of the dispersions remain the same. The different sizes of the GNRs might have caused the marginal variations in the calibration curves since this results in a slight change of the refractive index associated with the overall dispersion. The gradients of the calibration curve were recorded for each of the three GNR dispersions and used to relate the THz amplitude to its respective temperature value. A resolution of about 1 °C was attained after applying the signal post-processing algorithms.

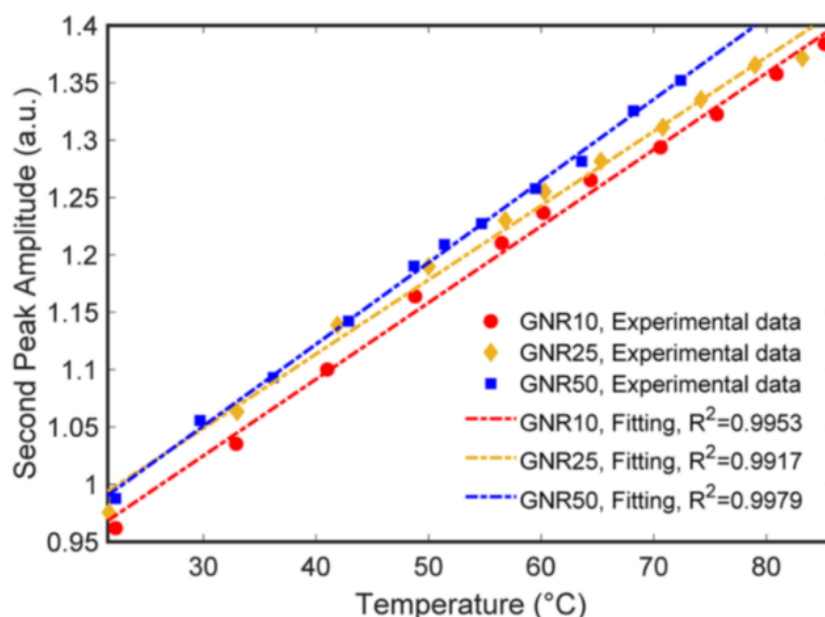


Figure 2.8: Calibration curves featuring a linear thermometric relationship between THz amplitude and temperature for each of the GNR dispersions. (Figure adapted from reference [137])

2.6 Quantification of the Photothermal Effect via THz-TDS

Temperature measurements by using THz-TDS were performed during the heating and cooling cycles to determine the PCE, as well as MHR of each of the three GNR dispersions. A NIR laser irradiation at a power intensity of 31.8 W/cm² was used for 12 minutes to photoexcite the GNRs inside the dispersion. At the same time, the heating cycle was recorded by employing THz-TDS.

Other studies [5] usually heat for around 30 minutes during vigorous stirring of the NP dispersion. In this study, no magnetic stirring was utilized during the heating process, which can potentially put a thermal strain on the NP samples. Therefore, the heating duration was restricted to just 12 minutes to keep this strain on the NPs as minimal as possible. This constraint preserved the NPs colloidal stability and thus ensured both data comparability and consistency. After the heating cycle, the laser was turned off, and the temperature inside the cuvette was recorded for 15 minutes during the cooling period. The temperature-time transient was obtained by tracing the THz peak amplitude of the 2nd THz echo, post-processing all THz echoes reflected off the sample's interfaces through a sparsity-based deconvolution and self-referencing method described in subchapter 2.2, as well as finally translating the resulting value to temperature using the respective calibration curve. The sampling period of the THz reflectivity was 10 seconds over 12 minutes for the heating and 15 minutes for the cooling cycle.

Figure 2.9 depicts the entire temperature profile of the three GNR dispersions. Equation 2.24 successfully reproduced the temperature rise under NIR laser radiation and its drop to the ambient value. GNR10 and GNR25 reached an equal steady-state temperature level of around 53 °C after 12 minutes of heating. GNR50 rose to approximately 45 °C instead. The GNR50 dispersion experienced temperature fluctuations starting from 37 °C. The dispersions GNR10 and GNR25 show similar fluctuations above ~44 °C but somehow dampened. A comparable behavior has been reported by Richardson *et al.* [144]. At this high-temperature difference with respect to the laboratory temperature (18 °C - 21 °C), heat exchange dynamics at the interface between the system and its surrounding environment play a significant role, which might cause these fluctuations. Their impact was mitigated by fitting the experimental data with the theoretical model.

The rate of energy absorption A and the rate of energy dissipation B were calculated by fitting the experimental temperature transients with equation 2.24. In this way, the PCE was determined for all three GNR dispersions. The rate of energy dissipation B among the GNRs and the surrounding environment can be measured from the cooling cycle of the thermal profile. Its theoretical model for the temperature transient is attained by setting $A = 0$ and $T_{\text{initial}} = T_{\text{max}}$ in equation 2.24:

$$T(t) = T_0 + (T_{\text{max}} - T_0)e^{-Bt} \quad 2.28$$

where T_{max} is the maximum temperature reached during the photothermal heating cycle. Equation 2.28 corroborates a linear relationship between time t and the heat dissipation rate B :

$$Bt = -\ln[(T(t) - T_0)/(T_{\text{max}} - T_0)] \quad 2.29$$

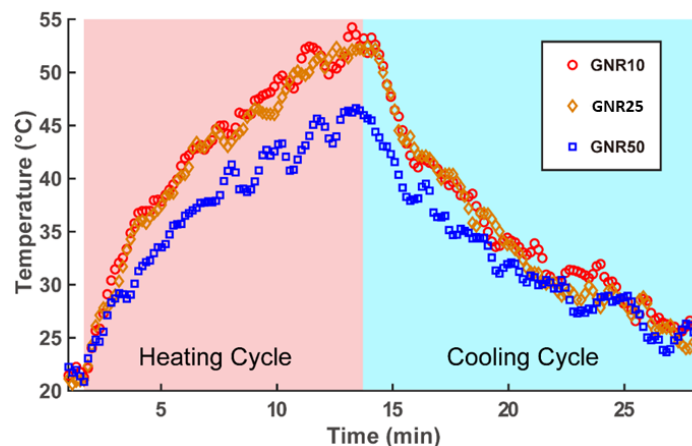


Figure 2.9: Typical temperature transients measured by THz-TDS. The procedure and parameters were the same for each of the three GNR dispersions. A constant NIR laser intensity of 31.8 W/cm^2 was exerted for 12 minutes to record the heating curve. Then, the laser was turned off to obtain the cooling curve. (Figure adapted from reference [137])

The heat dissipation rate B can be computed from the gradient of this curve, which confirms the first-order decay as the cooling system reaches equilibrium with the surrounding environment. The fitting of the experimental data with the theoretical model resulted in a similar value of around $3.0 \times 10^{-3} \text{ s}^{-1}$ for parameter B for all three GNR dispersions. Figure 2.10(a1)-(c1) depicts the fitting results of the cooling cycle curves. The heat dissipation rate is not influenced by the GNR sizes, as evidenced in equation 2.22. The energy absorption rate A can be calculated by fitting the heating cycles (Figure 2.10(a2)-(c2)) of the temperature transients with equation 2.24, once the heat dissipation rate B has been determined. The coefficient of determination R^2 is ~ 0.97 , which suggests a reasonably good fit.

Since no magnetic stirring was utilized inside the cuvette, the mass of the GNR dispersion was only partially heated by the photothermal process resulting in an inhomogeneous temperature distribution inside the sealed cuvette. This inhomogeneity was accounted for by measuring the effective mass of the sample heated during laser excitation. Therefore, THz thermograms based on a raster-scan technique were captured featuring an image size of $12 \text{ mm} \times 36 \text{ mm}$ and an image resolution of $250 \text{ }\mu\text{m}$. Thermograms were taken from the whole front and rear window of the cuvette before the heating cycle started and after a steady-state temperature level was reached. For measuring the THz thermograms, the cuvette containing the GNR dispersion was attached to a motorized X-Y translation stage (MTS50-Z8 from Thorlabs) to allow for THz raster-scans. The NIR laser beam was mounted on an optical cage system (Thorlabs) in such a way that it moved in unity with the cuvette, and consequently, both the NIR beam and the cuvette were translated together across the THz beam, see Figure 2.11. The NIR laser spot hit the cuvette at

normal incidence in the middle of the fill level at around 15 mm from the bottom and 6 mm from the left and right cuvette wall.

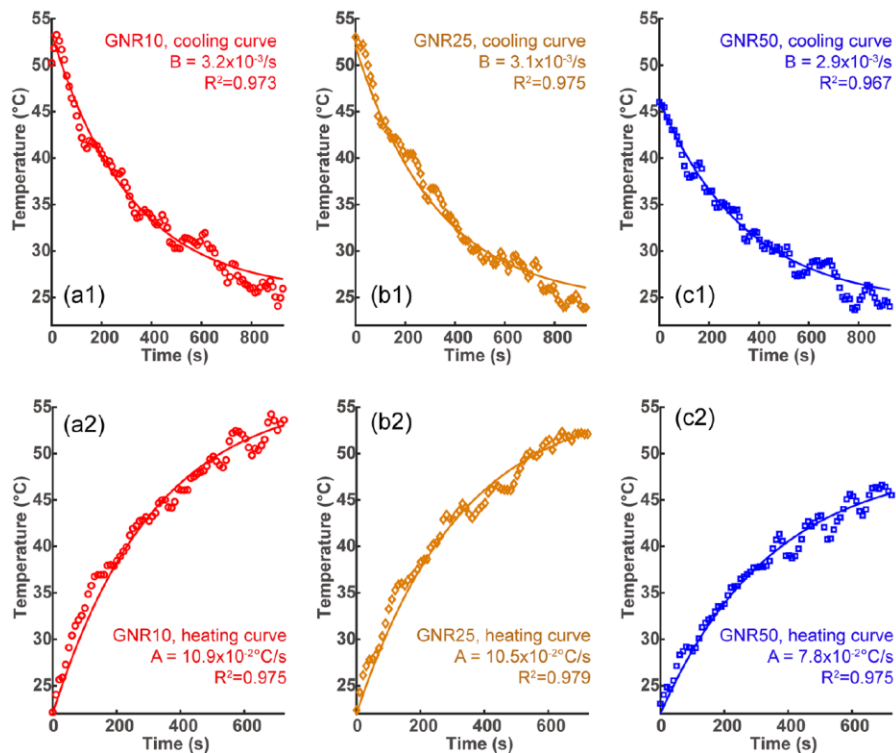


Figure 2.10: Extraction of the heat dissipation rate B and the energy absorption rate A by fitting the experimental data (symbols) with equation 2.24 for each of the three GNR dispersions. The fitting results (solid lines) for the cooling cycles are shown in (a1), (b1), and (c1), and the fitting results (solid lines) for the heating cycles are shown in (a2), (b2), and (c2), accordingly. (Figures adapted from reference [137])

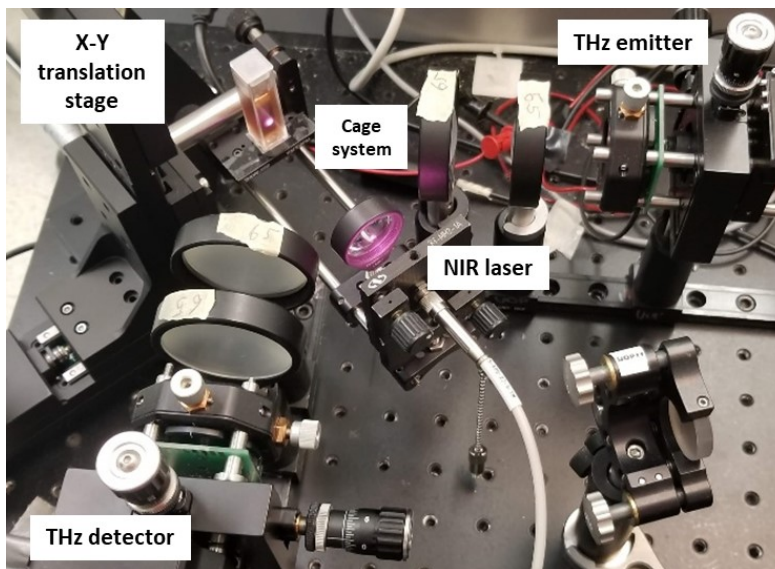


Figure 2.11: THz imaging setup configuration in reflection geometry. Both the cuvette and the NIR laser are attached to the same cage structure that can be moved by an X-Y translation stage. This geometry allowed them to traverse together across the THz beam.

Figure 2.12(b)-(c) illustrate the resulting THz thermographs taken from the front and rear window of the cuvette depicting the thermal distribution at the cuvette/GNR dispersion interface when a steady-state temperature level was reached.

The thermal images show the temperature variation (ΔT) with respect to the initial ambient temperature value of 22 °C. The image acquisition is fundamental to approximate the effective mass of the GNR dispersion. Notably, neither the temperature profiles nor their spatial distributions alone led to the measurement of the GNRs' PCE, but only their mutual correlation.

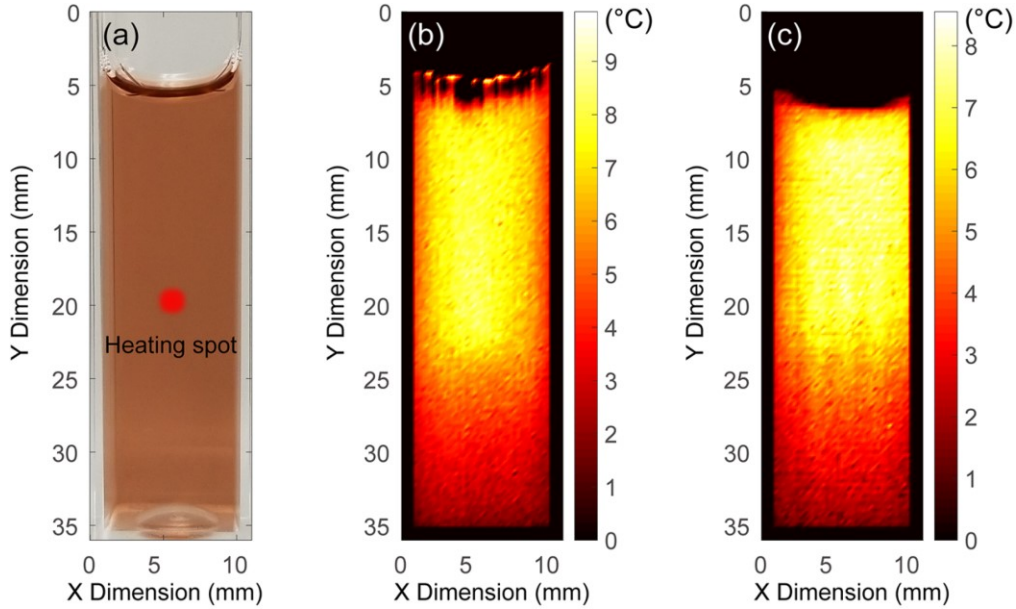


Figure 2.12: THz thermographs of the GNR10 dispersion taken by using THz-TDS raster-scans illustrating the thermal distribution when the steady-state level by plasmonic heating was reached. (a) Digital image of the front surface of the cuvette with the laser spot marked in red. THz thermographs of the temperature distribution ΔT (relative to the ambient value) of (b) the front and (c) rear window of the cuvette. (Figures adapted from reference [137])

The THz thermographs from the front and rear window of the cuvette corroborate a similar thermal distribution. The images substantiate that due to heat convection, the GNR dispersion near the cuvette's bottom was just marginally heated in comparison to the top of the cuvette. Thus, the effective mass of the photothermally heated NP dispersion inside the cuvette can be computed by the following formula:

$$m_{\text{eff}}^{\text{dis}} = \frac{\iint T(x,y) dx dy}{S_A} m_{\text{dis}} \quad 2.30$$

where $T(x,y)$ denotes the normalized thermal distribution, dx and dy describe the size of one pixel in the THz thermal image, S_A stands for the area of the whole surface, and m_{dis} is the mass

of the NP dispersion inside the cuvette. The effective mass of the NP dispersion inside the cuvette was determined to be 1.74 g, computed by calculating the average of the front and rear window of the cuvette.

Additionally, the mass of the cuvette was partially considered by computing the effective mass $m_{\text{eff}}^{\text{cuv}}$ of the cuvette:

$$m_{\text{eff}}^{\text{cuv}} = \frac{m_{\text{eff}}^{\text{dis}}}{m_{\text{dis}}} m_{\text{cuv}} \quad 2.31$$

where m_{cuv} represents the mass of cuvette surrounding the GNR dispersion. The cuvette's effective mass was calculated to be 0.9 g.

The PCEs of the three GNR dispersions were determined by combining the temperature transients and the thermal images taken via THz-TDS without the need of stirring the sample dispersion (Figure 2.13 (red bars)). The MHR was assessed according to equation 2.26 and plotted in Figure 2.13 (orange bars) by knowing the molar concentration (Table 2.1) combined with the calculated absorption rate A . The high PCE of around 93% attained by the GNR10 dispersion featuring the smallest particle volume (Figure 2.13) has been confirmed by other studies [8], [144], [145] for gold nanostructures of similar size.

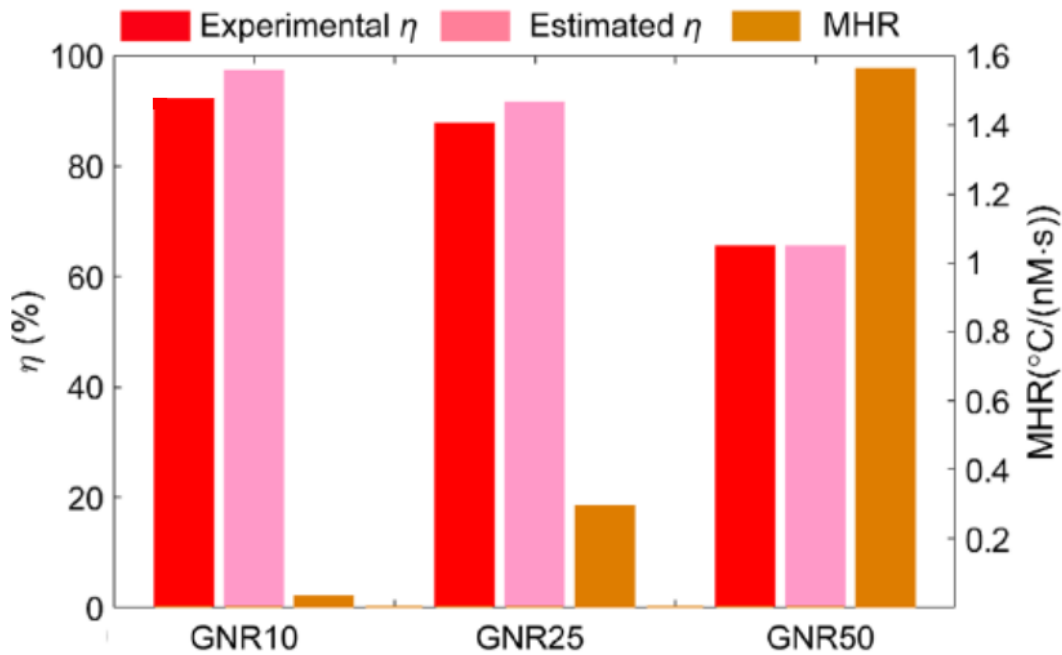


Figure 2.13: Experimentally attained PCEs η (red bars) and MHR (orange bars) of the three GNR dispersions with particle dimensions of 10 nm x 41 nm, 25 nm x 90 nm, and 50 nm x 150 nm. Furthermore, the PCEs approximated by the theoretical interaction cross-sections are displayed as well (pink bars). (Figure adapted from reference [137])

Moreover, Figure 2.13 illustrates that the PCE and MHR experience an opposing trend regarding the GNR volume. Although the conversion efficiency is the largest for the small-sized GNRs, the MHR is the highest for the large particle volumes. These results confirm the trend for this kind of plasmonic resonator, which attests to the trustworthiness of the described method.

The fidelity of the experimental results was confirmed by numerical simulations that were performed in collaboration with Prof. Alexander O. Govorov (Ohio University).

Figure 2.14(a) shows the GNRs' key characteristics, rooted in the underlying mechanism of their electromagnetic response during the photothermal heating process. The interaction cross-sections of a plasmonic NP increases with its polarizability and scales with its particle volume.

Figure 2.14(b) depicts the theoretical calculations of the extinction cross-sections (sum of absorption σ_{abs} and scattering σ_{scat}) of all three GNR dispersions. It confirms the trend of the MHR in Figure 2.13, i.e., that the absorption cross-section increases with particle size and lead to a rise in photothermal energy absorption on a single particle basis. It is important to note that all three GNR types possess a comparable absorbance value (Figure 2.4(d)). Hence, the GNR50 dispersion contains a significantly lower particle number concentration than the GNR10 dispersion.

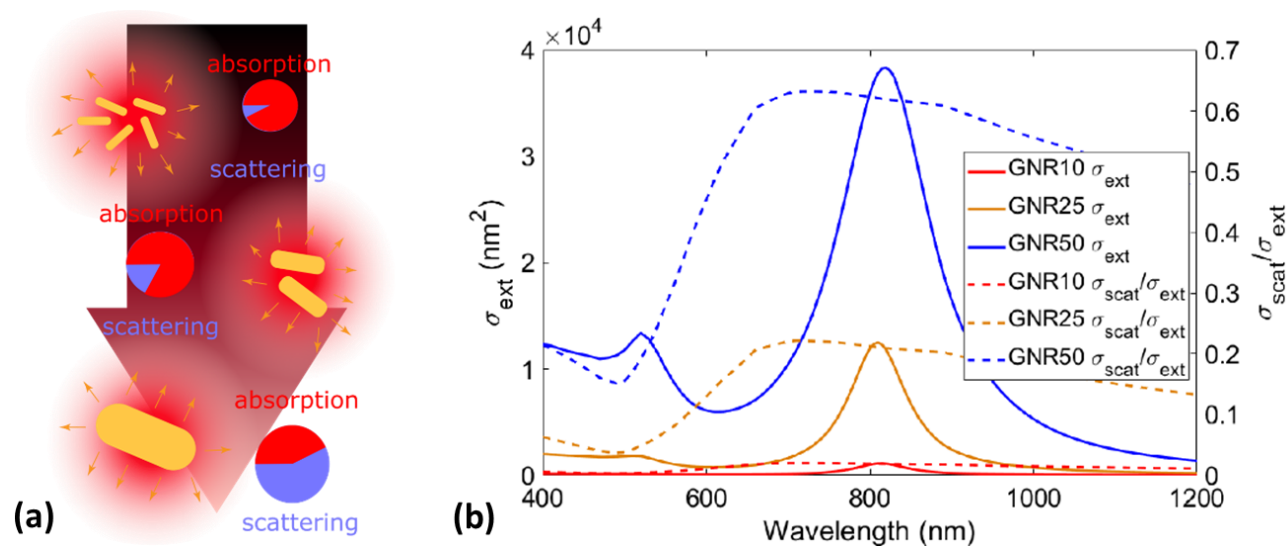


Figure 2.14: (a) Schematic illustration depicting the fundamental properties presented in Figure 2.13, especially the rise in overall extinction per NP and increasing significance of scattering as the NP volume enlarges. (b) Theoretical extinction cross-sections σ_{ext} of the three GNR dimensions and the ratio between their scattering cross-sections σ_{scat} to the total extinction. (Figures adapted from reference [137])

The relationship between the particle size and the scattering cross-section is as follows: the larger the volume of the NP, the more energy will be scattered relative to its extinction. Notably,

scattering is an event that does not deposit energy locally and, hence, does not contribute to the photothermal process. Figure 2.14(b) illustrates this relationship by plotting the ratio of the scattering σ_{scat} and extinction σ_{ext} cross-sections for all three GNR dimensions. This general property of light-matter interaction is caused by the different dependence of absorption and scattering on the polarizability of the NPs, which are linear and quadratic [84], respectively. Hence, the dominance of scattering over absorption in the large-sized GNRs observable in Figure 2.14(b) justifies the declining trend of the PCEs as a function of the GNR dimensions. Additionally, Figure 2.13 includes an approximation of the PCEs (pink bars) for the three GNR dimensions calculated entirely from the theoretical interaction cross-sections. The model confirms the same trend as the experimental data. The theoretical PCEs were computed using the equation:

$$\eta = \frac{Q_{\text{dispersion}} - Q_{\text{solvent}}}{Q_{\text{extinction}}} = \frac{e^{-\mu_{\text{water}}L} - e^{-(\sigma_{\text{abs}}n_{\text{GNR}} + \mu_{\text{water}})L}}{(1 - e^{-\sigma_{\text{ext}}n_{\text{GNR}}L})} \quad 2.32$$

where $Q_{\text{dispersion}}$ and Q_{solvent} denote the heat generation of the GNRs and the aqueous solution, respectively. $Q_{\text{extinction}}$ stands for the energy extinguished by the GNRs, thus scattered and absorbed. μ_{water} is the absorption coefficient of water [146]. σ_{abs} and σ_{ext} are the absorption and extinction cross-sections of the GNRs, respectively. L denotes the total thickness of the sample and n_{GNR} is the GNR concentration density. It is important to note that the photothermal heating effect caused by the light absorption of the solvent, in this case, water, is negligible at the NIR wavelength of 786 nm used in the experiments. However, it will significantly lower the efficiency of any photothermal heater operating at longer wavelengths. Figure 2.15 illustrates this point by plotting the PCEs of the three GNR dimensions covering the spectrum ranging from 400 nm to 1200 nm. This plot was computed by using equation 2.32 and the water absorption spectrum.

Full electrodynamic simulations calculated the theoretical results presented in Figure 2.13 (pink bars), Figure 2.14(b), and Figure 2.15. The interaction cross-sections of GNRs were computed by using the commercial software package COMSOL Multiphysics with implemented numerical solvers in a finite element method (FEM) approach. A continuous plane wave approximation simulated the NIR laser illumination. The surrounding environment was set to a homogeneous medium of dielectric index $n = 1.33$. The non-interacting GNRs were modeled, having the same geometries as the experimental samples. However, their lengths were adjusted to match the LSPR in the water of the three experimental GNR types, resulting in aspect ratios of 4.1, 3.65, and 2.9 for the GNR10, GNR25, and GNR50 specimens, respectively.

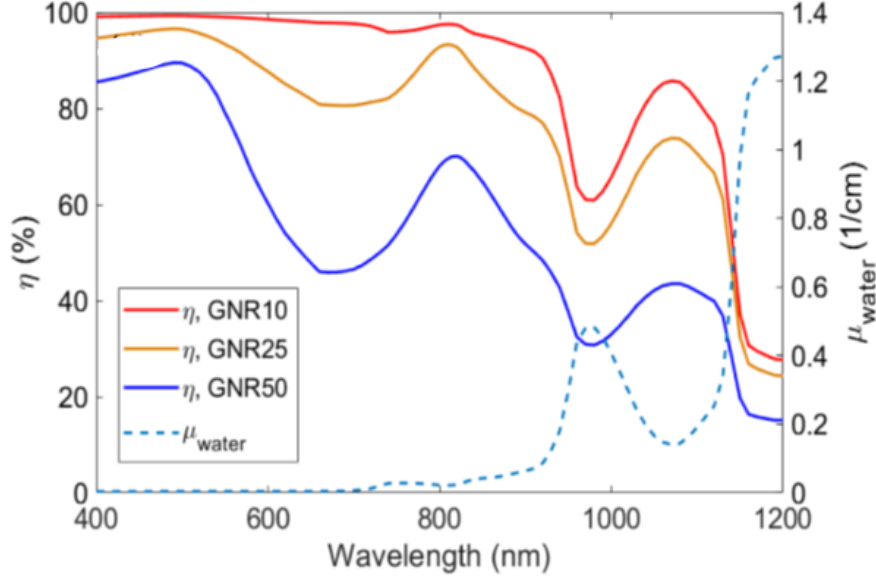


Figure 2.15: Theoretical assessment of the PCEs η , calculated by using equation 2.32, considering the calculated cross-sections and the absorption coefficient of water μ_{water} , also shown in this panel. Choosing an irradiation wavelength outside the absorption lines of water is crucial for efficient localized heat delivery. (Figure adapted from reference [137])

Following the anisotropy of the GNRs, the cross-sections in Figure 2.14(b) were computed as the average over six combinations of linear polarization and incidence directions of light over the GNRs, which reproduces the effect of randomly oriented ensembles of NPs illuminated by an unpolarized light source. The GNRs were described by using the following equation:

$$\begin{aligned}\varepsilon_{broad} &= \varepsilon_{gold,experimental} - \varepsilon_{Drude} + \varepsilon_{Drude,broad} \\ \varepsilon_{broad} &= \varepsilon_{gold,experimental} - \left(\varepsilon_{\infty} - \frac{\omega_p^2}{\omega(\omega + i\Gamma)} \right) + \left(\varepsilon_{\infty} - \frac{\omega_p^2}{\omega(\omega + i2\Gamma)} \right) \\ \varepsilon_{broad} &= \varepsilon_{gold,experimental} + \frac{\omega_p^2}{\omega(\omega + i\Gamma)} - \frac{\omega_p^2}{\omega(\omega + i2\Gamma)}\end{aligned}\quad 2.33$$

where ε_{broad} is the permittivity of gold, which has been broadened with respect to the bulk parameters. $\varepsilon_{gold,experimental}$ [147] is the experimentally determined bulk permittivity of gold. The theoretical gold permittivity ε_{Drude} and $\varepsilon_{Drude,broad}$ were derived from the Drude model in which the plasma frequency ω_p and damping rate Γ of gold were set to 8.9 eV and 0.076 eV [147], respectively. ω denotes the frequency and i the imaginary unit.

2.7 Characterization of the Photothermal Effects of Copper Sulfide Nanoparticle Dispersions

Many gold-based NPs feature high absorption properties and hence high photothermal conversion efficiencies in the first biological wavelength window of 650 nm to 950 nm. Since the absorbance of biological tissue is minimal within this wavelength band, the NPs are used as photothermal heating agents for biomedical applications, such as PTT for cancer treatments. However, gold-based NPs are expensive to synthesize, and depending on their LSPR frequency may feature a large size, sometimes exceeding 100 nm. For most biomedical applications, NPs should be small to be able to permeate the cell barriers of, e.g., cancer cells.

Additionally, the morphology of gold NPs can change during long and intense laser exposure due to the lower damage threshold of metals in comparison to dielectrics. The consequence is a partial or total loss of the LSPR, followed by a substantial decrease in PCE. These limits can be overcome by using CuS NPs [148].

In this study, a compound of CuS named covellite was used to synthesize the NPs. This compound is a degenerative p-type semiconductor, which means it is heavily doped and therefore offers a large free hole density in the valence band [149]–[151]. The CuS NPs show a metal-like behavior and exhibit a strong LSPR effect, leading to a high light absorption property and a large PCE. However, the free carrier density of CuS is still lower compared to gold-based photothermal agents (10^{20} – 10^{22} cm⁻³ vs. 10^{23} cm⁻³) [65], [95].

In contrast to gold NPs, CuS NPs feature a broader absorption spectrum in the NIR regime, they are smaller, significantly more cost-efficient to synthesize, and can be excited at higher laser intensities. The absorption frequency band of CuS NPs can be slightly tuned by modifying the size and geometry of the nanostructure. Ultimately, CuS NPs can achieve a PCE comparable to many metal-based NPs.

The utilized “green” synthesis approach for the CuS NPs deployed in the study [95] uses mild coordination capabilities that impart the CuS NPs with tailorable surface chemistry by tuning the reaction parameters. It offers the possibility to finely tune their surface chemistry, which means they can be passivated by using different ligands that are biocompatible and non-cytotoxic, hence specifically tailored for biomedical applications. In this study, the photothermal conversion properties of three different CuS types diluted in deionized water were investigated by using a THz-TDS system (subchapter 2.1) in order to determine which particle type yields the highest light-to-heat conversion capability. The three CuS NP types studied in this work have

approximately the same core size of around 15 nm and a nanoplatelet morphology, which was validated by TEM images, as shown in Figure 2.16.

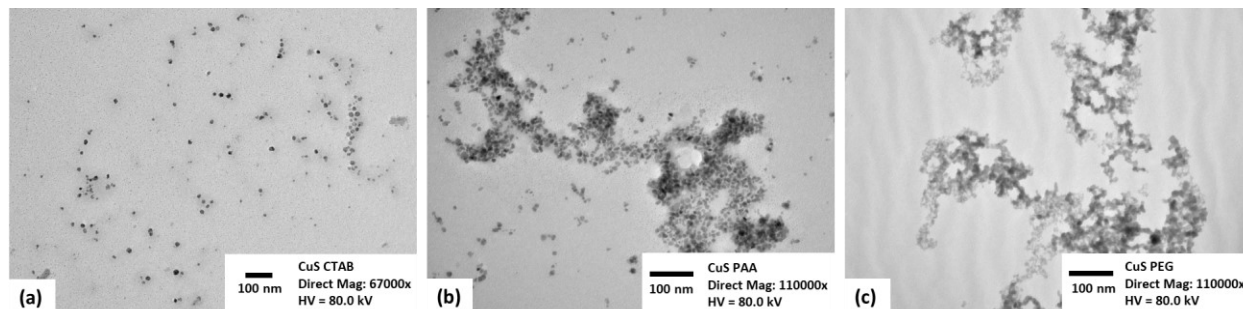


Figure 2.16: Representative TEM images of the CuS NP dispersions with different capping ligands: (a) CuS CTAB. (b) CuS PAA. (c) CuS PEG.

The difference between the three NP types is the ligand that was used to passivate them: hexadecyl-trimethyl-ammonium bromide (CTAB), polyacrylic acid (PAA), and polyethylene glycol (PEG) [79]. These ligands are responsible for the stabilization of the particles to prevent agglomeration and precipitation but also affect their biocompatibility and cytotoxicity. The CTAB capped CuS NPs constitute a reference, since they are an established particle system that offers high photothermal stability, but are cytotoxic and, therefore, cannot be used in biomedical applications. On the other hand, PAA and PEG passivated CuS NPs are biocompatible due to their organic nature.

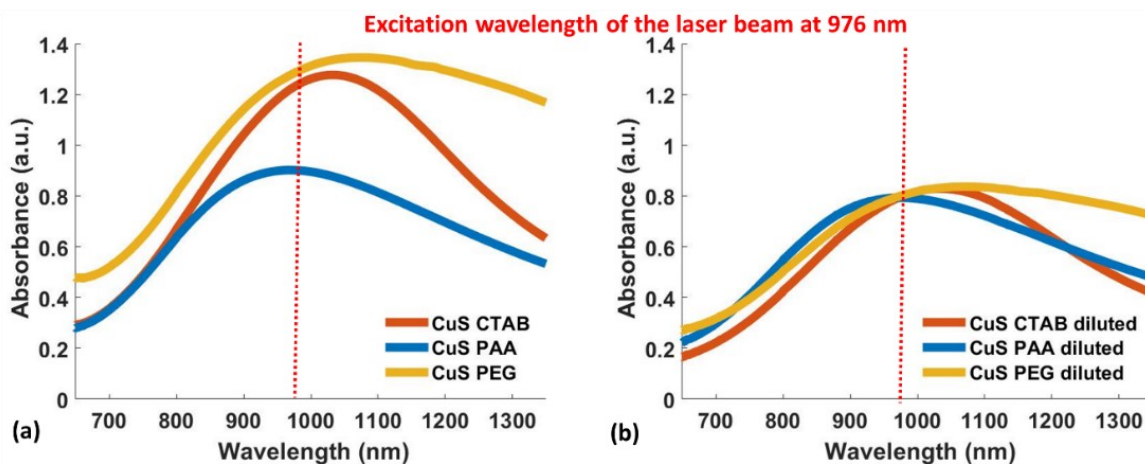


Figure 2.17: VIS-IR spectroscopy analysis of (a) the stock dispersions. (b) Dispersions adjusted to an absorbance value of 0.8 at 976 nm by dilution with deionized water.

All three CuS NP types were synthesized in the laboratories of Prof. Fiorenzo Vetrone (INRS-EMT). In this study, I characterized the NPs, designed, and assembled the THz setup.

Additionally, I also designed and built the customized sample vessels that I used during the experiment. Moreover, I carried out the measurements and analyzed the experimental data.

The three CuS NP types have approximately the same plasmonic resonance wavelength centered at around 976 nm. Due to their relatively broad absorbance band in comparison to, for example, gold NPs, they constitute a viable solution for efficient photothermal heating in the second biological window ranging from 1000 nm to 1350 nm, in which the absorbance of biological tissue is minimal. The VIS-IR absorbance spectra of the three CuS NPs are plotted in Figure 2.17(a). It is important to note that the width of the absorbance bands is varying between the three CuS NP types, with PEG capped CuS NPs possessing the broadest value. Figure 2.17(b) charts the optical absorbance bands of the three CuS NP dispersions adjusted by dilution with deionized water to ~0.8 units at 976 nm, which is the operating wavelength of the CW laser system that was used to photoexcite the CuS NPs in this study. The reason for the adjustment was a normalization of the optical absorbance to be able to compare their maximum achievable temperature values directly.

Table 2.2 lists the physico-optical properties of the three CuS NP dispersions. The concentration of copper (Cu) ions in the CuS NP stock dispersions was determined by inductively coupled plasma mass spectrometry (ICP-MS). CuS PEG showed the highest concentration of Cu ions among the three CuS NP dispersions.

Table 2.2: Specifics of the studied CuS NP dispersions.

Material	Copper Sulfide (CuS) covellite		
Capping Ligand	CTAB (hexadecyl-trimethyl- ammonium bromide)	PAA (polyacrylic acid)	PEG (polyethylene glycol)
Morphology	Nanoplatelets		
Average Core Diameter	Appr. 15 nm		
Adjusted Absorbance	Appr. 0.8 at 976 nm wavelength		
Cu Ion Concentration of Adjusted Dispersions	1.88 mM/L	1.65 mM/L	4.66 mM/L

0.3 mL of each dispersion was filled in a custom-made 380- μ m thin PE cuvette, firmly sealed and installed in the THz-TDS setup in reflection geometry, described in subchapter 2.1. The purpose of building a tailored cuvette was to establish a minimal volume, which the NIR laser can heat swiftly to a steady-state temperature level. Commonly used cuvettes of the size 12.5 mm \times 12.5 mm \times 45 mm typically need more than 15 minutes to reach this level. In the custom-made cuvette, the CuS NP dispersion under study required just 5 minutes to achieve the same

temperature plateau. Moreover, the temperature distribution within and around the heating spot is more uniform than for large conventional cuvettes. Therefore, no stirring was required for the $\sim 1.8 \mu\text{L}$ NP dispersion volume that was illuminated by the NIR laser beam.

Additionally, to further ensure the homogeneity of the temperature distribution within and around the heating/measuring spot, the beam diameter of the photoexciting NIR laser (976 nm wavelength) was around 7 mm ($1/e^2$). In the center of this spot, the temperature was sensed by a THz beam having a diameter of ~ 3 mm ($1/e^2$) impinging with an angle of 45 deg on the cuvette relative to its normal. Figure 2.18(a) displays a cross-section of the custom-made cuvette, including the THz propagation in reflection geometry. The THz propagation principle is the same as already described in subchapter 2.5. At first, the THz radiation impinges on the air/PE interface and is partly reflected and transmitted, leading to a 1st of two THz echoes in the time-domain plot (Figure 2.18(b)).

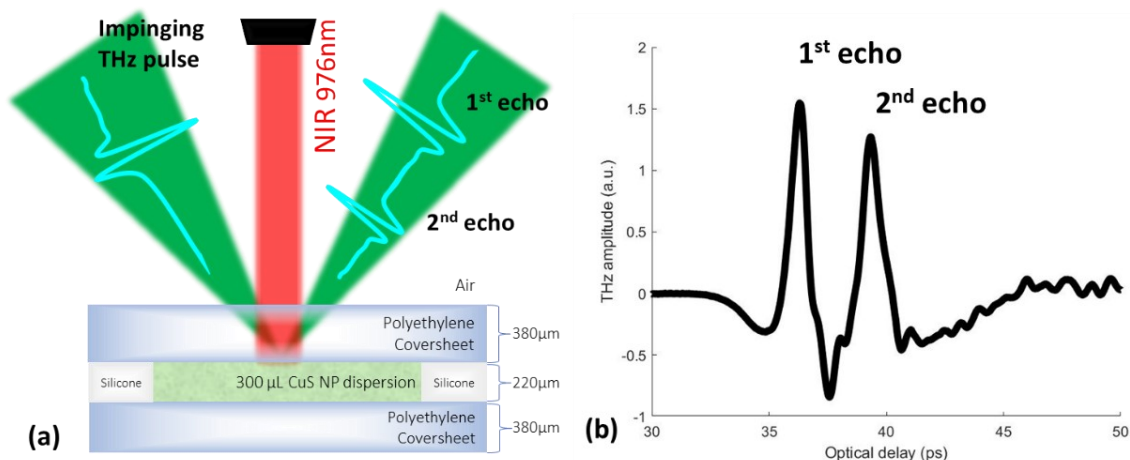


Figure 2.18: (a) THz propagation in reflection geometry through the interfaces air/PE and PE/NP dispersion. (b) The resulting two reflected THz pulse echoes in the time-domain are strongly overlapped.

The transmitted THz radiation then reaches the PE/NP dispersion interface and is again partly reflected, resulting in a 2nd THz echo in the time-domain plot. The cuvette thickness is below the THz diffraction limit; thus, the two reflected echoes partly overlap and cannot be distinguished since the 2nd echo's front interferes with the 1st echo's tail. The THz echoes were separated by using the post-processing methods sparsity-based deconvolution and self-referencing, explained in subchapter 2.2.1 and 2.2.3, respectively. Overlapping pulses lead ultimately to phase and amplitude modulations that distort the 2nd THz echo, which is required to extract the temperature information during the photothermal heating procedure of the CuS NP dispersions. The measurement is carried out directly at the 2nd interface between the PE window and the CuS NP dispersion where the THz pulse senses the modification of the refractive index of the CuS NP

dispersion introduced by the temperature change and represented by a rise or fall in the THz amplitude of the 2nd echo (Figure 2.19).

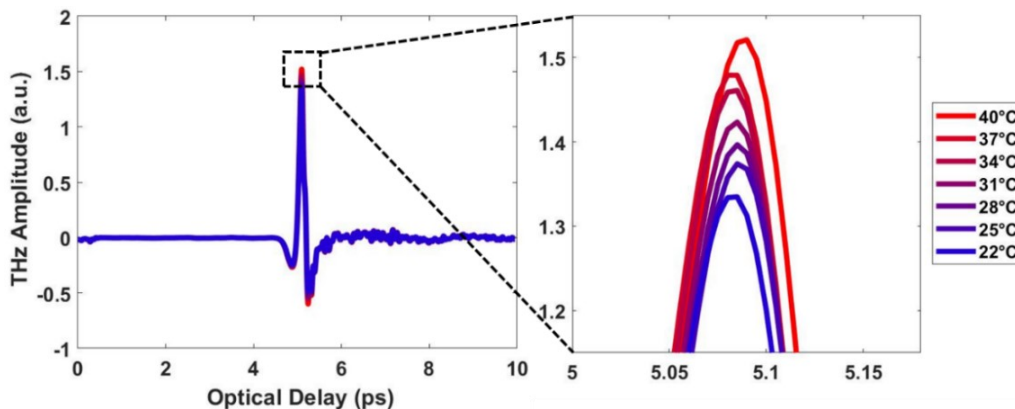


Figure 2.19: Time-domain plots of the temperature calibration measurements. The deconvolved 2nd THz reflection echo originating from the PE/NP dispersion interface exhibits a change in the amplitude depending on the temperature value.

Figure 2.20(a) and (b) plot the deconvolved 1st and 2nd echoes, respectively. The so-called baseline interference, observable at the tail of the 1st echo and known as the “ringing” effect, is mainly caused by the humidity of the surrounding environment [121]. This interference was removed from the 2nd echo.

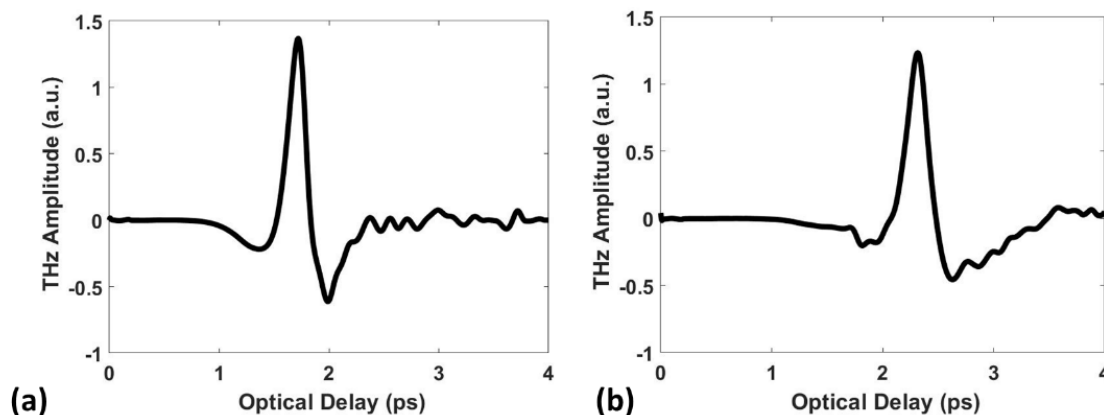


Figure 2.20: (a) Deconvolved 1st echo originating from the air/PE interface. (b) Deconvolved 2nd THz echo from the PE/NP dispersion interface cleaned from the interference with the 1st THz echo.

First, a thermometric relationship for each CuS NP dispersion was determined between temperature and THz amplitude by controllably changing the temperature value of a thermoelectric heating/cooling element (Figure 2.21(a)) in the range of 22 °C to 40 °C in three-degree increments (Figure 2.21(b)).

The resulting calibration curves show a linear relationship between the temperature increase and the reflected THz amplitude. It is important to note that a small amplitude change represents a

substantial temperature change; therefore, the precise determination of the THz amplitude is of crucial importance. The measurement reproducibility is mainly influenced by the noise fluctuation of the utilized THz-TDS system. Hence, the SNR and DR have been evaluated based on the method in subchapter 2.1. The power spectrum of the emitted THz pulses peaks at about 0.3 THz and exceeds 3 THz in bandwidth, resulting in a SNR of 419 and a DR of 60 dB for the deployed THz-TDS system.

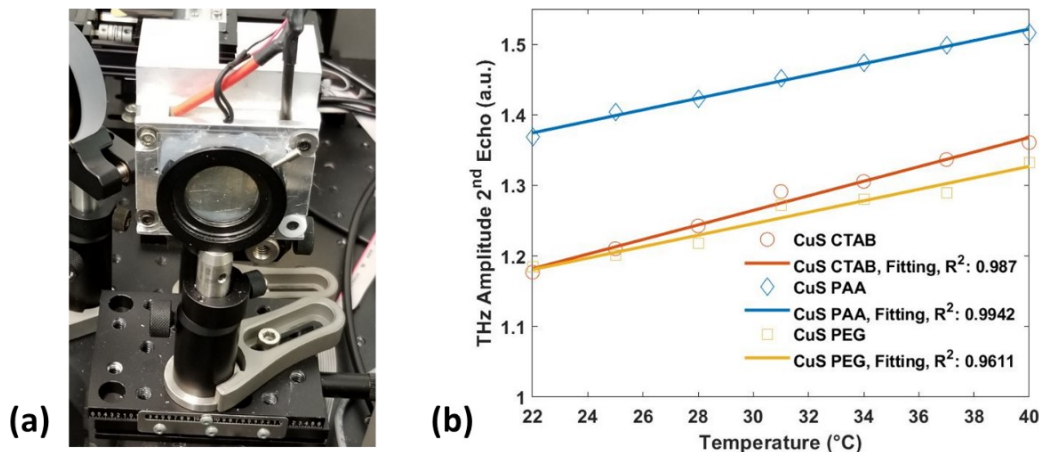


Figure 2.21: Calibration measurements: (a) Digital image of the thermoelectric heating/cooling element attached to the custom-made cuvette. (b) Calibration curves for the three CuS NP dispersions between 22 °C and 40 °C illustrating the thermometric relationship between temperature and THz amplitude.

Additionally, the signal post-processing algorithms of deconvolution and self-referencing were utilized to eliminate the influence of noise fluctuations, thus attaining a temperature resolution of around 1 °C together with well reproducible measurements.

The photothermal heating measurements were performed for each of the three CuS NP samples under NIR illumination with a constant laser intensity of 0.68 W/cm². The cuvette was mounted on a sample holder, as shown in Figure 2.22. A high-speed optical delay line featuring a sampling rate of 1 Hz was used to delay the probe with respect to the pump beam to read out the THz signal.

Following a waiting time of one minute, the laser was switched on and held at the constant power intensity for five minutes until a steady-state heating level was reached. Then, the laser was switched off, and within five minutes, the temperature returned to its ambient thermal equilibrium value. The resulting THz peak amplitudes are presented in Figure 2.23(a). By using the calibration curves, these THz reflectivity values were then translated into the respective temperature changes (Figure 2.23(b)). Finally, the temperature values were normalized to the Cu ion concentration of the dispersion to determine which dispersion heated most efficiently (Figure

2.23(c)). Consequently, CuS PAA and CuS CTAB capped NPs yielded the most efficient light-to-heat transfer capability in comparison to the PEG capped CuS NP dispersion.

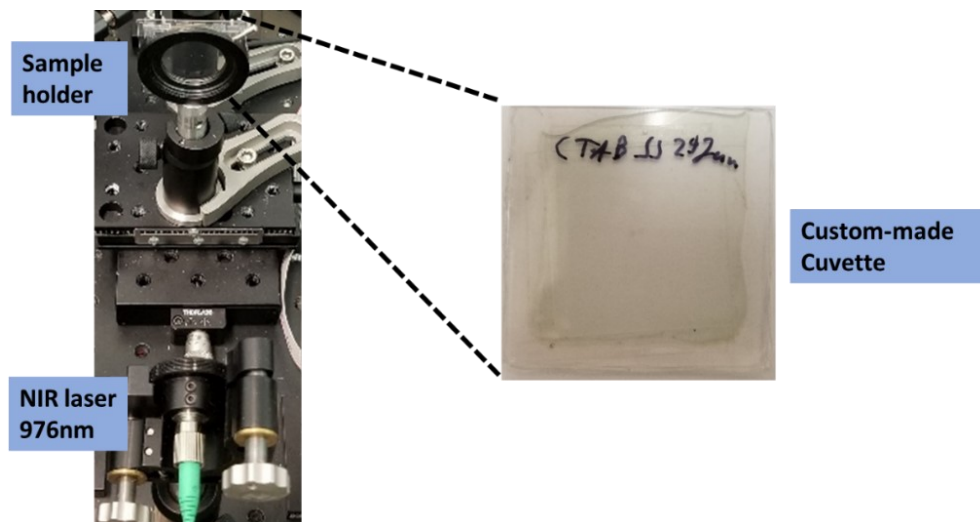


Figure 2.22: Digital image of the custom-made cuvette attached to a sample holder and illuminated by a NIR laser beam of 976 nm wavelength.

The results of a DLS analysis unveiled the hydrodynamic particle diameters of the NPs, which include not only the NP core but also their surrounding ligands. The normalized distributions are presented in Figure 2.24.

The plots show that the total size of the NPs is different for the three CuS NP types. PAA, for example, features two hydrodynamic particle sizes of 12 nm to 35 nm and 50 nm to 100 nm. The CTAB capped CuS dispersion exhibits NP sizes between 18 nm to 100 nm. However, the size of the PAA and CTAB capped CuS NPs are approximately equivalent. In contrast, the hydrodynamic NP diameter of the PEG capped CuS NPs shows two distinct distributions, ranging from 100 nm to 180 nm and 900 nm to 1800 nm, which also correlates to the width of the VIS-IR absorption band illustrated in Figure 2.17. The larger the size range of the NPs is spreading, the broader their absorption band.

Consequently, as described in the theoretical simulations in subchapter 2.6, the larger NPs experience far more scattering effects than the smaller ones, and this is substantiated in the normalized heat conversion results, illustrated in Figure 2.23(c). The CTAB and PAA capped CuS NPs heat to the same temperature level if normalized to their CuS ion concentration, in contrast to PEG capped NPs that show weaker heating behavior. Although PEG capped CuS NPs are biocompatible and could potentially be used in biomedical applications, they tend to form larger agglomerates that facilitate scattering, which in turn lowers their photothermal heat conversion capability significantly.

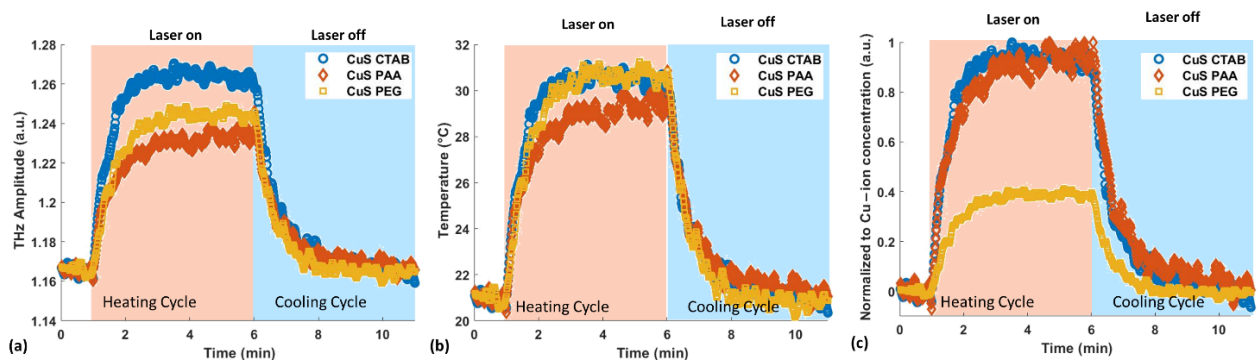


Figure 2.23: Time-resolved heating curves at a NIR power intensity of 0.68 W/cm^2 : (a) Change in THz reflectivity with time. (b) THz reflectivity correlation with temperature using the calibration values of each CuS NP system. (c) Temperature change normalized to the Cu ion concentration of the three dispersions.

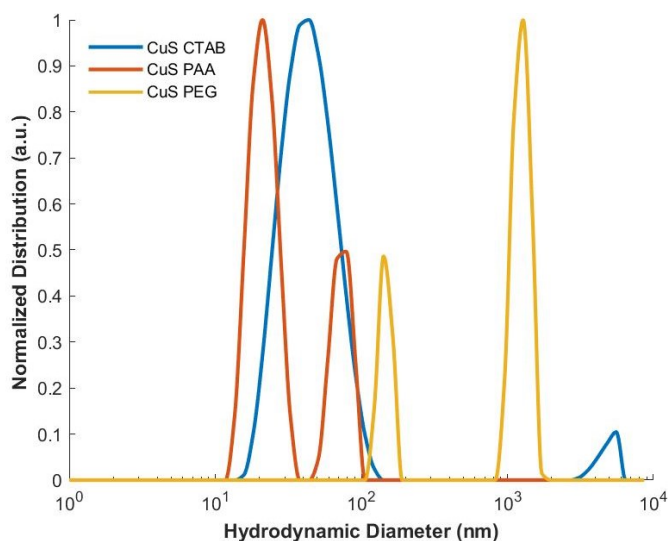


Figure 2.24: Normalized particle size distribution of the three CuS NP dispersions derived from a DLS analysis.

Consequently, the zeta potential of NP dispersions should be determined by, for example, using DLS measurements to evaluate their colloidal stability. A high value of the zeta potential (i.e., over 40 mV) indicates electrically stable NPs that form stable colloids and resist aggregation. In contrast, at low zeta potentials, the colloid tends to coagulate or flocculate, leading to precipitation, in turn lowering the effective colloidal concentration. In conclusion, the magnitude of the zeta potential of NPs helps to indirectly estimate the photothermal heating performance of NPs. A detailed study of the relation between zeta potentials and photothermal heating properties is an opportunity for future follow-up work because the zeta potential would also depend on the screening effects of specific ligands, the type of ions present in the medium, as well as other parameters during sample preparation and purification. These effects must be thoroughly studied and experimentally probed. In this study, the non-cytotoxic PAA capped CuS NPs are preferred due to their high photothermal performance and biocompatibility.

2.8 Accessing the Second Biological Window by Efficient Broadband Optical Parametric Amplification in Non-Uniform Bulk Crystals

Recently, light in the second near-infrared (NIR-II) window (1000 nm to 1350 nm) has attracted interest specifically for biomedical applications, because a laser beam in this wavelength region can penetrate deeper tissue regions in contrast to the conventional first near-infrared (NIR-I) window (650 nm to 950 nm). This phenomenon is caused by the lower effective attenuation coefficient (Figure 1.21) of biological tissue, a less intense autofluorescence background, and fewer photon scattering in the NIR-II window [152]. Additionally, PTT performed in the NIR-II window has the potential to minimize photothermal damage inflicted by intense laser radiation. The maximum permitted exposure in the NIR-II wavelength region is three times larger in comparison to the NIR-I window (1 W/cm^2 vs. 0.33 W/cm^2) according to the American National Standard Institute laser safety guide (ANSI Z136.1–2007, American National Standard for Safe Use of Lasers) [153]. However, the NIR-II window has been mainly used for biological imaging, but not for PTT applications. One reason is the lack of small-sized plasmonic NPs exhibiting strong absorption and high PCEs in the NIR-II window. Recently, plasmonic NPs utilizing the NIR-II wavelength region have been successfully designed and synthesized (e.g., the CuS NPs introduced in the previous subchapter 2.7), even though the preparation of the NIR-II range responsive photothermal agents within a limited size is still challenging. For example, a NP size of 200 nm is the cutoff size for NP penetration and accumulation in porous blood capillaries in tumors [154].

Moreover, the laser equipment is more expensive for the NIR-II than the NIR-I window or does not exist for specific wavelength regions, which limits its practical utilization capability. The desired solution is a wavelength-tunable laser source that is able to adjust the emitted wavelength to the LSPR of the NPs in the NIR-II wavelength window. This concept, in turn, enables the optimal excitation required to achieve the best possible PCE for PTT applications. Therefore, the development of low-cost wavelength-tunable NIR-II laser systems is an important step to realize NP-assisted practical applications for biomedicine.

Furthermore, high-power THz radiation can be generated via collinear optical rectification by shining a laser beam (NIR-II window) in organic crystals (e.g., DAST, DSTMS, OH1, HMQ-TMS) [155], where peak electric fields of GV/m can be achieved with promising potential applications in biomedicine, for example, photothermally induced damage evaluation during NP-assisted laser tissue soldering processes, as described in chapter 3. In this case, a more intense THz radiation could penetrate deeper into highly absorptive biological tissue than low power THz light commonly

generated by such sources as PCAs. Deeper penetrating THz light enables gathering information at greater tissue depths in order to improve the assessment of the photothermal damage during the tissue fusing procedure.

Additionally, a laser source in the NIR-II window is less harmful to eyes since the light at the so-called “eye-safe wavelengths” around 1.4 μm is highly absorbed in the eye’s lens and cornea. Thus, the laser light cannot reach the extremely delicate retina [156]. These laser systems can be used in free-space applications as well as in a clinical environment, depending on their optical power levels. Moreover, a tunable laser source in the NIR-II window can perform time-resolved pump-probe experiments investigating THz-matter interactions. For instance, the pump laser beam could be split into two lines, one that excites NPs in the NIR-II window and the other that generates intense THz radiation in an organic crystal.

Consequently, cost-efficient, reliable, and tunable pulsed laser sources in the NIR-II window are of notable interest for clinical applications. To this end, a straightforward scheme was demonstrated for optimizing the parametric gain of optical parametric amplifiers in the NIR-II wavelength window by performing wavelength conversion in a lithium triborate (LBO) nonlinear crystal based on a three-wave mixing (TWM) process, also called optical parametric amplification. TWM enables conversion to wavelength regions inaccessible by standard laser systems. Consequently, the method produces broadly tunable high energy ultrashort pulses in optical parametric amplifiers [157]. Figure 2.25 depicts a flow and energy diagram of the TWM process. Two input beams with different laser frequencies (the pump ω_{pump} and the seed ω_{seed}) enter a second-order nonlinear optical crystal. During the TWM process, the pump is weakened, and the seed amplified. The output beams are the signal ω_{signal} and a newly created third laser beam, the so-called idler ω_{idler} with a frequency relationship of $\omega_{pump} = \omega_{idler} + \omega_{signal}$. Phase matching, i.e. $\Delta k = k_{pump} - k_{signal} - k_{idler} = 0$, is required to effectively transfer energy from the pump to the signal/idler beam.

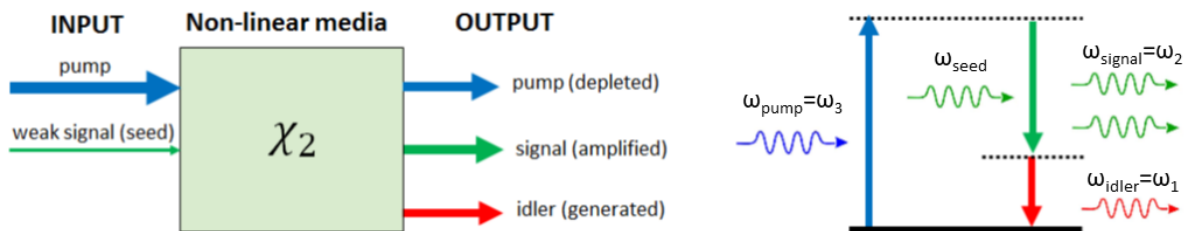


Figure 2.25: (a) Flow diagram of the TWM process in a nonlinear medium illustrating the input and output laser beams having different frequencies. (b) Energy diagram of the TWM process, which can be perceived as stimulated emission of signal photons from a virtual energy level excited by the pump. (Figure adapted from reference [158])

An adiabatic TWM process in a nonlinear crystal can achieve high conversion efficiencies over a broad bandwidth [159], [160] by utilizing the auto-resonance effect [157]. Auto-resonance is a property of nonlinear systems to remain in resonance with driving oscillations if the parameters of the system vary gradually in time and space, such as when applying a temperature gradient across a nonlinear crystal [157], [161]. In this way, the conversion of each frequency component occurs in a different position across the nonlinear crystal, corresponding to the position where the phase mismatch approaches zero for individual interacting waves. During the adiabatic TWM process, the phase mismatch is slowly varied along the propagation axis within the nonlinear medium, allowing the adiabatic conversion to adapt gradually to these changes [157], [162]. This temperature control technique increases the bandwidth and efficiency of the nonlinear process.

The adiabatic TWM process comprises the application of a non-uniform temperature gradient along an LBO crystal to optimize the phase-matching conditions, in turn, resulting in strongly improved conversion efficiency and bandwidth in the range between 1200 nm to 1550 nm.

An ultra-broad spectral bandwidth is essential for optical parametric amplifiers to operate. However, the output pulse duration from parametric processes is typically limited by the spectral acceptance of the phase-matching conditions in the nonlinear medium [157].

Autoresonant theory gives analytical expressions for the amplitudes of the propagating waves for a mono-dimensional problem in z-direction along the crystal. Therefore, it calculates the phase-matching conditions that are needed to ensure a stable operation as well as efficient TWM over a broad wavelength regime [160], [163]. The theory is articulated by a set of equations that formulate spatial evolution of the pump, signal, and idler waves in a non-uniform crystal using plane-wave approximation and assuming that the group velocity dispersion is insignificant [157]. The wave vectors, refractive indexes, and its mismatch depend on the position along the crystal. These generic equations are independent of the physical origin of the non-uniformity and describe the stability and efficiency conditions for the specific temperature induced non-uniform case. The set of equations represent the slowly varying envelopes of the three interacting waves [164]:

$$j \frac{\partial A_{1,2}}{\partial z} + \frac{\omega_{1,2}}{n_{1,2}c} \chi_{eff} A_{2,1} A_3 \exp \left[+j \int_0^z \Delta k(\zeta) d\zeta \right] = 0 \quad 2.34$$

$$j \frac{\partial A_3}{\partial z} + \frac{\omega_3}{n_3c} \chi_{eff} A_1 A_2 \exp \left[-j \int_0^z \Delta k(\zeta) d\zeta \right] = 0 \quad 2.35$$

$$\Delta k(z) = k_3(z) - k_1(z) - k_2(z), \quad k_{1,2,3}(z) = \frac{2\pi}{\lambda_{1,2,3}} n_{1,2,3}(z) \quad 2.36$$

where $A_j(z)$ is the envelope of the electric field of the j -th wave. The value of j is 1 for the idler, 2 for the signal, and 3 for the pump wave. z is the position along the crystal. ζ is the shifted normalized coordinate. $d_{eff} = \chi_{eff}/2$ represents the quadratic nonlinear coefficient of the optical medium. k denotes the j -th wave vector, and $\Delta k(z)$ signifies the phase-mismatch.

Comprehensive numerical simulations were carried out to optimize the temperature profile that yields the highest conversion efficiency between a wavelength of 1250 nm to 1850 nm. The adiabatic conversion process can be described by a system of nonlinear coupled equations [164], [165], where the phase mismatch changes along the propagation axis. The numerical model considered group velocity dispersion and mismatch, as well as diffraction. The rate of phase mismatch change must be minimized to improve conversion efficiency and bandwidth.

Figure 2.26(a) illustrates the computed conversion efficiencies of two different temperature profiles (exponential and linear) applying 100 °C and 160 °C on the extremities of a nonlinear crystal. A constant temperature profile of 130 °C along the crystal constituted a reference. The linear temperature distribution offered more than 50% efficiency over a bandwidth of 400 nm and represented the best option. Additionally, Figure 2.26(b) plots the numerical evaluation and comparison between the conversion efficiencies for temperature contrasts ranging from 10 °C to 60 °C (all centered at 130 °C). The temperature distribution featuring a 40 °C temperature difference attained the broadest bandwidth and the highest conversion efficiency.

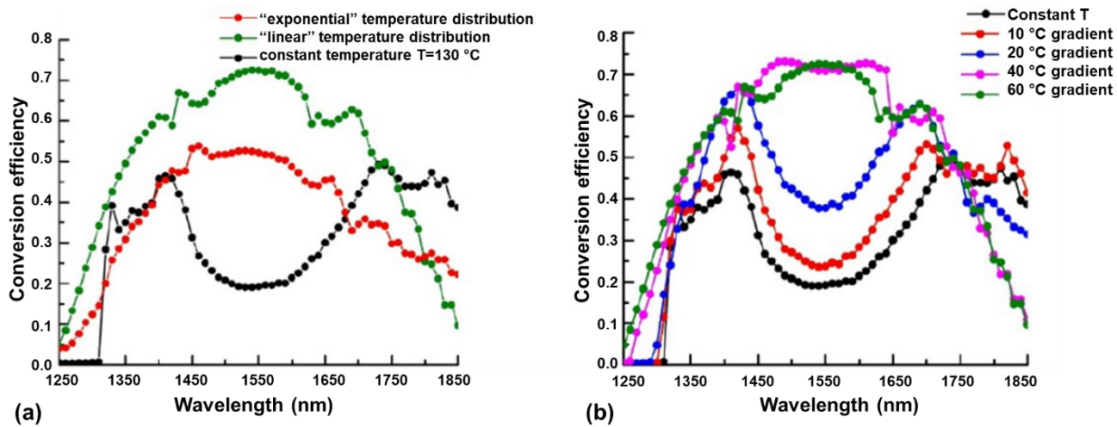


Figure 2.26: a) Simulated conversion efficiencies as a function of wavelength for three temperature distributions inside an LBO crystal. Exponential (red line) and linear (green line) temperature gradients having a temperature contrast of 60 °C (100 °C – 160 °C) are compared to the constant temperature profile of 130 °C (black line). b) Modeled conversion efficiencies as a function of wavelength for different linear temperature distributions inside an LBO crystal. Temperature contrasts of 40 °C (110 °C – 150 °C) and 60 °C (100 °C – 160 °C) possess the highest conversion efficiency and bandwidth. (Figures adapted from reference [157])

An experiment was carried out to confirm the numerical results of the adiabatic parametric amplification. My contribution laid in the experimental realization of this study by building the setup, aligning, and operating it.

Figure 2.27 shows the schematic representation of the setup. A dichroic beam splitter combined a 775 nm pump beam (up to 5 μJ pulse energy, 700 fs pulse duration, 6 nm spectral full width at half maximum). The tuning range of the seed beam was not restricted in the simulations. However, in the experiment, the output wavelength range of the commercial optical parametric amplifier deployed to generate the seed beam was limited to a wavelength range of 1200 nm to 1550 nm. (1 μJ pulse energy, 700 fs pulse duration, 6 nm spectral full width at half maximum) [157].

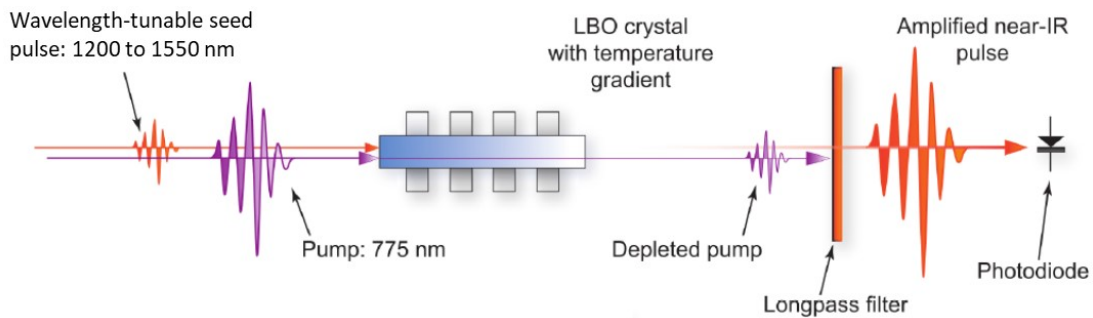


Figure 2.27: Schematic representation of the experimental setup. A pump and a seed beam were guided through the left facet of an LBO crystal with an applied temperature gradient along its length. After exiting the crystal, the residual depleted pump beam was blocked by a long-pass filter, whereas a photodiode measured the amplified signal wave. (Figure adapted from reference [157])

Both collinearly propagating beams were guided into the facet of a 5-cm long LBO crystal (Eksma Co., 3 mm x 3 mm x 50 mm, type 1, $\theta = 90$ deg, $\phi = 0$ deg, uncoated). A long-pass filter having a cut-on wavelength of 1000 nm eliminated the depleted 775 nm pump radiation after exiting the crystal. A pyroelectric energy meter (OPHIR PE9-SH) measured the signal power in an 1150 nm to 2000 nm wavelength range. The frequency-dependent response of the detector and the transmission of the long-pass filter varied for the signal and idler wavelengths and, therefore, were subsequently corrected [157].

A customized crystal holder (Figure 2.28) included four equidistantly spaced built-in thermoelectric heaters, which were controlled by four thermistors that maintained direct contact with the crystal surface. It took approximately 10 minutes for the 3-mm thick crystal to reach the required temperature distribution [157].

Various temperature profiles were applied along the 5-cm long LBO crystal to study the adiabatic phase-matching conditions and the resulting conversion efficiencies. First, two different temperature distributions were applied to the crystal to validate the simulated results: An

exponential temperature gradient in which the first heater was set to 100 °C and the fourth to 160 °C, as well as a linear temperature gradient in which the temperature of the four heaters constituted an arithmetic progression in the same temperature range.

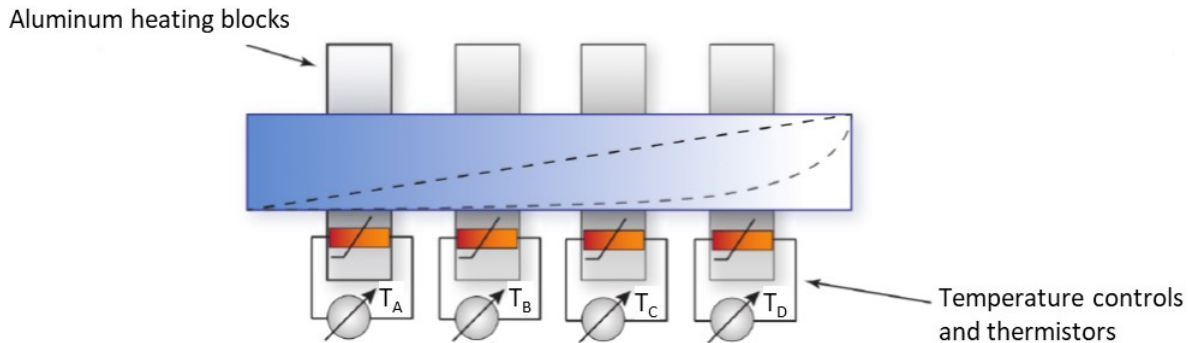


Figure 2.28: A customized crystal holder featuring four equidistantly spaced thermoelectric heaters and their respective thermistors for temperature control directly connected to the crystal surface. (Figure adapted from reference [157])

Figure 2.29(a) plots the conversion efficiency and demonstrates a peak conversion of up to 55%, as well as a conversion bandwidth over 250 nm. Consequently, the linear temperature gradient offers 10% more conversion efficiency and a broader bandwidth in comparison to the exponential gradient.

Next, the conversion efficiency in the crystal was characterized for a uniform temperature in which four heaters were set to 130 °C. These settings represented a reference for the subsequent temperature configuration in which varying gradients were applied, ranging from 10 °C up to 60 °C but always centered at 130 °C. Figure 2.29(b) plots an increasing trend in conversion efficiency with a rise in temperature contrast up to 40 °C. As simulated by numerical calculations, a higher temperature contrast beyond 40 °C did not yield a higher conversion efficiency nor a broader bandwidth [157].

A conversion efficiency difference of around 10% between the simulated and the experimental results are attributed to the partly unreliable control of the crystal temperature. Using only four heaters placed along the LBO crystal cannot ensure the desired linear temperature gradient. Therefore, the setup configuration can be upgraded by deploying more and smaller heating elements to provide a more accurate linear temperature profile [157].

The presented adiabatic TWM technique of controlling the phase-matching condition by applying a temperature gradient across nonlinear bulk crystals in order to increase the parametric gain in optical parametric amplifiers can be readily used in a new generation of highly efficient and

broadband industrial-grade amplifiers. It does not require any complex fabrication or alignment techniques [157].

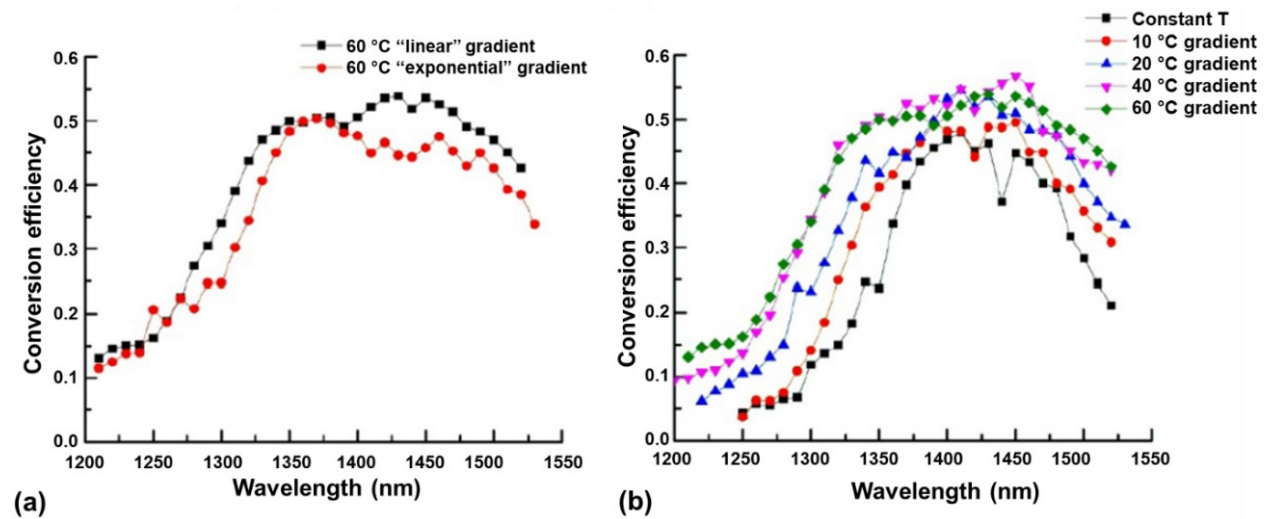


Figure 2.29: Measured conversion efficiencies as a function of the seed beam wavelength: a) exponential and linear temperature gradients (100 °C to 160 °C). b) Linear temperature gradients (each centered around 130 °C having a different total temperature contrast) and a constant temperature of 130 °C. (Figures adapted from reference [157])

The experiment that will be described in chapter 3 regarding NP-assisted laser tissue soldering still relies on PCAs for both THz generation and detection. However, it is well conceivable that, in future works, high-power THz emitters based on organic crystals can be pumped by low-cost wavelength-tunable NIR-II laser systems based on the TWM process in the nonuniform crystals discussed above. Additionally, the NIR-II signal beam could be used to photoexcite the NIR-II NP systems that were either injected into or deposited onto the tissue.

3 THREE-DIMENSIONAL MONITORING OF NANOPARTICLE-ASSISTED LASER TISSUE SOLDERING BY TERAHERTZ LIGHT

The NP-assisted laser tissue soldering of skin incisions is a minimally invasive treatment method for wound closures that surmounts the need for invasive conventional sutures. The concept is simple and requires a solder gel blend made of bovine serum albumin (BSA) dissolved in a NP dispersion constituting a protein – NP composite that is applied over a skin incision and plasmonically heated by laser irradiation. The NPs in the solder gel act as highly effective heating agents. Without the NPs, the laser photons would mostly be scattered and lost. When the temperature in the superficial skin layer reaches more than 60 °C, the processes of coagulation is initiated, specifically the denaturation of biological compounds like proteins. The solder gel serves as a “biological glue” that permanently fuses vessel edges. This procedure bears the potential to simplify surgical procedures and shorten the recovery time of patients. However, meticulous monitoring of the plasmonically-heated solder gel and the skin tissue underneath is essential to optimize the strength of the tissue bond [101] as well as minimize the procedure’s side effect of photothermal damage that is being inflicted on the tissue cells as a consequence of the incident laser illumination.

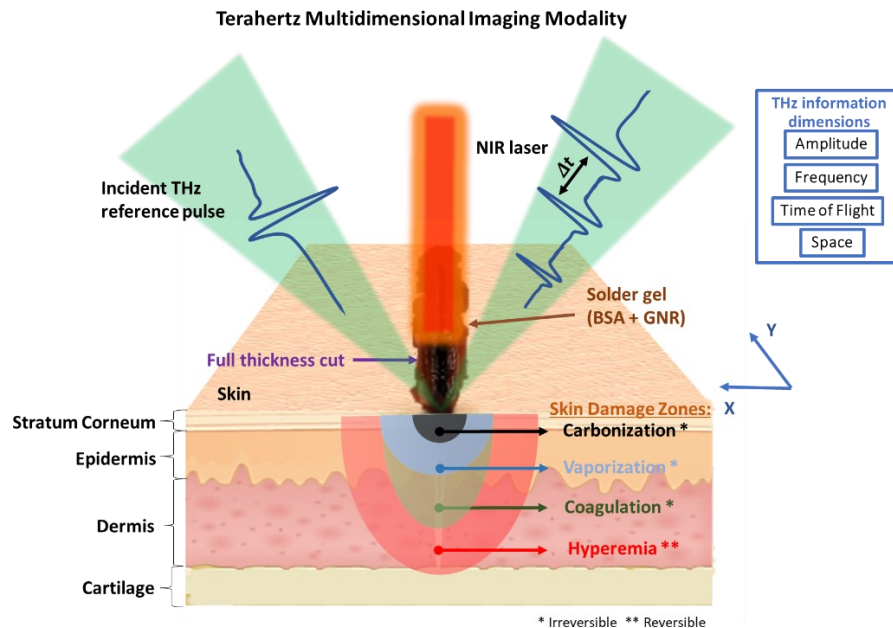


Figure 3.1: Schematic depiction of tissue excised from porcine ear skin plotting different stages of photothermal reactions during a NP-assisted laser tissue soldering process. Additionally, a THz multidimensional imaging modality is displayed represented by an incoming THz reference pulse being reflected multiple times off various interfaces. This produces a train of convolved THz echoes containing multidimensional information that is required to assess the depth and severity of the photothermal damage, which was inflicted on the skin incision area by NIR laser irradiation. (Figure adapted from reference [166])

Figure 3.1 shows the thermal damage zones that usually occur during the photothermal heating procedure [167]. The heat transfer process is driven by oscillating molecules that disperse the thermal energy radially into the deeper tissue. If the heat increase is moderate and can rapidly dissipate, no permanent thermal damage to the tissue will remain. However, if the heat input is too high and remains constant over a long period (41 °C to 48 °C for >60 min or 48 °C to 60 °C for 4 min to 6 min [168]) or the tissue temperature exceeds a threshold of 60 °C, tissue coagulation, i.e., the denaturation of biological compounds like proteins, will lead to irreversible tissue necrosis. This condition is a consequence of the premature cell death in living tissue caused by, for example, intense heat [115]. Further heat accumulation of up to 100 °C results in intense water evaporation and tissue volume reduction. When all the remaining skin moisture has evaporated, skin ablation, carbonization, and incineration of the affected cells occur, which becomes visible by the appearance of char on the skin surface [115].

First, a numerical finite element model was deployed to simulate the spatiotemporal heat transfer upon laser illumination and its resulting temperature distribution in skin tissue. Moreover, the photothermal damage was modeled and mapped over the skin area. Second, a dynamic THz single-point measurement study was carried out to trace the process of NP-assisted laser tissue interaction and interpret its implications for the skin tissue hydration level as well as tissue integrity. Additionally, *in vitro* THz reflective imaging in three-dimensions was carried out based on a multidimensional THz imaging modality. This modality utilizes THz amplitude, frequency, ToF, and spatial information to assess the dimensions and especially the depth of the photothermal damage incurred by the NP-assisted laser tissue soldering procedure. Figure 3.1 illustrates the principle of the modality in which the incident THz reference pulse is reflected off the surface as well as the various interfaces it encounters while partly penetrating the skin incision area and superficial skin layer. These multiple interfaces produce a train of convolved THz echoes, which must be deconvolved and analyzed to gain access to the desired information about the dimensions and condition of the photothermal damage within the incision area. In particular, the THz amplitude was used to attain imaging contrast, together with the frequency information to perform THz echo deconvolution, ToF information to assess the quantitative dimensions of the photothermal damage within the skin tissue, and spatial information enabled by a THz raster-scan technique to generate THz images in three-dimensions. During a THz raster-scan procedure, a sample is scanned across the THz beam while retrieving the THz waveform pixel-by-pixel.

3.1 Spatiotemporal Heat Transfer Modelling of Nanoparticle-Assisted Laser Tissue Interaction

The time-dependent heat transfer and spatial thermal distribution in the skin were simulated by a numerical finite element model using the software package COMSOL Multiphysics. This work was performed in collaboration with the group of Prof. Alexander O. Govorov (Ohio University).

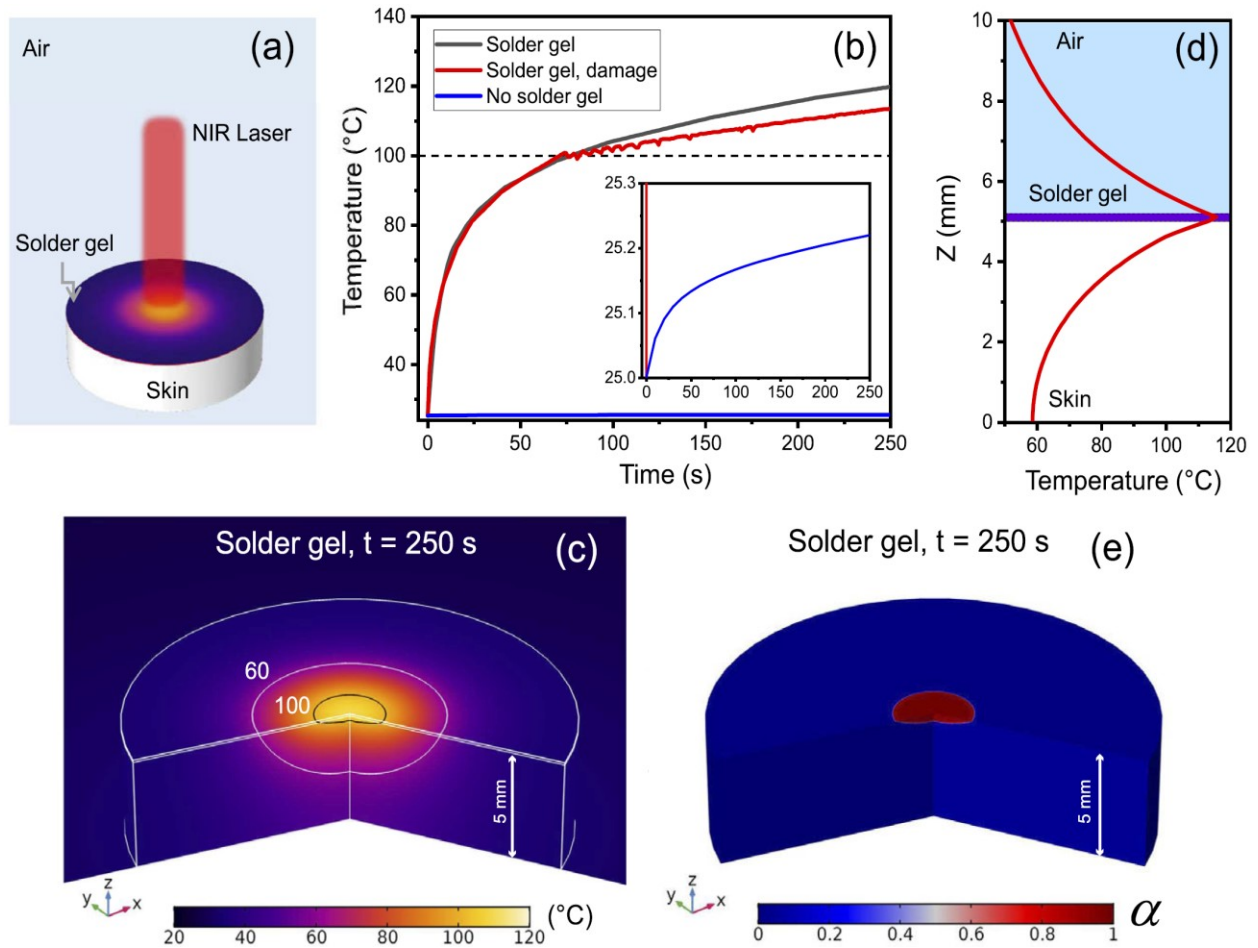


Figure 3.2: (a) Schematic diagram of the NP-assisted laser tissue interaction process created by a finite element model encompassing a two-layer structure made of solder gel and skin tissue surrounded by air. (b) Simulated temperature transients on the surface of the skin, with and without modeling the resulting tissue damage. The inset shows a zoom in on the temperature transient of the bare skin without the application of a solder gel. (c) Simulated three-dimensional thermal distribution in skin tissue coated with solder gel after a laser exposure time of 250 s. Temperature contours of 60 °C and 100 °C are highlighted in white and black, respectively. (d) The thermal distribution as a function of distance below and above the skin tissue surface. The surface was coated with a NP containing solder gel. (e) Estimated damage distribution in the skin with the application of the solder gel after 250 s of laser exposure. (Figures adapted from reference [166])

The skin sample was modeled as a two-layer structure comprising the skin and a solder gel surrounded by a large air layer (Figure 3.2(a)). The skin part was composed of a homogeneous layer of 5-mm thickness and 8-mm radius containing water and low-loss biological background.

The solder gel was designed with a thickness of 200 μm and a radius of 8 mm, comprising a homogeneous blend of bovine serum albumin (BSA) and an aqueous NP dispersion.

The NPs in the simulation had a rod-shaped morphology sized 10 nm \times 41 nm, a LSPR wavelength of around 808 nm, and an absorbance value of 100. This small GNR size guaranteed a high PCE and low scattering properties, in turn enabling highly efficient localized heating of the solder gel. Moreover, a CW NIR laser beam was simulated, possessing an emission line at 800 nm to match the LSPR wavelength of the GNRs, a power intensity of 5 W/cm², and a beam diameter of 4.4 mm ($1/e^2$) targeting the center of the solder gel.

The spatiotemporal thermal distribution in porcine skin in the absence of blood circulation was simulated by calculating the thermal transfer properties based on the heat conduction in biological tissue by using the heat transfer equation [169]:

$$Q_{\text{ext}} = \rho C_p \frac{\partial T}{\partial t} + \nabla(-k\nabla T) \quad 3.1$$

where Q_{ext} represents the heat input and outflow of the system, for instance, provided by an external heat source, such as a laser beam, ρ denotes the densities of the materials (1321 kg/m³ for solder gel [170], 1050 kg/m³ for porcine skin [171]), and C_p is the specific heat capacity (3.4 J/(g \cdot K) for solder gel [170], 3.6 J/(g \cdot K) for porcine skin [171]). The second term on the right side of the equation stands for the thermal diffusion, where k represents the thermal conductivity of 0.58 W/(m \cdot K) for the solder gel [170] and 0.5 W/(m \cdot K) for the porcine skin [171]. T and t are temperature and time, respectively.

Two boundary conditions were imposed to constrain the solution of equation 3.1. In the simulation, the skin was surrounded above and at its sides by an air layer that was modeled to be large in comparison to the skin. The air layer is sufficiently large to allow for an unimpeded thermal diffusion from the skin to the boundaries of the system. The temperature at the surface boundaries of the air layer was fixed at the ambient temperature value of 25 $^{\circ}\text{C}$. Thus, the irradiated heat from the skin can diffuse into the air and levels off at its boundaries to the ambient temperature level. The bottom of the skin was supported by a polyethylene plate. In the model, this plate represented a thermal insulator with a boundary condition resulting in a local heat flux density of $q = 0$.

The laser heat source Q_{laser} was simulated in a cylindrical coordinate system, and its deposited power was calculated using the Beer-Lambert law, which includes the absorbed part of the laser beam, as described by the following equations:

$$Q_{\text{laser}} = -\left. \frac{\partial I(r, z)}{\partial z} \right|_{\text{abs}} = \mu_{\text{abs}} I(r, z) \quad 3.2$$

$$I(r, z) = I_0(r) e^{-(\mu_{\text{abs}} + \mu_{\text{scat}})z} \quad 3.3$$

where $I_0(r)$ is the laser intensity at the surface, featuring an average intensity of 5 W/cm² and a Gaussian intensity profile. μ_{abs} and μ_{scat} are the absorption and scattering coefficients of porcine skin along the skin depth z , which are 0.02 cm⁻¹ and 6.5 cm⁻¹ [171], respectively. The attenuation coefficient μ_{abs} of the solder gel is estimated to be 100 cm⁻¹. Heat transfer through convection Q_{conv} and radiation Q_{rad} occurs between the skin surface and the surrounding air. This concept was implemented into the simulation by the commonly used equations:

$$Q_{\text{conv}} = -h(T - T_0) \quad 3.4$$

$$Q_{\text{rad}} = -\varepsilon\sigma(T^4 - T_0^4) \quad 3.5$$

where h indicates the heat transfer coefficient for convection (5 W/(m²·K)), ε is the surface emissivity (0.8), and σ is the Stefan-Boltzmann constant (5.67 x 10⁻⁸ W/(m²·K⁴)). The initial temperature T_0 was set to 25 °C.

Figure 3.2(b) illustrates the temperature evolution in time on the surface of the skin in three cases. First, the solder gel was applied to the skin and subsequently heated by NIR laser illumination. With the application of the GNR embedded solder gel, the temperature transient exponentially increased within 25 s to 60 °C, and then gradually saturated after 75 s at around 100 °C. The model did not account for any skin damage; therefore, the temperature reached around 120 °C after 250 s.

Second, the same scenario as the first case, but the model now includes skin damage appearing at 100 °C. The transition from normal to damaged tissue consumes energy in the form of heat (assuming a heat sink) originating from a local phase change. Therefore, the temperature rose slower than in the simulation without the damage. The skin damage was simulated by introducing a thermal damage model, which will be explained later in this subchapter.

In the third case, no solder gel was applied to the skin. Due to the low absorption coefficient of the porcine skin during the NIR photothermal heating process, the skin surface temperature increased insignificantly, with most of the light being scattered.

Figure 3.2(c) depicts a three-dimensional simulation of the thermal distribution in the solder gel and the skin tissue after 250 s of NIR laser illumination. The image maps the temperature dissipation from the center of the skin tissue where the temperature reaches almost 120 °C due to the Gaussian intensity profile of the laser. From this location, the temperature decays radially to around 20 °C. The temperature contours marking 60 °C and 100 °C are highlighted in white and black, respectively. At 60 °C, irreversible coagulation of biological components occurs, and at 100 °C, water swiftly evaporates from the skin surface, initiating a carbonization process observable by char formation on the skin surface. Notably, the thermal conductivity of the skin is low; therefore, most of the heat increase is limited to or near the surface around the laser illumination spot. The heat sharply decays already after a couple of millimeters. Thus, the temperature increases quickly and steeply in the center of the beam, inflicting severe photothermal damage to the skin surface and culminating in tissue carbonization.

Figure 3.2(d) illustrates the spatial distribution of the temperature inside the skin tissue and the surrounding air. The simulation proves that the accumulated heat generated by the strong absorption of the GNR blended solder gel is tightly deposited in a well-confined area in the proximity of the skin surface. Almost 120 °C is reached at the interface between the skin and the solder gel. This value decreases to less than 60 °C at 5 mm below the superficial skin layer, and 8 mm above the skin in the surrounding air.

The thermal damage was modeled by using equation 3.6 and 3.7 within the overall heat transfer calculation using the software suite COMSOL Multiphysics. The damage threshold was set to a critical temperature of $T = 100$ °C and a maximum time to full damage of $\tau_{\text{damage}} = 10$ s, according to the experimental evidence. At this temperature, the skin tissue not only becomes necrotic but also carbonizes. The severity of the thermal damage is indicated by the parameter α , which ranges between zero (non-damaged tissue) and one (carbonized necrotic tissue). The parameter α starts to increase as soon as the local temperature exceeds the critical temperature. α was computed using the following equations:

$$\frac{d\alpha}{dt} = \frac{1}{\tau_{\text{damage}}} \theta(T - 100 \text{ °C}) \quad , \quad \theta(x) = \begin{cases} 0 & x < 0 \\ 1 & x \geq 0 \end{cases} \quad 3.6$$

$$Q_{\text{damage}} = -L_h \rho \frac{d\alpha}{dt} \quad , \quad \alpha \in [0,1] \quad 3.7$$

where Q_{damage} represents the latent heat energy due to the vaporization of water, and x is an independent variable. L_h (2250 kJ/kg) denotes the damage enthalpy change of the water

vaporization. Figure 3.2(e) illustrates the damage severity distribution represented by the damage indicator α after a NIR irradiation exposure of 250 s.

The simulations conclude that the application of a GNR blended solder gel leads to a substantial well-confined temperature increase within the skin tissue sample. When the temperature exceeds certain temperature levels, the skin changes its water content, which ultimately leads to tissue damage zones with distinct severity levels.

3.2 Dynamic THz Investigation of Nanoparticle-Assisted Laser Tissue Interaction

THz radiation was utilized to investigate the process of NP-assisted laser tissue interaction and evaluate various zones featuring different thermal damage characteristics. A dynamic THz single-point measurement based on THz-TDS in reflection geometry (Figure 3.3) was deployed to trace the evolution of THz signals during the laser tissue interaction process. The THz setup has been described in subchapter 2.1.

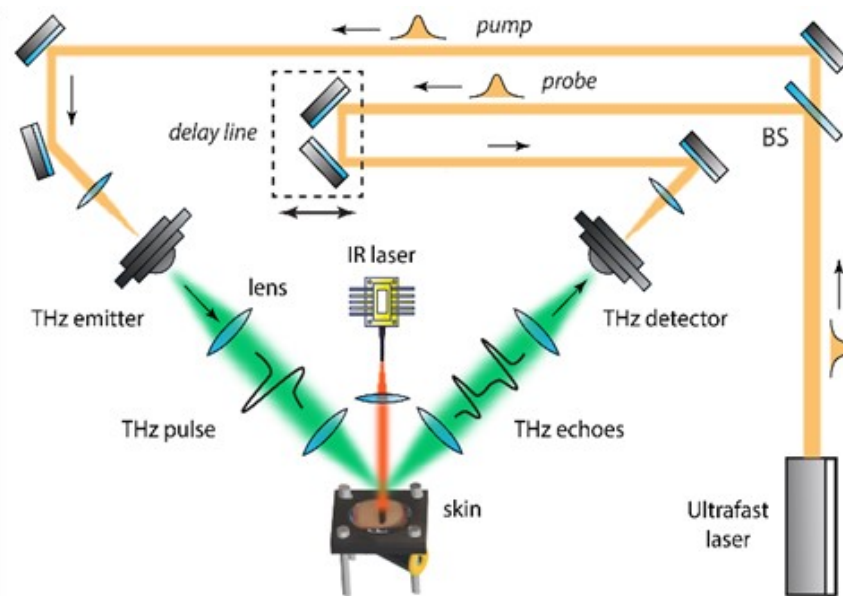


Figure 3.3: Experimental THz-TDS setup configured to reflection geometry depicting an ultrafast laser emitting pulses that are split by a beam splitter (BS) into a pump and probe beam. Both beams are guided to the THz emitter and detector, respectively. The probe beam passes through a delay line to introduce a temporal delay to perform THz-TDS. A 786-nm NIR CW laser beam plasmonically heated a GNR blended solder gel, which covered the porcine ear skin sample. (Figure adapted from reference [166])

Notably, I designed and built the THz-TDS setup with imaging modality to perform the measurements. Moreover, I prepared the skin samples, the solder gel, and performed the soldering as well as measurement procedures. Additionally, I carried out the post-processing of the experimental data using the deconvolution algorithm described in subchapters 2.2.1 and 2.2.3.

Porcine ear skin tissue was used as an *in vitro* model for human skin since their histological and physiological properties are very similar [172]. Therefore, the porcine skin is considered a proper surrogate and is indeed well suited for preclinical studies.

The GNR blended solder gel was prepared by dissolving 50% weight by volume concentration of BSA (Sigma-Aldrich) in a 1:1 mixture of a GNR dispersion and deionized water. The GNR dispersion was purchased from the company Nanopartz™ having an optical absorbance per 1 cm unit thickness of 140 at 816 nm (LSPR wavelength) and of 122 at 786 nm (NIR CW laser excitation wavelength) determined by using equation 1.7. The dimension of a GNR was 10 nm x 41 nm, featuring an aspect ratio of 4.1. Figure 3.4 shows a representative TEM image of the GNRs and plots the absorbance spectrum of the GNR dispersion.

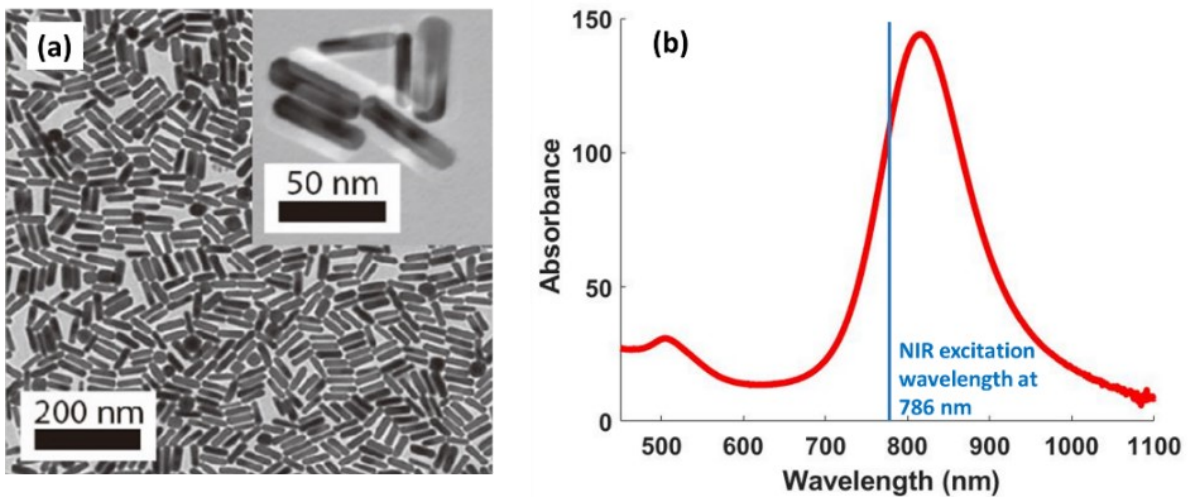


Figure 3.4: (a) Representative TEM image of GNRs featuring a dimension of 10 nm x 41 nm. (b) VIS-NIR absorbance spectrum of the GNR dispersion highlighting the excitation wavelength at 786 nm, which was used to excite plasmonically the GNRs during the experiment.

Table 3.1 lists the physico-optical properties of the GNR dispersion. The particle number concentration of the resulting solder gel was 2.2×10^{13} GNRs/mL.

A thin solder gel layer approximately 8-mm wide and 200- μ m thick was deposited on the surface of an excised porcine skin sample (Figure 3.5(a)). A NIR CW laser, irradiating at 786 nm, featuring a spot size diameter of 4.4 mm ($1/e^2$) and a power intensity of 4.2 W/cm², was exerted at the center of the solder gel. The power intensity I was calculated by using equation 2.27. The laser radiation excited the LSPR of the GNRs, which in turn converted the laser energy almost entirely into heat. The PCE was determined in subchapter 2.6 to be 93%. The generated heat dissipated in a narrow, superficial skin area around the laser spot.

Table 3.1: Physical and chemical parameters of the GNR dispersion blended with a BSA powder to form a solder gel.

	GNR dispersion
Longitudinal SPR Peak (nm)	816
Absorbance at LSPR peak	140
Absorbance at 786 nm [A_{λ}]	122
Transverse SPR Peak (nm)	509
Potential of Hydrogen pH	7
Weight Concentration ($^{mg}/_{ml}$)	4.9
Aspect Ratio	4.1
Length \times Diameter (nm)	41×10
Zeta Potential (mV)	35
Concentration ($^{NPs}/_{ml}$)	8.6×10^{13}
Molarity (nM)	143
Molar Extinction ($^{l}/_{M \cdot cm}$)	9.8×10^8

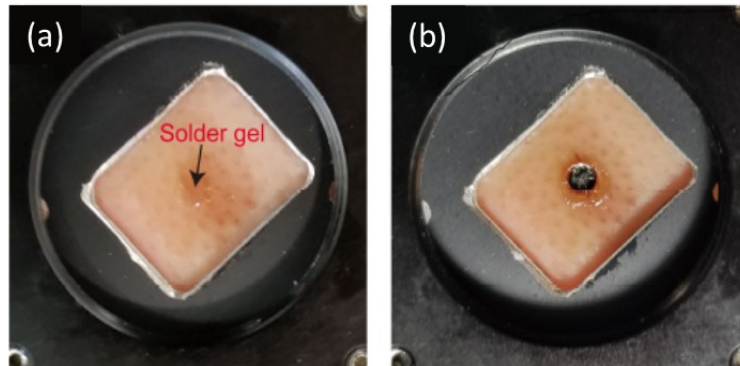


Figure 3.5 Digital images of a porcine ear skin sample coated with a GNR blended solder gel. (a) Thinly applied on the surface before NIR CW laser illumination. (b) After plasmonic laser heating for 250 s featuring a skin surface damage in the form of carbonized skin and solder gel. (Figures adapted from reference [166])

The THz beam impinged on the sample with an angle of 45 deg relative to the normal of the sample. The spot size diameter was approximately 1.4 mm ($1/e^2$) and superimposed with the NIR laser beam. The reflected THz transients were recorded at a sampling rate of 1 trace per second using a spring-driven high-speed optical delay line (APE Angewandte Physik und Elektronik).

The solder gel and the skin sample underneath were irradiated for 250 s by using the described NIR CW laser. The heating rate was modest over this period to allow the THz traces to trace the laser tissue interaction process. The heating process was discontinued after 250 s due to carbonization effects on the skin in the focus spot of the laser beam (Figure 3.5(b)), as predicted

by the numerical simulations in Figure 3.2(e). A THz single-point dynamic measurement consisted of 250 THz traces that were successively recorded, as shown in Figure 3.6(a).

The THz signal evolution over the 250 s experienced a sharp drop in the THz amplitude within the first 50 s, which can be explained by an intense dehydration process in the solder gel and skin tissue because of the sudden temperature increase leading to a lower THz reflectivity and higher THz penetration inside the skin tissue.

Moreover, the pulse duration of the THz trace was significantly prolonged by the formation of multiple zones (layers) with different dielectric properties (i.e., refractive indices) inside the solder gel and the skin. These zones formed a progressing photothermally inflicted tissue damage. The THz echoes in the time-domain trace are created by reflections off the interfaces between two adjacent layers. If the layer thickness is below the THz wavelength, the respective THz echoes partly superimpose. In this case, the THz trace consists of a train of successive THz echoes that need to be distinctly resolved in time. This enables an explicit interpretation of the tissue damage within the various zones that are created by the photothermal heating process.

The 250 successively recorded THz traces from the THz single-point dynamic measurement, shown in Figure 3.6(a), were post-processed by FWDD, described in subchapter 2.2.1, resulting in deconvolved THz traces (Figure 3.6(b)). Each peak in the deconvolved traces represents an interface within the sample structure. Its position in time and amplitude indicates the location and reflectivity of the specific interface, respectively.

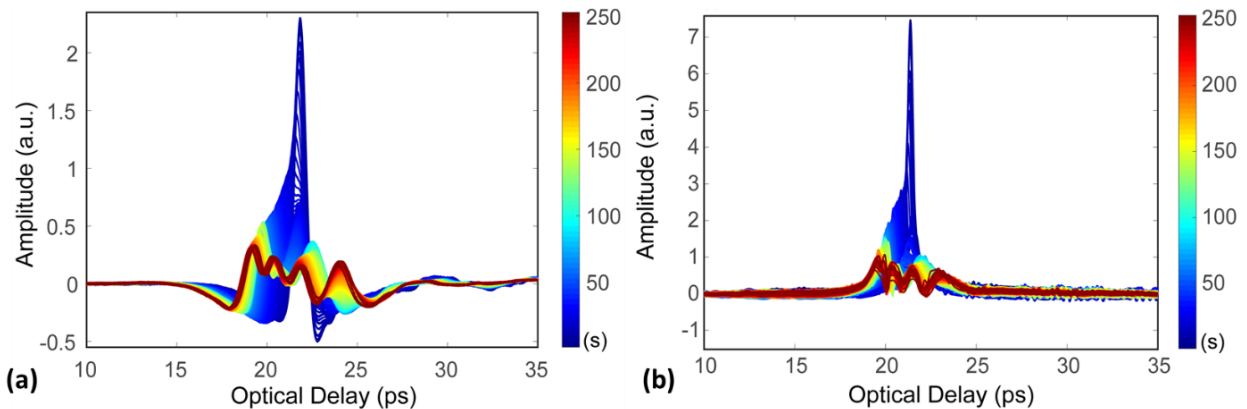


Figure 3.6: (a) Dynamic THz single-point measurement depicting 250 reflected THz traces successively recorded at a sampling rate of one THz trace per second during NIR laser illumination with an intensity of 4.2 W/cm². (b) Dynamic THz single-point measurement presenting 250 deconvolved THz time-domain traces attained after the application of an FWDD algorithm. (Figures adapted from reference [166])

Additionally, the sign of the peak amplitude depends on the value of the refractive indices of the respective opposing interfaces. A positive peak amplitude means that the THz echo originates

from an interface where the refractive index transitions from a lower towards a higher value. In the opposite case, the THz echo is flipped, and the peak amplitude becomes negative. In Figure 3.6(b), the peaks are all positive, since the refractive index always increases at each consecutive interface as a consequence of the gradual dehydration of the skin sample that evolves from the outside (lower water content equals lower refractive index zone) to the inside (higher water content equals higher refractive index zone) of the skin. Typical recorded THz raw and deconvolved traces, at specific time intervals, are plotted in Figure 3.7 and explained in Table 3.2 to illustrate the signal evolution during the plasmonic heating process. Note that the deconvolved signal was normalized to its maximum amplitude.

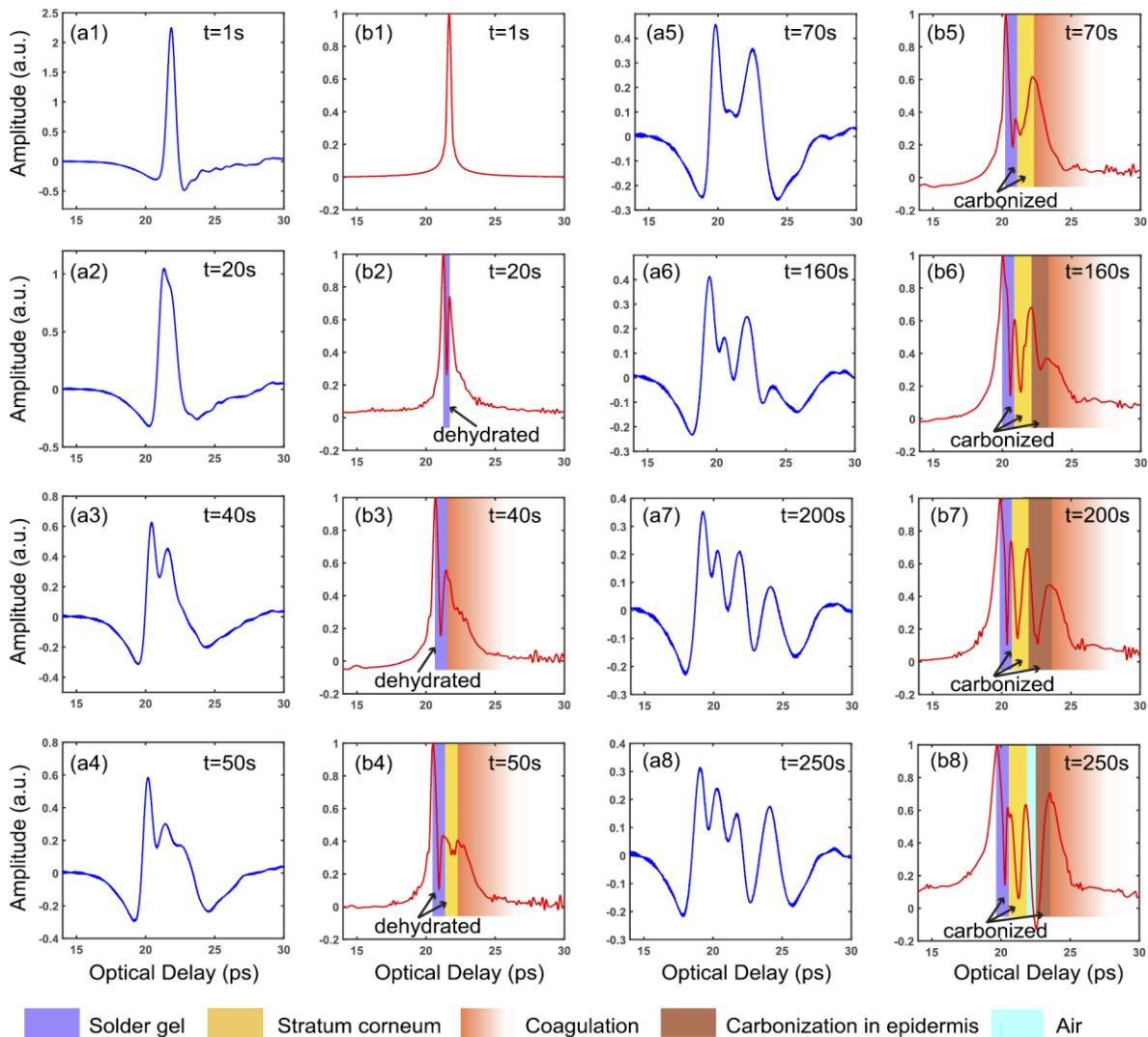


Figure 3.7: Typical THz raw and deconvolved signals at specific time steps t derived from the dynamic THz single-point measurement. (a1-a8) Correspond to the raw THz signals recorded at $t = 1$ s, 20 s, 40 s, 50 s, 70 s, 160 s, 200 s, and 250 s, respectively. (b1-b8) Correspond to the deconvolved signals after applying an FWDD algorithm to the raw THz signals. The deconvolved signal is normalized to its maximum peak level. (Figures adapted from reference [166])

Table 3.2: Description of the photothermal effects in the porcine ear skin sample during the single-point measurement.

Timestep	Figure 3.7	Observation
1 s	(a1) and (b1)	Both raw and deconvolved signals show only one THz echo that was reflected off the solder gel surface. The high hydration level of the solder gel prevented deeper THz penetration into the material. During the subsequent seconds, the temperature increased rapidly inside the solder gel and the skin sample, leading to gradual dehydration. Therefore, the THz radiation was able to penetrate the solder gel reaching the underlying skin surface.
20 s	(a2) and (b2)	A broader THz reflection echo with reduced amplitude is illustrated, which indicates two convolved echoes. After the application of FWDD, the two peaks were separated (Figure 3.7(b2)) and originated from the reflections off the solder gel surface and the solder gel/skin interface. Then, the solder gel solidified, and the skin dehydrated from the outside towards the inside gradually over time creating a dehydration gradient within the skin, which allowed THz waves to travel deeper into the skin tissue and encounter more layers that were formed by the progressively spreading photothermal damage incurred by the laser irradiation.
40 s	(a3) and (b3)	The partially superimposed echoes became even broader, which is also observable in the post-processed THz trace in Figure 3.7(b3). The heat-induced hydration gradient created a gradual interface, which means that the refractive index increased slightly in depth, forming an initial region of tissue coagulation.
50 s	(a4) and (b4)	An additional echo in the raw signal was identified as another layer in the deconvolved signal corresponding to the skin's stratum corneum, which was dry and, therefore, resolvable by THz radiation.
70 s	(a5) and (b5)	The solder gel and stratum corneum started to carbonize, visible as char forming on the skin surface.
160 s	(a6) and (b6)	A further rise in temperature caused the formation of a carbonization zone in the epidermis.

200 s	(a7) and (b7)	The carbonization layer in the epidermis broadened.
250 s	(a8) and (b8)	The NIR laser was turned off since the skin started to vaporize and bulged (Figure 3.8) due to an emerging air layer between the carbonization and coagulation zone. The air layer is evident in the THz trace by a flipped THz echo with a negative peak due to a transition from a higher to a lower refractive index.

Figure 3.8 illustrates a digital cross-sectional image of the skin sample exhibiting the remaining bump on the skin and the thermal damage caused by the plasmonic NIR heating effect after 250 s of laser exposure.

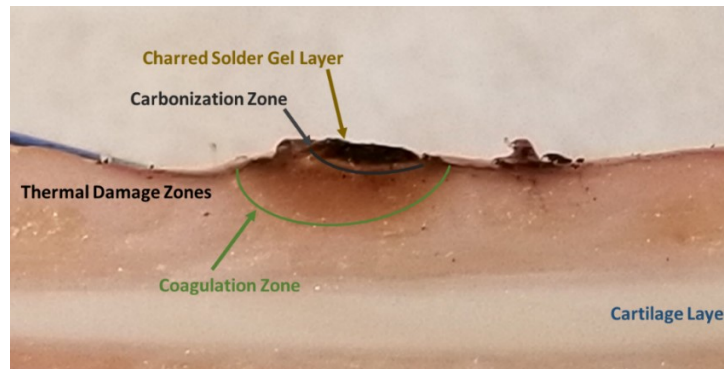


Figure 3.8: Digital cross-sectional image of the porcine ear skin sample coated with solder gel after 250 s of NIR laser exposure. The thermal damage subdivided into different zones is visible. The superficial layer bulged, causing a bump on the skin.

Consequently, the deconvolved THz signal revealed the transition of thermally affected zones in the solder gel and the skin tissue during plasmonic heating through NIR laser illumination. Information about these thermally affected tissue zones, such as depth, layer thickness, humidity level, and dielectric properties, can be obtained from the temporal width of the various echoes and the location of the peaks in the deconvolved THz traces. Depth information can be derived from translating the optical delay to distance by knowing the refractive index of the respective layer. For instance, in Figure 3.7(b2), the two THz peaks confining the BSA layer are 0.75 ps apart. The refractive index of BSA at 107 °C is about 1.80 [173]. The layer thickness of the dehydrated solder layer was calculated by using equation 1.5, resulting in approximately 44 μm . The refractive index of skin tissue changes significantly with water content. Unfortunately, the indices of differently hydrated and damaged skin tissues in the THz frequency regime are not available in the literature. Hence, an effective refractive index of 1.20 [174] was used for dehydrated porcine skin to approximate the depth of the incurred thermal damage in the tissue. The entire optical delay due to the thermal damage at time step $t = 250$ ps in Figure 3.7(a8) is

5.35 ps, which translates to a thickness of around 315 μm for the damaged dehydrated porcine skin tissue. The THz radiation is unable to penetrate the coagulation zone further since the water concentration is too high [175]. Thus, the penetrable thermal damage zone is limited to the superficial part of the skin.

3.3 THz Three-Dimensional Characterization of Nanoparticle-Assisted Laser Tissue Soldering

NP-assisted laser tissue soldering of a skin incision was carried out *in vitro* and subsequently imaged by THz radiation in a reflection geometry setup. The THz image data was further analyzed to derive information about the thermal damage incurred by the skin tissue resolved in three dimensions.

A 5-mm deep and 10-mm long incision was made on the surface of a porcine skin sample (dimension: 25 mm \times 20 mm) using a surgical blade. After that, the incision and its etches were coated by a GNR containing solder gel (Figure 3.9(a)).

The skin tissue sample was attached to a motorized two-dimensional X-Y translation stage (Figure 3.9(c)). A NIR laser beam with an emission line at 786 nm and a spot size diameter of 1.1 mm ($1/e^2$) was used to plasmonically heat the GNRs in the blended BSA solder gel. This heating effect, in turn, increased the temperature of the tissue surrounding the incision, leading to the reconnection of collagen and consequently fusing the edges of the wound opening (Figure 3.9(b)).

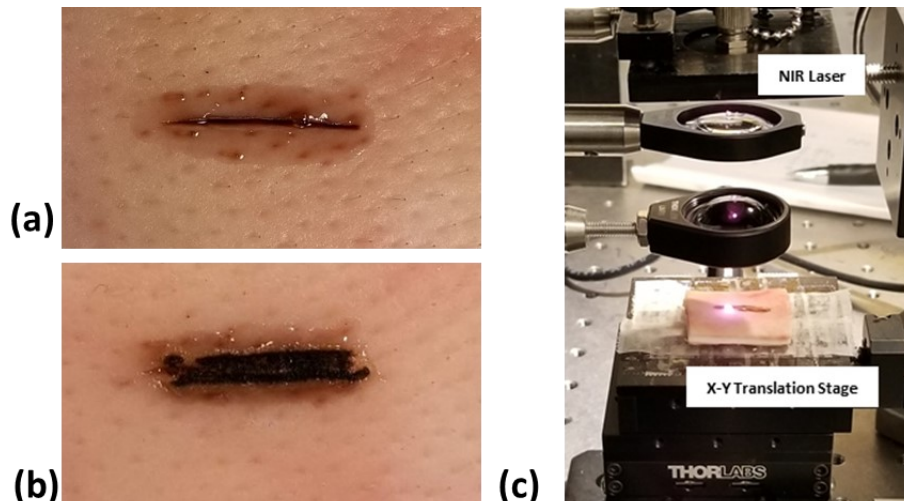


Figure 3.9: (a) Porcine ear skin sample with a line-shaped incision of 10-mm length was evenly coated with a GNR blended protein solder gel. (b) Soldered skin incision after 250 s of plasmonic NIR CW laser heating achieved by exerting a laser intensity of 40 W/cm^2 . (c) NIR laser tissue soldering procedure. The solder gel covering the skin incision was plasmonically heated by NIR laser radiation to fuse the incision edges. A two-dimensional translation stage moved the skin to perform three consecutive line scans.

During the laser-driven soldering process, the stage moved with a speed of $75 \mu\text{m/s}$ to cover slightly more than the length of the line-shaped incision. The incision was soldered three consecutive times, each time the sample was shifted by a small vertical offset of 1 mm to broaden the soldered area. The entire soldering procedure required 8 minutes and resulted in a strong skin tissue bonding effect. The small spot size of the NIR laser limited the thermally affected region to a minimum and lowered the dehydration of the surrounding tissue. In turn, this reduced the thermal damage of the peripheral tissue [176].

Three porcine ear tissue samples with skin incisions were soldered under different laser beam intensities of 20 W/cm^2 (Figure 3.11(a1)), 30 W/cm^2 (Figure 3.11(a2)), and 40 W/cm^2 (Figure 3.11(a3)). The severity of the thermal tissue damage advanced with increasing laser power intensity, showing various levels of carbonization effects in the superficial layer of the skin.

After the laser soldering process had been completed, the samples were raster-scanned with a resolution of 0.5 mm in a THz reflective imaging setup described in subchapter 2.1 (Figure 3.3 and Figure 3.10). A high-speed optical delay line running at a sampling frequency of 1 Hz deployed during the THz raster-scan kept the image acquisition time below 30 minutes. Three-dimensional imaging data were acquired for each sample encompassing an entire THz trace for each pixel position. The FWDD algorithm was utilized to deconvolve the traces, which were subsequently normalized to their maximum peak value.

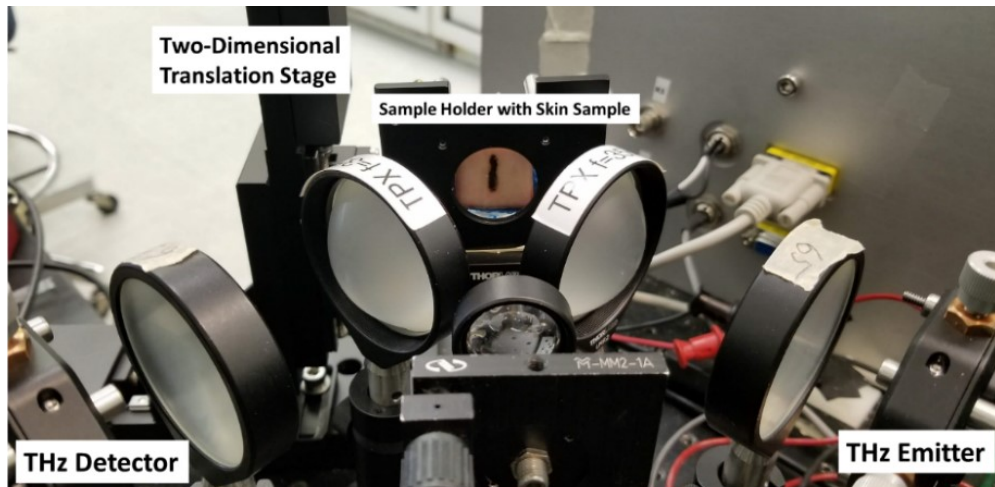


Figure 3.10: THz reflective imaging configuration composed of a THz emitter, detector, 2D translation stage, and TPX lenses to guide the THz radiation to the sample stage and the THz detector. The sample holder could be moved in the X-Y direction to perform THz raster-scans.

THz C-scan images (X-Y direction) of the soldered skin samples are presented for laser intensities of 20 W/cm^2 , 30 W/cm^2 , and 40 W/cm^2 in Figure 3.11(b1-b3), respectively. The peak amplitude of the deconvolved THz traces was used to confer image contrast. The images were normalized

to their peak amplitude. The THz amplitude was influenced by the dehydration level of the skin area, which served, therefore, as the dominant contrast mechanism. The areas in the center of the incision showed a lower THz amplitude, which was caused by a smaller THz reflectivity since the plasmonic heating effect dehydrated these zones the most.

THz cross-sectional images, known as B-scans, provide depth information (X-Z direction) and are shown for the laser intensities of 20 W/cm², 30 W/cm², and 40 W/cm² in Figure 3.11(c1-c3), respectively. These THz cross-sectional images plot the temporal width of the deconvolved THz echoes across a line in the center of the soldered incision that can be translated into layer thickness information by using equation 1.5 and knowing the refractive index of the respective material. The contrast parameter was the normalized magnitude of the deconvolved THz echoes in each pixel. A threshold of 0.3 eliminated the noise from the image.

Binary THz cross-sectional images are shown for laser intensities of 20 W/cm², 30 W/cm², and 40 W/cm² in Figure 3.11(d1-d3), respectively. They were attained by assigning the value 1.0 to every identified THz peak amplitude that represents a layer interface. All the other THz amplitudes in the time-domain trace were set to zero. These images distinctively show the number and depth position of the identified interfaces within a material.

At the laser intensity of 20 W/cm² in Figure 3.11(c1), the air/solder gel surface and solder gel/skin interface are distinguishable. The solder gel/skin interface across the X-direction constitutes a continuous crest offering a sharper contrast than the reflection from the air/solder gel surface. This effect proves that the plasmonic heating procedure highly dehydrated the solder gel and that THz radiation was able to reach the skin surface. However, the skin at this point was not severely damaged, as shown in Figure 3.11(d1), since no significant interface reflections originated from beneath the surface.

At the laser intensity of 30 W/cm² in Figure 3.11(c2), the echo width of the solder gel/skin interface broadened significantly, which indicates a deeper penetration of the THz radiation into the skin due to an increased dehydration level and hence more substantial thermal damage. Additional interfaces in the subsurface area of the skin (Figure 3.11(d2)) suggest the formation of carbonization and coagulation zones.

At the laser intensity of 40 W/cm² in Figure 3.11(c3), the echoes originating from the solder gel and skin surface were strongly broadened and became indiscernible due to severe carbonization. Moreover, no additional subsurface interface was identified in Figure 3.11(d3). Hence, the thermal damage zone broadened and shifted deeper into the epidermis.

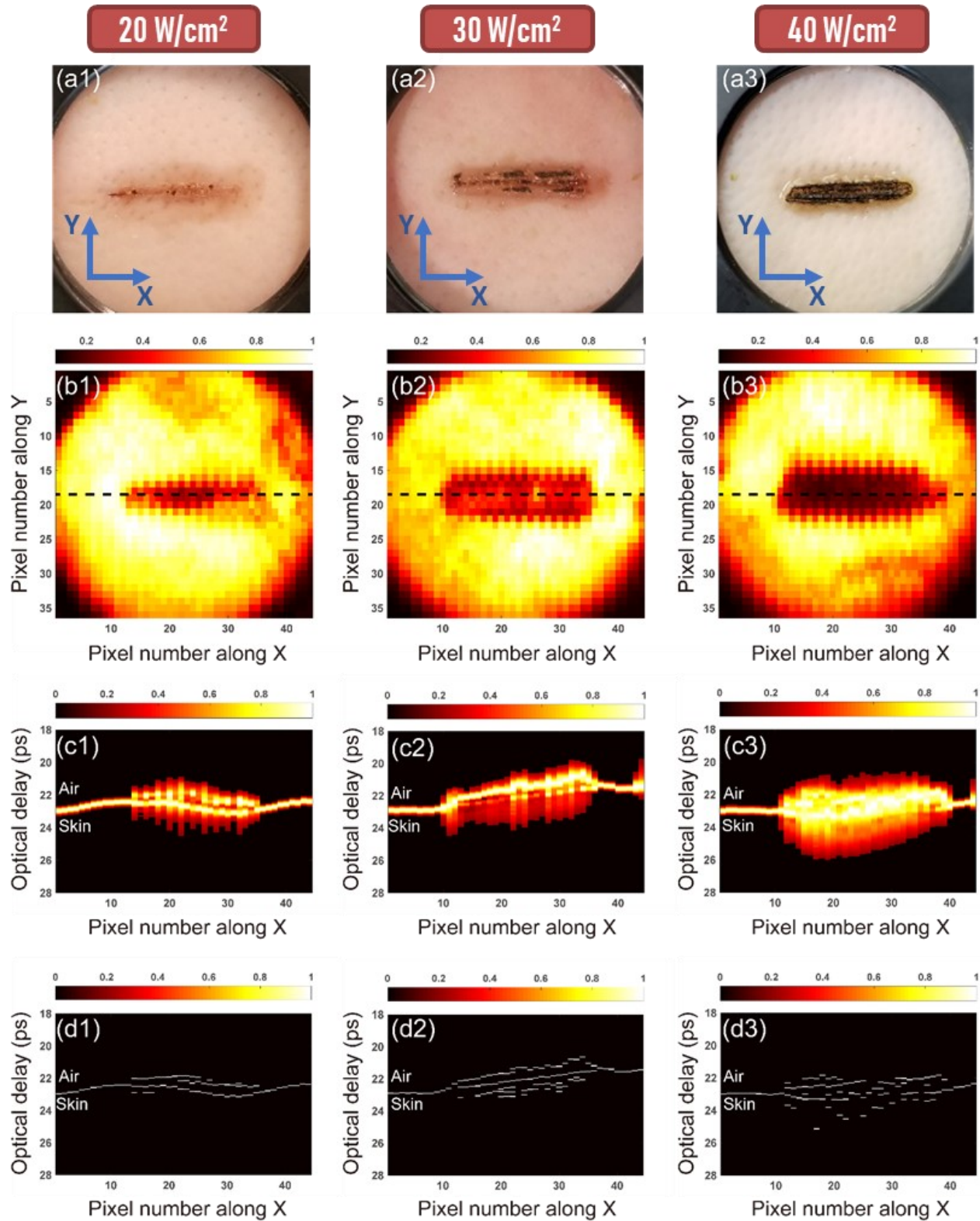


Figure 3.11: (a1-a3) Digital images of the porcine ear skin samples after NP-assisted laser soldering with a 20 W/cm², 30 W/cm², and 40 W/cm² laser intensity. (b1-b3) THz C-scan images, (c1-c3) THz cross-sectional images, and (d) binary THz cross-sectional images. The cross-sectional images (c1-c3) and (d1-d3) are taken along the dashed line marked in (b1-b3). (Figures adapted from reference [166])

Figure 3.12 depicts three-dimensional images acquired by THz raster-scan imaging showing the depth of the thermal damage as a consequence of the plasmonic heating effect during the NP-assisted laser soldering process for the NIR laser power intensities of 20 W/cm², 30 W/cm², and 40 W/cm². The most thermally damaged area resided along the center of the incision area. It grew in depth and extended up to the fringes of the skin incision. The depth of the thermal damage was estimated by approximating the refractive index of the damaged skin region and measuring the optical delay of the THz echoes. The damaged area reached up to about 600 μm into the skin at a laser intensity of 40 W/cm². Consequently, this study demonstrated that it is possible to quantitatively estimate the distribution of the photothermal damage induced by laser tissue soldering in three dimensions.

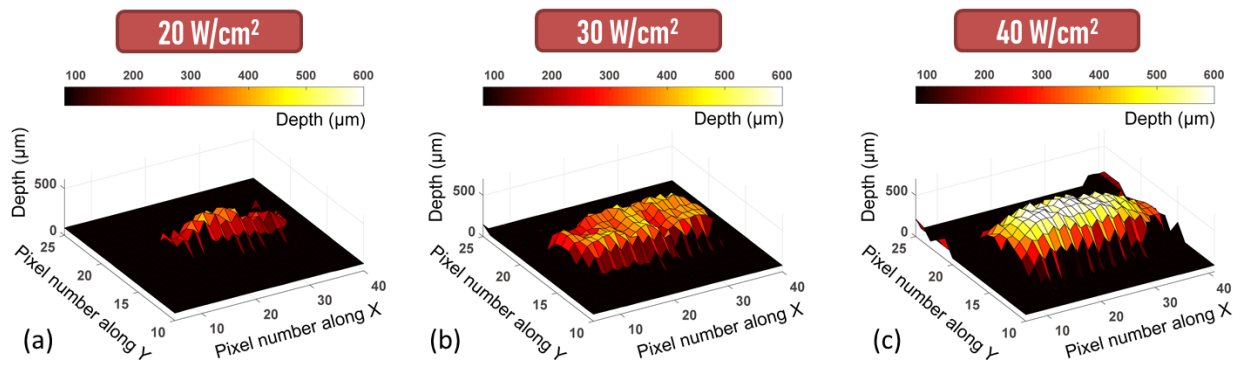


Figure 3.12: THz three-dimensional images of the porcine ear skin samples after NP-assisted laser tissue soldering with an intensity of (a) 20 W/cm², (b) 30 W/cm², and (c) 40 W/cm² depicting the depth of the photothermal damage inflicted by plasmonic heating effect after 250 s of NIR CW laser exposure. (Figures adapted from reference [166])

The monitoring and 3D evaluation of the thermal damage by THz radiation for the laser tissue soldering procedure have its limitations concerning, e.g., the deployed THz setup, THz penetration depth, and THz imaging resolution.

Specifically, the deployed THz setup is based on a free space system in which the probe and the pump beams, as well as the THz beam, are guided by using either mirrors or lenses. These three beam paths can become misaligned over time due to, e.g., temperature fluctuations in the ambient environment and vibrations resulting in a sudden or gradual decrease in system performance. Moreover, the installation of samples and even the usage of the system for *in vivo* studies outside of the lab environment requires stable, compact, and long-term reliable THz systems. Recently developed and already commercially available fiber-based THz systems are promising candidates to solve these problems. Another limiting factor is the restricted THz penetration depth in tissue due to the high THz absorbance of water. In general, THz radiation generated by PCAs can only reach a depth penetration in fully hydrated tissue of several hundred

microns (up to 1 mm in strongly adipose tissue or specific regions of the skin). The penetration depth strongly depends on the THz signal strength and the hydration level of the tissue to be analyzed during the laser tissue soldering procedure. The emitted THz power of PCAs is weak in comparison with other THz generation methods, such as via optical rectification in nonlinear media, e.g., zinc telluride and organic crystals. By using an alternative THz source, the depth penetration into the tissue can be significantly enhanced, yet at the expense of higher system complexity and costs.

Another constraint of the current THz system, and specifically of the deployed THz raster-scan technique, is the THz imaging resolution and time duration that is required to record an image of the sample. The THz imaging resolution was restricted to the 1.5 mm diameter spot size of the deployed THz system due to the diffraction limit of the focused THz beam, which depends on the central frequency of the THz pulses (0.3 THz). The time duration required to record an image of the sample by using the THz raster-scan technique depends mainly on the image resolution (0.5 mm) and the speed of the optical delay line (1 Hz). To avoid intense dehydration of the sample or for *in vivo* experiments, the imaging time duration must be significantly lowered by using alternative imaging techniques. An improvement to significantly reduce this duration could be a single-pixel imaging approach that constitutes an alternative to the deployed THz raster-scan method. A recently developed technique by Zanotto *et al.* [177] allows the reconstruction of THz temporal waveforms at each spatial position of an object without the need for mechanical raster-scanning.

Another hampering factor related to the pulse width of the THz pulse is the limited depth resolution. The shorter the THz pulse, the better is the ability to resolve thin layers of thermally damaged tissue. In the presented study, FWDD was used to increase the depth resolution and separate overlapping echoes in order to be able to thoroughly resolve the internal interfaces. This procedure can deliver an improved depth resolution when alternative THz sources that feature a shorter pulse width below 1 ps are used.

Up to now, the most important applications of laser tissue bonding are limited to soft tissues. However, laser tissue bonding is also being investigated for its applicability for hard tissues, such as the welding of dental tissue to repair fractured teeth [178]. In the future, the presented THz imaging method might also be used to evaluate heat-related damages in hard tissues (such as teeth and bones). Notably, THz radiation can deeply penetrate hard tissue due to its low water content. Thus, changes in the refractive index of hard tissue in the THz frequency range introduced by the photothermal damage incurred during the laser tissue bonding procedure could,

therefore, be assessed. Future work could investigate, for example, the internal structure of teeth that were treated with filling materials such as polyacid-modified resin composite. Moreover, the presented imaging method could also detect and locate cavities, hematoma, and caries in dentistry due to the refractive index discontinuities in depth and varying hydration levels. A previous study [179], for example, has already diagnosed dental cavities and osteoporosis using THz imaging in transmission geometry. The study found that tooth cavities can be detected due to their higher transmissivity in comparison to dentin. A recent study [180] investigated bone tissue under intense heat and found that there is a well-defined absorption peak at 2.1 THz that can be correlated to the temperature to which the bone tissue was heated.

Besides, in future work, the presented THz imaging method might be used to evaluate the tensile strength, and thus the wound healing quality of laser fused tissue and its correlation with THz reflectivity. The tensile strength is an essential parameter to evaluate the quality of the laser based wound healing procedure. Recent studies [110], [181], [182] have assessed the tensile strength of laser bonded tissue, for example, as a function of induced temperature in the tissue. There are many parameters to consider which could increase or decrease the adhesion of the incision edges and thereby the quality of a laser bonding procedure, for example, the exerted laser intensity, the time duration of the laser exposure, the concentration of albumin and NPs in the solder gel, and the amount of solder gel applied on the skin edges. The tensile strength of the porcine ear skin samples that were soldered at three different power intensities has not been measured in the presented study. The reason is the long time duration of the measurement cycle to image the skin sample using THz raster-scanning. During this procedure, the skin samples were exposed to the ambient atmosphere for a long time resulting in a diffused skin dehydration effect. Moreover, the optimization of the tensile strength was not a goal of this study, which was more concerned with the development of a new imaging method to monitor the photothermal damage evolution and distribution during the laser tissue soldering procedure. Finding a way to measure the tensile strength of the samples in a repeatable way is a topic for future studies. Such a topic could revolve around the change in THz reflectivity at external and internal interfaces resolved in depth as a function of fusing strength. Here, the strength is related to the synthesis of the extracellular matrix and the renaturation of biological compounds.

A further topic for future work could also be the validation in animal models featuring different cellular dynamics, in order to assess the applicability of the presented method for different tissue types and thus hydration levels. Additionally, laser tissue soldering experiments performed *in vivo* could solve the problem of the tissue drying effect experienced during the bonding process and

the subsequent THz imaging procedure. This would help to study the laser tissue soldering procedure in more realistic settings.

4 CONCLUSION

Photoexcitation of light-sensitive agents, such as nanoparticles (NPs) introduced into the human body, can affect biological tissue and cells in various ways. Chemical reactions (photochemical), biological processes (photobiological), as well as heat (photothermal) can be triggered by light. Optical therapy utilizes these effects in a controlled fashion, for example, photothermal therapy (PTT) aims to induce photothermal effects based on the principle that the local temperature of tissue increases as a result of laser absorption. PTT, as a minimally invasive treatment option, is foreseen to make its most substantial impact on the destruction of cancerous tumor cells in a controllable, spatially confined, and selective way to minimize collateral tissue damage by employing photothermal agents, such as NPs. Cancer has been one of the significant threats to human health for centuries, and according to the International Agency for Research on Cancer (IARC) report, the global casualty rate and new cases of cancer-related diseases in 2018 amounted to 9.6 million and 18.1 million worldwide, respectively [183]. Extensive research efforts have been directed towards improved synthesis strategies to design multimodal nanomaterials with tumor-targeting as well as highly efficient heating properties. Hence, the accurate determination of the photothermal response of nanomaterials represents an essential aspect of PTT treatments that can be used to achieve the desired temperature-induced effects in cancerous tissue. However, even nowadays, the quantification of the photothermal conversion efficiency (PCE) has not been adequately addressed by current methods, such as thermocouples, infrared (IR) thermometers, and IR thermography. They are either invasive and could potentially contaminate the fragile ecosystem of the NP dispersion or cannot measure the temperature beyond-line-of-sight directly at the interface where the photothermal excitation of the NP dispersion occurs. In this thesis, these challenges were addressed by a novel method for the characterization of the photothermal effect of NPs in aqueous NP dispersions, carried out in a non-contact and non-invasive manner to be implemented in a typical THz time-domain-spectroscopy (THz-TDS) system.

The presented method combines spatial and temporal thermal information acquired at THz frequencies in a THz-TDS system operating in reflection geometry to determine the PCE as well as the molar heating rate (MHR) of aqueous NP dispersions. To corroborate the new method, three types of gold NP dispersions featuring the same rod-shaped structure but differing in size (GNR10: 10 nm x 41 nm, GNR25: 25 nm x 90 nm, GNR50: 50 nm x 150 nm) were analyzed. The GNR10, having the smallest particle volume, attained 93% conversion efficiency, followed by the

GNR25 with 89%, and GNR50 achieved 67%. Other existing studies corroborate this trend for gold nanostructures featuring a similar size, as well as numerical simulations. Although, the PCE is the highest for the small-sized GNRs, the MHR, which corresponds to the heating speed of the NP dispersion relative to its molar concentration, is the highest for the large particle volumes (GNR10: 0.05 °C/nMs, GNR25: 0.3 °C/nMs, GNR50: 1.57 °C/nMs). The key photothermal characteristics of the GNRs are rooted in the underlying mechanism of their electromagnetic response during the photothermal heating process. The interaction cross-section of a plasmonic NP increases with its polarizability and scales with its particle volume. Therefore, smaller NPs exhibit a higher PCE but feature a smaller absorption cross-section on a single particle basis in comparison to more voluminous NPs. It is important to note that the proposed technique was tested with commercially available NPs; however, it can be readily applied to the characterization of all materials, which feature a temperature-dependent change of the refractive index in the THz regime.

Moreover, the thermal measurement by using pulsed THz radiation occurs directly at the interface of the enclosure with the NP dispersion, i.e., directly where the exciting laser encounters the NP dispersion. No other conventional measurement method can provide this type of characterization. THz time-of-flight (THz-ToF) evaluations in combination with signal post-processing, such as deconvolution and self-referencing, enable the presented method to be not only precise but also to work under ambient conditions as an open system which can be deployed in an out-of-the lab environment.

Another advantage of the devised method in contrast to commonly used techniques is that the obligatory stirring of the NP dispersion to homogenize the temperature distribution during the heating cycle by a magnetic bar becomes redundant. This approach alleviates the issue of potential contamination and falsification since temperature differences throughout the cuvette persist during the conventional stirring process. By using the presented imaging method, the temperature gradient caused by convection dynamics within the cuvette is accurately captured by taking THz thermograms of the front and rear window of the cuvette. This method allows the computation of the effective mass, which was heated during the procedure. This mass is a necessary parameter to determine the PCE.

In the light of recent developments of compact and affordable THz-TDS systems with fast imaging capabilities, this work paves the way to simplify and improve the automation of the thermal characterization process of nanomaterials within confined aqueous-based systems, such as microfluidic chips. It offers an appealing alternative to more invasive conventional methods.

Besides, due to an urge of the NP community to develop methods to synthesize NPs that can be photoexcited in the second biological window ranging from 1000 nm to 1350 nm, our novel method based on a THz-TDS system was tested by benchmarking three recently designed and optimized copper sulfide (CuS) covellite NP types possessing the same small core size of around 15 nm but different capping ligands (CTAB, PAA, PEG). These particles have been suggested as a viable alternative to noble metal-based photothermal heaters [95]. Their LSPR, which is independent of the surrounding medium, was centered around a wavelength of 980 nm covering partly the second biological window by its broad absorbance spectrum band. Moreover, their small size allows them to cross the cell barrier and permeate into biological cells easily. The study concluded that although all three CuS NP dispersions heated to almost the same temperature value, their copper (Cu) ion concentration was different. It can be assumed that the organic capping ligand PEG has influenced their tendency to form agglomerates, in turn leading to massive particle formations. This results in an increase in scattering effects during laser irradiation and, consequently, can be the reason for their low concentration-normalized heat performance. Moreover, to help to gain better access to the previously mentioned second biological window, the parametric gain of an optical parametric amplifier was optimized, achieving an almost equal conversion efficiency of more than 50% over a wide ~250 nm spectral bandwidth.

The next step in this study was a transfer of the NP related THz sensing and imaging capabilities from a cuvette-based system to a biomedical application. The heating properties of plasmonic NPs are crucial for laser tissue interaction in which the NPs function as local heating agents to transfer the laser's energy effectively into heat. NP-assisted laser tissue soldering is a minimally invasive treatment procedure to approximate incisions and promote wound healing. This treatment procedure has not been applied so far in clinical practice since a reliable diagnostic tool was unavailable to monitor the laser-assisted fusing process and simultaneously assess the treatment's inherent side effects of radiation-incurred photothermal tissue damage. Therefore, to address this issue, a novel approach has been developed to perform a rigorous investigation of the photothermal damage inflicted by NP-assisted laser tissue soldering. Our novel approach relies on the unique sensitivity of THz radiation to the hydration level of biological tissue. THz radiation is being used as a non-contact, non-invasive, and non-ionizing sensing and imaging modality to evaluate the localized photothermal damage. Specifically, it has been demonstrated (*in vitro*) that the application of a GNR blended solder gel leads to a significant and well-confined increase of temperature and thus to rapid and robust soldering of an incision made in a porcine ear skin sample. This skin type mimics well the histological and physiological properties of human skin. During the soldering procedure, the thermal gradient in the skin leads to a humidity variation

inside the tissue, resulting in the creation of distinct thermal damage zones. By performing dynamic THz single-point measurements, the temporal evolution of THz signals associated with the incurred photothermal damage was identified as tissue dehydration, coagulation, carbonization, and vaporization effects, finally leading to a bulging of the skin surface. The presented method provides a solid foundation for real-time monitoring of the thermal dynamics in biological tissue using a THz-TDS system.

Moreover, THz reflective imaging was utilized to quantitatively characterize the photothermal damage in three dimensions. By using THz-ToF analysis, it was revealed that the damaged area reached up to about 600 μm into the skin tissue at a laser intensity of 40 W/cm^2 . Within this thesis, the capability of THz radiation to carry out a three-dimensional tomographic characterization of the photothermal damage induced by NP-assisted laser tissue soldering in a non-contact, non-invasive, and non-destructive manner has been demonstrated for the first time. The proposed THz-TDS system does not need to be purged during the measurements, which allows it to be mobile and could be deployed in clinical procedures in the future.

Moreover, our measurements can be performed via small and cost-efficient THz-TDS systems capable of producing reliable THz images in a short time, in turn offering a non-contact, non-ionizing, and inexpensive clinical imaging modality that can be easily extended and applied across a broad range of clinical applications, including laser ablation, real-time burn depth, and severity evaluations, as well as photothermal therapies to prevent overheating of skin tissue. Our method can provide unique information currently unavailable from other medical imaging techniques, such as IR or magnetic resonance imaging. It has the potential to provide the level of sensitivity and specificity required in clinical decision making of the future.

In summary, in this thesis, a novel method based on THz-TDS has been devised to quantify the photothermal effects of NPs in combination with its application in biomedical imaging for NP-assisted laser tissue interaction, specifically for the study of photothermal tissue damage in real-time and in three dimensions. This work constitutes a step in the direction of establishing THz radiation as a powerful non-contact, non-invasive, and non-ionizing tool to bridge the fast-growing field of nanotechnology and medicine.

5 BIBLIOGRAPHY

- [1] W. Wei, X. Zhang, S. Zhang, G. Wei, and Z. Su, "Biomedical and bioactive engineered nanomaterials for targeted tumor photothermal therapy: A review," *Mater. Sci. Eng. C*, vol. 104, p. 109891, 2019.
- [2] J. B. Vines, J.-H. Yoon, N.-E. Ryu, D.-J. Lim, and H. Park, "Gold Nanoparticles for Photothermal Cancer Therapy," *Front. Chem.*, vol. 7, pp. 1–16, 2019.
- [3] G. Baffou and R. Quidant, "Thermo-plasmonics: Using metallic nanostructures as nano-sources of heat," *Laser Photonics Rev.*, vol. 7, no. 2, pp. 171–187, 2013.
- [4] Z. Qin and J. C. Bischof, "Thermophysical and biological responses of gold nanoparticle laser heating," *Chem. Soc. Rev.*, vol. 41, no. 3, pp. 1191–1217, 2012.
- [5] Z. Qin *et al.*, "Quantitative Comparison of Photothermal Heat Generation between Gold Nanospheres and Nanorods," *Sci. Rep.*, vol. 6, no. 1, p. 29836, 2016.
- [6] X. Wang, G. Li, Y. Ding, and S. Sun, "Understanding the photothermal effect of gold nanostars and nanorods for biomedical applications," *RSC Adv.*, vol. 4, no. 57, pp. 30375–30383, 2014.
- [7] Y. Wang *et al.*, "Comparison study of gold nanohexapods, nanorods, and nanocages for photothermal cancer treatment," *ACS Nano*, vol. 7, no. 3, pp. 2068–2077, 2013.
- [8] K. Jiang, D. A. Smith, and A. Pinchuk, "Size-dependent photothermal conversion efficiencies of plasmonically heated gold nanoparticles," *J. Phys. Chem. C*, vol. 117, no. 51, pp. 27073–27080, 2013.
- [9] X. Liu *et al.*, "Laser heating of metallic nanoparticles for photothermal ablation applications," *AIP Adv.*, vol. 7, no. 2, p. 25308, 2017.
- [10] M. Tonouchi, "Cutting-edge terahertz technology," *Nat. Photonics*, vol. 1, no. 2, pp. 97–105, 2007.
- [11] S. S. Dhillon *et al.*, "The 2017 terahertz science and technology roadmap," *J. Phys. D: Appl. Phys.*, vol. 50, no. 4, p. 043001, 2017.
- [12] X. C. Zhang and J. Xu, *Introduction to THz wave photonics*. Springer Science+Business Media, LLC, 2010.
- [13] H. Chen, L. Shao, Q. Li, and J. Wang, "Gold nanorods and their plasmonic properties,"

- Chem. Soc. Rev.*, vol. 42, no. 7, pp. 2679–2724, 2013.
- [14] W. He, J. Frueh, N. Hu, L. Liu, M. Gai, and Q. He, “Guidable thermophoretic janus micromotors containing gold nanocolorifiers for infrared laser assisted tissue welding,” *Adv. Sci.*, vol. 3, no. 12, p. 1600206, 2016.
- [15] A. J. Baragwanath, G. P. Swift, D. Dai, A. J. Gallant, and J. M. Chamberlain, “Silicon based microfluidic cell for terahertz frequencies,” *J. Appl. Phys.*, vol. 108, no. 1, p. 013102, 2010.
- [16] O. A. Smolyanskaya *et al.*, “Terahertz biophotonics as a tool for studies of dielectric and spectral properties of biological tissues and liquids,” *Prog. Quantum Electron.*, vol. 62, pp. 1–77, 2018.
- [17] M. Dutta, A. S. Bhalla, and R. Guo, “THz Imaging of Skin Burn: Seeing the Unseen—An Overview,” *Adv. Wound Care*, vol. 5, no. 8, pp. 338–348, 2016.
- [18] M. R. Grootendorst *et al.*, “Use of a handheld terahertz pulsed imaging device to differentiate benign and malignant breast tissue,” *Biomed. Opt. Express*, vol. 8, no. 6, 2017.
- [19] X. Yang *et al.*, “Biomedical Applications of Terahertz Spectroscopy and Imaging,” *Trends Biotechnol.*, vol. 34, no. 10, pp. 810–824, 2016.
- [20] M. C. Beard, G. M. Turner, and C. A. Schmuttenmaer, “Subpicosecond carrier dynamics in low-temperature grown GaAs as measured by time-resolved terahertz spectroscopy,” *J. Appl. Phys.*, vol. 90, no. 12, pp. 5915–5923, 2001.
- [21] J. Dong *et al.*, “Visualization of subsurface damage in woven carbon fiber-reinforced composites using polarization-sensitive terahertz imaging,” *NDT E Int.*, vol. 99, pp. 72–79, 2018.
- [22] K.-E. Peiponen, A. Zeitner, and M. Kuwata-Gonokami, *Terahertz Spectroscopy and Imaging*, vol. 140. Springer, 2012.
- [23] S. Fan, Y. He, B. S. Ung, and E. Pickwell-MacPherson, “The growth of biomedical terahertz research,” *J. Phys. D. Appl. Phys.*, vol. 47, no. 37, p. 374009, 2014.
- [24] Q. Sun, Y. He, K. Liu, S. Fan, E. P. J. Parrott, and E. Pickwell-MacPherson, “Recent advances in terahertz technology for biomedical applications,” *Quant. Imaging Med. Surg.*, vol. 7, no. 3, pp. 345–355, 2017.
- [25] J. Son, S. J. Oh, J. Choi, J. Suh, Y. Huh, and S. Haam, “Imaging of Nanoparticle Delivery Using Terahertz Waves,” in *Intracellular Delivery: Fundamentals and Applications*,

- Springer Science+Business Media, LLC, 2011, pp. 701–711.
- [26] J. H. Son, “Terahertz electromagnetic interactions with biological matter and their applications,” *J. Appl. Phys.*, vol. 105, no. 10, p. 102033, 2009.
- [27] A. Tomasino *et al.*, “Wideband THz Time Domain Spectroscopy based on Optical Rectification and Electro-Optic Sampling,” *Sci. Rep.*, vol. 3, no. 1, p. 3116, 2013.
- [28] A. Nahata, A. S. Weling, and T. F. Heinz, “A wideband coherent terahertz spectroscopy system using optical rectification and electro-optic sampling,” *Appl. Phys. Lett.*, vol. 69, no. 16, pp. 2321–2323, 1996.
- [29] D. H. Auston, “Picosecond optoelectronic switching and gating in silicon,” *Appl. Phys. Lett.*, vol. 26, no. 3, pp. 101–103, 1975.
- [30] C. H. Lee, “Picosecond optoelectronic switching in GaAs,” *Appl. Phys. Lett.*, vol. 30, no. 2, pp. 84–86, 1977.
- [31] M. Tani, S. Matsuura, K. Sakai, and S. Nakashima, “Emission characteristics of photoconductive antennas based on low-temperature-grown GaAs and semi-insulating GaAs,” *Appl. Opt.*, vol. 36, no. 30, pp. 7853–7859, 1997.
- [32] Y. C. Shen *et al.*, “Generation and detection of ultrabroadband terahertz radiation using photoconductive emitters and receivers,” *Appl. Phys. Lett.*, vol. 85, no. 2, pp. 164–166, 2004.
- [33] D. H. Auston, “Picosecond semiconductor electronic switch controlled by optical means,” US 3,917,943, 1975.
- [34] S. Matsuura, M. Tani, and K. Sakai, “Generation of coherent terahertz radiation by photomixing in dipole photoconductive antennas,” *Appl. Phys. Lett.*, vol. 70, no. 5, pp. 559–561, 1997.
- [35] Q. Wu and X. C. Zhang, “Free-space electro-optic sampling of terahertz beams,” *Appl. Phys. Lett.*, vol. 67, no. 1995, pp. 3523–3525, 1995.
- [36] A. Nahata, D. H. Auston, T. F. Heinz, and C. Wu, “Coherent detection of freely propagating terahertz radiation by electro-optic sampling,” *Appl. Phys. Lett.*, vol. 68, no. 2, pp. 150–152, 1996.
- [37] Y. S. Lee, *Principles of terahertz science and technology*. Springer Science+Business Media, LLC, 2009.

- [38] J.-H. Son, *Terahertz Biomedical Science and Technology*. CRC Press, 2014.
- [39] M. Stellmacher, J. P. Schnell, D. Adam, and J. Nagle, "Photoconductivity investigation of the electron dynamics in GaAs grown at low temperature," *Appl. Phys. Lett.*, vol. 74, no. 9, pp. 1239–1241, 1999.
- [40] M. Scheller, "Data extraction from terahertz time domain spectroscopy measurements," *J. Infrared, Millimeter, Terahertz Waves*, vol. 35, no. 8, pp. 638–648, 2014.
- [41] I. Pupeza, R. Wilk, and M. Koch, "Highly accurate optical material parameter determination with THz time-domain spectroscopy," *Opt. Express*, vol. 15, no. 7, pp. 4335–4350, 2007.
- [42] J. P. Guillet *et al.*, "Review of terahertz tomography techniques," *J. Infrared, Millimeter, Terahertz Waves*, vol. 35, no. 4, pp. 382–411, 2014.
- [43] V. P. Wallace, E. MacPherson, J. A. Zeitler, and C. Reid, "Three-dimensional imaging of optically opaque materials using nonionizing terahertz radiation," *J. Opt. Soc. Am. A*, vol. 25, no. 12, p. 3120, 2008.
- [44] D. M. Mittleman, S. Hunsche, L. Boivin, and M. C. Nuss, "T-ray tomography," in *Optics letters*, 1997, vol. 22, no. 12, pp. 904–906.
- [45] K. Su, Y. C. Shen, and J. A. Zeitler, "Terahertz sensor for non-contact thickness and quality measurement of automobile paints of varying complexity," *IEEE Trans. Terahertz Sci. Technol.*, vol. 4, no. 4, pp. 432–439, 2014.
- [46] Y. C. Shen and P. F. Taday, "Development and application of terahertz pulsed imaging for nondestructive inspection of pharmaceutical tablet," *IEEE J. Sel. Top. Quantum Electron.*, vol. 14, no. 2, pp. 407–415, 2008.
- [47] B. B. Hu and M. C. Nuss, "Imaging with terahertz waves," *Opt. Lett.*, vol. 20, no. 16, pp. 1716–1718, 1995.
- [48] J. Dong *et al.*, "Terahertz frequency-wavelet domain deconvolution for stratigraphic and subsurface investigation of art painting," *Opt. Express*, vol. 24, no. 23, pp. 26972–26985, 2016.
- [49] J. Dong, A. Locquet, M. Melis, and D. S. Citrin, "Global mapping of stratigraphy of an old-master painting using sparsity-based terahertz reflectometry," *Sci. Rep.*, vol. 7, no. 1, pp. 1–12, 2017.
- [50] D. M. Mittleman, M. Gupta, R. Neelamani, R. G. Baraniuk, J. V Rudd, and M. Koch, "Recent

- advances in terahertz imaging,” *Appl. Phys. B Lasers Opt.*, vol. 68, no. 6, pp. 1085–1094, 1999.
- [51] B. E. Cole, R. M. Woodward, D. A. Crawley, V. P. Wallace, D. D. Arnone, and M. Pepper, “Terahertz imaging and spectroscopy of human skin in vivo,” *Proc. SPIE - Int. Soc. Opt. Eng.*, vol. 4276, pp. 1–10, 2001.
- [52] N. J. Crane, S. W. Huffman, F. A. Gage, I. W. Levin, and E. A. Elster, “Evidence of a heterogeneous tissue oxygenation : renal ischemia / reperfusion injury in a large animal,” *J. Biomed. Opt.*, vol. 18, no. 3, pp. 035001–7, 2003.
- [53] R. M. Woodward *et al.*, “Terahertz pulse imaging of ex vivo basal cell carcinoma,” *J. Invest. Dermatol.*, vol. 120, no. 1, pp. 72–78, 2003.
- [54] V. P. Wallace *et al.*, “Terahertz pulsed imaging of basal cell carcinoma ex vivo and in vivo,” *Br. J. Dermatol.*, vol. 151, no. 2, pp. 424–432, 2004.
- [55] Y. Bin Ji *et al.*, “Feasibility of terahertz reflectometry for discrimination of human early gastric cancers,” *Biomed. Opt. Express*, vol. 6, no. 4, pp. 1398–1406, 2015.
- [56] T. C. Bowman, M. El-Shenawee, and L. K. Campbell, “Terahertz Imaging of Excised Breast Tumor Tissue on Paraffin Sections,” *IEEE Trans. Antennas Propag.*, vol. 63, no. 5, pp. 2088–2097, 2015.
- [57] S. J. Oh *et al.*, “Nanoparticle-enabled terahertz imaging for cancer diagnosis,” *Opt. Express*, vol. 17, no. 5, pp. 3469–3475, 2009.
- [58] S. J. Oh *et al.*, “Molecular imaging with terahertz waves,” *Opt. Express*, vol. 19, no. 5, pp. 4009–4016, 2011.
- [59] S. J. Oh, Y.-M. Huh, J.-S. Suh, J. Choi, S. Haam, and J.-H. Son, “Cancer Diagnosis by Terahertz Molecular Imaging Technique,” *J. Infrared, Millimeter, Terahertz Waves*, vol. 33, no. 1, pp. 74–81, 2012.
- [60] R. Naccache *et al.*, “Terahertz Thermometry: Combining Hyperspectral Imaging and Temperature Mapping at Terahertz Frequencies,” *Laser Photon. Rev.*, vol. 11, no. 5, p. 1600342, 2017.
- [61] K. Gajanan and S. N. Tijare, “Applications of nanomaterials,” in *Materials Today: Proceedings*, 2018, pp. 1093–1096.
- [62] M. Pelton and G. Bryant, *Introduction to Metal-Nanoparticle Plasmonics*. Wiley, 2013.

- [63] S. Kawata, Y. Inouye, and P. Verma, "Plasmonics for near-field nano-imaging and superlensing," *Nature Photonics*, vol. 3, no. 7, pp. 388–394, 2009.
- [64] S. Schlücker, "Surface-enhanced raman spectroscopy: Concepts and chemical applications," *Angew. Chemie - Int. Ed.*, no. 53, pp. 2–42, 2014.
- [65] L. V. Besteiro *et al.*, "The fast and the furious: Ultrafast hot electrons in plasmonic metastructures. Size and structure matter," *Nano Today*, vol. 27, pp. 120–145, 2019.
- [66] L. A. Lane, X. Qian, and S. Nie, "SERS Nanoparticles in Medicine: From Label-Free Detection to Spectroscopic Tagging," *Chem. Rev.*, vol. 115, no. 19, pp. 10489–10529, 2015.
- [67] K. Ataka, S. T. Stripp, and J. Heberle, "Surface-enhanced infrared absorption spectroscopy (SEIRAS) to probe monolayers of membrane proteins," *Biochim. Biophys. Acta - Biomembr.*, vol. 1828, no. 10, pp. 2283–2293, 2013.
- [68] A. Toma *et al.*, "Squeezing terahertz light into nanovolumes: Nanoantenna enhanced terahertz spectroscopy (NETS) of semiconductor quantum dots," *Nano Lett.*, vol. 15, no. 1, pp. 386–391, 2015.
- [69] R. Naccache *et al.*, "High resolution fluorescence imaging of cancers using lanthanide ion-doped upconverting nanocrystals," *Cancers (Basel)*, no. 4, pp. 1067–1105, 2012.
- [70] R. D. Near, S. C. Hayden, R. E. Hunter, D. Thackston, and M. A. El-Sayed, "Rapid and efficient prediction of optical extinction coefficients for gold nanospheres and gold nanorods," *J. Phys. Chem. C*, vol. 117, no. 45, pp. 23950–23955, 2013.
- [71] P. K. Jain, K. S. Lee, I. H. El-sayed, and M. A. El-sayed, "Calculated Absorption and Scattering Properties of Gold Nanoparticles of Different Size, Shape, and Composition: Applications in Biological Imaging and Biomedicine," *J. Phys. Chem. B*, vol. 14, no. 110, pp. 7238–7248, 2006.
- [72] P. K. Jain, X. Huang, I. H. El-Sayed, and M. A. El-Sayed, "Noble metals on the nanoscale: Optical and photothermal properties and some applications in imaging, sensing, biology, and medicine," *Acc. Chem. Res.*, vol. 41, no. 12, pp. 1578–1586, 2008.
- [73] P. N. Njoki *et al.*, "Size correlation of optical and spectroscopic properties for gold nanoparticles," *J. Phys. Chem. C*, vol. 111, no. 40, pp. 14664–14669, 2007.
- [74] M. F. Tsai *et al.*, "Au nanorod design as light-absorber in the first and second biological near-infrared windows for in vivo photothermal therapy," *ACS Nano*, vol. 7, no. 6, pp. 5330–

- 5342, 2013.
- [75] K. L. Kelly, E. Coronado, L. L. Zhao, and G. C. Schatz, "The Optical Properties of Metal Nanoparticles: The Influence of Size, Shape, and Dielectric Environment," *J. Phys. Chem. B*, vol. 107, no. 3, pp. 668–677, 2003.
- [76] L. Vigderman and E. R. Zubarev, "Therapeutic platforms based on gold nanoparticles and their covalent conjugates with drug molecules," *Adv. Drug Deliv. Rev.*, vol. 65, no. 5, pp. 663–676, 2013.
- [77] Y. Liu, P. Bhattarai, Z. Dai, and X. Chen, "Photothermal therapy and photoacoustic imaging: Via nanotheranostics in fighting cancer," *Chem. Soc. Rev.*, vol. 48, no. 7, pp. 2053–2108, 2019.
- [78] J. A. Yang, S. E. Lohse, and C. J. Murphy, "Tuning cellular response to nanoparticles via surface chemistry and aggregation," *Small*, vol. 10, no. 8, pp. 1642–1651, 2014.
- [79] J. V. Jokerst, T. Lobovkina, R. N. Zare, and S. S. Gambhir, "Nanoparticle PEGylation for imaging and therapy," *Nanomedicine*, vol. 6, no. 4, pp. 715–728, 2012.
- [80] X.-M. Zhu *et al.*, "Cellular uptake behaviour, photothermal therapy performance, and cytotoxicity of gold nanorods with various coatings," *Nanoscale*, vol. 6, no. 19, pp. 11462–11472, 2014.
- [81] M. Almada *et al.*, "Photothermal conversion efficiency and cytotoxic effect of gold nanorods stabilized with chitosan, alginate and poly(vinyl alcohol)," *Mater. Sci. Eng. C*, vol. 77, pp. 583–593, 2017.
- [82] G. Chen, I. Roy, C. Yang, and P. N. Prasad, "Nanochemistry and Nanomedicine for Nanoparticle-based Diagnostics and Therapy," *Chem. Rev.*, vol. 5, no. 116, pp. 2826–2885, 2016.
- [83] J. Cao, T. Sun, and K. T. V. Grattan, "Gold nanorod-based localized surface plasmon resonance biosensors: A review," *Sensors Actuators, B Chem.*, vol. 195, pp. 332–351, 2014.
- [84] S. A. Maier, *Plasmonics: fundamentals and applications*. Springer Science+Business Media, LLC, 2007.
- [85] V. Amendola, R. Pilot, M. Frasconi, O. M. Maragò, and M. A. Iati, "Surface plasmon resonance in gold nanoparticles: a review," *J. Phys. Condens. Matter*, vol. 29, no. 20, p. 203002, 2017.

- [86] K. A. Willets and R. P. Van Duyne, "Localized Surface Plasmon Resonance Spectroscopy and Sensing," *Annu. Rev. Phys. Chem.*, no. 58, pp. 267–297, 2007.
- [87] G. V Hartland, "Optical studies of dynamics in noble metal nanostructures," *Chem. Rev.*, vol. 111, no. 6, pp. 3858–3887, 2011.
- [88] L. Dykman and N. Khlebtsov, *Gold Nanoparticles in Biomedical Applications*. CRC Press, 2018.
- [89] L. M. Maestro *et al.*, "Gold nanorods for optimized photothermal therapy: the influence of irradiating in the first and second biological windows," *RSC Adv.*, vol. 4, no. 96, pp. 54122–54129, 2014.
- [90] A. M. Smith, M. C. Mancini, and S. Nie, "Bioimaging: Second window for in vivo imaging," *Nat. Nanotechnol.*, vol. 4, no. 11, pp. 710–711, 2009.
- [91] H. Chen *et al.*, "Understanding the photothermal conversion efficiency of gold nanocrystals," *Small*, vol. 6, no. 20, pp. 2272–2280, 2010.
- [92] O. A. Savchuk, J. J. Carvajal, J. Massons, M. Aguiló, and F. Díaz, "Determination of photothermal conversion efficiency of graphene and graphene oxide through an integrating sphere method," *Carbon N. Y.*, vol. 103, pp. 134–141, 2016.
- [93] D. K. Roper, W. Ahn, and M. Hoepfner, "Microscale heat transfer transduced by surface plasmon resonant gold nanoparticles," *J. Phys. Chem. C*, vol. 111, no. 9, pp. 3636–3641, 2007.
- [94] V. P. Pattani and J. W. Tunnell, "Nanoparticle-mediated photothermal therapy: A comparative study of heating for different particle types," *Lasers Surg. Med.*, vol. 44, no. 8, pp. 675–684, 2012.
- [95] R. Marin *et al.*, "Highly Efficient Copper Sulfide-Based Near-Infrared Photothermal Agents: Exploring the Limits of Macroscopic Heat Conversion," *Small*, vol. 14, no. 49, pp. 1–9, 2018.
- [96] F. Novelli, J. W. M. Chon, and J. A. Davis, "Terahertz thermometry of gold nanospheres in water," *Opt. Lett.*, vol. 41, no. 24, pp. 5801–5804, 2016.
- [97] D. Jaque and F. Vetrone, "Luminescence nanothermometry," *Nanoscale*, vol. 4, no. 15, pp. 4301–4326, 2012.
- [98] J.-R. Macairan, D. B. Jaunky, A. Piekny, and R. Naccache, "Intracellular ratiometric

- temperature sensing using fluorescent carbon dots,” *Nanoscale Adv.*, vol. 1, no. 1, pp. 105–113, 2019.
- [99] R. Urie, S. Quraishi, M. Jaffe, and K. Rege, “Gold Nanorod-Collagen Nanocomposites as Photothermal Nanosolders for Laser Welding of Ruptured Porcine Intestines,” *ACS Biomater. Sci. Eng.*, vol. 1, no. 9, pp. 805–815, 2015.
- [100] N. K. Rajendran, S. S. D. Kumar, N. N. Houreld, and H. Abrahamse, “A review on nanoparticle based treatment for wound healing,” *J. Drug Deliv. Sci. Technol.*, vol. 44, no. 10, pp. 421–430, 2018.
- [101] P. Matteini, F. Ratto, F. Rossi, and R. Pini, “Emerging concepts of laser-activated nanoparticles for tissue bonding,” *J. Biomed. Opt.*, vol. 17, no. 1, p. 010701, 2012.
- [102] A. J. Kirsch *et al.*, “Skin flap closure by dermal laser soldering: A wound healing model for sutureless hypospadias repair,” *Urology*, vol. 50, no. 2, pp. 263–272, 1997.
- [103] A. Capon *et al.*, “Laser assisted skin closure (LASC) by using a 815-nm diode-laser system accelerates and improves wound healing,” *Lasers Surg. Med.*, vol. 28, no. 2, pp. 168–175, 2001.
- [104] M. Gulsoy, Z. Dereli, H. O. Tabakoglu, and O. Bozkulak, “Closure of skin incisions by 980-nm diode laser welding,” *Lasers Med. Sci.*, vol. 21, no. 1, pp. 5–10, 2006.
- [105] L. Hu *et al.*, “Closure of skin incisions by laser-welding with a combination of two near-infrared diode lasers: preliminary study for determination of optimal parameters,” *J. Biomed. Opt.*, vol. 16, no. 3, p. 038001, 2011.
- [106] B. H. Al-jarrah and A. S. Mahmood, “Tissue Welding Using ($800 \pm 10\text{nm}$) Diode and (1064nm) Nd : YAG Lasers,” *Iraqi J. Laser*, vol. 14, pp. 19–24, 2015.
- [107] K. McNally, B. Sorg, W. AJ, J. Dawes, and E. Owen, “Photothermal effects of laser tissue soldering,” *Phys Med Biol.*, vol. 6, no. 44, pp. 983–1002, 1999.
- [108] M. Aliannezhadi, M. Minbashi, and V. V Tuchin, “Effect of laser intensity and exposure time on photothermal therapy with nanoparticles heated by a 793-nm diode laser and tissue optical clearing,” *Quantum Electron.*, vol. 48, no. 6, pp. 559–564, 2018.
- [109] C. S. Cooper, I. P. Schwartz, D. Suh, and A. J. Kirsch, “Optimal solder and power density for diode laser tissue soldering (LTS),” *Lasers Surg. Med.*, vol. 29, no. 1, pp. 53–61, 2001.
- [110] L. C. Fung, G. C. Mingin, M. Massicotte, D. Felsen, and D. P. Poppas, “Effects of

- temperature on tissue thermal injury and wound strength after photothermal wound closure,” *Lasers Surg. Med.*, vol. 25, no. 4, pp. 285–290, 1999.
- [111] N. M. Fried and J. T. Walsh, “Laser skin welding: In vivo tensile strength and wound healing results,” *Lasers Surg. Med.*, vol. 27, no. 1, pp. 55–65, 2000.
- [112] J. M. Massicotte, R. B. Stewart, and D. P. Poppas, “Effects of endogenous absorption in human albumin solder for acute laser wound closure,” *Lasers Surg. Med.*, vol. 23, no. 1, pp. 18–24, 1998.
- [113] M. S. Nourbakhsh and M. E. Khosroshahi, “An in-vitro investigation of skin tissue soldering using gold nanoshells and diode laser,” *Lasers Med. Sci.*, vol. 26, no. 1, pp. 49–55, 2011.
- [114] M. Khosroshahi and M. S. Nourbakhsh, “In vitro skin wound soldering using SiO₂/Au nanoshells and a diode laser,” *Med. Laser Appl.*, vol. 26, no. 1, pp. 35–42, 2011.
- [115] M. A. Ansari, M. Erfanzadeh, and E. Mohajerani, “Mechanisms of laser-tissue interaction: II. tissue thermal properties,” *J. Lasers Med. Sci.*, vol. 4, no. 3, pp. 99–106, 2013.
- [116] J. De Boer, S. Srinivas, A. Malekafzali, Z. Chen, and J. Nelson, “Imaging thermally damaged tissue by Polarization Sensitive Optical Coherence Tomography,” *Opt. Express*, vol. 3, no. 6, pp. 212–218, 1998.
- [117] J. C. Jeng *et al.*, “Laser Doppler imaging determines need for excision and grafting in advance of clinical judgment: A prospective blinded trial,” *Burns*, vol. 29, no. 7, pp. 665–670, 2003.
- [118] J. Miccio *et al.*, “Forward-looking infrared imaging predicts ultimate burn depth in a porcine vertical injury progression model,” *Burns*, vol. 42, no. 2, pp. 397–404, 2016.
- [119] J. D. Medina-Preciado, E. S. Kolosovas-Machuca, E. Velez-Gomez, A. Miranda-Altamirano, and F. J. González, “Noninvasive determination of burn depth in children by digital infrared thermal imaging,” *J. Biomed. Opt.*, vol. 18, no. 6, p. 061204, 2012.
- [120] M. Naftaly and R. Dudley, “Methodologies for determining the dynamic ranges and signal-to-noise ratios of terahertz time-domain spectrometers,” *Opt. Lett.*, vol. 34, no. 8, pp. 1213–1215, 2009.
- [121] S. Huang *et al.*, “Improved sample characterization in terahertz reflection imaging and spectroscopy,” *Opt. Express*, vol. 17, no. 5, pp. 3848–3854, 2009.
- [122] E. P. J. Parrott, S. M. Y. Sy, T. Blu, V. P. Wallace, and E. Pickwell-MacPherson, “Terahertz

- pulsed imaging in vivo: measurements and processing methods,” *J. Biomed. Opt.*, vol. 16, no. 10, p. 106010, 2011.
- [123] J. Dong, X. Wu, A. Locquet, and D. S. Citrin, “Terahertz Superresolution Stratigraphic Characterization of Multilayered Structures Using Sparse Deconvolution,” *IEEE Trans. Terahertz Sci. Technol.*, vol. 7, no. 3, pp. 260–267, 2017.
- [124] A. M. Bruckstein, D. L. Donoho, and M. Elad, “From Sparse Solutions of Systems of Equations to Sparse Modeling of Signals and Images,” *SIAM Rev.*, vol. 51, no. 1, pp. 34–81, 2009.
- [125] S. Gazit, A. Szameit, Y. C. Eldar, and M. Segev, “Super-resolution and reconstruction of sparse sub-wavelength images,” *Opt. Express*, vol. 17, no. 26, pp. 23920–23946, 2009.
- [126] Y. Shechtman, Y. C. Eldar, A. Szameit, and M. Segev, “Sparsity based sub-wavelength imaging with partially incoherent light via quadratic compressed sensing,” *Opt. Express*, vol. 19, no. 16, pp. 14807–14822, 2011.
- [127] T. Blumensath and M. E. Davies, “Iterative Thresholding for Sparse Approximations,” *J. Fourier Anal. Appl.*, vol. 14, no. 5–6, pp. 629–654, 2008.
- [128] I. Daubechies, M. Defrise, and C. De Mol, “An iterative thresholding algorithm for linear inverse problems with a sparsity constraint,” *Commun. Pure Appl. Math.*, vol. 57, no. 11, pp. 1413–1457, 2004.
- [129] Y. Chen, S. Huang, and E. Pickwell-MacPherson, “Frequency-wavelet domain deconvolution for terahertz reflection imaging and spectroscopy,” *Opt. Express*, vol. 18, no. 2, p. 1177, 2010.
- [130] J. Dong, A. Locquet, and D. S. Citrin, “Terahertz quantitative nondestructive evaluation of failure modes in polymer-coated steel,” *IEEE J. Sel. Top. Quantum Electron.*, vol. 23, no. 4, pp. 1–7, 2017.
- [131] N. Palka, R. Panowicz, M. Chalimoniuk, and R. Beigang, “Non-destructive evaluation of puncture region in polyethylene composite by terahertz and X-ray radiation,” *Compos. Part B Eng.*, vol. 92, pp. 315–325, 2016.
- [132] G. C. Walker *et al.*, “Terahertz deconvolution,” *Opt. Express*, vol. 20, no. 25, p. 27230, 2012.
- [133] J. Dong, A. Locquet, and D. S. Citrin, “Depth resolution enhancement of terahertz deconvolution by autoregressive spectral extrapolation,” *Opt. Lett.*, vol. 42, no. 9, pp. 1828–

1831, 2017.

- [134] J. R. Fletcher, G. P. Swift, D. Dai, J. M. Chamberlain, and P. C. Upadhyaya, "Pulsed terahertz signal reconstruction," *J. Appl. Phys.*, vol. 102, no. 11, 2007.
- [135] B. Ferguson and D. Abbott, "De-noising techniques for terahertz responses of biological samples," *Microelectronics J.*, vol. 32, no. 12, pp. 943–953, 2001.
- [136] J. Dong, A. Locquet, and D. S. Citrin, "Enhanced Terahertz Imaging of Small Forced Delamination in Woven Glass Fibre-reinforced Composites with Wavelet De-noising," *J. Infrared, Millimeter, Terahertz Waves*, vol. 37, no. 3, pp. 289–301, 2016.
- [137] H. Breitenborn *et al.*, "Quantifying the photothermal conversion efficiency of plasmonic nanoparticles by means of terahertz radiation," *APL Photonics*, vol. 4, no. 12, p. 126106, 2019.
- [138] G. Margheri, S. Trigari, M. Berti, M. Muniz Miranda, and R. Traversi, "Chitosan-Capped Au Nanoparticles for Laser Photothermal Ablation Therapy: UV-Vis Characterization and Optothermal Performances," *J. Spectrosc.*, vol. 2018, pp. 1–11, 2018.
- [139] D. B. Peckys and N. De Jonge, "Visualizing Gold Nanoparticle Uptake in Live Cells with Liquid," *Nano Lett.*, vol. 11, pp. 1733–1738, 2011.
- [140] V. S. R. Aaryasomayajula *et al.*, "Assembly of a Dual Aptamer Gold Nanoparticle Conjugate Ensemble in the Specific Detection of Thrombin when Coupled with Dynamic Light Scattering Spectroscopy," *J. Nanomed. Nanotechnol.*, vol. 5, no. 4, p. 1000210, 2014.
- [141] C. S. Kim *et al.*, "Co-Delivery of protein and small molecule therapeutics using nanoparticle-stabilized nanocapsules," *Bioconjug. Chem.*, vol. 26, no. 5, pp. 950–954, 2015.
- [142] X. Chen, E. P. J. Parrott, B. S. Y. Ung, and E. Pickwell-MacPherson, "A Robust Baseline and Reference Modification and Acquisition Algorithm for Accurate THz Imaging," *IEEE Trans. Terahertz Sci. Technol.*, vol. 7, no. 5, pp. 493–501, 2017.
- [143] S. Fan, E. P. J. Parrott, B. S. Y. Ung, and E. Pickwell-MacPherson, "Calibration method to improve the accuracy of THz imaging and spectroscopy in reflection geometry," *Photonics Res.*, vol. 4, no. 3, pp. A29–A35, 2016.
- [144] H. H. Richardson, M. T. Carlson, P. J. Tandler, P. Hernandez, and A. O. Govorov, "Experimental and theoretical studies of light-to-heat conversion and collective heating effects in metal nanoparticle solutions," *Nano Lett.*, vol. 9, no. 3, pp. 1139–1146, 2009.

- [145] J. R. Cole, N. a Mirin, M. W. Knight, G. P. Goodrich, and N. J. Halas, "Photothermal Efficiencies of Nanoshells and Nanorods for Clinical Therapeutic Applications," *J. Phys. Chem. C*, no. 113, pp. 12090–12094, 2009.
- [146] L. Kou, D. Labrie, and P. Chylek, "Refractive indices of water and ice in the 065- to 25- μ m spectral range," *Appl. Opt.*, vol. 32, no. 19, pp. 3531–3540, 1993.
- [147] P. B. Johnson and R. W. Christy, "Optical constants of the noble metals," *Phys. Rev. B*, vol. 6, no. 12, pp. 4370–4379, 1972.
- [148] Y. Li, W. Lu, Q. Huang, C. Li, and W. Chen, "Copper sulfide nanoparticles for photothermal ablation of tumor cells," *Nanomedicine*, vol. 5, no. 8, pp. 1161–1171, 2010.
- [149] J. M. Luther, P. K. Jain, T. Ewers, and A. P. Alivisatos, "Localized surface plasmon resonances arising from free carriers in doped quantum dots," *Nat. Mater.*, vol. 10, no. 5, pp. 361–366, 2011.
- [150] C. I. Pearce, R. A. D. Pattrick, and D. J. Vaughan, "Electrical and magnetic properties of sulfides," *Reviews in Mineralogy and Geochemistry*, vol. 61. pp. 127–180, 2006.
- [151] H. Nozaki, K. Shibata, and N. Ohhashi, "Metallic hole conduction in CuS," *J. Solid State Chem.*, vol. 91, no. 2, pp. 306–311, 1991.
- [152] J.-E. Park, M. Kim, J.-H. Hwang, and J.-M. Nam, "Golden Opportunities: Plasmonic Gold Nanostructures for Biomedical Applications based on the Second Near-Infrared Window," *Small Methods*, vol. 1, no. 3, p. 1600032, 2017.
- [153] X. Ding *et al.*, "Surface plasmon resonance enhanced light absorption and photothermal therapy in the second near-infrared window," *J. Am. Chem. Soc.*, vol. 136, no. 44, pp. 15684–15693, 2014.
- [154] J. Wang *et al.*, "The Role of Micelle Size in Tumor Accumulation, Penetration, and Treatment," *ACS Nano*, vol. 9, no. 7, pp. 7195–7206, 2015.
- [155] C. Vicario, B. Monoszlai, and C. P. Hauri, "GV/ m single-cycle terahertz fields from a laser-driven large-size partitioned organic crystal," *Phys. Rev. Lett.*, vol. 112, no. 21, pp. 1–5, 2014.
- [156] Y. T. Chang, K. W. Su, H. L. Chang, and Y. F. Chen, "Compact efficient Q-switched eye-safe laser at 1525 nm with a double-end diffusion-bonded Nd:YVO₄ crystal as a self-Raman medium," *Opt. Express*, vol. 17, no. 6, pp. 4330–4335, 2009.

- [157] A. Markov *et al.*, “Broadband and efficient adiabatic three-wave-mixing in a temperature-controlled bulk crystal,” *Opt. Express*, vol. 26, no. 4, pp. 4448–4458, 2018.
- [158] A. G. Ciriolo *et al.*, “Optical parametric amplification techniques for the generation of high-energy few-optical-cycles IR pulses for strong field applications,” *Appl. Sci.*, vol. 7, no. 3, 2017.
- [159] O. Yaakobi, M. Clerici, L. Caspani, F. Vidal, and R. Morandotti, “Complete pump depletion by autoresonant second harmonic generation in a nonuniform medium,” *J. Opt. Soc. Am. B*, vol. 30, no. 6, pp. 1637–1642, 2013.
- [160] O. Yaakobi, L. Caspani, M. Clerici, F. Vidal, and R. Morandotti, “Complete energy conversion by autoresonant three-wave mixing in nonuniform media,” *Opt. Express*, vol. 21, no. 2, pp. 1623–1632, 2013.
- [161] O. Y. Jeon, M. J. Jin, H. H. Lim, B. J. Kim, and M. Cha, “Broadband optical parametric generation in the telecommunication band and simultaneous RGB generation by quasi-phase-matched parametric conversion processes,” *J. Korean Phys. Soc.*, vol. 49, pp. 589–591, 2006.
- [162] H. Suchowski, D. Oron, A. Arie, and Y. Silberberg, “Geometrical representation of sum frequency generation and adiabatic frequency conversion,” *Phys. Rev. A*, vol. 78, no. 6, pp. 1–5, 2008.
- [163] O. Yaakobi and L. Friedland, “Autoresonant four-wave mixing in optical fibers,” *Phys. Rev. A - At. Mol. Opt. Phys.*, vol. 82, no. 2, 2010.
- [164] W. Boyd, R. *Nonlinear Optics*. Academic Press, 2008.
- [165] M. M. Fejer, D. H. Jundt, R. L. Byer, and G. A. Magel, “Quasi-Phase-Matched Second Harmonic Generation: Tuning and Tolerances,” *IEEE J. Quantum Electron.*, vol. 28, no. 11, pp. 2631–2654, 1992.
- [166] J. Dong *et al.*, “Terahertz Three-dimensional Monitoring of Nanoparticle-assisted Laser Tissue Soldering,” *Biomed. Opt. Express*, vol. 11, no. 4, pp. 2254–2267, 2020.
- [167] R. R. Anderson and J. A. Parrish, “Selective photothermolysis: precise microsurgery by selective absorption of pulsed radiation,” *Sci. AAAS*, vol. 220, no. 4596, pp. 524–527, 1983.
- [168] D. Jaque *et al.*, “Nanoparticles for photothermal therapies,” *Nanoscale*, vol. 6, no. 16, pp. 9494–9530, 2014.

- [169] M. Mushaben, R. Urie, T. Flake, M. Jaffe, K. Rege, and J. Heys, "Spatiotemporal modeling of laser tissue soldering using photothermal nanocomposites," *Lasers Surg. Med.*, vol. 50, no. 2, pp. 143–152, 2018.
- [170] K. M. McNally, B. S. Sorg, N. C. Bhavaraju, M. G. Ducros, A. J. Welch, and J. M. Dawes, "Optical and thermal characterization of albumin protein solders," *Appl. Opt.*, vol. 38, no. 31, pp. 6661–6672, 1999.
- [171] Y. Ren, H. Qi, Q. Chen, and L. Ruan, "Thermal dosage investigation for optimal temperature distribution in gold nanoparticle enhanced photothermal therapy," *Int. J. Heat Mass Transf.*, vol. 106, pp. 212–221, 2017.
- [172] U. Jacobi *et al.*, "Porcine ear skin: An in vitro model for human skin," *Ski. Res. Technol.*, vol. 13, no. 1, pp. 19–24, 2007.
- [173] X. Li, X. Fu, J. Liu, Y. Du, and Z. Hong, "Investigation of thermal denaturation of solid bovine serum albumin by terahertz dielectric spectroscopy," *J. Mol. Struct.*, vol. 1049, pp. 441–445, 2013.
- [174] D. B. Bennett, W. Li, Z. D. Taylor, W. S. Grundfest, and E. R. Brown, "Stratified media model for Terahertz reflectometry of the skin," *IEEE Sens. J.*, vol. 11, no. 5, pp. 1253–1262, 2011.
- [175] P. Tewari *et al.*, "In vivo terahertz imaging of rat skin burns," *J. Biomed. Opt.*, vol. 17, no. 4, p. 040503, 2012.
- [176] J. Jiao and Z. Guo, "Thermal interaction of short-pulsed laser focused beams with skin tissues," *Phys. Med. Biol.*, vol. 54, no. 13, pp. 4225–4241, 2009.
- [177] L. Zanotto, R. Piccoli, J. Dong, D. Caraffini, R. Morandotti, and L. Razzari, "Time-domain terahertz compressive imaging," *Opt. Express*, vol. 28, no. 3, p. 3795, 2020.
- [178] C. Fornaini *et al.*, "Hard dental tissues laser welding: A new help for fractured teeth? a preliminary ex vivo study," *Laser Ther.*, vol. 27, no. 2, pp. 105–110, 2018.
- [179] J. Ryu *et al.*, "Diagnosis of dental cavity and osteoporosis using terahertz transmission images," *Springer Ser. Chem. Phys.*, 2001.
- [180] M. Plazanet *et al.*, "Time-domain THz spectroscopy of the characteristics of hydroxyapatite provides a signature of heating in bone tissue," *PLoS One*, vol. 13, no. 8, 2018.
- [181] R. Urie *et al.*, "Rapid Soft Tissue Approximation and Repair Using Laser-Activated Silk

- Nanosealants,” *Adv. Funct. Mater.*, vol. 1802874, pp. 1–11, 2018.
- [182] S. Basov *et al.*, “Robot-assisted laser tissue soldering system,” *Biomed. Opt. Express*, vol. 9, no. 11, p. 5635, 2018.
- [183] World Health Organisation, “Latest global cancer data: Cancer burden rises to 18.1 million new cases and 9.6 million cancer deaths in 2018,” *Int. Agency Res. Cancer*, 2018.

6 ANNEX I

6.1 Articles Published in Peer-Reviewed Scientific Journals

- [1] **H. Breitenborn**, J. Dong, R. Piccoli, A. Bruhacs, L.V. Besteiro, A. Skripka, Z.M. Wang, A.O. Govorov, L. Razzari, F. Vetrone, R. Naccache, and R. Morandotti, “Quantifying the Photothermal Conversion Efficiency of Plasmonic Nanoparticles by means of Terahertz Radiation,” *APL Photonics*, vol. 4, no. 12, 126106 (2019). Featured article with a press release
- [2] J. Dong, **H. Breitenborn**, R. Piccoli, L.V. Besteiro, P. You, D. Caraffini, Z.M. Wang, A.O. Govorov, R. Naccache, F. Vetrone, L. Razzari, and R. Morandotti, “Terahertz Three-dimensional Monitoring of Nanoparticle-assisted Laser Tissue Soldering,” *Biomedical Optics Express*, vol. 11, no. 4, pp. 2254 - 2267 (2020).
- [3] A. Markov, A. Mazhorova, **H. Breitenborn**, A. Bruhacs, M. Clerici, D. Modotto, O. Jedrkiewicz, P. Di Trapani, A. Major, F. Vidal, and Roberto Morandotti, “Broadband and efficient adiabatic three-wave-mixing in a temperature-controlled bulk crystal,” *Optics Express*, vol. 26, no. 4, pp. 4448–4458 (2018).

6.2 Conference Proceedings

- [1] J. Dong, **H. Breitenborn**, D. Caraffini, R. Piccoli, A.O. Govorov, L. Razzari, R. Naccache, F. Vetrone, and R. Morandotti, “Investigation of Nanoparticle-assisted Laser Tissue Soldering by Terahertz Radiation,” *CLEO/Europe-EQEC*, Munich, Germany (2019).
- [2] **H. Breitenborn**, J. Dong, R. Piccoli, D. Caraffini, L. Razzari, F. Vetrone, R. Naccache, and R. Morandotti, “Terahertz Subsurface Imaging of Nanoparticle-mediated Plasmonic Heating in Skin,” *Photonics North*, Quebec, Canada (2019).
- [3] **H. Breitenborn**, J. Dong, A. Bruhacs, D. Caraffini, R. Piccoli, R. Marin, A. Skripka, F. Vetrone, L. Razzari, R. Naccache, and R. Morandotti, “Characterization of the Photothermal Heating Properties of Nanoparticles by Terahertz Radiation,” *Photonics North*, Montreal, (2018).
- [4] L. Zanotto, R. Piccoli, J. Dong, **H. Breitenborn**, R. Naccache, R. Morandotti, and L. Razzari, “Single-Pixel Terahertz Imaging Using a Time-Domain Spectroscopy Setup,” *Photonics North*, Montreal, (2018).

- [5] **H. Breitenborn**, R. Naccache, A. Mazhorova, M. Clerici, R. Piccoli, L.K. Khorashad, A.O. Govorov, L. Razzari, F. Vetrone, and R. Morandotti, "Terahertz Spectral Imaging and Thermal Sensing for Biomedical Applications," IRMMW-THz, Cancun, Mexico (2017).
- [6] A. Markov, A. Mazhorova, **H. Breitenborn**, A. Bruhacs, M. Clerici, D. Modotto, O. Jedrkiewicz, P. Di Trapani, A. Major, F. Vidal, and R. Morandotti, "Adiabatic Broadband Optical Parametric Amplification in Crystals with a Temperature Gradient," Photonics North, Ottawa, Canada (2017).
- [7] **H. Breitenborn**, R. Naccache, A. Mazhorova, M. Clerici, R. Piccoli, L.K. Khorashad, A.O. Govorov, L. Razzari, F. Vetrone, and R. Morandotti, "Temperature and Spectral Mapping at Terahertz Frequencies," Photonics North, Ottawa, Canada (2017).
- [8] A. Markov, A. Mazhorova, **H. Breitenborn**, A. Bruhacs, M. Clerici, D. Modotto, O. Jedrkiewicz, P. Di Trapani, A. Major, F. Vidal, and R. Morandotti, "Efficient Broadband Optical Parametric Amplification in Non-uniform Bulk Crystals," CLEO, San Jose, USA (2017).
- [9] **H. Breitenborn**, R. Naccache, A. Mazhorova, M. Clerici, R. Piccoli, L.K. Khorashad, A.O. Govorov, L. Razzari, F. Vetrone, and R. Morandotti, "Multi-dimensional Imaging in the Terahertz Regime for Theranostic Applications," CLEO, San Jose, USA (2017).
- [10] **H. Breitenborn**, R. Naccache, A. Mazhorova, M. Clerici, R. Piccoli, L.K. Khorashad, A.O. Govorov, L. Razzari, F. Vetrone, and R. Morandotti, "Spectral and Thermal Imaging at Terahertz Frequencies for Biomedical Applications," CREATE Autumn Conference of the Université Laval, Quebec, Canada (2017).
- [11] **H. Breitenborn**, A. Mazhorova, R. Naccache, M. Clerici, L.K. Khorashad, A.O. Govorov, L. Razzari, F. Vetrone, and R. Morandotti, "Spatial Mapping of Nanoplasmonic-Induced Photothermal Effects in the THz Regime," Plasma-Quebec, Montreal, Canada (2016).
- [12] **H. Breitenborn**, A. Mazhorova, R. Naccache, M. Clerici, L.K. Khorashad, A.O. Govorov, L. Razzari, F. Vetrone, and R. Morandotti, "Spatial Mapping of Nanoplasmonic-Induced Photothermal Effects in the THz Regime," Photonics North, Quebec, Canada (2016).
- [13] **H. Breitenborn**, A. Mazhorova, R. Naccache, M. Clerici, L.K. Khorashad, A.O. Govorov, L. Razzari, F. Vetrone, and R. Morandotti, "THz Spatial Mapping of Photothermal Effects," IONS International OSA Conference, Quebec, Canada (2016)
- [14] R. Naccache, A. Mazhorova, M. Clerici, **H. Breitenborn**, L. Khorashad, A. Govorov, L. Razzari, F. Vetrone, and R. Morandotti, "Nanoparticles as "Contrast Agents" in Imaging Applications," 9th International Conference on High Temperature Ceramic Matrix Composites (HTCMC-9) & Global Forum on Advanced Materials and Technologies for Sustainable Development (GFMAT), Toronto, Canada (2016).

- [15] A. Tomasino, M.K. Mridha, A. Mazhorova, D. Caraffini, **H. Breitenborn**, M. Clerici, M. Peccianti, L. Razzari, A.C. Cino, S. Stivala, A. Busacca, and R. Morandotti, "Waveguide-Integrated THz Spectral Filter," Photonics North 2015, Ottawa, Canada (2015).
- [16] A. Tomasino, M.K. Mridha, A. Mazhorova, D. Caraffini, **H. Breitenborn**, M. Clerici, M. Peccianti, L. Razzari, A.C. Cino, S. Stivala, A. Busacca, and R. Morandotti, "Two-Wire Waveguide-Based THz Spectral Filter," Colloque de Plasma-Quebec, Montreal, Canada (2015).
- [17] A. Tomasino, M.K. Mridha, A. Mazhorova, D. Caraffini, **H. Breitenborn**, M. Clerici, M. Peccianti, L. Razzari, A.C. Cino, S. Stivala, A. Busacca, and R. Morandotti, "Two-Wire Waveguide-Based THz Spectral Filter," Fotonica 2015, Turin, Italy (2015).

6.3 Filed Patent

- [1] **H. Breitenborn**, J. Dong, R. Piccoli, L. Razzari, F. Vetrone, R. Naccache, and R. Morandotti, "Method for the Determination of the Photothermal Properties of Nanoparticles by Terahertz Radiation," US patent application 62/878,026 (2019).

SOMMAIRE RÉCAPITULATIF

1. Motivation et objectifs

La chaleur est l'énergie cinétique totale des particules d'un système, tandis que la température est une mesure de l'énergie cinétique moyenne des particules de ce système. Une compréhension approfondie des propriétés et de la répartition de la chaleur, non seulement à l'échelle macroscopique, mais aussi à l'échelle microscopique et nanométrique, augmentera la capacité des nouvelles applications de chauffage modernes dans lesquelles la conversion de l'énergie optique en énergie thermique dans des systèmes aqueux est requise, comme par exemple le traitement photo-thermique du cancer, la nano-chirurgie, l'administration de médicaments, l'imagerie photo-thermique, le suivi de protéines, l'imagerie photoacoustique, la nano-chimie et l'optofluidique [1], [2]. Les systèmes plasmoniques ouvrent la voie à la nanophotonique en raison de leur capacité unique à confiner l'énergie électromagnétique à des volumes extrêmement petits qui permettent une manipulation de la lumière à l'échelle nanométrique. Le chauffage à l'échelle nanométrique à l'aide de nanostructures métalliques, appelé thermo-plasmonique, a connu un essor considérable ces dernières années, car il fournit des sources de chaleur contrôlables à distance et à l'échelle nanométrique pour contrôler la température. Sous illumination avec des champs électromagnétiques intenses à sa résonance plasmonique, tels que ceux provenant de sources laser émettant de la lumière, une nanoparticule métallique (NP) présente une absorption lumineuse améliorée, la transformant en une nano-source de chaleur contrôlable à distance idéale pour les systèmes aqueux [3], [4]. Des travaux de recherche récents ont été consacrés à l'optimisation du rendement de conversion photo-thermique (Photothermal Conversion Efficiency - PCE) des NPs [5]–[8], quantifiant leur capacité à convertir la lumière en chaleur. Plus le PCE est élevé, plus la puissance laser et la dose de NPs nécessaires pour induire les effets de chauffage souhaités sont faibles, ce qui est particulièrement important pour les applications biomédicales dans les tissus. Cependant, même de nos jours, il est encore difficile de mesurer avec précision la température des dispersions de NPs dans des conditions d'obstruction. La mesure de la température et de la distribution thermique précises obtenues lors des procédures de chauffage et de refroidissement des dispersions de NPs est cruciale pour pouvoir déterminer le PCE afin de pouvoir comparer différentes NPs, par exemple en ce qui concerne les propriétés, la composition, la taille et la morphologie du matériau. Les méthodes conventionnelles de contact et de non-contact pour quantifier le PCE des dispersions de NPs sont peu pratiques et imprécises. Les méthodes de contact, par exemple les thermocouples [8], sont invasives, influencent la mesure et ne fonctionnent pas lorsque le

système aqueux est fermé et donc inaccessible. Les méthodes de mesure sans contact, utilisant par exemple des thermomètres à infrarouge (IR) [9], déterminent uniquement la température de surface du récipient contenant le système aqueux en ligne de mire, ce qui ne représente pas nécessairement la valeur de la température d'un liquide à l'intérieur du conteneur. De plus, la dispersion des NPs doit être uniformément homogénéisée à l'aide d'un agitateur magnétique pour obtenir une distribution de température égalisée, ce qui est invasif et peut donc entraîner une contamination. Durant cette thèse des sources de rayonnement laser pulsé récemment développées aux fréquences térahertz (THz) (plage de longueurs d'onde de 30 μm à 3 mm) [10], [11] ont été utilisées pour mesurer la température résolue dans le temps et dans l'espace à l'intérieur de récipients contenant des systèmes aqueux (chapitre 2). Le rayonnement THz a une faible énergie photonique et est donc de nature non-ionisante. De plus, il est très sensible aux changements d'indice de réfraction des systèmes à base d'eau en fonction de la température. Le rayonnement THz pulsé peut être détecté de manière cohérente, ce qui signifie que les informations d'amplitude et de phase résolues en temps sont accessibles pour la spectroscopie et les évaluations de temps de vol (Time of Flight - ToF) [12]. L'analyse ToF, combinée à la capacité du rayonnement THz à pénétrer dans des matériaux non métalliques et non-polaires, tels que les plastiques, permet de déterminer la température directement à l'interface entre un système aqueux et son récipient. Dans cette thèse, une nouvelle méthode a été conçue, et consiste à combiner des informations d'impulsions à fréquences THz résolues dans le temps et dans l'espace pour quantifier le PCE des dispersions de NPs dans des récipients sans nécessiter d'agitation. La technique exploite divers paramètres physiques intrinsèques du rayonnement THz pulsé, tels que l'amplitude, la fréquence, le ToF, ainsi que des informations spatiales pour la détermination précise du PCE des NPs dans des dispersions aqueuses. Comme référence bien étudiée pour corroborer la nouvelle méthode, des NPs d'or en forme de bâtonnets, appelés nanorods d'or (Gold Nanorods - GNR), ont été utilisés. Parmi de nombreuses applications, les GNR ont été utilisés dans les thérapies biomédicales basées sur la conversion photo-thermique [13], en raison de leur inertie chimique, de leur recette de synthèse bien connue, qui aboutit à une uniformité de taille et de morphologie, à une section efficace d'extinction élevée et à leur résonance plasmonique de surface longitudinale réglable (Localized Surface Plasmon Resonance - LSPR) dans le domaine de longueur d'onde proche infrarouge (Near Infrared - NIR) dans laquelle le tissu biologique permet une pénétration plus profonde. Trois volumes de GNR différents ont été étudiés, avec le même pic longitudinal de LSPR, approximativement le même rapport de longueur, mais des dimensions différentes.

Des mesures expérimentales et des simulations ont été utilisées pour élucider l'effet du volume des GNR sur le PCE. La nouvelle méthode mise au point dans cette thèse ainsi que ses capacités peuvent être étendues à d'autres situations dans lesquelles la température modifie l'indice de réfraction de systèmes aqueux, par exemple de l'eau biologique dans les tissus cutanés. Comme preuve de concept, les changements induits par la température dans un système de modèle biologique multicouche contenant une forte teneur en eau ont été étudiés en utilisant la lumière THz (chapitre 3). Plus précisément, une nouvelle procédure médicale prometteuse appelée soudage laser assisté de tissus [14] a été utilisée. Contrairement aux sutures conventionnelles, un gel de soudure contenant des NPs facilite l'approximation des bords d'incision. L'effet secondaire de cette procédure est un dommage thermique qui est infligé au tissu entourant l'incision en raison du rayonnement laser intense. Ce dommage thermique dans le tissu forme une structure multicouche avec différents indices de réfraction. L'évolution des dommages thermiques au cours de la procédure de soudage a été contrôlée au moyen d'une source de rayonnement THz, tandis que sa distribution spatiale a été cartographiée afin de révéler l'étendue des modifications structurelles de surface et de subsurface dans le tissu. Les résultats expérimentaux ont été complétés par des simulations théoriques de la dynamique de la température à l'intérieur du tissu montrant l'ampleur des dommages photo-thermiques causés par la procédure de chauffage au laser. La nouvelle méthode a le potentiel d'être utilisée dans des procédures médicales telles que la thérapie photo-thermique (Photo-thermal Therapie - PTT) pour surveiller le tissu traité afin de minimiser ou même de prévenir des dommages thermiques supplémentaires. Cela pourrait être un facteur important pour rendre ces traitements médicaux prometteurs plus applicables lors de pratiques clinique.

2. Radiation Terahertz

Le rayonnement THz couvre le spectre électromagnétique de 0.1×10^{12} to 10×10^{12} Hz, ce qui correspond à une plage de longueurs d'onde de 3 mm à 30 μm , ce qui le positionne entre le régime des fréquences infrarouge et hyperfréquence (Figure 1).

Le rayonnement THz a des propriétés non-invasives et non-ionisantes du fait de sa faible énergie photonique (0,4 à 40 meV) qui assure l'intégrité physicochimique d'un échantillon sans influencer la mesure. Cela rend les ondes THz adaptées à l'imagerie médicale, car sa nature non invasive peut être utilisée pour le diagnostic in vivo en temps réel sans causer de dommages d'ionisation, contrairement aux rayons X, par exemple.

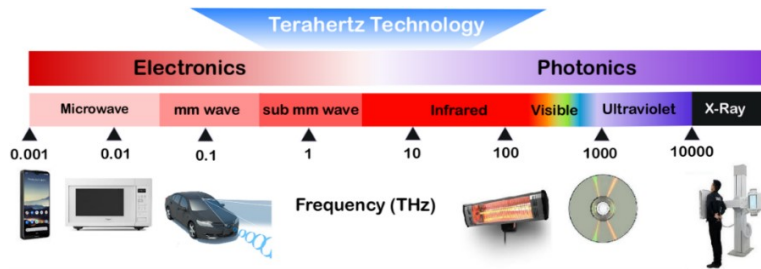


Figure 1: Spectre électromagnétique soulignant la section THz. (Adapté de National Institute of Information and Communications Technology (NICT))

De plus, la longueur d'onde du rayonnement THz étant plus longue que celle de la lumière visible et infrarouge, les pertes par diffusion dans les tissus biologiques sont négligeables [19]. De plus, les matériaux diélectriques non polaires, tels que le tissu, le papier et le plastique, qui sont opaques aux ondes visibles et NIR, sont transparents dans la gamme de fréquences THz. Cette propriété permet une détection sans contact et non-invasive au-delà de la ligne de vue, par exemple pour les mesures à l'intérieur d'enceintes ou de récipients. Cela peut avoir des applications percutantes en biomédecine pour une détection sous des gazes médicales, à l'intérieur de cuvettes ou de capillaires, ainsi que sur les dispositifs microfluidiques de laboratoire sur puce [15]. De plus, le rayonnement THz présente une forte absorption par les molécules polaires, telles que l'eau. Par conséquent, il est très sensible à l'humidité de l'environnement et au niveau d'hydratation des objets, par exemple les tissus biologiques [16]. Cette propriété est largement utilisée pour les applications biomédicales afin, par exemple, de discriminer avec précision les tissus normaux et les tissus cancéreux, ainsi que pour l'évaluation des brûlures [17] en raison de la teneur en eau différente ou changeante [18]. De plus, les solutions aqueuses subissent une variation significative de l'indice de réfraction et du coefficient d'absorption en fonction de la température dans le régime THz (Figure 2 (a-b)), ce qui permet une détermination précise de la température. Ce principe fondamental a été utilisé pour développer une nouvelle méthode de caractérisation photo-thermique des NPs décrite dans cette thèse.

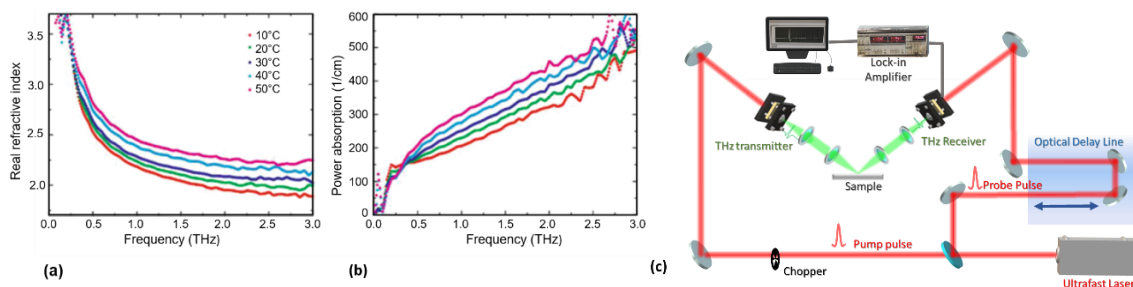


Figure 2: (a) Indice de réfraction et (b) coefficient d'absorption de l'eau en fonction de la température dans le régime de fréquence THz. (Figure adaptée des références [25], [26]) (c) Configuration de spectroscopie dans le domaine temporel THz basée sur des antennes photoconductrices (Photoconductive Antennas – PCA) en configuration de réflexion.

Plusieurs méthodes peuvent être déployées pour la génération THz et la détection d'impulsions THz à spectre large bande. Les techniques de génération les plus répandues sont les courants photo-induits transitoires dans une antenne photoconductrice (PCA) et la rectification optique dans un milieu non linéaire de second ordre [27], [28], tandis que la détection par échantillonnage photoconducteur [29]–[34] et l'électro-échantillonnage optique [35], [36] représentent des techniques largement utilisées. Dans les expériences de cette étude, des (Photoconductive Antennas) PCA ont été utilisés comme émetteur et détecteur THz dans un système dit de spectroscopie THz temps-domaine (THz-TDS). Ce système permet de détecter simultanément les informations d'amplitude et de phase du champ THz. La figure 2 (c) montre la configuration expérimentale de base du système THz-TDS pour la génération et la détection d'ondes THz sur la base de PCA en configuration de réflexion. Les impulsions d'un laser femtoseconde sont divisées par un séparateur de faisceau. Une partie, appelée « faisceau de pompage », est dirigée vers l'émetteur THz pour générer des impulsions THz. Le faisceau THz généré est collimaté soit par des miroirs paraboliques hors axe, soit par des lentilles en polymère, puis envoyé à l'échantillon. Ensuite, le rayonnement THz réfléchi est dirigé vers un récepteur THz et est concentré sur celui-ci. L'autre partie du faisceau d'impulsions femtoseconde, appelée "faisceau de sonde", parcourt un retard variable, avant d'être focalisée sur le récepteur THz. En faisant varier le retard du faisceau de sonde et en enregistrant la valeur du détecteur en fonction du retard optique, il est possible de suivre de manière cohérente le champ électrique THz en fonction du temps, ce qui signifie que la mesure enregistre non seulement l'amplitude, mais aussi l'information de phase de l'impulsion THz qui peut ensuite être utilisée pour calculer des informations spectrales en utilisant la transformation de Fourier. Un échantillon introduit dans le trajet du faisceau THz affecte à la fois la phase et l'amplitude des impulsions THz. En comparant les impulsions THz avec et sans échantillon présent dans la configuration, il est possible de caractériser l'échantillon et d'obtenir son spectre d'absorption THz et ses propriétés de dispersion. Ainsi, la détection cohérente permet une caractérisation complète des propriétés optiques de l'échantillon, c'est-à-dire de sa fonction diélectrique complexe [40], [41]. Cette technique de détection cohérente d'impulsions THz à large bande est appelée THz-TDS.

3. Nanoparticules Plasmoniques

Le terme "nanomatériaux" désigne des matériaux dont les dimensions, au moins selon un axe, sont comprises entre 1 et 100 nm. En particulier, les NPs possèdent plusieurs propriétés uniques qui les distinguent de leur version massive, notamment un rapport surface / volume élevé, une énergie de surface élevée, des comportements mécaniques, thermiques, électriques,

magnétiques et optiques uniques. Ces propriétés peuvent être adaptées, élargissant ainsi considérablement la gamme de leurs capacités par rapport à leurs équivalents massif. En particulier, les NPs inorganiques conviennent le mieux à de nouvelles applications médicales, car elles sont de petite taille, très stables et résistantes à la dégradation. Cela a conduit à une augmentation des activités de recherche dans le développement de nanosondes pour l'imagerie médicale de type diagnostique ainsi que d'agents chauffants pour les thérapies activées de l'extérieur. Les NPs plasmoniques en métaux nobles (or, argent, platine, etc.) ont été largement utilisés dans diverses applications d'imagerie biomédicale et de chauffage en raison de leur inertie chimique (c'est-à-dire leur faible toxicité) et des voies de synthèse colloïdales bien établies qui les rendent physico-chimiquement stables et confèrent une accordabilité de leurs propriétés optiques [70]–[74]. Les propriétés de diffusion et d'absorption des NPs peuvent être facilement modifiées [8], [75] en variant par exemple, leur morphologie (sphères, bâtonnets, étoiles, coques, cages, etc.), les conditions de surface et la taille, c.-à-d. les NPs plus grandes ont tendance à disperser davantage la lumière et à absorber moins [71]. Ainsi, la conception de NPs en métaux nobles est optimisable pour des applications biomédicales spécifiques. Pour les applications basées sur l'absorption, telles que l'imagerie PTT ou photoacoustique, les NPs plus petites sont préférées en raison de leur PCE plus élevé (c'est-à-dire que l'absorption domine par rapport à la diffusion). Plus précisément, les NP en or se distinguent par le fait qu'ils présentent des propriétés d'absorption intrinsèque extrêmement fortes, ce qui induit une chaleur confinée dans l'espace, applicable aux traitements PTT. Ici, les NPs d'or plasmoniques agissent comme des agents de chauffage intenses pour endommager et par conséquent détruire les cellules cancéreuses. Cette option de traitement sélectif relativement récente et peu invasive [77] implique la conversion de la lumière en chaleur afin d'induire une hyperthermie dans les cellules malignes. Cela se produit lorsque les cellules sont exposées à des températures supérieures à 42 ° C pendant plusieurs minutes, entraînant la mort cellulaire par endommagement irréversible des protéines et des structures membranaires. De plus, la chimie de surface des NPs d'or peut être ajustée pour permettre aux NPs de cibler sélectivement les populations de cellules sans affecter de manière défavorable les tissus non ciblés situés à proximité.

Le principe physique à la base des fortes propriétés d'absorption des NPs d'or plasmoniques est un effet de résonance plasmonique [83]–[85]. Les plasmons sont des oscillations collectives d'électrons libres dans des métaux à une longueur d'onde bien définie. Ils peuvent être décrits comme un nuage d'électrons chargé négativement, déplacé de manière cohérente depuis sa position d'équilibre autour d'un réseau constitué d'ions chargés positivement. Des modes plasmoniques spécifiques peuvent exister à la surface de la particule, qui est généralement

entourée d'un milieu diélectrique, et être excités par un champ électrique externe. Les plasmons dans les NPs de taille beaucoup plus petite que la longueur d'onde du photon sont des excitations non propagatrices, appelées par conséquent résonance de plasmon de surface localisée (LSPR), car l'oscillation de plasmon est répartie sur tout le volume des particules. Le déplacement cohérent des électrons provoque une force d'attraction qui ramène les électrons polarisés sur le réseau. Par conséquent, le plasmon dans une NP peut être décrit par un modèle d'oscillateur harmonique masse-ressort, piloté par le champ électrique résonant d'une onde lumineuse. Seule la lumière avec une longueur d'onde en résonance avec l'oscillation peut exciter le LSPR. Plus particulièrement, les NPs d'or en forme de bâtonnet, connus sous le nom de nanorodes d'or (GNR), sont généralement préférés pour les applications biomédicales, car leur longueur d'onde LSPR peut facilement être décalée vers le domaine de longueur d'onde NIR, entre 650 nm et 1350 nm. Cette fenêtre dite biologique, dans laquelle l'atténuation tissulaire et sanguine est minimisée, convient le mieux à la pénétration de la lumière laser dans les tissus en profondeur, par exemple lors de traitements au PTT [89]. Par conséquent, les GNR ont été utilisés dans les expériences de cette thèse. Tout d'abord, pour évaluer leur PCE, puis pour les appliquer ensuite dans un contexte biomédical basé sur la conversion photo-thermique.

4. Quantification de l'effet photo-thermique des nanoparticules

Le grand intérêt que suscitent les NPs plasmoniques est principalement dû à la capacité de les modéliser, de les synthétiser de manière fiable et de les caractériser [85]. Cela a conduit à la mise au point de NPs aux propriétés améliorées et ayant un impact significatif sur la nanomédecine. Par conséquent, les recherches actuelles [5]–[7] portent par exemple sur l'optimisation de la taille et de la morphologie des NPs d'or afin d'accroître leur accumulation dans les tumeurs et augmenter leur PCE, de sorte que des puissances laser plus faibles puissent être utilisées pour effectuer des procédures de type PTT. Le PCE est une propriété des NPs utilisée comme indicateur standard pour évaluer leur capacité à convertir la lumière en chaleur. Il est défini comme le rapport entre la chaleur générée par une dispersion de NPs et la perte de puissance associée du laser à excitation. Le PCE des NPs dispersés dans des solutions aqueuses ne peut malheureusement pas être facilement quantifié par une simple mesure. Dans un premier temps, la valeur d'absorbance de la dispersion des NPs étudiée doit être déterminée par un spectromètre UV-VIS-NIR. Cette valeur dépend de la taille, de la concentration, de la morphologie et de l'agrégation des NPs. Il contient une partie diffusion et absorption dont cette dernière est liée à l'augmentation de chaleur des NPs. Une méthode de bilan énergétique est la méthode standard la plus souvent utilisée reposant sur un modèle numérique présenté par Roper et al. [93] pour

calculer le PCE. Il permet d'étudier directement les performances thermiques des NPs comparant, par exemple, différentes morphologies [6], [94], les matériaux [95], les tailles [8] et les longueurs d'onde LSPR [91]. Cette méthode englobe la récupération des phénomènes transitoires de température pendant le chauffage photo-thermique et les cycles de refroidissement ultérieurs d'une dispersion de NPs étudiée. Le PCE peut ensuite être calculé en ajustant les températures en régime transitoires au modèle numérique et en prenant en compte des paramètres d'entrée, tels que la masse et la capacité thermique des constituants, la puissance laser incidente ainsi que le coefficient d'extinction de l'échantillon. Jusqu'ici, la méthode la plus répandue pour mesurer les changements de température induits par la lumière dans les dispersions de NPs utilise des thermomètres à résistance. On utilise fréquemment des thermocouples fonctionnant sur la base de l'effet thermoélectrique [8]. Habituellement, un ou plusieurs thermomètres à résistance ou thermocouples sont insérés dans une cuvette contenant la dispersion de NPs pour mesurer les changements de température pendant la procédure de chauffage photo-thermique. Les deux méthodes de mesure de la température reposent sur le contact physique avec l'échantillon de NPs, ce qui peut l'endommager ou le contaminer et conduire à la précipitation des NPs, etc. En outre, un agitateur magnétique doit être utilisé comme requis par le modèle numérique qui calcule le PCE. Cependant, cette méthode ne permet pas de mesurer de manière instantanée et fiable la dynamique thermique au niveau du faisceau laser éclairant. De plus, il nécessite un contact direct, pouvant ainsi endommager et / ou contaminer l'échantillon, et ainsi modifier la mesure elle-même. Des méthodes plus sophistiquées telles que la thermométrie infrarouge et la thermographie reposent sur la détection du rayonnement infrarouge émis par un objet pour en déduire la température [9], [94]. Bien qu'elles offrent des capacités de détection sans contact et non destructives, ces méthodes ne peuvent mesurer que les températures de surface dans le champ de vision direct, car les textiles, par exemple, sont opaques au rayonnement infrarouge. Pour surmonter ces problèmes, une nouvelle méthode basée sur le THz-TDS pour caractériser l'effet photo-thermique des NPs de manière sans-contact et non invasive a été développée dans cette thèse. Trois dimensions distinctes des GNRs disponibles dans le commerce ont été utilisées comme référence pour valider la nouvelle méthode. Leurs performances ont été comparées pour démontrer le mécanisme physique sous-jacent et déterminer la taille des particules produisant l'augmentation de température la plus élevée sous excitation plasmonique NIR à une longueur d'onde de 786 nm. Le rapport diamètre / longueur moyen des trois dimensions de GNRs était de 10 nm x 41 nm, 25 nm x 90 nm et 50 nm x 150 nm. Les trois dispersions de GNRs seront appelées GNR10, GNR25 et GNR50 dans tout le texte. Leurs proportions longueur / largeur étaient respectivement de 3, 3,6 et 4,1. Ces trois

types de GNRs ont été spécialement conçus pour fournir la même longueur d'onde LSPR d'environ 808 nm. Un système THz-TDS et un système d'imagerie en mode réflexion ont été déployés pour les mesures. La figure 3(a) montre la partie centrale de l'installation THz contenant une cuvette refermable en macro-polyéthylène (PE) présentant une longueur de trajet de 10 mm et qui était positionnée au point de focalisation THz. Un laser NIR produisant un faisceau laser à onde continue à une longueur d'onde de 786 nm a été utilisé pour photo-exciter les particules de GNRs à l'intérieur de la cuvette scellée.

La figure 3(b) montre un champs THz représentatif réfléchi par un échantillon constitué d'une dispersion de GNRs à l'intérieur d'une cuvette en PE. On peut reconnaître trois échos THz qui se rapportent à chaque interface: premier écho (air / cuvette), deuxième écho (cuvette / dispersion de GNRs) et troisième écho (réflexion du deuxième tour due à l'effet étalon). Le deuxième écho provenant de l'interface de dispersion cuvette / GNR a été utilisé pour enregistrer le changement de température au cours des cycles de chauffage et de refroidissement lorsque le laser NIR a photo-excité les GNRs dans la solution aqueuse. Le premier écho reflété sur la surface de la cuvette a été exploité pour un auto-référencement afin d'éliminer l'influence du bruit intrinsèque du système et des fluctuations de la température ambiante. Les mesures thermiques fiables nécessitent une extraction précise de l'amplitude THz du 2^{ème} écho (interface de dispersion cuvette / GNR). La queue étendue du 1^{er} écho subit une modulation appelée effet de « Résonance » qui provient de l'humidité de l'air ambiant. Cet effet interfère avec le 2^{ème} écho, qui contient les informations de température de la dispersion de GNRs chauffée. Une mesure thermique précise n'est pas possible sans prendre en compte cette interférence. Ainsi, une technique de déconvolution basée sur la parcimonie [123] a été utilisée pour extraire les formes d'onde THz authentiques et les séparer pour éviter toute interférence, comme illustré à la figure 3 (b). Communément, les expériences THz ont été effectuées sous une atmosphère d'azote pour éliminer l'absorption de THz par l'humidité de l'environnement environnant. Cela se fait généralement en mettant en place l'ensemble de la configuration THz dans un boîtier scellé. Cette procédure prend du temps, est coûteuse et rend la configuration THz encombrante et immobile. L'élimination de l'effet de « résonance » sur l'impulsion THz permet l'utilisation de la méthode présentée dans des conditions atmosphériques normales et peut donc être déployée dans un environnement hors du laboratoire. De plus, les systèmes THz-TDS subissent des fluctuations d'amplitude inhérentes et des dérives de phase qui empêchent des mesures précises et cohérentes [142]. Ces modulations intrinsèques résultent des fluctuations du bruit et de la température du système environnant et ont été efficacement atténuées par l'application d'une technique d'auto-référencement [143].

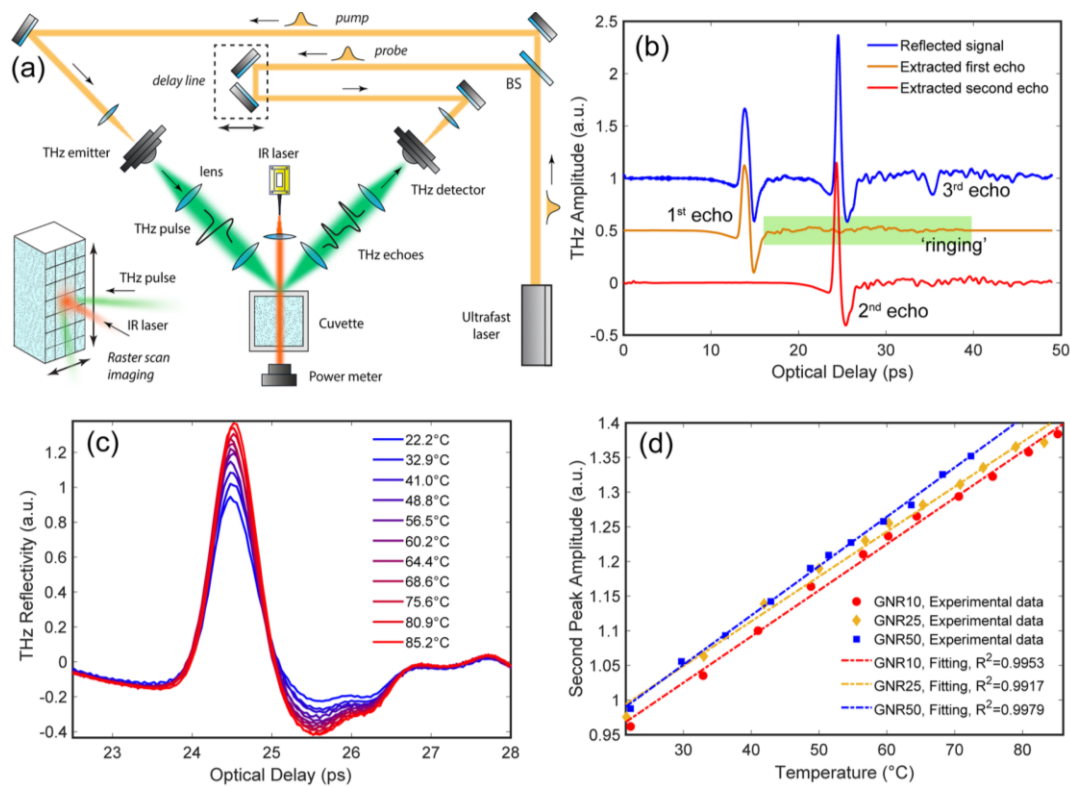


Figure 3: (a) Schéma de principe d'un système THz-TDS en géométrie de réflexion. Un faisceau NIR de 786 nm utilisé pour chauffer de manière plasmonique les dispersions de GNRs chevauche le point de focalisation THz. La puissance de l'éclairage NIR transmis à travers la cuvette est enregistrée avec un wattmètre. L'encadré présente un diagramme schématisant un processus d'imagerie par balayage de type raster THz de l'avant et de l'arrière de la cuvette. Au cours du processus de balayage, le faisceau THz était rigide et la cuvette s'est déplacée avec le laser NIR, pixel par pixel. (b) Exemple représentatif d'un champ THz enregistré réfléchi par la cuvette. Les premier et deuxième échos séparés après l'application d'un algorithme de déconvolution à faible densité sont également affichés, ce qui permet d'éliminer l'influence de la « résonance » due à la vapeur d'eau ambiante dans l'air. (c) Réflectivité dépendant de la température du deuxième écho THz en fonction de la température pour GNR10. d) Courbes d'étalonnage présentant une relation thermométrique linéaire entre l'amplitude THz et la température pour chacune des dispersions de GNRs. (Figure adaptée des références [137])

Par conséquent, le 2^{ème} écho a été ajusté aux fluctuations de son premier écho correspondant, dont l'amplitude a été comparée à une référence. Par conséquent, une mesure réelle et précise de la valeur de pointe du 2^{ème} écho a été obtenue en utilisant les techniques de post-traitement du signal mentionnées: algorithme de déconvolution basé sur la paracimétrie et auto-référencement.

Premièrement, la détection thermique utilisant des modulations de réflectivité THz provenant des modifications de l'indice de réfraction induites par la température d'un échantillon de NPs en solution aqueuse nécessite une courbe d'étalonnage dépendante de la température. Cette courbe est une fonction mappant les amplitudes THz réfléchies aux variations de température réelles de l'échantillon et a été déterminée expérimentalement pour les trois dispersions de GNRs (figure 3 (d)). Pendant la mesure, la cuvette contient 3 mL de la dispersion de GNRs à l'étude. La cuvette

a été soigneusement scellée à l'aide d'un couvercle en téflon afin d'empêcher toute évaporation de la dispersion à l'intérieur de la cuvette. Les mesures d'étalonnage ont été effectuées par chauffage plasmonique NIR des dispersions de GNRs en faisant varier l'intensité de la puissance laser dans la plage de 0,95 à 60,4 W/cm². La température a été mesurée en insérant un thermomètre numérique dans la cuvette à proximité du point laser éclairant une fois que la température a atteint un niveau stable. La température a été enregistrée en traçant les modulations de réflectivité THz du 2^{ème} écho rebondissant sur l'interface de dispersion cuvette / GNR (figure 3 (c)). Le principe fondamental est un changement induit par la chaleur de la propriété diélectrique de la solution aqueuse, qui modifie son indice de réfraction dans le domaine fréquentiel THz. La valeur de température a donc été adaptée à la valeur d'amplitude THz respective du 2^{ème} écho qui a révélé une relation thermométrique linéaire avec un coefficient de détermination R² d'environ 0,99 (figure 3 (d)).

Deuxièmement, des mesures de température à l'aide du montage THz-TDS ont été effectuées pendant les cycles de chauffage et de refroidissement afin de déterminer le PCE de chacune des trois dispersions de GNRs. Une irradiation laser NIR à une puissance de 31,8 W/cm² a été utilisée pendant 12 minutes pour photo-exciter les GNRs à l'intérieur de la dispersion et enregistrer le cycle de chauffage au moyen du montage THz-TDS. Même si d'autres études [5] chauffent habituellement pendant environ 30 minutes lors d'une agitation vigoureuse de la dispersion des NPs, dans cette étude, aucun agitateur magnétique n'a été utilisé pendant le processus de chauffage, ce qui risquerait d'affecter thermiquement les échantillons des NPs. Par conséquent, la durée de chauffage a été limitée à 12 minutes seulement afin de réduire autant que possible la tension sur les NPs, ce qui préserve leur stabilité colloïdale et garantit ainsi la comparabilité et la cohérence des données. Après le cycle de chauffage, le laser a été éteint et la température à l'intérieur de la cuvette a été enregistrée pendant 15 minutes au cours de la période de refroidissement. La courbe température-temps a été obtenue en traçant l'amplitude du pic THz du 2^{ème} écho THz, en post-traitant tous les échos THz réfléchis par les interfaces de l'échantillon au moyen d'une méthode de déconvolution et d'auto-référencement basée sur la paracimétrie, puis en traduisant la valeur obtenue à la température en utilisant la courbe d'étalonnage correspondante. La fréquence d'échantillonnage de la réflectivité THz était de 10 s sur une période de 12 minutes pour le chauffage et de 15 minutes pour le cycle de refroidissement. La figure 4 (a) décrit le profil de température complet des trois dispersions de GNRs. GNR10 et GNR25 ont atteint un niveau de température d'équilibre constant d'environ 53 °C après 12 minutes de chauffage. Le GNR50 a atteint environ 45 °C.

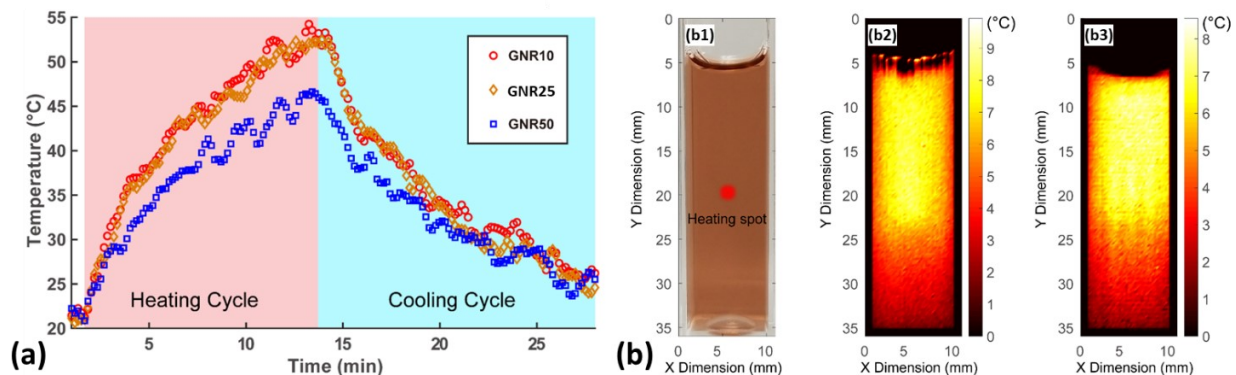


Figure 4: (a) Courbes de température typiques mesurés par THz-TDS. La procédure et les paramètres étaient les mêmes pour chacune des trois dispersions de GNRs: une puissance laser NIR constante de $31,8 \text{ W/cm}^2$ a été exercée pendant 12 minutes pour enregistrer la courbe de chauffage. Ensuite, le laser a été éteint pour obtenir la courbe de refroidissement. (b) Les thermographes THz de la dispersion de GNR10 obtenus à l'aide de balayages de type raster THz-TDS illustraient la distribution thermique lorsqu'un niveau d'équilibre par chauffage plasmonique était atteint. (b1) Image numérique de la surface avant de la cuvette avec le point laser marqué en rouge. Thermographes THz de la distribution de température ΔT (par rapport à la valeur ambiante) de (b2) à l'avant et (b3) à l'arrière de la cuvette. (Figure adaptée des références [137])

Les taux d'absorption et de dissipation d'énergie ont été calculés en ajustant les courbes de température expérimentales. De cette manière, le PCE a été déterminé pour les trois dispersions de GNRs. Puisqu'aucun agitateur magnétique n'a été utilisé à l'intérieur de la cuvette, la masse de la dispersion de GNRs a été chauffée partiellement par le procédé de chauffage au laser photo-thermique. Il en a résulté une distribution thermique non homogène à l'intérieur de la cuvette scellée, ce qui doit être pris en compte en mesurant la masse effectivement chauffée de l'échantillon pendant l'excitation laser. Par conséquent, des thermogrammes THz basés sur une technique de balayage par trame ont été créés avec une résolution d'image de $250 \mu\text{m}$. Des thermogrammes ont été prélevés sur tout l'avant et l'arrière de la cuvette avant le début du cycle de chauffage et après que le niveau de température à l'équilibre ait été atteint. Les thermogrammes THz résultants montrent la répartition thermique à l'interface de dispersion cuvette / GNR lorsque le cycle de chauffage atteint un niveau stable. La figure 4 (b2-b3) illustre les images thermiques THz prises depuis les fenêtres avant et arrière de la cuvette pour la dispersion de GNRs. L'image montre la variation de température (ΔT) au niveau de l'état d'équilibre par rapport à la valeur ambiante initiale. L'acquisition de l'image est fondamentale pour approcher la masse effective de la dispersion GNR. Notamment, ni les profils de température ni leurs distributions spatiales n'ont permis à eux seuls de mesurer le PCE des GNRs, mais uniquement leur corrélation mutuelle. La masse efficace de la dispersion de NPs dans la cuvette a été déterminée à $1,74 \text{ g}$. En combinant les courbes de température dans le temps et les images thermiques dans l'espace enregistrées en utilisant le rayonnement THz dans un système THz-TDS, il a été déterminé que les PCE

permettaient d'obtenir un rendement de conversion de 93% atteint par la dispersion GNR10 et présentant le plus petit volume de particules, suivie du GNR25 avec 89% et le GNR50 avec 67%. Les résultats ont été confirmés par d'autres études [8], [144], [145] pour des nanostructures d'or de taille similaire. Les principales caractéristiques photo-thermiques des GNRs sont enracinées dans le mécanisme sous-jacent de leur réponse électromagnétique au cours du processus de chauffage photo-thermique. La section transversale d'interaction d'une NP plasmonique augmente avec sa polarisabilité et se met à l'échelle en fonction de son volume de particules. Par conséquent, les NPs les plus petites présentent un PCE plus élevé, mais présentent une section efficace d'absorption sur une base de particule inférieure à celle des NPs plus volumineux.

5. Thérapie à base de conversion photo-thermique pour les procédures de fermeture de plaie

Une procédure médicale minimalement invasive récemment mise au point pour les fermetures de plaies [99] utilisant des NPs et assistée par laser offre un potentiel élevé de modification des procédures de traitement des plaies pour les cliniques du futur [100], [101]. Relier des bords de tissus humains est une étape importante dans la plupart des procédures chirurgicales. Aujourd'hui, les procédures standard pour la fermeture de la plaie reposent sur des sutures chirurgicales, qui impliquent une aiguille avec un fil attaché, ou sur des agrafes métalliques ou polymères. Ces technologies s'adaptent facilement à la plupart des types de tissus. Cependant, ces procédures sont intrinsèquement traumatiques, blessent les tissus et laissent un corps étranger à l'intérieur. De plus, la fermeture de la plaie n'est pas complète, il peut rester de petits écarts entre les points de suture. Dans les années 1970, des études ont révélé que l'effet du chauffage local des tissus accélère la fermeture et la cicatrisation des plaies, un processus apparenté à la soudure de solides. Plusieurs études ont porté sur la technique de soudure au laser en tant que nouvelle méthode sans suture minimalement invasive pour le collage de coupures dans des tissus, utilisant différentes longueurs d'onde laser [102]–[106]. De plus, divers travaux ont exploré les effets photo-thermiques de la soudure laser-tissu [107], le temps d'exposition laser optimal [108], l'intensité du laser [109], ainsi que son potentiel de dommage thermique et la résistance de la plaie [110], [111]. Des travaux récents suggèrent qu'une substance biologique à base de protéines, telle que l'albumine, pourrait être appliquée sur l'incision et chauffée avec le tissu sous-jacent, la protéine chauffée localisée jouant alors le rôle de colle biologique [112]. Cette procédure de soudage au laser produit généralement une liaison plus forte. L'idée de base est d'utiliser la lumière laser en combinaison avec une solution de soudure pour « coudre » les ouvertures de la plaie en surface. Lorsque la lumière laser illumine

la solution de soudure appliquée, le tissu sous-jacent se réchauffe et une liaison continue est créée, ce qui permet de reconnecter le collagène. Le processus de soudage peut être amélioré en combinant l'albumine avec des NPs plasmoniques, par ex. des GNRs, pour former un nanocomposite photo-thermique facilitant le scellement rapide des plaies en utilisant des modifications induites par la chaleur du matériau de soudure et du tissu [99], [112]–[114]. Les NPs agissent comme des absorbeurs localisés qui transfèrent de manière très efficace la lumière laser incidente dans la chaleur de manière contrôlable et limitée dans l'espace à la zone d'incision du tissu. De cette manière, moins de puissance laser NIR est nécessaire, ce qui réduit les effets thermiques néfastes potentiels sur les tissus cutanés environnants, et qui facilite le processus de guérison ultérieur. Le résultat est un sceau étanche complet le long de la plaie, bloquant l'accès aux agents pathogènes et ne nécessitant pas le retrait de la suture. Pourtant, la soudure assistée par laser n'a pas été largement utilisée en milieu clinique. La raison sous-jacente est que les températures élevées atteintes par l'absorption de la lumière laser et la génération de chaleur concomitante peuvent causer des dommages photo-thermiques importants aux tissus, ce qui pourrait limiter le succès de l'approche. Lorsque la température locale dans les tissus atteint une limite critique d'environ 60 °C, les cellules se coagulent, ce qui entraîne une perturbation de l'activité cellulaire et éventuellement la mort cellulaire [115]. Par conséquent, une surveillance rigoureuse de la solution de soudure chauffée et du tissu sous-jacent est nécessaire pour minimiser les dommages et optimiser la force de liaison. Les méthodes actuelles d'imagerie biomédicale non invasive et sans contact classiques pour mesurer la profondeur et la gravité de la brûlure souffrent de diverses limitations. Par exemple, la tomographie par cohérence optique sensible à la polarisation mesure une modification de la polarisation optique des tissus résultant de la destruction thermique des fibres de collagène en détectant uniquement les photons directement réfléchis [116]. La technique souffre d'une forte diffusion optique et est incapable de distinguer les différents degrés de brûlures cutanées. L'imagerie laser Doppler est apparue comme un phénomène couplé de la débit-métrie Doppler et de l'imagerie laser [117]. Il s'agit d'une mesure indirecte de la profondeur de la brûlure. Elle établit une corrélation entre le flux de sang dans une zone brûlée et la profondeur de la plaie afin d'évaluer sa gravité, ce qui peut éventuellement conduire à des erreurs d'interprétation. Le principe de base de la thermographie infrarouge pour l'imagerie des brûlures est de distinguer les brûlures d'épaisseur partielle des brûlures d'épaisseur totale en fonction des différences de température à la surface des tissus brûlés. La température de surface des tissus diminue avec l'augmentation de la profondeur de brûlure au fil du temps, en raison d'un changement de la circulation sanguine. Cependant, l'imagerie IR souffre d'effets de diffusion, d'un contraste limité entre les tissus et d'une

interprétation erronée, car elle pourrait fausser le diagnostic de la perte de chaleur naturelle des tissus brûlés comme étant une profondeur de brûlure profonde [118], [119]. Motivé par ces défis, une nouvelle méthode pour réaliser une imagerie THz non invasive, sans contact et non ionisante pour surveiller les changements liés à la chaleur dans les tissus cutanés a été développée dans cette thèse.

La figure 5 présente les zones de dommages thermiques qui se produisent généralement lors d'une procédure de chauffage photo-thermique [167]. Le processus de transfert de chaleur est commandé par des molécules oscillantes qui dissipent l'énergie thermique radialement dans les tissus les plus profonds. Si l'augmentation de chaleur est modérée et peut rapidement se dissiper, il ne restera aucun dommage thermique permanent sur les tissus. Cependant, si l'apport de chaleur est trop élevé et / ou reste constant pendant une longue période (41 - 48 °C pendant > 60 min ou 48 - 60 °C pendant 4 - 6 min [168]) ou la température du tissu dépasse un seuil de 60 °C, la coagulation des cellules et la dénaturation des protéines conduiront à une nécrose tissulaire irréversible, qui correspond à la mort prématurée des cellules dans les tissus vivants par lésion cellulaire ou par chaleur intense [115]. Une accumulation de chaleur allant jusqu'à 100 °C entraîne une forte évaporation de l'eau et une réduction du volume des tissus. Lorsque toute l'humidité restante de la peau s'évapore, il se produit une carbonisation et une incinération des cellules touchées, qui deviennent visibles par l'apparition de carbonisation à la surface de la peau [115].

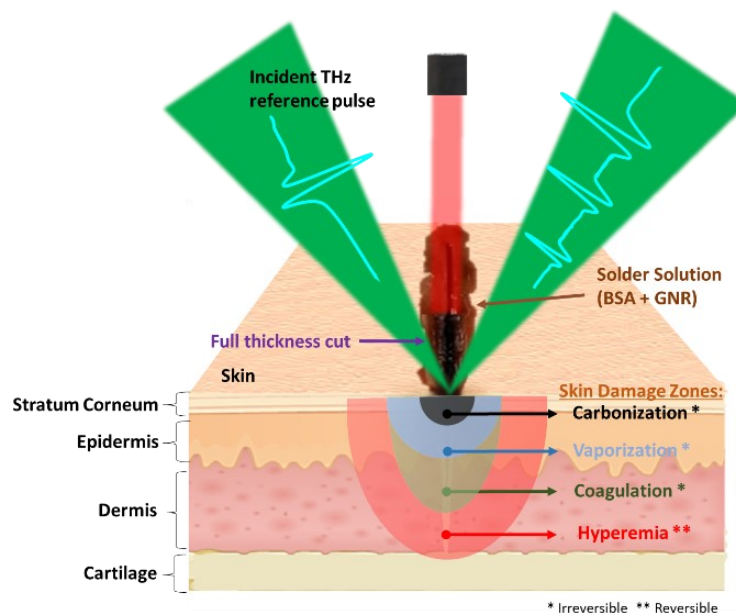


Figure 5: Représentation schématique d'un tissu excisé de la peau d'une oreille porcine décrivant différentes étapes de réactions photo-thermiques au cours d'un processus de soudage au laser assisté par des NPs. (Figure adaptée des références [137])

Le transfert de chaleur en fonction du temps et la distribution thermique spatiale dans la peau ont été simulés par un modèle numérique d'éléments finis à l'aide du logiciel COMSOL Multiphysics (Figure 6 (a)). Le gel de soudure contenait un mélange homogène d'albumine de sérum bovin (BSA) et une dispersion de NPs à base d'eau. Les NPs ont été modélisés avec une morphologie en forme de barre de taille 10 nm × 41 nm, une longueur d'onde de LSPR d'environ 808 nm et une valeur d'absorbance de 100. De plus, un faisceau laser NIR à onde continue a été simulé avec une raie d'émission de 800 nm pour correspondre à la longueur d'onde LSPR des GNRs, une intensité de puissance de 5 W/cm² et un diamètre de faisceau de 4,4 mm ciblant le centre du gel de soudure.

La figure 6 (b) illustre l'évolution de la température dans le temps à la surface de la peau dans trois cas. Tout d'abord, le gel de soudure a été appliqué sur la peau, puis chauffé par illumination laser NIR. Avec l'application du gel de soudure incorporant les GNRs, la température transitoire a augmenté de manière exponentielle en l'espace de 25 secondes, jusqu'à 60 °C, puis s'est progressivement saturée au bout de 75 secondes à environ 100 °C. Le modèle ne prend en compte aucun dommage cutané, la température atteint donc environ 120 °C après 250 s. Dans le second cas, le gel de soudure était également pris en compte. Cependant, le modèle comprenait des lésions cutanées apparaissant à 100 °C. La transition d'un tissu normal à un tissu endommagé consomme de l'énergie sous forme de chaleur (puits de chaleur) provenant d'un changement de phase local. Par conséquent, la température a augmenté plus lentement que dans la simulation sans dommage. Les dommages cutanés ont été simulés en introduisant un modèle de dommages thermiques. Dans le troisième cas, aucun gel de soudure n'a été appliqué sur la peau. En raison du faible coefficient d'absorption de la peau de porc pendant le processus de chauffage photo-thermique NIR, la température de la surface de la peau a augmenté de manière insignifiante, la majeure partie de la lumière étant simplement dispersée.

La figure 6 (c) illustre une simulation tridimensionnelle de la distribution thermique dans le gel de soudure et le tissu cutané après 250 s d'éclairage au laser NIR. L'image cartographie la dissipation de la température à partir du centre du tissu cutané où la température atteint presque 120 °C en raison du profil d'intensité gaussien du laser. À partir de cet endroit, la température diminue radialement jusqu'à environ 20 °C. Les contours de température marquant 60 °C et 100 °C sont surlignés en blanc et en noir, respectivement. À 60 °C, une coagulation irréversible de biomolécules se produit et à 100 °C, l'eau s'évaporerait fortement de la surface de la peau, ce qui déclencherait un processus de carbonisation observable en formant des brûlures à la surface de la peau. En particulier, la conductivité thermique de la peau est faible. Par conséquent, la plus

grande partie de l'augmentation de la chaleur est limitée à la surface autour du point d'éclairage laser ou à proximité de celle-ci. Elle décroît fortement au bout de quelques millimètres seulement. Cela entraîne une augmentation rapide et abrupte de la température au centre du faisceau, qui provoque de graves dommages thermiques à la surface de la peau, aboutissant à la carbonisation des tissus.

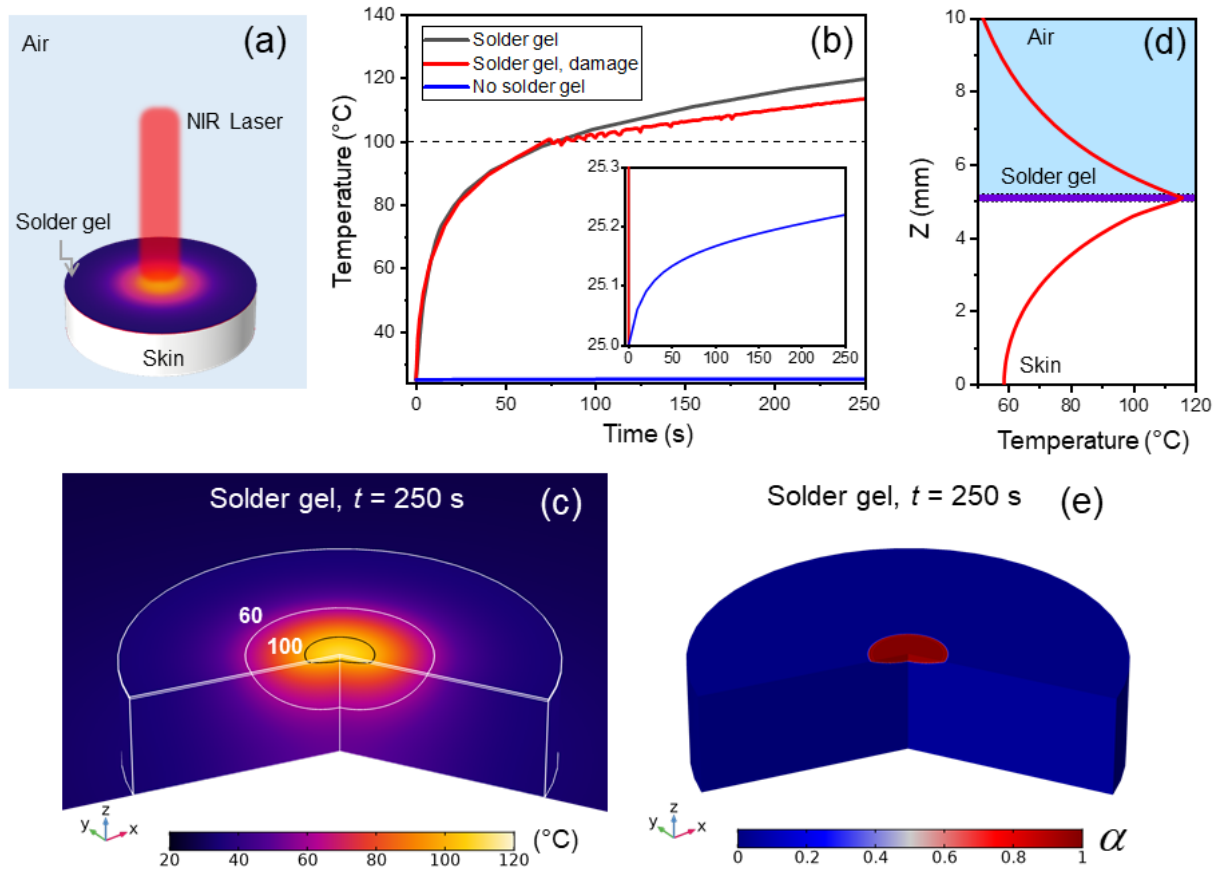


Figure 6: Modèle de transfert de chaleur spatiotemporal de l'interaction laser-tissu. (a) Schéma du modèle d'éléments finis de l'interaction laser-tissu assistée par les NPs. (b) Simulations de température dans le haut, au centre de la peau, avec et sans modélisation des lésions tissulaires. L'encart montre la courbe de température sans l'application de gel de soudure. (c) Simulation d'une distribution tridimensionnelle de la température dans la peau avec l'application de gel de soudure au temps d'exposition laser de 250 secondes. Les contours de température de 60 °C et de 100 °C sont surlignés en noir et blanc, respectivement. (d) Distribution spatiale de la température le long de la profondeur au centre de l'échantillon de peau. (e) Estimation de la répartition des dommages sur la peau lors de l'application de gel de soudure au temps d'exposition laser de 250 secondes. (Figure adaptée des références [137])

La figure 6 (d) illustre la distribution spatiale de la température à l'intérieur du tissu cutané et de l'air environnant. La simulation prouve que la chaleur accumulée générée par la forte absorption du gel de soudure mélangé aux GNRs est déposée de manière étanche dans une zone bien confinée à proximité de la surface de la peau. Près de 120 °C est atteint à l'interface entre la peau et le gel de soudure. Cette valeur chute en dessous de 60 °C à 5 mm sous la couche superficielle

de la peau et à 8 mm au-dessus de la peau dans l'air ambiant. Les dommages thermiques ont également été modélisés à l'aide de la suite logicielle COMSOL Multiphysics. Le seuil d'endommagement a été fixé à une température critique $T = 100\text{ °C}$ et à un délai maximum de 10 s. À cette température, le tissu cutané devient non seulement nécrotique, mais se carbonise également. La gravité des dommages thermiques est indiquée par le paramètre α , compris entre zéro (tissu non endommagé) et un (tissu nécrosé carbonisé). La figure 6 (e) montre la distribution de la gravité des dommages après un temps d'irradiation dans le proche infrarouge de 250 secondes représenté par l'indicateur de dommages α . Les simulations concluent que l'application d'un gel de soudure mélangé aux GNRs permet d'obtenir une forte augmentation de température bien confinée dans l'échantillon de tissu cutané. Lorsque la température dépasse certains niveaux de température, la peau change de teneur en eau, ce qui finit par créer des zones de lésions tissulaires de niveaux de gravité différents.

Le rayonnement THz a été utilisé pour étudier le processus d'interaction laser-tissu assisté par les NPs et pour évaluer diverses zones présentant différentes caractéristiques de dommages thermiques. Une mesure dynamique THz basée sur le schéma THz-TDS en réflexion (figure 7 (a)) a été déployée pour suivre l'évolution des signaux THz au cours d'un processus d'interaction laser-tissu. Le tissu cutané de l'oreille porcine a été utilisé comme modèle in vitro pour la peau humaine, car ses propriétés histologiques et physiologiques sont très similaires [158]. Par conséquent, la peau de porc est considérée comme un substitut approprié et convient bien aux études précliniques. Une fine couche de gel de soudure d'épaisseur d'environ 200 μm et de 8 mm de large a été déposée à la surface d'un échantillon de peau de porc excisé (figure 7 (b)). Un laser NIR à onde continue irradiant à 786 nm ayant un diamètre de tache de 4,4 mm et une intensité de puissance de 4,2 W/cm^2 a été appliqué au centre du gel de soudure. Le rayonnement laser a excité le LSPR des GNRs, qui à leur tour ont transformé l'énergie du laser presque entièrement en chaleur. La chaleur générée s'est dissipée dans une zone superficielle de la peau autour du point laser. Le faisceau THz était incident sur l'échantillon avec un angle de 45° et un diamètre de tache de spot d'environ 1,4 mm superposé au faisceau laser NIR. Le gel de soudure et l'échantillon de peau en dessous ont été irradiés pendant 250 secondes à l'aide du laser NIR décrit. La vitesse de chauffage était modeste au cours de cette période pour permettre aux mesures THz de suivre le processus d'interaction laser-tissu. Le processus de chauffage a été interrompu après les 250 secondes en raison d'effets de carbonisation sur le point de focalisation du faisceau laser (Figure 7 (c)), comme prédit par les simulations numériques de la Figure 7 (e). Une mesure dynamique THz consistait en 250 mesures THz qui ont été successivement enregistrées comme indiqué à la figure 7 (d).

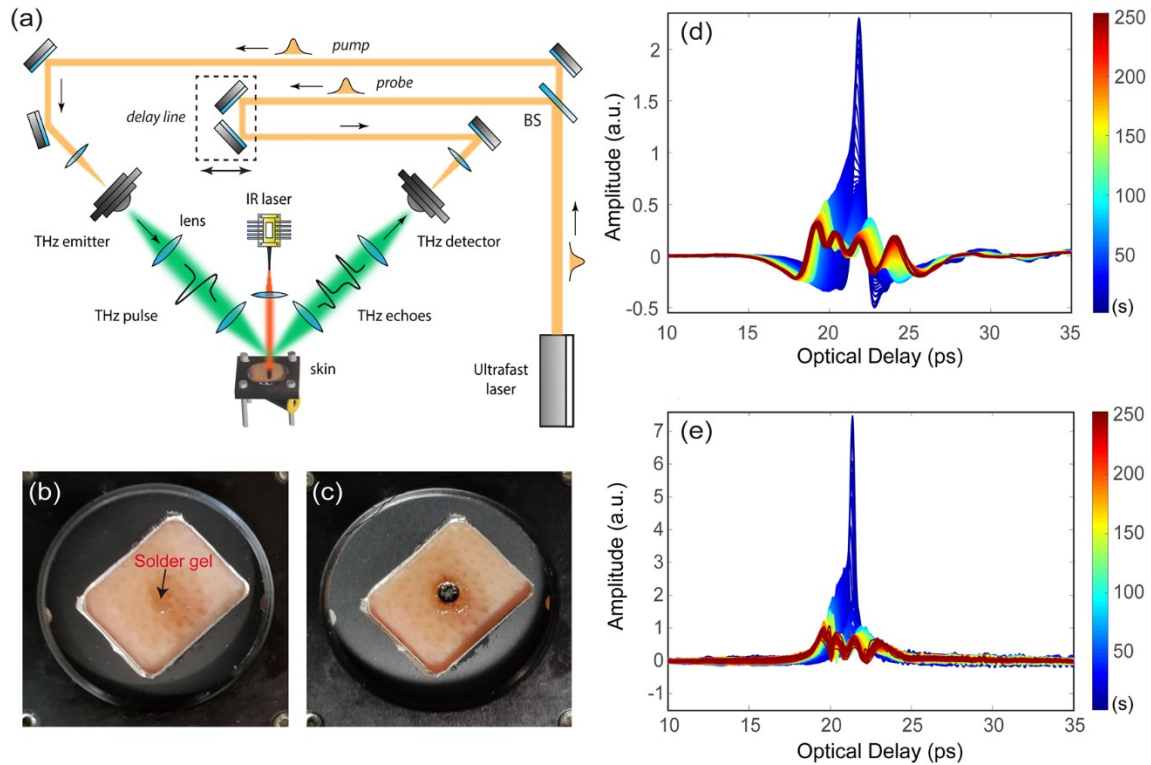


Figure 7: Mesures dynamiques THz. (a) Configuration expérimentale du montage THz-TDS en géométrie de réflexion. Le faisceau NIR à 786 nm est utilisé pour chauffer de manière plasmonique le gel de soudure incorporé dans les GNRs et l'échantillon de peau de porc. Photographies numériques de l'échantillon de peau de porc (b) avec du gel de soudure et incorporation de GNRs appliqué sur la surface, (c) après chauffage plasmonique pendant 250 secondes. Ici, on observe une carbonisation à la surface. (d) Les 250 signaux THz réfléchis enregistrés (une trace THz par seconde) pendant l'éclairage laser. (e) Déconvolution des 250 signaux obtenus après l'application de l'algorithme FWDD aux signaux THz bruts de (d). (Figure adaptée des références [137])

L'évolution du signal THz au cours des 250 secondes a connu une chute brutale d'amplitude du signal THz dans les 50 premières secondes. Cela peut s'expliquer par un fort processus de déshydratation dans le gel de soudure ainsi que dans le tissu cutané en raison de l'augmentation soudaine de la température conduisant à une réflectivité plus faible du faisceau THz et à une pénétration plus élevée du faisceau THz dans le tissu cutané. De plus, la durée temporelle de la trace d'impulsion THz s'est prolongée de manière significative, causée par la formation de multiples zones (couches) avec différentes propriétés diélectriques (c.-à-d. Indices de réfraction) à l'intérieur du gel de soudure et de la peau en raison d'une lésion tissulaire progressive provoquée par la photo-thermie. Les échos THz observables dans la trace de domaine temporel sont créés par des réflexions sur les interfaces entre deux couches adjacentes. Si l'épaisseur de la couche est inférieure à la longueur d'onde THz, les échos THz respectifs se superposent partiellement. Dans ce cas, la trace THz consistait en une suite d'échos successifs qui devaient être résolus distinctement dans le temps. Cela a permis une interprétation explicite des

dommages des tissus dans les différentes zones créées par le processus de chauffage photothermique. Les 250 traces THz enregistrées successivement à partir de la mesure dynamique, illustrées à la figure 7 (d), ont été post-traitées par la technique de déconvolution dite « frequency-wavelet domain deconvolution » (FWDD) [48], voir (figure 7 (e)). Chaque pic dans les traces déconvoluées représente une interface dans la structure de l'échantillon. Sa position dans le temps et l'amplitude indique respectivement l'emplacement et la réflectivité de l'interface spécifique. De plus, le signe de la valeur du pic dépend de la valeur des indices de réfraction des interfaces opposées. Une valeur de crête positive signifie que l'écho THz provient d'une interface où l'indice de réfraction passe d'une valeur inférieure à une valeur supérieure. Dans le cas contraire, l'écho THz est inversé et la valeur maximale devient négative. Sur la figure 7 (e), les pics sont tous positifs, car l'indice de réfraction augmente toujours à chaque interface consécutive. Cela est dû à la déshydratation progressive de l'échantillon de peau qui évolue de l'extérieur (faible teneur en eau = zones inférieures d'indice de réfraction) vers l'intérieur (teneur élevée en eau = zones de plus haut indice de réfraction) de la peau. Les traces brutes et déconvolution THz enregistrées à des intervalles de temps spécifiques sont tracées à la figure 8 et expliquées dans le tableau 1 pour illustrer l'évolution du signal au cours du processus de chauffage plasmonique. Notez que le signal déconvolué a été normalisé à son amplitude maximale. En conséquence, le signal THz déconvolué a révélé la transition de zones affectées thermiquement dans le gel de soudure et le tissu cutané au cours du chauffage plasmonique au moyen de l'éclairage au laser NIR. Des informations sur ces zones tissulaires affectées thermiquement, telles que la profondeur, l'épaisseur de la couche, le taux d'humidité, les propriétés diélectriques, peuvent être obtenues à partir de la largeur temporelle des échos et de la localisation des pics dans les traces THz déconvoluées. Les informations de profondeur peuvent être dérivées de la traduction du retard optique en distance en connaissant l'indice de réfraction de la couche respective. Par exemple, sur la figure 8 (b2), les deux pics THz qui confinent la couche de BSA sont distants de 0,75 ps.

L'indice de réfraction de la BSA à 107 °C est d'environ 1,80 [173]. L'épaisseur de couche de la couche de soudure déshydratée a été estimée à environ 44 μm . L'indice de réfraction du tissu cutané change de manière significative avec la teneur en eau. Malheureusement, les indices des tissus cutanés différemment hydratés et endommagés dans le régime de fréquence THz ne sont pas encore disponibles dans la littérature. Un indice de réfraction effectif de 1,20 [174] a été utilisé pour la peau de porc déshydratée afin de déterminer approximativement la profondeur des dommages thermiques causés aux tissus. Le retard optique total dû au dommage thermique au temps $t = 250$ ps de la figure 8 (a8) est de 5,35 ps. Cela se traduit par une épaisseur d'environ

315 μm pour le tissu cutané porcine déshydraté et endommagé. Le rayonnement THz ne peut plus pénétrer dans la zone de coagulation car la concentration en eau est trop élevée [175]. Par conséquent, la zone de dommages thermiques pénétrable est limitée à la partie superficielle de la peau.

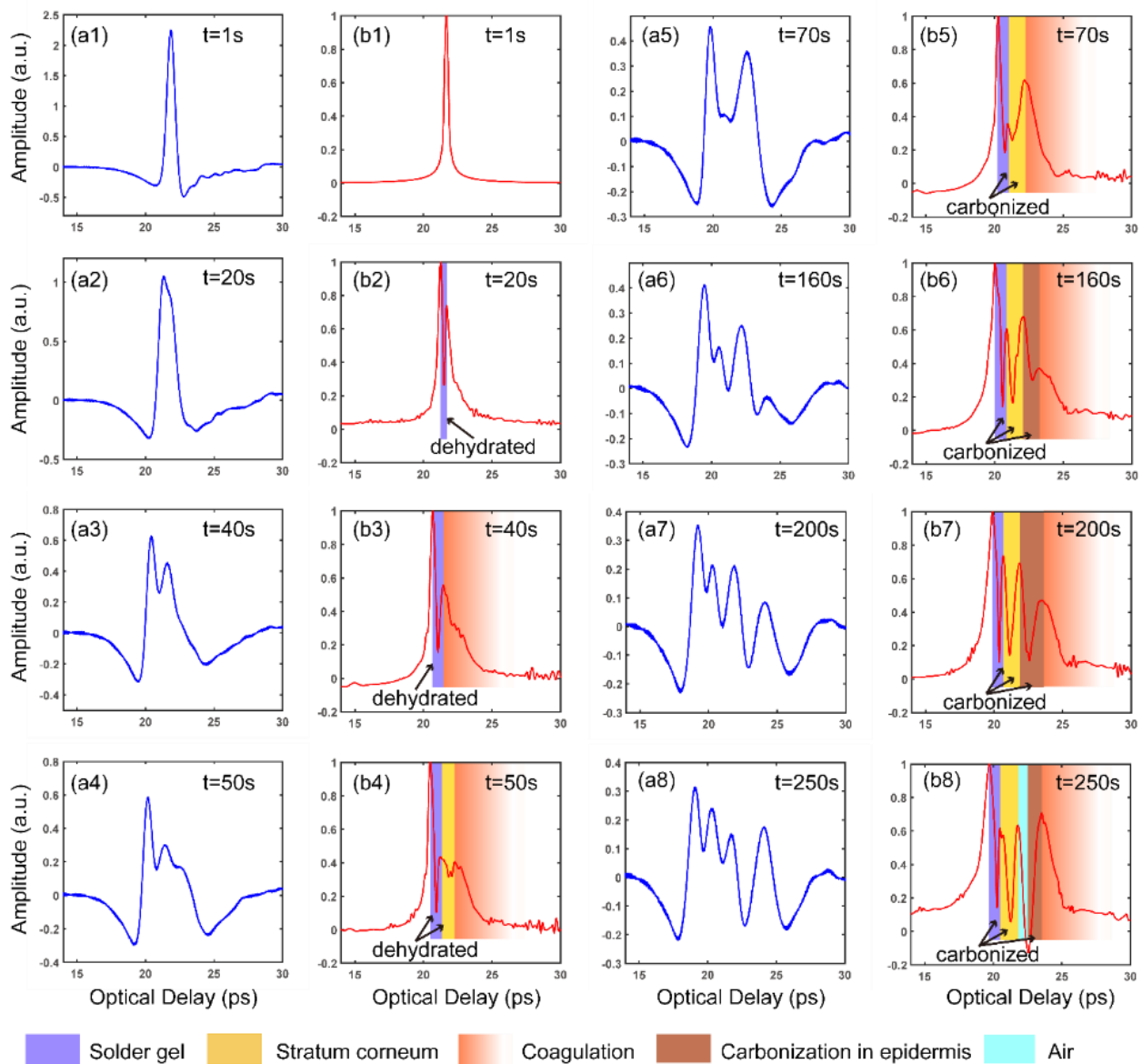


Figure 8: Signaux bruts et déconvolution typiques THz à des instants spécifiques t dérivés de la mesure dynamique en THz. (a1-a8) correspondent aux signaux bruts THz enregistrés à $t = 1\text{ s}$, 20 s , 40 s , 50 s , 70 s , 160 s , 200 s et 250 s , respectivement. (b1-b8) correspondent aux signaux déconvolutionnés après application d'un algorithme de type FWDD aux signaux THz bruts. Le signal déconvolué est normalisé à son niveau de crête maximal. (Figure adaptée des références [137])

Tableau 1: Description des effets photo-thermiques sur l'échantillon de peau de porc lors de la mesure THz.

Temps	Figure 8	Observation
1 s	(a1) et (b1)	Les signaux bruts et déconvolués ne montrent qu'un seul écho THz qui a été réfléchi par la surface du gel de soudure. Le niveau d'hydratation élevé du gel de soudure empêchait toute pénétration de THz plus en profondeur dans le matériau. Durant les secondes qui ont suivi, la température a augmenté rapidement à l'intérieur du gel de soudure et de l'échantillon de peau, entraînant une déshydratation progressive. Par conséquent, le rayonnement THz était capable de pénétrer dans le gel de soudure pour atteindre la surface de la peau sous-jacente.
20 s	(a2) et (b2)	Un écho de réflexion THz plus large à amplitude réduite est illustré, ce qui indique deux échos convolutés. Après l'application de la technique FWDD, les deux pics ont été séparés. Ceux-ci proviennent des réflexions sur la surface du gel de soudure et de l'interface gel de soudure / peau. Ensuite, le gel de soudure s'est solidifié et la peau s'est déshydratée de l'extérieur vers l'intérieur créant au fil du temps, un gradient de déshydratation au sein de la peau. Cela a permis aux ondes THz de pénétrer plus profondément dans le tissu cutané et de rencontrer plus de couches formées par les dommages photo-thermiques engendrés par l'irradiation laser.
40 s	(a3) et (b3)	Les échos partiellement superposés sont devenus encore plus larges, ce qui a également pu être observé dans le tracé THz post-traité. Le gradient d'hydratation induit par la chaleur crée une interface progressive, ce qui signifie que l'indice de réfraction augmente légèrement en profondeur, formant une région initiale de la coagulation cellulaire.
50 s	(a4) et (b4)	Un écho supplémentaire dans le signal brut a été identifié comme une autre couche dans le signal déconvolué correspondant à la couche de type cornée de la peau, qui était sèche et pouvait donc être résolue par le rayonnement THz.
70 s	(a5) et (b5)	Le gel de soudure et la couche de cornée ont commencé à se carboniser, ce qui était visible à la surface de la peau.

160 s	(a6) et (b6)	La formation d'une zone de carbonisation dans l'épiderme a été provoquée par une nouvelle augmentation de la température.
200 s	(a7) et (b7)	La couche de carbonisation dans l'épiderme s'est élargie.
250 s	(a8) et (b8)	Le laser NIR a été éteint depuis que la peau a commencé à se vaporiser et s'est gonflé à cause d'une couche d'air émergente située entre la zone de carbonisation et la zone de coagulation. La couche d'air est mise en évidence dans le tracé THz par un écho THz inversé avec un pic négatif dû à la transition d'indice de réfraction plus élevé à un indice plus faible.

De plus, une incision cutanée a été soudée au laser, assistée par un gel de soudure de NPs dans une configuration *in vitro*, puis visualisée par un rayonnement THz en mode réflexion. Les données d'image THz ont ensuite été analysées pour obtenir des informations sur les dommages thermiques causés par le tissu cutané et résolus en trois dimensions. Une incision de 5 mm de profondeur et de 10 mm de long a été pratiquée à la surface d'échantillons de peau de porc à l'aide d'une lame chirurgicale. Ensuite, l'incision et ses gravures ont été recouvertes d'un gel de soudure. Un faisceau laser NIR avec une raie d'émission à 786 nm et un diamètre de focalisation de 1,1 mm a été utilisé pour chauffer de manière plasmonique les GNRs dans le gel de soudure du BSA. Ceci, a chauffé le tissu environnant de l'incision, conduisant à la reconnexion du collagène et par conséquent à la fusion de la plaie. Trois échantillons de tissus avec des incisions cutanées ont été soudés sous différentes intensités de faisceau laser de 20 W/cm² (figure 9 (a1)), 30 W/cm² (figure 9 (a2)) et 40 W/cm² (figure 9 (a3)). La gravité des dommages causés aux tissus thermiques a augmenté avec l'intensité croissante de la puissance laser, montrant différents niveaux d'effets de carbonisation dans la couche superficielle de la peau. Une fois le processus de soudure au laser terminé, les échantillons ont été analysés avec une résolution de 0,5 mm dans une configuration d'imagerie par réflexion THz. Les données d'imagerie 3D ont été acquises pour chaque échantillon comprenant une trace THz complète pour chaque position de pixel. L'algorithme FWDD a été utilisé pour déconvoluer les traces, qui ont ensuite été normalisées par leur valeur maximale. Les images THz de type C-scan (direction X-Y) des échantillons de peau soudés sont présentées pour des intensités laser de 20 W/cm², 30 W/cm² et 40 W/cm² sur la figure 9 (b1-b3). L'amplitude maximale des traces THz déconvoluées a été utilisée pour conférer un contraste à l'image. Les images ont été normalisées par leur valeur d'amplitude maximale. L'amplitude THz est influencée par le niveau de déshydratation de la zone cutanée, qui servait donc de mécanisme de contraste dominant. Les zones situées au centre de l'incision présentent

une valeur d'amplitude inférieure, ce qui est dû à une réflectivité THz plus faible, ces zones étant le plus souvent déshydratées par l'effet de chauffage plasmonique. Les images en coupe THz, appelées B-scans, fournissent des informations en profondeur (direction X-Z) et sont représentées pour les intensités laser de 20 W/cm^2 , 30 W/cm^2 et 40 W/cm^2 sur la figure 9 (c1-c3). Ces images en coupe transversale THz tracent la largeur temporelle des échos THz déconvolués sur une ligne au centre de l'incision soudée qui peut être traduite en informations d'épaisseur de couche réelle en connaissant l'indice de réfraction du matériau. Le paramètre de contraste représente l'amplitude normalisée des échos THz déconvolutionnés dans chaque pixel. Des images en coupe binaires THz sont représentées pour des intensités laser de 20 W/cm^2 , 30 W/cm^2 et 40 W/cm^2 sur la figure 9 (d1-d3). Ils ont été obtenus en attribuant la valeur de 1 à chaque pic THz identifié qui représente une interface de couche. Toutes les autres amplitudes THz de la trace dans le domaine temporel ont été définies à zéro. Ces images montrent distinctement le nombre et la position en profondeur des interfaces identifiées dans un matériau. À l'intensité du laser 20 W/cm^2 dans la figure 9 (c1), la surface air / gel de soudure et l'interface gel de soudure / peau sont clairement distinguables. Apparemment, l'interface gel de soudure / peau dans la direction X constitue une crête continue offrant un contraste plus fort que la réflexion de la surface air / gel de soudure. Cela prouve que le gel de soudure était fortement déshydraté par la procédure de chauffage plasmonique et que le rayonnement THz était capable d'atteindre la surface de la peau. Cependant, la peau à ce moment-là n'était pas gravement endommagée, comme le montre la figure 9 (d1), car il n'y a pas de réflexions d'interface significatives provenant de la zone sous la surface. À l'intensité laser 30 W/cm^2 de la figure 9 (c2), la largeur de l'écho de l'interface gel de soudure / peau s'est considérablement élargie, ce qui indique une pénétration plus profonde du rayonnement THz dans la peau en raison d'une déshydratation accrue et donc de dommages thermiques plus importants. Des interfaces supplémentaires dans la sous-cutanée (Figure 9 (d2)) suggèrent la formation de zones de carbonisation et de coagulation. À une intensité laser de 40 W/cm^2 sur la figure 9 (c3), le gel de soudure et la surface de la peau ont été fortement carbonisés car les échos provenant du gel de soudure et de la surface de la peau sont fortement élargis et ne peuvent donc plus être discernés. De plus, il n'y a pas d'interface supplémentaire sous la surface visible sur la figure 9 (d3). La zone de dommages thermiques s'est donc élargie et déplacée plus profondément dans l'épiderme.

La figure 10 présente des images tridimensionnelles acquises par imagerie à balayage THz montrant la profondeur des dommages thermiques résultant du réchauffement plasmonique pendant le processus de soudage au laser avec assistance de NPs pour des intensités de puissance laser NIR de 20 W/cm^2 , 30 W/cm^2 et 40 W/cm^2 . La zone la plus endommagée

thermiquement se situe au centre de la zone d'incision et a grandi en profondeur et s'est étendue jusqu'aux limites de l'incision cutanée. La profondeur des dommages thermiques a été estimée en approximant l'indice de réfraction de la région de peau endommagée et en mesurant le retard optique des échos THz. La zone endommagée atteint environ 600 μm de profondeur avec une intensité laser de 40 W/cm^2 . En conséquence, cette étude a démontré qu'il était possible d'estimer quantitativement la distribution des dommages thermiques induits par le soudage laser en trois dimensions.

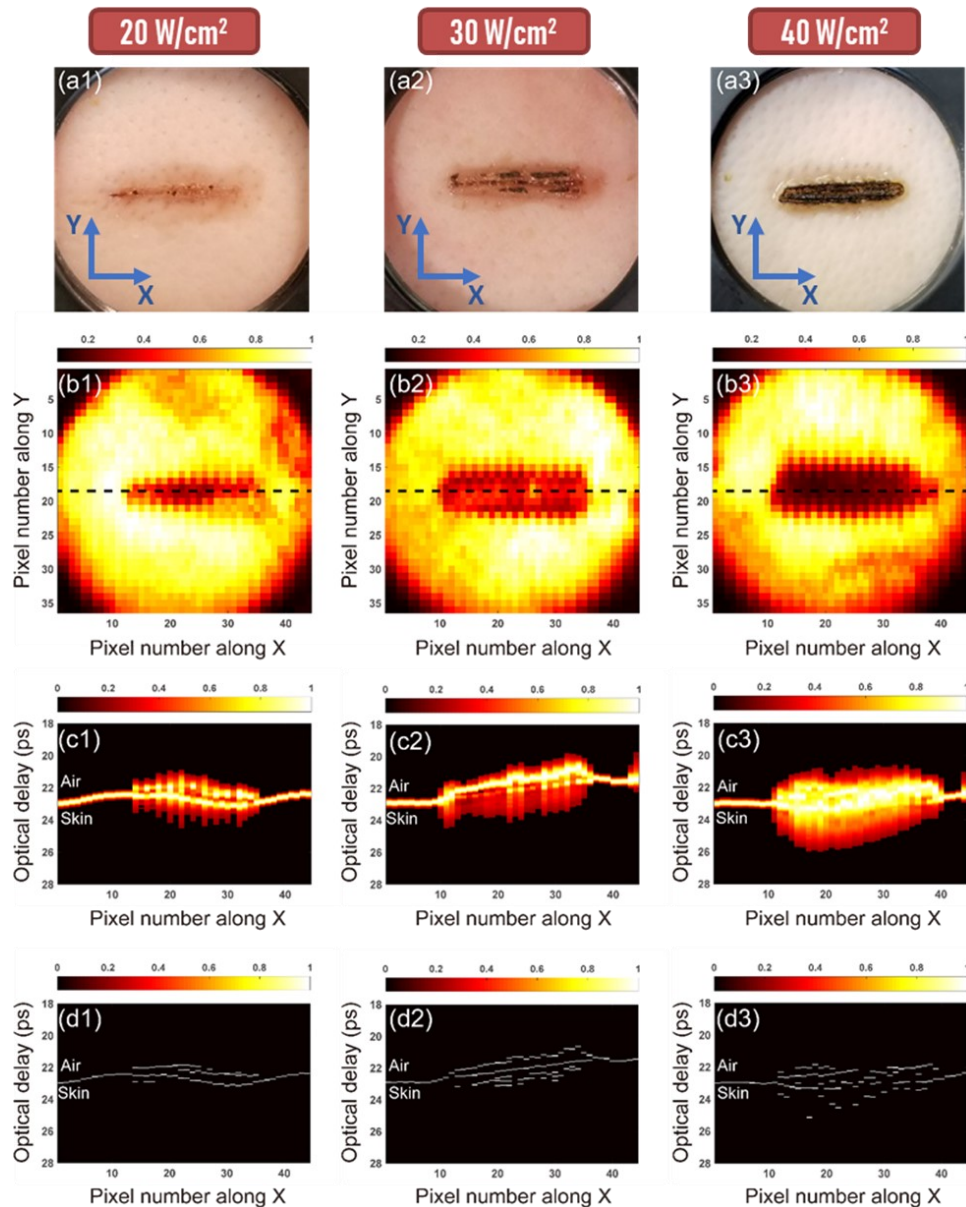


Figure 9: Image THz d'échantillons de peau de porc après soudure au laser avec une intensité de 20 W/cm^2 , 30 W/cm^2 et 40 W/cm^2 . (a) image numérique, (b) image THz C-scan, (c) image en coupe transversale THz et (d) image en coupe transversale binaire THz. Les images en coupe transversale (c) et (d) sont extraites de la ligne pointillée marquée en b1-b3. (Figure adaptée des références [137])

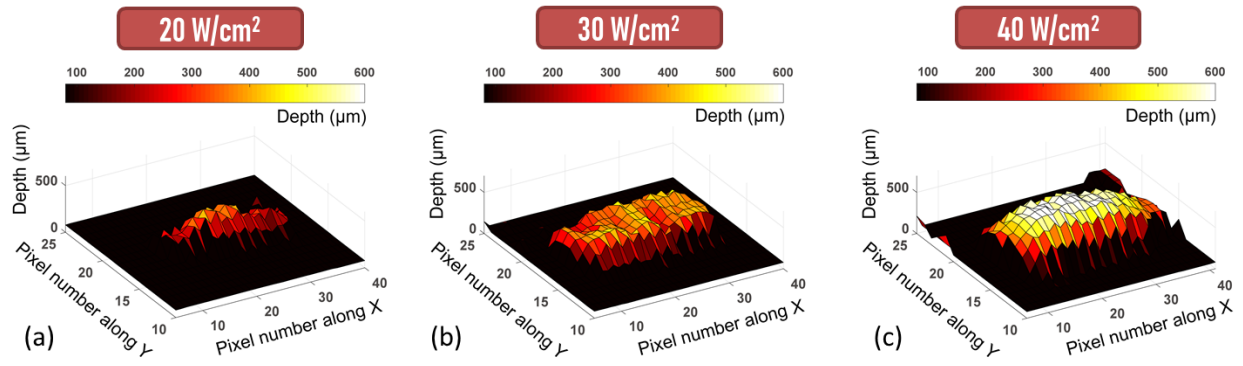


Figure 10: Images THz tridimensionnelles de l'échantillon de peau de porc après soudure au laser avec une intensité de (a) 20 W/cm², (b) de 30 W/cm² et (c) de 40 W/cm² illustrant la profondeur des dommages thermiques infligé par l'effet de chauffage plasmonique lors de l'illumination laser NIR. (Figure adaptée des références [137])